TOPICS IN CURRENT CHEMISTRY 270

Volume Editor K. Naka

Biomineralization I

Crystallization and Self-Organization Process

Springer

270
Topics in Current Chemistry

Topics in Current Chemistry

Recently Published and Forthcoming Volumes

Bioactive Confirmation I
Volume Editor: Peters, T.
Vol. 272, 2007

Biomineralization II
Mineralization Using Synthetic Polymers and Templates
Volume Editor: Naka, K.
Vol. 271, 2007

Biomineralization I
Crystallization and Self-Organization Process
Volume Editor: Naka, K.
Vol. 270, 2007

Novel Optical Resolution Technologies
Volume Editors:
Sakai, K., Hirayama, N., Tamura, R.
Vol. 269, 2007

Atomistic Approaches in Modern Biology
From Quantum Chemistry
to Molecular Simulations
Volume Editor: Reiher, M.
Vol. 268, 2006

Glycopeptides and Glycoproteins
Synthesis, Structure, and Application
Volume Editor: Wittmann, V.
Vol. 267, 2006

Microwave Methods in Organic Synthesis
Volume Editors: Larhed, M., Olofsson, K.
Vol. 266, 2006

Supramolecular Chirality
Volume Editors: Crego-Calama, M.,
Reinhoudt, D. N.
Vol. 265, 2006

Radicals in Synthesis II
Complex Molecules
Volume Editor: Gansäuer, A.
Vol. 264, 2006

Radicals in Synthesis I
Methods and Mechanisms
Volume Editor: Gansäuer, A.
Vol. 263, 2006

Molecular Machines
Volume Editor: Kelly, T. R.
Vol. 262, 2006

Immobilisation of DNA on Chips II
Volume Editor: Wittmann, C.
Vol. 261, 2005

Immobilisation of DNA on Chips I
Volume Editor: Wittmann, C.
Vol. 260, 2005

Prebiotic Chemistry
From Simple Amphiphiles to Protocell Models
Volume Editor: Walde, P.
Vol. 259, 2005

Supramolecular Dye Chemistry
Volume Editor: Würthner, F.
Vol. 258, 2005

Molecular Wires
From Design to Properties
Volume Editor: De Cola, L.
Vol. 257, 2005

Low Molecular Mass Gelators
Design, Self-Assembly, Function
Volume Editor: Fages, F.
Vol. 256, 2005

Anion Sensing
Volume Editor: Stibor, I.
Vol. 255, 2005

Organic Solid State Reactions
Volume Editor: Toda, F.
Vol. 254, 2005

Biomineralization I

Crystallization and Self-Organization Process

Volume Editor: Kensuke Naka

With contributions by

C. K. Carney · M. Fricke · S. R. Harry · H. Imai
R. Kniep · K. Sato · S. L. Sewell · P. Simon
D. Volkmer · D. W. Wright

Springer

The series *Topics in Current Chemistry* presents critical reviews of the present and future trends in modern chemical research. The scope of coverage includes all areas of chemical science including the interfaces with related disciplines such as biology, medicine and materials science. The goal of each thematic volume is to give the nonspecialist reader, whether at the university or in industry, a comprehensive overview of an area where new insights are emerging that are of interest to a larger scientific audience.

As a rule, contributions are specially commissioned. The editors and publishers will, however, always be pleased to receive suggestions and supplementary information. Papers are accepted for *Topics in Current Chemistry* in English.

In references *Topics in Current Chemistry* is abbreviated Top Curr Chem and is cited as a journal.

Visit the TCC content at springerlink.com

ISSN 0340-1022
ISBN-10 3-540-46379-8 Springer Berlin Heidelberg New York
ISBN-13 978-3-540-46379-5 Springer Berlin Heidelberg New York
DOI 10.1007/978-3-540-46380-1

Springer is a part of Springer Science+Business Media

springer.com

Cover design: WMXDesign GmbH, Heidelberg
Typesetting and Production: LE-TEX Jelonek, Schmidt & Vöckler GbR, Leipzig

Printed on acid-free paper 02/3100 YL – 5 4 3 2 1 0

Volume Editor

Dr. Kensuke Naka

Kyoto University
Graduate School of Engineering
Department of Polymer Chemistry
Katsra, 615-8501 Kyoto, Japan
ken@chujo.synchem.kyoto-u.ac.jp

Editorial Board

Topics in Current Chemistry
Also Available Electronically

For all customers who have a standing order to Topics in Current Chemistry, we offer the electronic version via SpringerLink free of charge. Please contact your librarian who can receive a password or free access to the full articles by registering at:

springerlink.com

If you do not have a subscription, you can still view the tables of contents of the volumes and the abstract of each article by going to the SpringerLink Homepage, clicking on "Browse by Online Libraries", then "Chemical Sciences", and finally choose Topics in Current Chemistry.

You will find information about the

- Editorial Board
- Aims and Scope
- Instructions for Authors
- Sample Contribution

at springer.com using the search function.

Preface

In nature, biological organisms produce mineralized tissues such as bone, teeth, diatoms, and shells. Biomineralization is the sophisticated process of production of these inorganic minerals by living organisms. Construction of organic–inorganic hybrid materials with controlled mineralization analogous to those produced by nature has recently received much attention because it can aid in understanding the mechanisms of the biomineralization process and development of biomimetic materials processing. The biomineralization processes use aqueous solutions at temperatures below 100 °C and no toxic intermediates are produced in these systems. From a serious global environmental problem point of view, the development of processes inspired by biomineralization would offer valuable insights into material science and engineering to reduce energy consumption and environmental impact. One of the most challenging scientific problems is to gain greater insight into the molecular interactions occurring at the interface between the inorganic mineral and the macromolecular organic matrix. Model systems are often regarded as a straight-forward experimental approach toward biomimetic crystallization. Hierarchical architectures consisting of small building blocks of inorganic crystals are often found in biominerals. Studies of nanocrystal self-organization in solution systems would also be helpful for understanding biomineralization.

In these volumes, we focus on construction of organic–inorganic hybrid materials with controlled mineralization inspired by natural biomineralization. In the first volume, the reader will find contributions providing a basic scope of the mineralization process in aqueous solution. The first chapter by Marc Fricke and Dirk Volkmer introduce Mollusk shell formation, crystallization of $CaCO_3$ underneath monolayer via epitaxial and non-epitaxial growth. Hiroaki Imai describes hierarchically structured crystals formed through self-organization in solution systems. A wide variety of complex morphologies including fractals, dendrites, and self-similar structures are reviewed. Fluoratite-gelatine nanocomposites, reviewed by Rüdiger Kniep and Paul Simon, are suited to obtaining deeper insight into processes of self-organization, and can help to learn about essentials in the formation of inorganic–organic nanocomposites of biological relevance. There is considerable academic and commercial interest in the development of hydroxyapatite (HAp) bioceramics and HAp-loaded polymer for bone replacement. Kimiyasu Sato summarized inorganic–organic

interfacial interactions in hydroxyapatite mineralization process. Biominerals are most often considered in either their more traditional roles as critical structural components of organisms. The biominerals are also important ion reservoirs for cellular function. It is becoming apparent that biominerals act as critical detoxification sinks within certain organisms. In the final chapter of the first volume, David Wright and his co-workers explain that the detoxification process make noble metal nanoparticles.

In the mineralized tissues, crystal morphology, size, and orientation are determined by local conditions and, in particular, the presence of "matrix" proteins or other macromolecules. Because the proteins that have been found to be associated with biominerals are usually highly acidic macromolecules, several water-soluble polyelectrolytes have been examined for the model of biomineralization in aqueous solution. The second volume will focus on controlled mineralization by synthetic templates. We start this volume with the latest advances in hydrophilic polymer controlled morphosynthesis and bioinspired mineralization of crystals reviewed by Helmut Cölfen. He also summarizes classical crystallization pathways as well as non-classical nanoparticle mediated crystallization routes. These basic overviews will be very useful for the reader to understand this field. Shu-Hong Yu reviews controlled mineralization by synthetic additives and templates, not only with simple water-soluble polymers, but also artificial interfaces and matrixes including monolayers and synthetic polymer matrix. In the next chapter, I will introduce delayed action of polymeric additives as a new method for controlled mineralization by synthetic polymers. Finally, Norikazu Ueyama and his co-workers describe the detailed chemistry of the interface between the inorganic mineral and the macromolecular organic matrix by their designed polymer ligands. Coordination information on synthetic Ca carboxylate complexes is important for the elucidation of the Ca–O bond on the surface of Ca-based biominerals.

It was my great pleasure to invite leading international scientists to contribute to this issue and write excellent and detailed reviews of recent developments in the field of biomineralization. Although several books about biomineralization have been published, those books focused on the progress of biomineralization in biology and molecular biology. No book about biomineralization has focused on the viewpoint of constructing the bio-inspired organic–inorganic hybrid materials. The continuous cooperation of organic and polymer chemists with inorganic and biochemists for the field of biomineralization is desirable for discovering new concepts and method for producing composite materials and crystalline forms analogous to those produced by nature.

Kyoto, September 2006 Kensuke Naka

Contents

Contents of Volume 271

Biomineralization II

Volume Editor: Kensuke Naka
ISBN: 978-3-540-46376-4

Top Curr Chem (2007) 270: 1–41
DOI 10.1007/128_063

Published online: 16 September 2006

Crystallization of Calcium Carbonate Beneath Insoluble Monolayers: Suitable Models of Mineral–Matrix Interactions in Biomineralization?

Marc Fricke[1,2] · Dirk Volkmer[1] (✉)

[1]Anorganische Chemie II, Universität Ulm, Albert-Einstein-Allee 11, 89081 Ulm, Germany
dirk.volkmer@uni-ulm.de

[2]ISIS, groupe BASF, ULP, 8, allée Gaspard Monge, 67083 Strasbourg, France

Abstract The growth of inorganic materials below negatively charged monolayers is frequently considered to be a suitable model system for biomineralization processes. The fact that some monolayers give rise to oriented overgrowth of calcium carbonate crystals has been interpreted in terms of a geometrical and stereochemical complementarity between the arrangement of headgroups in the monolayer and the position of Ca ions in the crystal plane that attaches to the monolayer. However, comparative investigations of the growth of calcium carbonate beneath monolayers of macrocyclic polyacids have demonstrated that non-directional electrostatic parameters, such as the average charge density or the mean dipole moment of the monolayer, determine the orientation and the polymorph of the overgrowing crystals. The results show that it is possible to control the surface charge densities in monolayers by the appropriate design of amphiphilic molecules. A switch in polymorph occurs above a critical monolayer charge density at

which aragonite or vaterite nucleation takes place, presumably via a kinetically controlled precipitation process.

Keywords Calcium carbonate · Biomineralization · Mollusc shell · Nacre · Monolayers · Template mechanism · Epitaxy

1 Introduction

Many organisms have developed sophisticated strategies for directing the growth of the inorganic constituents of their mineralized tissues. Active control mechanisms are effective at almost all levels of structural hierarchy, ranging from the nanoscopic regime (the nucleation of a crystallite at a specific site) up to the macroscopic regime, where the biophysical properties of the mineralized tissue are matched to certain functions [1]. Among the many open questions, one of the most challenging scientific problems is to gain greater insight into the molecular interactions occurring at the interface between the inorganic mineral and the macromolecular organic matrix. Biogenic crystals often express exceptional habits that are seemingly unrelated to the morphology of the same type of crystals grown under equilibrium conditions.

The morphology of the calcified tissue is ultimately encoded in the genome governing the biosynthesis of required materials at the cellular level of structural hierarchy. Therefore, biomineralization, as a highly complex phenomenon involving living organisms, cannot be reduced to a single mechanistic aspect (Fig. 1). The following representation of $CaCO_3$ mineralization in molluscs, and its mimesis by simple model systems, is admittedly a crude simplification that concentrates mainly on structural aspects, while at the same time ignoring the dynamic character of the biological process. Special emphasis here is placed on $CaCO_3$ crystal nucleation, i.e., the early stages of crystal growth where the system properties might be described by (supra-)molecular recognition events occurring at the mineral–matrix interface. At this level, a common feature seems to exist for many mineralizing organisms: the interaction of highly specialized acidic macromolecules with different surfaces of the growing single crystal [4, 5]. For the most widespread calcified tissues it is frequently assumed that a structurally rigid composite matrix consisting of fibrous proteins and acidic macromolecules adsorbed thereon acts as a "supramolecular blueprint" that templates nucleation of the inorganic phase. Subsequent crystal growth proceeds within a specialized compartment enclosing a suitable aqueous microenvironment. The particular composition of solutes, which is often comprised of a complex mixture of dissolved electrolytes and macromolecules, has a strong influence on the morphology of the crystals. In the course of mineral deposition, growth mod-

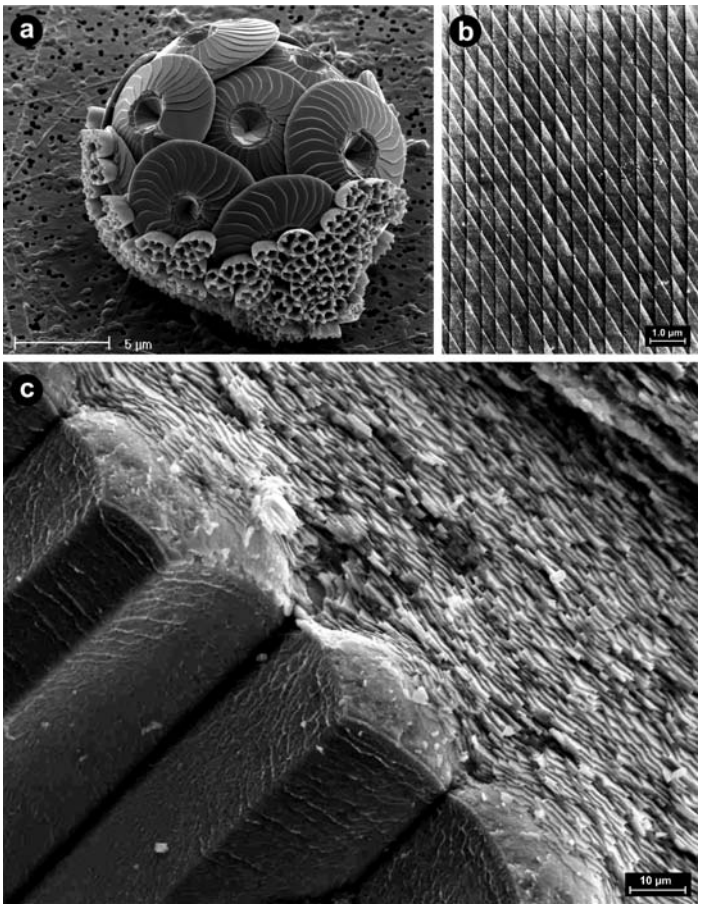

Fig. 1 Examples of biologically produced highly oriented calcerous structures exemplifying the astonishing degree of sophistication with which certain organisms can control the growth of inorganic crystals. **a** SEM of the calcerous test ("coccosphere") produced by a coccolithophorid, a unicellular marine photosynthetic alga. Note the interlocked arrangement of minute calcite plates that cover the cell. Shown here is a combination coccosphere with both hetero- and holococcoliths (*Calcidiscus leptoporus* & *Syracolithus quadriperforatus*). Combination coccospheres are thought to represent a transitional state between heterococcolithophorid and holococcolithophorid phases of the life cycle [2]. (Micrograph courtesy of J. Young, Natural History Museum, London and M. Geisen, AWI Bremerhaven). **b** Freshly fractured shell of a Devonian brachiopod (*Pholidostrophia nacrea*) showing a crisscrossed pattern of calcite crystals that acts as a natural optical diffraction grating. This pattern gives rise to a nacreous luster and pearly iridescence that is unusual for calcite [3]. (Single-stage platinum-carbon replica. Approximately 20 000×. TEM photo courtesy of K.M. Towe, Smithsonian Institution). **c** SEM of a fractured shell of *Anodonta cygnea* showing the transition from the prismatic to the nacreous layer (prisms *bottom*, nacre *top*). Note that in this species both morphologically distinct layers consist of aragonite, whereas in most mollusc shells the prisms are normally made of calcite. (Micrograph courtesy of F. Marin, Université de Bourgogne)

ifiers may interact with the maturing crystal in different ways: dissolved macromolecules may be adsorbed onto specific crystal faces, thus slowing down or inhibiting deposition rates along certain crystallographic directions. Adsorbed macromolecules may be completely overgrown by the mineral to produce lattice defects or to introduce discontinuities in the crystal texture. Current research efforts of biologists and biochemists are focused on the isolation and characterization of macromolecules from calcified tissues, and the functional properties of isolated macromolecules or fractions of macromolecules are systematically investigated regarding their ability to influence $CaCO_3$ nucleation, growth, and polymorphism. Biologically inspired synthetic strategies attempt to assemble artificial matrices in order to mimic structural and functional properties of mineralizing tissues.

Special emphasis in this review is laid upon the crystallization of calcium carbonate underneath insoluble monolayers – a model system that is often regarded as a straight-forward experimental approach toward biomimetic crystallization. A summary of the most important experimental data gained from such monolayer investigations is presented here, with particular emphasis placed on our own work in this field. As will be shown, the numerous enthusiastic early reports of epitaxial growth of inorganic crystals beneath membrane-like monolayers might require some profound revision of the suggested mechanisms. Evidence from recent investigations suggests that the commonly held view of a structure-directing organic template matrix represents an oversimplified concept of the complex crystallization process. The current debate on the various roles of amorphous inorganic precursors, which were recently identified in biological specimen and biomimetic crystallization assays, reflects the many contradictory experimental findings and statements concerning this topic. An updated view on the putative crystallization stages taking place at the mineral/organic matrix interface is presented in the final chapter, which highlights the dynamic cooperative character of the process.

2
Crystallochemical Aspects of $CaCO_3$ Biomineralization

$CaCO_3$, together with amorphous silica, is the most abundant biomineral. There exist three $CaCO_3$ polymorphs – *calcite*, *aragonite*, and *vaterite* – all of which occur in calcified tissues. A monohydrate (*monohydrocalcite*) and a hexahydrate form (*ikaite*) of $CaCO_3$ have been characterized as metastable precursor phases during the incipient stages of crystal formation (Table 1).

At ambient conditions, calcite is the thermodynamically most stable $CaCO_3$ polymorph. However, from supersaturated aqueous solutions containing Mg^{2+} at a molar ratio Mg/Ca > 4 (comparable to the composition of seawater), the only observed crystalline phase is aragonite, while at high su-

Table 1 Characteristics of the most important $CaCO_3$ mineral phases

Mineral (formula)	Crystal system (space group)	Spec. density [g/cm^3]	Solubility [$-\log K_{sp}$]	Biologic occurrence	Crystal data ref.
Calcite ($CaCO_3$)	Trigonal ($R\bar{3}c$)	2.71	8.48	Very common	[6]
Aragonite ($CaCO_3$)	Orthorhombic ($Pmcn$)	2.93	8.34	Very common	[7]
Vaterite ($CaCO_3$)	Hexagonal ($P6_3/mmc$)	2.54	7.91	Rare	[8]
Monohydrocalcite ($CaCO_3 \cdot H_2O$)	Trigonal ($P3_121$)	2.43	7.60	Very rare	[9]
Ikaite ($CaCO_3 \cdot 6H_2O$)	Monoclinic ($C2/c$)	1.77	7.12	Unknown	[10]

Data adapted in part from [11]

persaturation the metastable polymorph vaterite precipitates from solution. The arrangement of the ions in crystalline $CaCO_3$ can be described in terms of separate layers of cations and anions. Coordination environments for Ca^{2+} ions (CO_3^{2-}, respectively) in the polymorphs differ from each other, as a result of different successions of layers, as well as different crystallographic orientations of the planar carbonate groups in the crystal lattices (Fig. 2). In calcite, each single densely packed Ca layer parallel to the *ab* plane is situated between single layers of CO_3^{2-}, with each layer containing anions oriented in opposite directions. Each Ca^{2+} ion is situated in a distorted octahedral coordination environment of six CO_3^{2-} anions. In aragonite, the positions of the

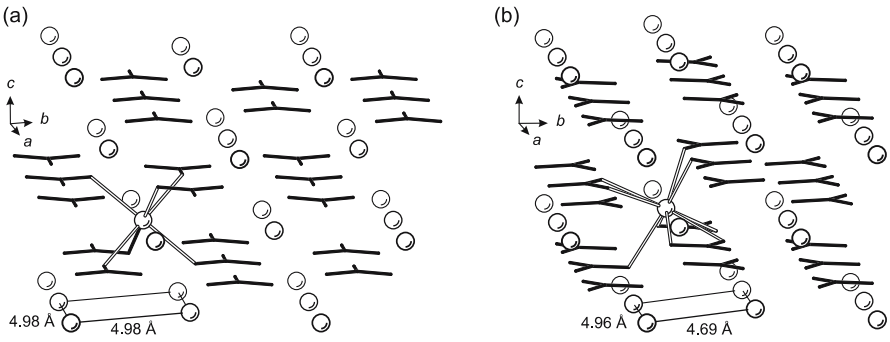

Fig. 2 Ion packing arrangement in the crystal structures of **a** calcite and **b** aragonite. The coordinative bonds between CO_3^{2-} anions (*black sticks*) and one of the Ca^{2+} ions (*open circles*) are emphasized with *open lines*. The minimum distances of Ca^{2+} ions in the *ab* planes for both crystal lattices are indicated at the *bottom*. (Reprinted from [18] with permission)

Ca^{2+} ions in the *ab* plane are nearly identical to those in the calcite structure. In contrast, the CO_3^{2-} anions below and above the Ca layer are separated into two layers, which are lifted by 0.98 Å along the *c* direction, leading to an overall ninefold coordination of Ca^{2+} ions [12].

Single crystals (regardless of crystal system, space group symmetry, and chemical composition) are intrinsically anisotropic, that is, most physical properties depend strongly on direction. For ionic crystals, such as calcium carbonate, this leads to a pronounced brittleness and cleavability along special directions of the crystal lattice. Typical cleavage planes of calcite are the six symmetry equivalent {10.4} crystal faces of the trigonal lattice, which leads to the rhombohedral shape of single crystals grown from supersaturated solution. The primary reason for the high stability and easy cleavage of the {10.4} crystal faces of calcite is that they consist of a close-packed, non-polar arrangement of calcium and carbonate ions (Fig. 3). In contrast, many low-index cleavage planes of the calcite lattice (such as (00.1) or (01.2)) represent

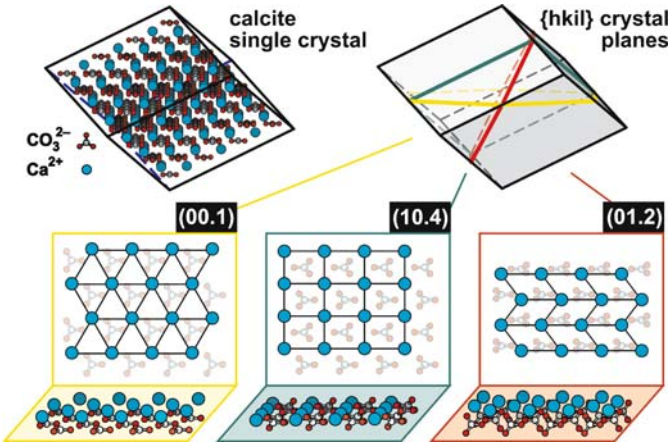

Fig. 3 Crystal planes resulting from cutting a calcite single crystal along different crystallographic directions. Calcite crystallographic indices are presented in the Miller–Bravais four-index system *hkil* for planes and faces. The graphical schemes are based on the hexagonal unit cell for calcite (unit cell parameters: $a = 4.989$ Å, $c = 17.062$ Å). The displayed shape of the calcite crystal corresponds to its {10.4} crystal form, i.e., the single crystal is enclosed by a set of symmetry-equivalent {10.4} crystal faces. Note that for the trigonal crystal system of calcite, four-membered ("Miller–Bravais") indices of the common form {*hkil*} are frequently used, however the index "i" is redundant and can be calculated from h+k+i = 0 or i = –(h+k). Therefore, in the literature the fourth index i is often omitted or symbolized by a dot. *Lower part*: Three different cleavage planes of the calcite crystal lattice are shown. Note that the resulting 2-D tilings differ by their plane crystallographic ("wallpaper symmetry") groups, of which a total of 17 exist. Another distinction is the separation of ionic groups into different layers. Cleaving a calcite crystal along (00.1) or (01.2), as opposed to (01.4), leads to the formation of highly polar crystal faces, which are energetically unfavorable

highly polar crystal faces, that is, each sort of ion is situated in a separate layer, leading to a macroscopic dipole moment. Polar crystal faces are normally not expressed in the equilibrium growth form of crystals. However, crystal growth from strongly polar solvents or the presence of (charged) inhibitors may result in slowing down the growth rate in a particular direction.

Since a cleavage plane of an ionic crystal is uniquely defined by its plane crystallographic symmetry and its polarity, it should in principle be possible to define a kind of "blueprint", i.e., a planar arrangement of ions or molecules that perfectly mirrors the geometrical and stereochemical properties of the mineral surface. If the developing single crystals grow totally co-aligned with respect to oriented domains of the organic matrix, the growth process is termed heteroepitaxy. As illustrated in Fig. 4, different epitaxial growth modes are distinguishable, depending on the structural similarity of the substrate and its overgrowing phase.

Layer-by-layer growth (*Frank van der Merwe* mode) is typically observed if a strict epitaxial relationship exists between the overgrowing film and the substrate. Island (*Volmer–Weber*) growth is observed when the attraction between molecules of the film is stronger than that between the film and the substrate, such that the film tends to coalesce as 3-D islands rather than wetting the substrate. An intermediate case between these two growth modes is also encountered – *Stranski–Krastanov* growth – which is described by the initial formation of a film layer followed by island growth on that layer. This can result if there is a slight lattice mismatch, but still favorable interaction, between the film and substrate [14].

If calcifying organisms were able to produce such "blueprints", and to expose them at defined sites of their soft tissues, inorganic crystals would be expected to grow epitaxially there, much as they do on inorganic substrates providing similar lattice constants and surface energies. This *Ansatz* represents in short the commonly held view of templated or epitaxial crystal growth as a fundamental characteristic of many biomineralizing organisms. In fact, some (but not all) calcifying organisms are able to produce highly organized crystal architectures with an astonishing degree of perfection (some prominent examples are shown in Fig. 1). However, the occurrence of highly regular and oriented biogenic crystal textures does not *automatically* imply

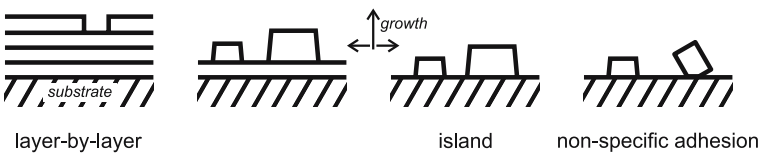

Fig. 4 Schematic representation of different epitaxial growth modes. The 3-D alignment of the over-growing phase relative to the substrate is primarily dependent on the matching of the two different lattices. The structural similarity is most pronounced in the layer-by-layer growth mode. (Adapted from [13])

the validity of epitaxy as a control mechanism involved in biomineral formation, since there are many periodic tilings and patterns in nature made of organic (macromolecular and cellular) materials (e.g., epithelial surface reliefs and color patterns) [15, 16], that can hardly be presumed to form by virtue of epitaxy.

In fact there are many puzzling details of the growth characteristics of biogenic crystals that cannot be explained by epitaxy models, i.e., by a structural commensurability between the organic template surface and the overgrowing crystals. Some of these contradictory facts will be discussed in the following chapters.

3
Mollusc Shell Formation

Molluscs, which are among the most thoroughly investigated organisms in biomineralization studies, build concrete shells from $CaCO_3$ [17]. The mollusc shell may be regarded as a microlaminate composite consisting of layers of highly oriented $CaCO_3$ crystals interspersed with thin sheets of an organic matrix. Crystals within separate shell layers usually consist of either pure aragonite or pure calcite. Vaterite, when present, is usually associated with shell repair. Shell formation occurs in two principal phases. The first involves the cellular processes of ion transport and organic matrix synthesis, which occur in different compartments of the molluscan mineralizing system. The second phase consists of a series of crystal nucleation and growth processes taking place in a specialized mineralization compartment, the *extrapallial space* (Fig. 5, left) [18].

In the past, special attention has been paid to the microstructure of nacre (the iridescent inner layer of mollusc shells) which exhibits an exceptionally regular arrangement of tabular aragonite crystals (Fig. 5, right). In order to grow crystals into a highly regular brickwork-like pattern, numerous nucleation events would have to be synchronized to each other at distant locations. An alternative growth mechanism was proposed recently to explain the precision by which aragonite platelets are uniformly co-aligned within the same and consecutive layers. According to this model, nacre may be assembled from extended, continuous single-crystalline domains of aragonite platelets that are interconnected by mineral bridges through perforated sheets of an organic matrix [19].

Considered as a whole, the physiological processes that ultimately lead to the formation of a complete mineralized mollusc shell are largely unknown. However, the general consensus is that the crystal nucleation and growth events are strictly regulated by a number of highly specialized organic macromolecules. Unfortunately, a deeper understanding of the biomineralization processes at the molecular level of structural hierarchy is hampered by our

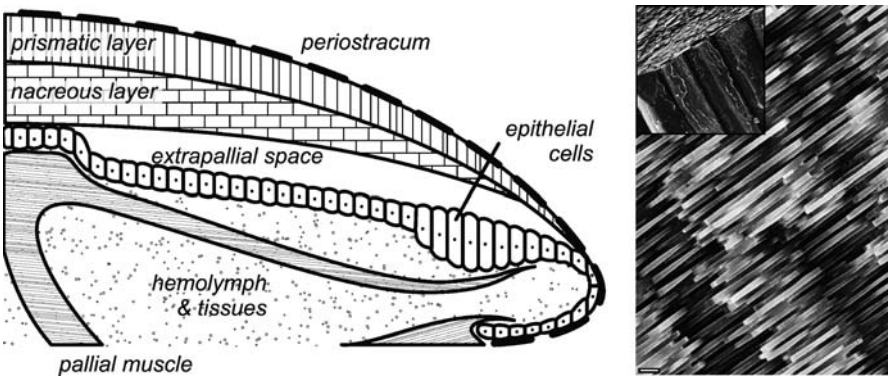

Fig. 5 *Left*: Transverse section of the mantle edge of a bivalve showing the system of compartments. *Right*: Fractured surface of the nacreous layer of the bivalve mollusc *Atrina rigida*. The *inset* shows the inner nacreous layer of tabular aragonite crystals (*top*) and the outer prismatic layer of columnar calcite crystals (*bottom*). (SEM micrographs, *scale bar* denotes 1 μm). Note that the particular crystal morphologies in different layers are not stringently linked to a single $CaCO_3$ polymorph: some organisms build up crystal textures similar to nacre (so-called semi-nacre) from calcite instead of aragonite, whereas others deposit a prismatic layer consisting entirely of aragonite (Fig. 1). (Reprinted from [18] with permission)

lack of knowledge of the 3-D structures of macromolecules that are directly associated with the mineral layer.

A recent literature search yielded very few examples in which complete or partial information about the *primary* structure of the macromolecules directly involved in mineralization was obtained (Tables 2 and 3). Traditionally, macromolecules isolated from mollusc tissues have been distinguished into two different classes based on solubility properties [20]. Chemical analysis showed that the water-insoluble fraction consists mainly of fibrous proteins (collagen, chitin) and/or polysaccharides. These macromolecules together build a rigid framework upon which specific macromolecules from the soluble fraction may become adsorbed. The primary function of the insoluble organic matrix is to subdivide the mineralization compartment into an organized network of microcompartments and thus to delimit the available space for crystal growth and/or to constrain the crystal packing arrangement to a certain extent. The surface of this macromolecular assembly may serve as a supramolecular template for oriented nucleation of single crystals, and in fact crystallization experiments employing reconstructed matrices of purified mollusc shell macromolecules have shown that it is possible to switch between different $CaCO_3$ polymorphs [21, 22] and to rebuild in vitro the gross structural features of the nacreous layer [23].

The macromolecules present in the soluble fraction share common sequence motifs consisting of repeating oligomeric units of acidic residues.

Table 2 Summary of *water-insoluble* proteins isolated from mollusc shells

Name	Source	Characteristic sequence motif	Associated mineral	Proposed function	Refs.
MSI60	Pearl oyster protein from the nacrous layer	[Ala_{9-13}] and [Gly_{3-15}]	Aragonite	Framework protein, binding of *Asp*-rich soluble glycoproteins	[24]
MSI31	Pearl oyster protein from the prismatic layer	[Gly_{3-5}] and [*Glu*–Ser–*Glu*–*Glu*–*Asp*–X], (X = Thr or Met)	Calcite	Framework protein, binding of *Asp*-rich soluble glycoproteins	[24]
MSI7	Pearl oyster protein from the epithelia of the mantle	[Gly_{x-y}]	Aragonite Calcite	Framework protein, acceleration of nucleation and precipitation of $CaCO_3$	[25]
N14, N66	Pearl oyster protein from the nacreous layer	$[Asn–Gly]_{12}$ and $[Asn–Gly]_{57}$	Aragonite	Carbonic anhydrase (N66)	[26]
N16	Pearl oyster protein from the nacreous layer	$[Asn–Gly]_6$ (as well as 4 acidic domains)	Aragonite	Control of crystal growth and morphology	[23]
Lustrin A	Abalone protein from the nacreous layer	[Gly–Ser–Ser–Ser] and [Gly–Ser] (as well as one basic domain)	Aragonite	Adhesion protein	[27]
Prismalin-14	Pearl oyster protein from the prismatic layer	[*Asp*]- and [Gly/Tyr]-rich domains [Pro–Ile–Tyr–Arg] repeats	Calcite	Framework protein	[28]

Table 3 Summary of *water-soluble* proteins isolated from mollusc shells

Name	Source	Characteristic sequence motif	Associated mineral	Proposed function	Refs.
MSP-1	Scallop shell glycoprotein from the foliated layer	[*Asp*–Gly–Ser–*Asp*] and [*Asp*–Ser–*Asp*]	Calcite	Induction of crystal nucleation, control of $CaCO_3$ polymorphism	[29]
Nacrein	Pearl oyster protein from the nacreous layer	[Gly–*X*–Asn], (*X* = *Glu*, Asn, or *Asp*)	Aragonite	Carbonic anhydrase, Ca-binding	[30]
Mucoperlin	Fan mussel protein from the nacreous layer	Tandem repeats rich in [Pro], [Ser] and [Thr]	Aragonite	Induction of crystal nucleation, control of $CaCO_3$ polymorphism	[31]
Perlucin	Abalone protein from the nacreous layer	C-type lectin domains	Aragonite	Glycoprotein receptor	[32]
Perlustrin	Abalone protein	[Cys–X–Cys–Cys–X–X–Cys]	Aragonite	Insulin-like growth factor binding protein	[33]
Aspein	Pearl oyster highly acidic protein from the prismatic layer	[Asp_{2-10}] punctuated with [Ser–Gly] dipeptides	Calcite	Control of $CaCO_3$ polymorphism	[34]
AP7 ***AP8*** ***AP24***	Abalone protein from the nacreous layer	[*Asp*–*Asp*] [*Asp*]-rich [*Asp*–*Asp*–*Asp*–*Glu*–*Asp*]	Aragonite	Control of $CaCO_3$ polymorphism	[35, 36]
Calprismin	Fan mussel protein from the prismatic layer	[*Asp*]-rich [Pro]- and [Thr]-rich	Calcite	Cell signalling, matrix-cell interactions	[37]
Caspartin	Fan mussel protein from the prismatic layer	[Asp_{75}]	Calcite	Control of $CaCO_3$ prism formation	[37]
Asprich 1–3	Bivalve proteins from the prismatic layer	[*Asp*]-rich [*Asp*–Glu–Ala–*Asp*]	Calcite	Control of $CaCO_3$ prism formation	[38]

Table 3 contains the available data of fully characterized water-soluble proteins isolated from morphologically different locations of calcified mollusc tissues. However, the heterogeneity of sources/organisms for isolating these macromolecules, their different chemical natures, and their association with different mineral phases clearly rule out a uniform function.

For the induction of calcite and aragonite nucleation, systematic investigations on biological and suitably assembled artificial systems have shed some light on the structural requirements of a putative nucleation site, especially in mollusc shells [39–41]. The model proposes the existence of structurally pre-organized domains of acidic residues, which could serve as a supramolecular template for oriented crystal nucleation. Such highly ordered domains could result from acidic macromolecules being adsorbed on a rigid scaffold of insoluble matrix proteins (Fig. 6).

In fact, investigations of demineralized mollusc shells have shown that the interlamellar organic sheets of nacre consist of thin layers of β-chitin (β-chitin is a water-insoluble $(1 \rightarrow 4)$-linked 2-acetamido-2-deoxy β-D-glucan) [42] sandwiched between thicker layers of silk fibroin-like proteins (Table 2) [43]. Silk fibroin itself possesses microcrystalline domains of repeating $[Gly–Ala–Gly–Ala–Gly–Ser]_n$ units that adopt an antiparallel β-pleated sheet conformation. These domains have a highly regular and hydrophobic surface upon which acidic macromolecules are adsorbed from solution. In the course of adsorption, the acidic macromolecule must fold into the appropriate conformation in order to maximize its hydrophobic interactions with the silk fibroin surface. Possible candidates for acidic macromolecules that

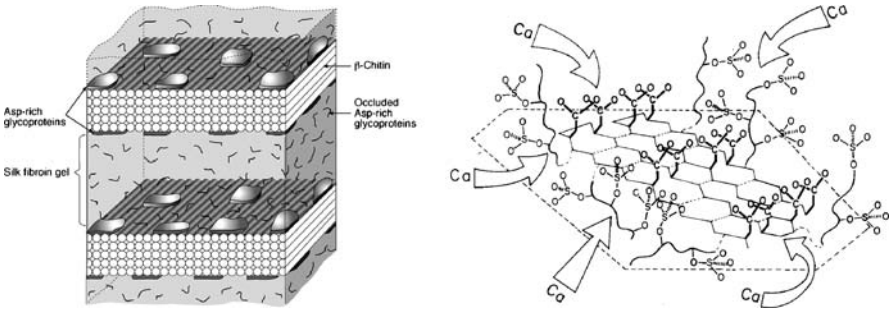

Fig. 6 *Left*: Schematic representation of the organic matrix in the nacreous layer of *Atrina* according to Weiner and Addadi. (Reprinted from [43] with permission.) The β-chitin lamellae are interspersed in a highly hydrated silk fibroin gel. The gel contains soluble *Asp*-rich glycoproteins, which can bind to the β-chitin surface by means of hydrophobic or electrostatic interactions. *Right*: Structure model of a putative nucleation site in molluscan tissues. The sulfate groups, linked to flexible oligosaccharide side chains, concentrate Ca^{2+} ions on an Asp-rich oligopeptide domain that is assumed to adapt a highly regular β-sheet conformation. A first layer of Ca^{2+} ions may thus be fixed and oriented in space upon which further mineral growth ensues. (Reprinted from [39] with permission)

interact with silk fibroin in the described way are oligopeptides containing sequence motifs of $[Asp\text{-}X]_n$, (X = Gly, Ser), which have a strong tendency to fold into a β-sheet conformation in the presence of Ca^{2+} ions [44]. As a consequence, the aspartic acid residues of $[Asp\text{-}X]_n$ sequences would be positioned at only one side of the β-pleated sheet, resulting in an organized 2-D array of carboxylate ligands.

It is tempting to assume that carboxylate residues coordinate a first layer of Ca^{2+} ions, which would in turn become the first layer of an epitaxially growing $CaCO_3$ crystal. However, studies have so far failed to provide evidence for an epitaxial growth mechanism or a close stereochemical complementarity between the nucleating macromolecules and the incipient $CaCO_3$ crystal surface. Rather, some properties of the mollusc shell ultrastructure point to less-sophisticated nucleation strategies: examination of the common crystal orientations in a variety of calcifying organisms reveals that aragonite and calcite single crystals most frequently nucleate from the *ab* planes. The arrangement of Ca^{2+} ions in this plane (the shortest distance between Ca^{2+} ions is 4.99 Å in calcite and 4.69 Å in aragonite, Fig. 2) is geometrically *not* commensurate with the period of amino acid residues in a protein β-strand (approx. 6.9 Å). Moreover – pointing more or less perpendicular to the Ca^{2+} ions in the *ab* plane – the carboxylate residues of the β-pleated sheet cannot continue the parallel arrangement of planar carbonate anions in the underlying layer(s). The current nucleation model thus does not support the picture of a calcite or aragonite single crystal being nucleated from (00.1) crystal faces by virtue of stereochemical selection principles and epitaxial crystal growth [45–47].

Despite the similar positioning of Ca^{2+} ions in the *ab* planes of calcite and aragonite, mollusc shells discriminate between the two polymorphs by secreting them separately in different layers (e.g., prismatic layer and nacre). This suggests that additional factors participate in nucleation. One possibility is that different Mg^{2+} concentrations in the fluids of aragonitic and calcitic layers may be present that could help to shift the balance between the two polymorphs. Another possibility is the presence of polymorph-specific macromolecules that interact with more than one face of the nascent crystal. For a valid explanation of selective nucleation of either polymorph, the current, essentially geometric model will have to be refined. Much is expected to be learned from the first 3-D structure of a "crystal nucleating" macromolecule, although its "active" conformation may depend on the accompanying insoluble organic matrix in the biological tissues. It is worth mentioning that there exists a (genealogically unrelated) group of crystallization-inhibiting proteins, the so-called antifreeze proteins (AFPs) [48, 49], for some of which precise X-ray structural data are now available. Some of these proteins assume rigid molecular conformations and prevent ice crystal nuclei from growing into larger crystals by specific adsorption to specific crystal faces. However, as Evans pointed out in a critical

review [50], the structural aspects of AFPs and proteins involved in biomineralization processes are quite different: in contrast to ice-interaction proteins, which typically adopt stable secondary structures (α-helix, β-sheet, β-helix, etc.), biomineral-interaction proteins typically adopt unfolded, open conformations, and, where mineral binding motifs have been identified, these sequences exhibit structural trends toward extended, random coil, or other unstable secondary structures.

It should also be noted that molluscs show a much wider variety of textures than indicated so far (other typological crystal textures include cross-lamellar or foliated shell structures) [51–53]. In many (but not all!) molluscs the outer shell is composed of calcite and the inner shell of aragonite displays a brick-like microstructure. Crystallographic texture analysis indicates that in the nacre of most molluscs, *c*-axes are oriented more or less perpendicular to the surface of the shell, but *a*-axis orientations display characteristic patterns. In some species (e.g., the shells of most land snails) the *a*-axes of the aragonitic platelets all have the same orientation, or they display a texture pattern with $\{110\}$ twinning as in *Nautilus*, or they spin randomly about the *c*-axis with a [001] fiber texture as in *Haliotis* (Abalone). Chateigner et al. surveyed a large number of mollusc species and concluded that the diverse texture patterns are related to phylogeny and presumably to the protein type [54].

From a materials scientist's point of view, nacre can be regarded as a *hierarchical* biological nanocomposite [56]. Though nacre is mainly composed of a brittle inorganic material, its highly organized design (Fig. 7) leads to extraordinary mechanical performance owing to an excellent combination of stiffness, strength, impact resistance, and toughness [57–59]. The structure of nacre has been reviewed repeatedly [60–62], and numerous reports indicate that nacre is composed of pseudo-hexagonal, polygonal, or rounded aragonite tablets having lateral dimensions of ~ 5–$20\,\mu m$ and a thickness of ~ 0.3–$1.5\,\mu m$ (as shown in Fig. 7). For gastropod nacre, SEM micrographs suggest that each aragonite tablet is subdivided by radial vertical organic membranes into a varying number of sectors (Fig. 7c), which have been interpreted to be polysynthetically twinned crystalline lamellae [63]; this interpretation, however, has been at least partly refuted by subsequent investigations [64].

The surface of nacre tablets (Fig. 7c) from California red abalone (*Haliotis rufescens*) possesses nanoasperities (~ 30–$100\,nm$ diameter and $\sim 10\,nm$ in height) [57, 65] and mineral "bridges" (Fig. 7b) (~ 25–$34\,nm$ in size, ~ 91–$116\,\mu m^{-2}$ surface density) between sheets that pass through the organic intertablet layers [19, 66]. The organic matrix constitutes the remaining ~ 5 wt % of the material. The intertabular polymer layer has a thickness varying between ~ 30 and 300 nm [67], with pores that allow the mineral bridges to pass through [66], and intracrystalline proteins present within the tablets themselves [21, 22].

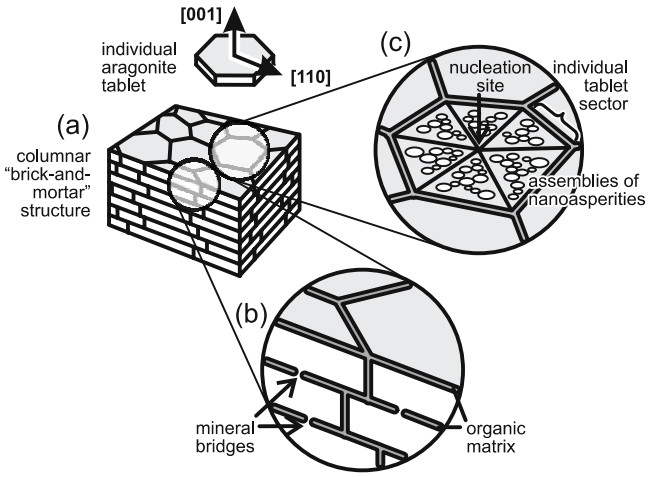

Fig. 7 Schematic illustration of the multiscale hierarchical structure of nacre: **a** 10 μm length scale, **b**, **c** 2 μm length scale, showing individual tablet features at a 200 nm length scale consisting of assemblies of nanoasperities. (Scheme redrawn after [55]). In "columnar" nacre, the tablets are relatively uniform in size and stacked vertically along the *c*-axis direction (with a slightly staggered arrangement laterally), thereby forming microlaminate sheets and tessellated bands. A domain structure has been found parallel to the *c*-axis direction consisting of 3–10 tablets with *a*-axes parallel to each other, while in the plane of the sheet, the *a*-axis orientation is variable

A natural adhesive protein (*Lustrin A*) has been isolated from the organic matrix of California red abalone nacre and was found to have a "modular" structure, i.e., a multidomain architecture composed of folded, nanometer-sized modules, covalently linked together in series along a single macromolecular chain [27]. While the primary structure of *Lustrin A* has approximately ten alternating Cys- and Pro-rich domains, it contains only a very short polyelectrolyte ("acidic") segment that could be responsible for attachment to the mineral surface [68]. It is not yet clear whether *Lustrin A* has a functional role similar to the acidic water-soluble proteins summarized in Table 3. However, a biophysical model of its elastic properties has been proposed that relates its modular structure to the mechanical toughness and fracture resistance of nacre [69].

This short summary of mollusc shell formation and the morphological properties of nacre indicates that the biological growth processes involved are much more complex than the seemingly primitive, brickwork-like structure might at first glance suggest. Nevertheless, scientists have sought out different kinds of bottom-up approaches to mimic different aspects of the molluscan mineralization system [70]. Especially, the quest for a possible epitaxial relation between the organic matrix and the overgrowing inorganic crystals has been subject of many experimental studies.

4
Crystallization of $CaCO_3$ Beneath Monolayers

4.1
Experimental Setup for the Growth of Inorganic Crystals Beneath Monolayers

Several studies have been devoted to the putative mechanisms underlying the formation of highly organized mineral structures in molluscs and similar organisms. Due to the various experimental difficulties of observing crystal growth in living molluscs, scientists have sought out suitable model systems for biomineralization processes reflecting the mineral/matrix interactions active at the atomic or molecular level of structural complexity. Seminal contributions were made by Mann and Heywood, who studied the influence of charged monolayers on crystal nucleation [71]. The group made use of a Langmuir film balance that allows for the spreading of surfactant molecules as a water-insoluble monolayer at the air–water interface. The basic principle of the experimental setup is shown in Fig. 8, in which the surfactant molecules are symbolized by a wire-model of hydrocarbon chains and the charged head groups (symbolized by triangles) point toward the aqueous subphase.

In studies relating to the biomimetic crystallization of $CaCO_3$, a freshly prepared ~ 9–10 mM aqueous solution of $Ca(HCO_3)_2$ is often used, which becomes instable with respect to the dissociation of bicarbonate anions into carbon dioxide and carbonate anions. Due to slow decomposition of the intermediate carbonic acid – yielding carbon dioxide and a water molecule – $CaCO_3$ precipitation is relatively slow (in the optical microscope, the first

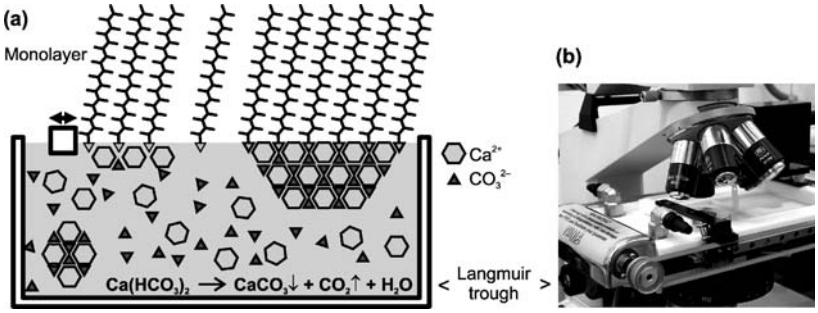

Fig. 8 **a** Illustration of a Langmuir film balance used for biomimetic crystallization of $CaCO_3$ and other inorganic phases beneath insoluble monolayers of amphiphilic molecules. **b** Computer-controlled miniature film balance replacing the stage of an optical microscope. The balance is equipped with two mechanically coupled barriers used for compression of the monolayer and a sapphire window, which permits the observation of crystal growth with transmitted light

macroscopic crystals become visible within some minutes to hours, depending on the experimental conditions). The slowness of crystal formation allows for adjustment of the compression state of the monolayer, i.e., to limit the average surface area available for a single molecule in the monolayer and/or to induce a monolayer phase transformation [72, 73].

The monolayer crystallization method has both technical advantages and disadvantages. As a general advantage, the use of a Langmuir film balance allows for creating a smooth and clean interface and for depositing a measured quantity of amphiphilic molecules in a controlled way. The average area per molecule is adjusted by a movable barrier, and the surface pressure or tension is monitored by a pressure sensor. The simple technical setup can be augmented by various analytical characterization methods, e.g., by Brewster-angle or fluorescence microscopy for imaging domain structures of the monolayer, or by surface potential measurements, to name just a few [72, 73]. In many cases it is straightforward to obtain a first-approximation model of the arrangement and packing of molecules in the monolayer. Over many years this technique has been used, mainly by the group of Leiserowitz and Lahav, to investigate epitaxy and chiral discrimination of molecular (nonionic) crystals growing beneath specially designed monolayers [74, 75].

A technical disadvantage of the Langmuir setup is the mobility and the thinness of the monolayer, which renders structural investigations at high resolution (i.e., at the atomic or molecular level) a difficult task. In principle, it is possible to deposit a monolayer as a Langmuir–Blodgett film on a substrate surface and to employ surface analytical techniques, such as scanning force or tunneling microscopy, in order to obtain high resolution images of the interface structure. This strategy, however, has rarely been utilized in studies related to biomimetic crystallization [76].

A particular advantage of crystallizing calcium carbonate beneath monolayers is that the three main crystal polymorphs (i.e., calcite, aragonite, and vaterite) can be distinguished easily by their characteristic crystal habits. While aragonite and vaterite crystals normally adopt complex acicular or floret-type morphologies (see examples shown later in Fig. 20), calcite crystals often appear as sharply defined single crystals displaying the shape of a (truncated) {10.4} cleavage rhombohedron (Fig. 9).

The orientations of calcite crystals with respect to the monolayer can be deduced from optical or scanning electron micrographs. A projection of rhombohedral faces onto the image plane yields characteristic interfacial angles, based upon which crystal orientations can be determined by comparing the measured angles and the general outline evident in micrograph images to computer-generated crystal models cleaved along various crystallographic planes (Fig. 9c). This procedure, however, strictly requires the sample to be aligned perpendicular to the viewing direction, while at the same time perspective aberrations of the optical system must be kept to a minimum. Owing to the fact that only a very limited number of crystal specimen can be

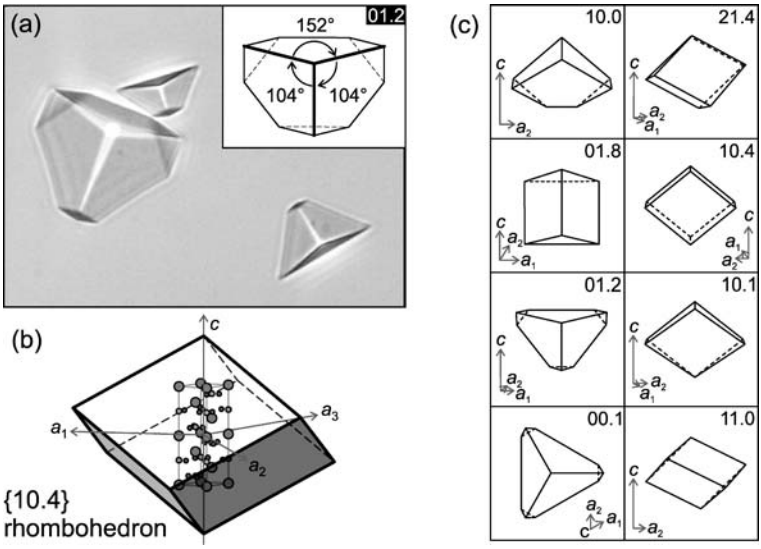

Fig. 9 **a** In situ optical micrograph of calcite crystals attaching to a monolayer. The *inset* shows the model of a truncated calcite {10.4} rhombohedron cut along its (01.2) plane. The displayed numbers represent interfacial angles of crystal edges projected onto the image plane. (Crystallographic angles between the edges of the {10.4} crystal face are 101.90° and 78.10°, respectively). **b** Model of a calcite crystal bounded by six symmetry-equivalent {10.4} faces. The *overlay* shows the orientation of the hexagonal unit cell of calcite with respect to the crystal edges. Lattice vectors a_i and c are sketched as *red arrows*. **c** Outlines of calcite single crystals cleaved along various crystallographic planes (specified by their Miller–Bravais indices). Models of crystals are oriented such that their cleavage planes coincide with the image plane

analyzed in this manner within a reasonable timeframe, the method suffers from the inherent disadvantage that crystals tend to be neglected when their orientations are difficult to determine (e.g., because the crystals are small) or when the crystals grow as polycrystalline aggregates. Unfortunately, there are no simple-to-use analytical techniques for simultaneously determining the phase composition, average crystallite size, and orientation distribution function (ODF) of the loose assembly of macroscopic crystals that is typically encountered in monolayer investigations. There *are* dedicated methods for these tasks, such as X-ray pole-figure measurements or automated analysis of Kikuchi line patterns using electron backscatter diffraction (EBSD) systems [77]. These methods, however, are not readily available for in situ measurements of crystal growth beneath monolayers, and they normally impose strict requirements on sample preparation, such as a uniform sample thickness or a flat (= polished) sample surface. Given the technical difficulties described above, any statements in the literature referring to the epitaxial growth of inorganic crystals beneath monolayers should be interpreted with

caution, since the presentation and evaluation of crystal orientation data are somewhat arbitrary. Moreover, many studies describing the heteroepitaxy of calcite crystals focus explicitly on the particular crystal texture of nacre, which, however, consists of aragonite and not calcite. The reason for the latter contradiction might lie in the fact that aragonite single crystals are difficult to prepare at ambient conditions [78–80], and they rarely manifest the pseudohexagonal shape of the tabular aragonite crystals that constitute the brick-and-mortar structure of nacre (Fig. 7).

4.2 Crystallization of $CaCO_3$ Beneath Monolayers of Simple Aliphatic Surfactants

Nucleation of calcite single crystals was observed with monolayers of aliphatic monocarboxylic acids, sulfates, or phosphonates as summarized in [81]. In general, the crystals that grew beneath monolayers showed a significantly narrower size distribution and reduced nucleation time in comparison to calcite crystals precipitated spontaneously from supersaturated solutions. Moreover, the crystals grew with preferential orientations relative to the monolayer. Calcite single crystals nucleated predominantly from the $\{10.0\}$ face underneath compressed monolayers of monofunctional amphiphilic carboxylic acids [82], while monolayers of alkylsulfates and -phosphonates led to calcite single crystals that nucleated from the $\{00.1\}$ face [83]. In contrast, monolayers of octadecylamine induced the precipitation of vaterite crystals, and monolayers of octadecanol inhibited crystal growth. Detailed schemes were proposed for rationalizing the different modes of interaction between the different head groups of amphiphiles in the monolayers and the corresponding faces from which the crystals were nucleated [84]. It was suggested that the orientation of calcite crystals growing below a monolayer is dictated by geometric and stereochemical complementarity between the (charged) headgroups of the monolayer and the ionic constituents of the nucleated crystal face. The outcome of these investigations was regarded as experimental justification for the "template model of biomineralization" discussed in the previous chapter. The seemingly clear and unequivocal interpretation of the crystal growth mechanism as an epitaxial phenomenon has stimulated a host of subsequent model investigations of the biologically inspired crystallization of inorganic solids beneath Langmuir monolayers. Many of the latter studies provided further impetus to the notion of the "molecular blueprinting" of inorganic materials by a pre-organized organic matrix.

Crystallization underneath monolayers of stearic acid (**1**) spread on aqueous calcium bicarbonate solution (9 mM), for instance, yielded two sets of morphologically distinct forms of calcite, termed type I and type II (Fig. 10) [82]. Both crystal morphologies nucleated from a (10.0) plane. The plate-like crystal habit at early growth stages changed into capped rhombohedral plates of type I crystals in mature crystals and a related triangular

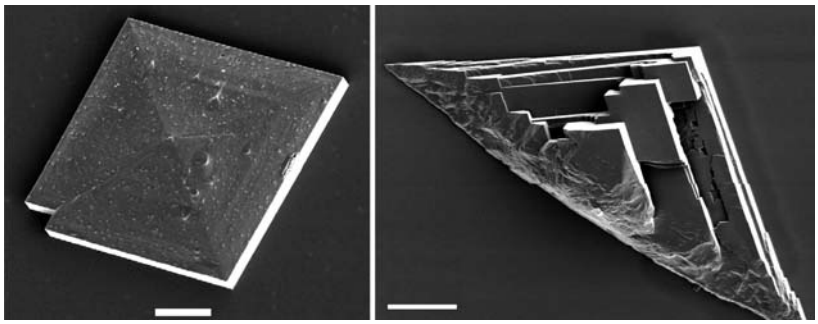

Fig. 10 Scanning electron micrographs of type I and type II calcite crystals nucleated from a {10.0} face beneath monolayers of **1**. *Scale bars* denote 10 μm. (Reprinted from [82] with permission)

morphology of type II crystals. When the Ca ion concentration of the subphase was reduced (4.5 mM), only vaterite crystals were observed, which is a quite remarkable result, since one would ordinarily expect the thermodynamically less stable crystal polymorph to form at *higher* supersaturation, rather than vice versa.

The preferential orientation of calcite crystals with respect to the monolayer plane was discussed in terms of a geometrical and stereochemical match between the stearic acid monolayer and the nucleated crystal face. It was argued that the spacing of the carboxylate headgroups in the monolayer matches the spacing of carbonate ions in the {10.0} face of calcite. Stereochemical complementarity was suggested to exist between rows of anions in the {10.0} face of calcite – where the C_{2v} axis of the carbonate moieties is perpendicular to the cleavage plane of the crystal – and the arrangement of carboxylate head groups in the monolayer (Fig. 11).

Uniformly oriented calcite crystals were also produced underneath monolayers of eicosyl sulfate (**2**) and eicosyl phosphonate (**3**), but in contrast to stearate monolayers, the calcite crystals exposed their {00.1} face to the monolayer and developed an equilateral triangular shape. In contrast to stearic acid, the headgroups of eicosyl sulfate and eicosyl phosphonate exhibit trigonal symmetry, which could mirror the planar arrangement of carbonate ions in the {00.1} face of calcite. It was proposed that in this case the stereochemical complementarity overrides the approximate geometrical match between the monolayer and the nucleated crystal plane (Fig. 12) [83].

The dynamic behavior of fatty acids with different hydrocarbon chain lengths was characterized by Brewster-angle microscopy (BAM) and correlated to changes in crystal growth behavior [85]. While palmitic acid ($C_{15}H_{31}COOH$, **4**) simultaneously induced the growth of aragonite, vaterite, and non-oriented calcite crystals, tricontanoic acid ($C_{29}H_{59}COOH$, **5**) almost

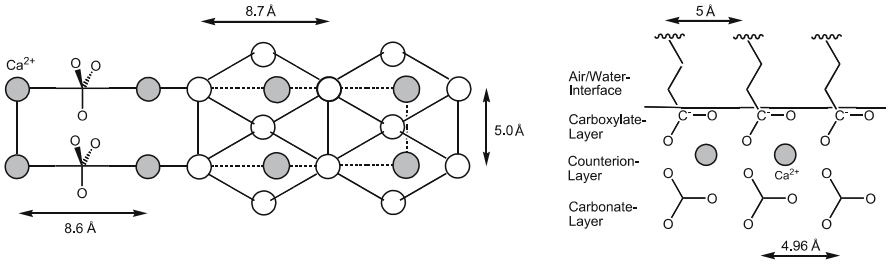

Fig. 11 **a** Schematic diagram showing the geometrical match between the headgroup spacing in the monolayer of stearic acid (**1**) and the carbonate–carbonate spacing in the {10.0} face of calcite. (*Gray dots* calcium ions, *white dots* carboxylate ions.) **b** Schematic diagram showing the stereochemical complementarity between the orientation of carboxylate groups of the monolayer molecules of **1** and the carbonate ions in the {10.0} face of calcite. (Redrawn after [82])

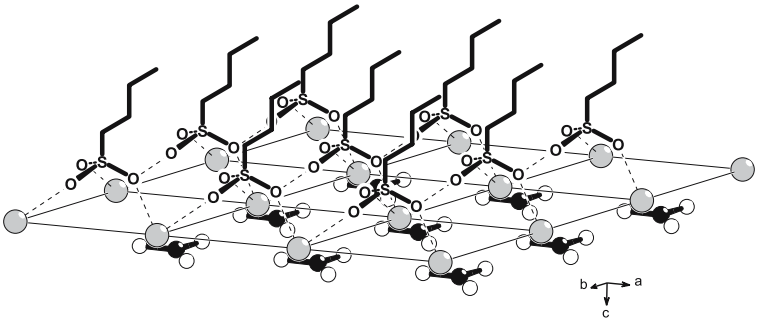

Fig. 12 Orientation of (00.1) oriented calcite crystal relative to monolayers of eicosyl sulfate or eicosyl phosphonate, according to Heywood and Mann [83]. Close-up of the interface between the monolayer of an anionic surfactant with a C_{3v}-symmetric headgroup (here: a sulfonate) and the (00.1) plane of the calcite crystal lattice. The selection of the (00.1) plane is dictated by a stereochemical and geometrical match between sulfonate groups and the underlying first layer of Ca ions. In the displayed μ_3-tridentate coordination mode, each sulfonate group replaces a CO_3^{2-} anion at a crystallographically equivalent position. Note, however, that the proposed isostructural replacement of CO_3^{2-} by $R-SO_3^-$ ions should lead to an unbalanced accumulation of charges, which constitutes an energetically unfavorable situation

exclusively led to the growth of uniformly (10.0) oriented calcite crystals having a triangular shape.

Polymorph selectivity was attributed to changes in the rate of carbon dioxide diffusion through the monolayer, indicating a kinetic effect. BAM analysis showed that the crystals preferentially nucleated under condensed monolayer domains and at domain boundaries, which was related to relaxation of the ordered monolayer structure. The size of condensed phase domains and the

amount of uniformly oriented calcite crystals grown beneath such domains increased with the chain length. Therefore, changes in crystal morphology were attributed to changes in the monolayer structure as a function of chain length.

Prior to these studies, monolayers of *N*-(10,12-pentacosadiynoyl)glycine (**6**) were analyzed by BAM [86]. Calcite crystals were found to grow beneath a monolayer of **6** at low surface pressure ($\pi = 0–5$ mN/m), where the BAM image of the monolayer indicated smectic domains. At high surface pressure ($\pi = 20$ mN/m), where the micrographs revealed a pseudo-focal-tonic monolayer texture, only vaterite was observed. It was pointed out that the distance between the foci of the monolayer texture almost exactly corresponds to the separation of the vaterite crystals, suggesting a spatial correlation between the monolayer and the crystals. In addition, it was argued that the monolayer packing density seems to play an important role in polymorph selection, since vaterite nucleation predominates at high surface pressure.

A well-defined alignment of $CaCO_3$ crystals was further achieved with polymeric Langmuir–Schaefer films of 10,12-pentacosadiyonic acid (**7**) [87].

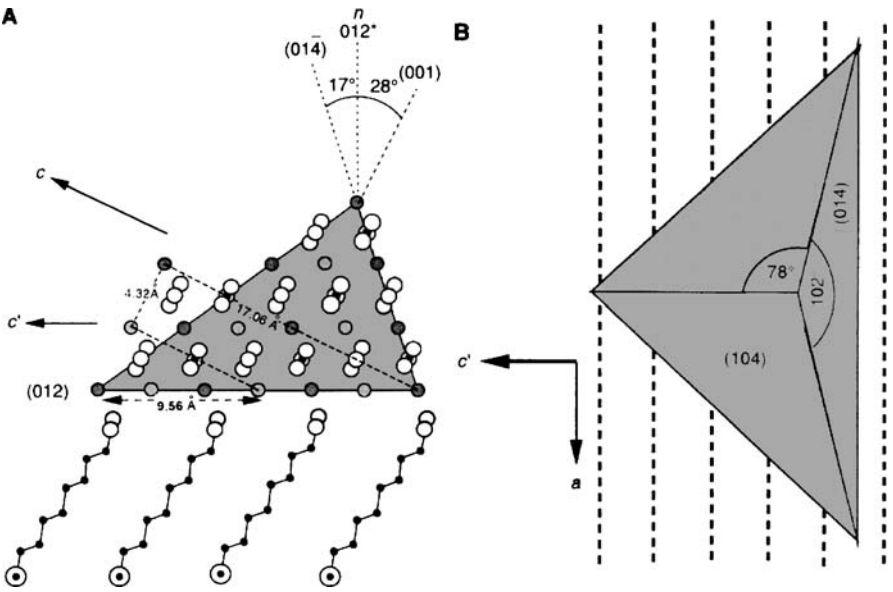

Fig. 13 Schematic diagram showing a potential geometric relationship between monolayers of **7** and the {01.2} face of calcite, according to [87]. *Left*: View along the *a* axis of calcite, down the polymer backbone direction and edge-on the (01.2) plane. Alternating calcium and tilted carbonate layers of the (01.2) plane of calcite are depicted. The calcite unit cell is shown as the *dashed, truncated rectangle*. *Right*: Schematic diagram of (01.2) oriented calcite single crystal with respect to the polymer backbone direction, indicating the dihedral angles

Langmuir monolayers of the monomeric 10,12 pentacosadiyonic acid first were polymerized with ultraviolet light and then transferred horizontally onto hydrophobized solid supports. Crystallization of $CaCO_3$ was performed by adding a drop of supersaturated $CaCO_3$ solution to the polymer film where the carboxylic headgroups were exposed to air. Calcite crystals nucleated from a $\{01.2\}$ face and, moreover, in each single domain of the film of **7** they became co-aligned to each other with the crystals' *a*-axes oriented parallel to the polymer backbone. Along this direction both the (01.2) crystal plane and the polymer have a periodicity of about 5 Å, and a close geometric match between the carboxylate groups and the calcite crystal structure was proposed. To explain the nucleation of calcite from the $\{01.2\}$ crystal face, a stereochemical complementarity between the monolayer and the crystal surface was suggested: in the $\{01.2\}$ face of calcite, the carbonate ions are tilted 28° with respect to the normal of the (01.2) plane, a spatial arrangement that is matched by the 30° tilt of the side chains and carboxylate groups in the polymer (Fig. 13). The reorientation of side groups of the monolayer molecules upon crystallization was investigated by in situ FTIR measurements of the Langmuir–Schaefer films and interpreted as adaptability of the monolayer for achieving a stereochemical match [88].

4.3
Hydrogen Bonded Systems

Control over polymorph selection and calcium carbonate crystal orientations was also reported for self-organized hydrogen-bonded molecular ribbons consisting of monolayers of *N*,*N*′-dioctadecyltriazine-2,4,6-triamine mixed with different cyanuric acid derivatives as soluble component (**8**, Scheme 1) [89]. Residues of $-CH_2-CH_2-R$ were appended to the cyanuric acid moiety, differing in the functional groups R that point into the aqueous subphase. For monolayers comprised of alcohol (R = OH), amino (R

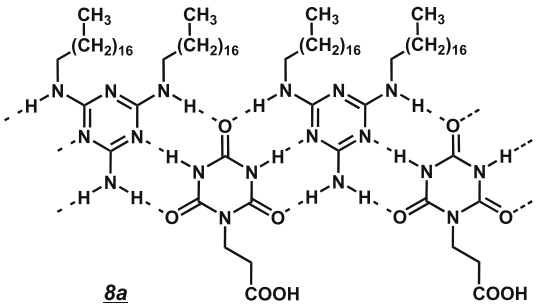

8a

Scheme 1 Structural formula of **8a**. Monolayers of *N*,*N*′-dioctadecyltriazine-2,4,6-triamine self-organize with a carboxylic acid derivative of cyanuric acid at the air–water interface

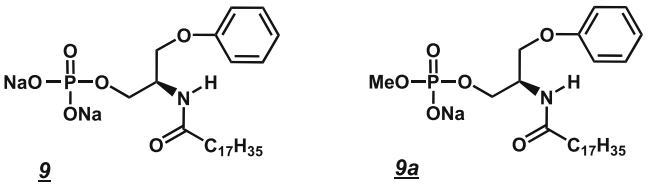

9 **9a**

Scheme 2 Structural formula of disodium (–)-(2S)-3-phenoxy-2-octadecanoylaminopropan-1-yl phosphate (**9**) and the corresponding methoxy derivative (**9a**)

= NH_2), or phosphate groups (R = OPO_3^{2-}), the observed crystal growth results resembled those of simple aliphatic surfactants possessing the same head group R. The carboxy-terminated derivative (**8a**, R = COOH) induced formation of (01.2) oriented calcite crystals. Again, control over crystal orientation was attributed to a geometrical and stereochemical matching between the putative positions of the functional groups R in the monolayer and the positions of ions in the adjacent calcite crystal face, although the periodicity and arrangement of functional groups in the monolayer of **8a** should differ significantly from the positions of the carboxylate residues in the Langmuir–Schaefer film (**7**) described above, which nevertheless led to the same (01.2) orientation of the crystal specimen.

By analogy to stearic acid (**1**), the nucleation and growth of (10.0) oriented calcite crystals has been reported for structurally different monolayers forming a network of strong intermolecular hydrogen bonds, such as (–)-(2S)-3-phenoxy-2-octadecanoylaminopropan-1-yl phosphate (**9**) or dioleyl phosphatidyl ethanolamine modified with (Leu – Glu) octapeptides (**10**) [90, 91]. Monolayers of **9** induced the crystallization of oriented calcite crystals either in a condensed liquid or in a solid monolayer phase, whereas monolayers of the methyl-substituted derivative (**9a**) having a decreased charge density yielded the same results in a solid monolayer phase only. The effect was related to geometrical lattice matching and stereochemical complementarity, as well as to the structural reorganization of molecules of **9a** arising from the state of compression. In addition to a proposed geometrical match between lipopeptide **10** and the {10.0} face of calcite, the observed epitaxy was attributed to the ability of the flexible monolayer to adapt to geometric constraints of the nucleated inorganic phase.

4.4
Aragonite Crystallization Induced by Monolayers of Bifunctional Surfactants

Monolayers of 5-hexadecyloxyisophthalic acid (**11**) induced the formation of acicular aragonite crystal aggregates at medium surface pressure (π = 10 mN/m) and at an ionic composition of the aqueous subphase that would normally yield the thermodynamically more stable calcite [92]. It was pos-

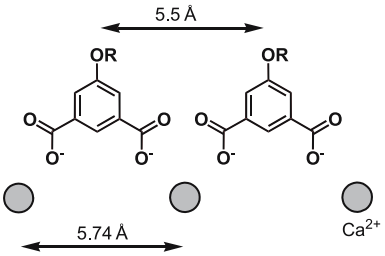

Fig. 14 Diagram showing the geometrical match between the headgroup spacing in the monolayer of **11** and the spacing of Ca^{2+} ions (*gray circles*) in the *c* direction of aragonite, according to [92]

tulated that the molecules (**11**) form a periodic arrangement on the aqueous subphase in such a way that the carboxylate groups are displaced by 4.4 Å in the *a* direction and 5.5 Å in the *c* direction, which corresponds geometrically to the position of Ca ions in the *ac* face of aragonite (Fig. 14). It was furthermore proposed that a bidentate coordination motif of the carboxylate substituents could complement the stereochemical arrangement of the carbonate groups in the *ac* face.

4.5 Crystallization of $CaCO_3$ beneath Monolayers of Macrocyclic Amphiphiles

The partially contradictory experimental findings reported for the growth of calcium carbonate beneath structurally different insoluble monolayers led us to design a small library of macrocyclic amphiphiles, which we based on calix[*n*]arene (*n* = 4,6,8) and resorc[4]arene moieties, respectively.

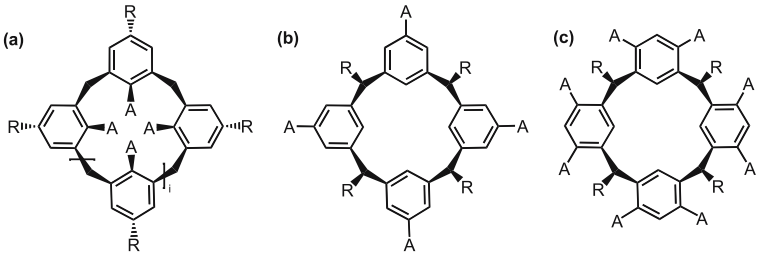

Scheme 3 Structural diagrams of calixarene (**a**, *i* = 0, 2, or 4), and resorcarene macrocycles (**b**, **c**) used in monolayer investigations, where R represents a strongly hydrophobic residue, and A represents an acidic (= metal ion coordinating) group. Although many different ring sizes and substitution patterns might be realized experimentally, few derivatives can be synthesized efficiently, due to their amphiphilic and multifunctional nature and the existence of different interchanging conformers

The use of these particular compounds might be rationalized in terms of their modular structure, which allowed us to synthesize amphiphilic compounds of different sizes and shapes, varying charge distributions and stereochemical arrangements of the coordinating head groups A (Scheme 3). In order to distinguish as much as possible between the various physical parameters that are known to influence the epitaxial growth of inorganic crystalline materials, we defined several working hypotheses that we tested in comparative crystal growth studies.

In a first set of experiments, the growth of calcite crystals beneath monolayers of the tetracarboxy-calix[4]arenes – namely, 5,11,17,23-tetrakis-(1,1,3,3-tetramethylbutyl)-25,26,27,28-tetra(carboxymethoxy)calix[4]arene (**12**) and 5,11,17,23-tetra-*t*-butyl-25,26,27,28-tetrakis(carboxymethoxy)calix

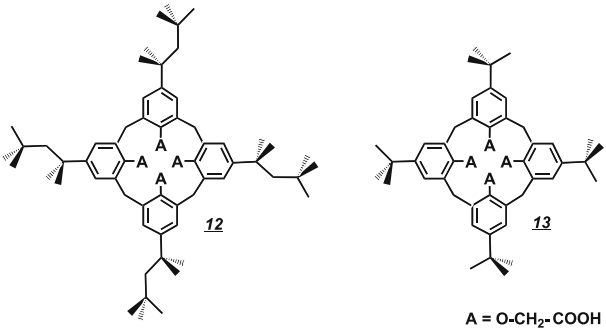

Scheme 4 Structural formulae of tetracarboxy-calix[4]arenes (**12**, **13**) bearing different hydrophobic substituents. The average area/molecule of **12** in a compressed monolayer is more than 15% larger than the corresponding value of **13** (at equal surface pressure)

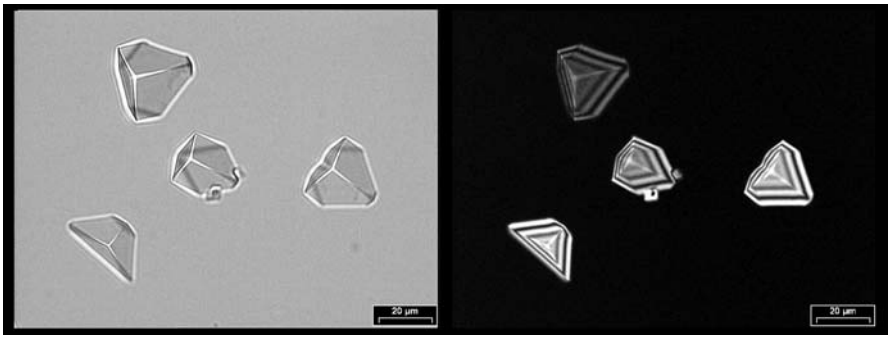

Fig. 15 *Left*: Optical micrograph (*bright field*) of (01.2) oriented calcite single crystals grown under a monolayer of **12** and **13**, respectively, after 3 h ($\pi = 0.1$ mN m^{-1}, $[Ca(HCO_3)_2]_{t=0} = 9$ mM). *Right*: Same crystal specimen observed in plane polarized light. The viewing direction is parallel to the monolayer surface normal, and crystals are observed from below the aqueous subphase. (Reprinted from [93] with permission)

[4]arene (**13**) – were investigated, which differ from each other by *the bulkiness of hydrophobic substituents* at the upper-rim of the macrocyclic backbone (Scheme 4).

Crystal growth experiments have shown that the same uniformly (01.2) oriented calcite single crystals grow beneath monolayers of **12** as well as **13** (Fig. 15) [93, 94]. The fact that identically oriented calcite crystals are obtained under monolayers of differently sized calix[4]arenes gives a strong indication *against* the assumption that an epitaxial match between the monolayer and the juxtaposed crystal surface is required for inducing a certain crystal growth behavior. However, according to these results it was still possible that the calix[4]arene ligands **12, 13** might afford a common, highly specific coordination motif by which they could bind to the {01.2} crystal face of the overgrown calcite crystals.

4.6
Influence of Coordination Geometry

In order to answer this critical question, a second type of macrocyclic ligands, the tetracarboxy-resorc[4]arene *rccc*-5,11,17,23-tetracarboxy-4,6,10,12,16,18,22,24-octa-*O*-methyl-2,8,14,20-tetra(*n*-undecyl)resorc[4]arene (**14**; Scheme 5), was designed and used in crystallization assays [95].

The single crystal X-ray structure analysis of a number of Ca^{2+} complexes of **12, 13** and **14** showed that the typical Ca^{2+} coordination motifs of these ligands are largely different (Fig. 16) [93–95]. However, in spite of these fundamental differences in molecular structure, crystallization assays employing monolayers of **14** gave (01.2) oriented calcite crystals that were virtually indistinguishable from those that grew beneath monolayers of **12** or **13**.

This unexpected experimental observation led us to examine the phase behavior of **12, 13** and **14** monolayers in more detail, for which we simultaneously recorded Langmuir and surface potential isotherms. Brewster-angle microscopy (BAM) images were taken for monolayers at different compression states.

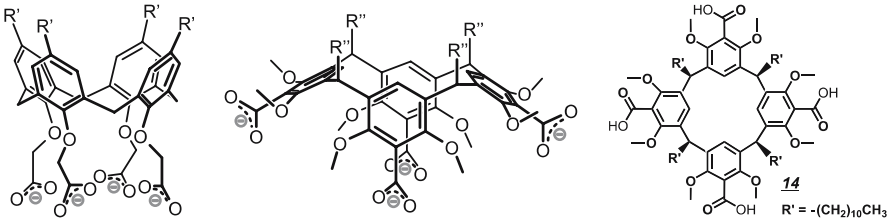

Scheme 5 *Left*: Typical arrangements of carboxylate moieties in calix[4]arene-type (**12, 13**) and resorc[4]arene-type (**14**) ligands (R′ *tert*-butyl or *tert*-octyl, R″ *n*-undecyl). *Right*: Structural formula of tetracarboxy-resorc[4]arene **14**, which according to X-ray analytical investigations and NMR studies assumes a C_{2v}-symmetric *boat* conformation [95]

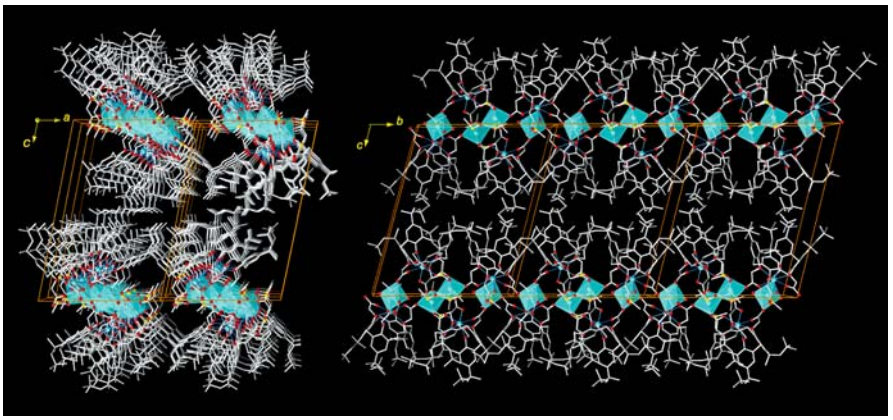

Fig. 16 Wire model of the coordination polymer of the calcium complex of **12** showing the packing arrangement of the one-dimensional polymeric strands in the crystal lattice. Solvent DMSO molecules occluded in the crystal lattice and hydrogen atoms are omitted for clarity. Coordination polyhedrons are displayed for interconnecting Ca ions only. (Reprinted from [93] with permission)

In summary, the results of these investigations demonstrated that neither calixarene nor resorcarene derivatives have a tendency to form highly ordered liquid-crystalline phases during compression. Moreover, the growth of (01.2) oriented calcite crystals exclusively occurred at low surface pressure ($\pi = 0.1–1$ mN m^{-1}), where the monolayers show a transition from the liquid-expanded to the liquid-condensed state of matter. The morphology of

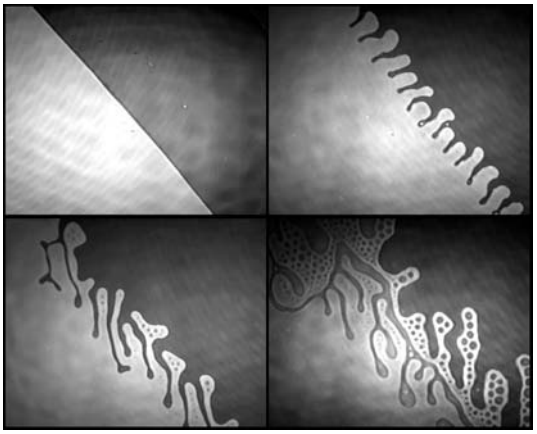

Fig. 17 Typical BAM micrographs of monolayers of **12** at 24 °C on 10 mM $CaCl_2$. Monolayer domains appear as *light regions*. All micrographs were recorded at identical surface pressure ($\pi = 0.1$ mN m^{-1}) within a period of 5 min. (Scanned image area 450 × 400 μm.) (Reprinted from [93] with permission)

the monolayer in this pressure regime is characterized by a high mobility of the molecules, as can be concluded from the typical foamy texture observed in BAM micrographs (Fig. 17).

4.7 Influence of Surface Charge Density

In order to gain additional insight into the interactions between monolayers and hydrated calcium and carbonate ions, the *non-charged* amphiphilic alcohol 5,11,17,23-tetrakis-(1,1,3,3-tetramethylbutyl)-25,26,27,28-tetra(2-hydroxyethoxy)calix[4]arene (**15**) was employed. Monolayers of **15** were found to strongly inhibit heterogeneous nucleation of $CaCO_3$ crystals [96]. The surface potential of a monolayer arises from the dipole moment of the constituent molecules, from the change of orientation of water molecules, and also from interactions between the headgroups and electrolytes dissolved in the subphase [97–99]. In this study electrostatic interactions between monolayers of structurally related amphiphilic calix[4]arene derivatives **12** and **15** and subphase ions was examined. In the low pressure region ($\pi = 0.0–0.5$ mN/m) of the monolayer phase diagram, the experimental surface potential values for monolayers of **12** and **15** on H_2O are almost identical. On a Ca-containing subphase (10 mM $CaCl_2$) the surface potential shows a significant increase only for monolayers of **12**, which clearly demonstrates that the calix[4]arene derivative **15** is unable to bind Ca ions by virtue of electrostatic and/or coordinative interactions. Furthermore, the experimental results indicated that a *low* surface pressure ($\pi = 0.1–0.5$ mN/m) is a necessary condition for the growth of uniformly (01.2) oriented calcite crystals. The phase diagram of **12** and previous investigations of the monolayer structure show no indication for long-range order in the monolayer – that is, the x and y-components of the molecular dipole moments are laterally uncorrelated.

The growth of calcite single crystals showing a preferential (01.2) orientation has been reported for other monolayer systems, including the polymeric Langmuir–Schaefer films of 10,12-pentacosadiynoic acid (**7**) mentioned above, as well as hydrogen-bonded molecular ribbons (**8**). Much effort has been spent in correlating the periodicity of the calcite $\{01.2\}$ cleavage plane with the proposed monolayer structures (although experimental evidence, such as crystallographic investigations of characteristic molecular packing arrangements and Ca ion coordination motifs, has not been presented). However, it is hard to believe that the coincident growth of (01.2) oriented calcite crystals beneath structurally highly dissimilar monolayers is a consequence of a strict geometrical or even a stereochemical matching. In fact, this coincidence (that we laxly designate the "012-syndrome" in our group), indicated to us that non-directional interactions between the monolayer and the juxtaposed crystal face might be the most important factor.

To further support this hypothesis the crystallization of $CaCO_3$ below monolayers of two structurally different macrocyclic octacarboxylic acids, *rccc*-4,6,10,12,16,18,22,24-octakis-*O*-(carboxymethyl)-2,8,14,20-tetra(*n*-undecyl)resorc[4]arene (**16**) and 5,11,17,23,29,35,41,47-octakis-(1,1,3,3-tetramethylbutyl)-49,50,51,52,53,54,55,56-octa(carboxymethoxy)-calix[8]arene (**17**), were investigated (Scheme 6) [100]. Compounds **16** and **17** were chosen for these investigations because they differ by a factor of two in molecular surface area. It is thus possible to adjust the surface charge density underneath monolayers by a proper molecular design.

Interestingly, $CaCO_3$ crystallization beneath monolayers of **17** led to the formation of (01.2) oriented calcite crystals, despite the fact that the monolayer of **16** manifests a completely different growth characteristic: namely, the formation of acicular aragonite crystal aggregates at high surface pressure and at an ionic composition of the aqueous subphase that would normally yield the thermodynamically more stable calcite (Fig. 18).

In summary, these investigations provide compelling experimental evidence that the crystallization of $CaCO_3$ below monolayers of amphiphilic polyacids is largely controlled by the *surface charge density* that accumulates underneath the monolayer. Unfortunately, this functional correlation is difficult to confirm, since there exists (to the best of our knowledge) no analytical technique for measuring the absolute value of the surface charge density beneath the monolayer. The measurable *surface potential* of a monolayer is dependent on many factors, including the molecular structure of the surfactant, the packing arrangement and the composition of the aqueous subphase [97–99]. Moreover, it is not clear whether control over crystal nucleation by an increased surface charge density is gained through polarity matching between the surface monolayer and the incipient crystal surface, or if crystal nucleation and growth processes are kinetically controlled,

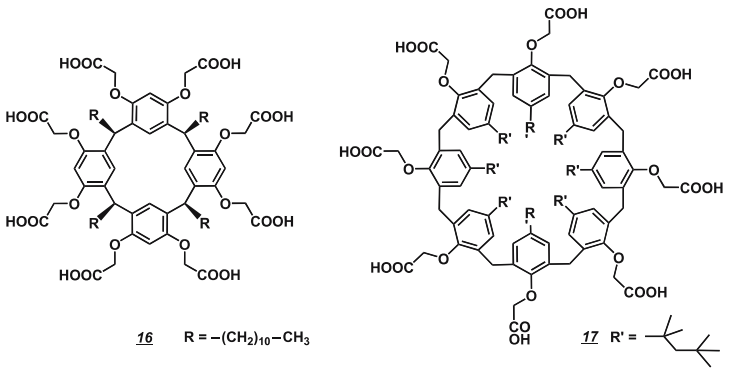

Scheme 6 Structural formulae of octacarboxy-resorc[4]arene (**16**) and octacarboxy-calix[8]arene (**17**) having the same number (= 8) of carboxylate residues but differing largely in molecular size

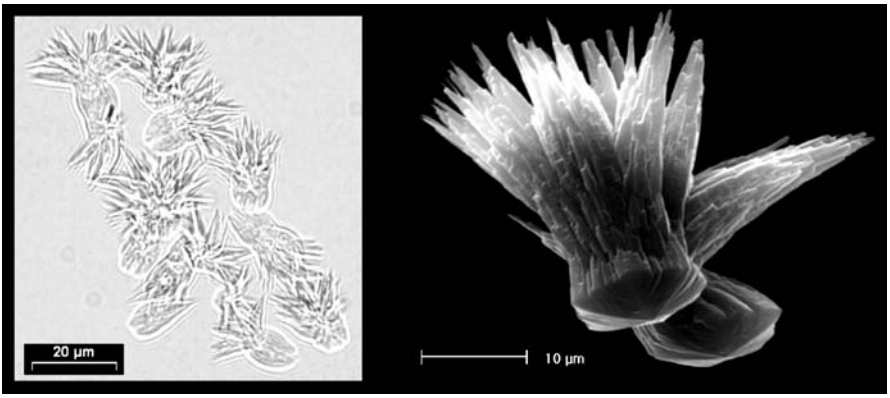

Fig. 18 *Left*: Bright-field optical micrograph of aragonite crystals grown beneath a monolayer of **16** after 3 h ($\pi = 20$ mN m^{-1}, $CaCl_2/NaHCO_3$ 9/18 mM)). *Right*: Scanning electron micrographs (crystals collected after 6 h) of crystals grown under a monolayer of **16**. (Reprinted from [100] with permission)

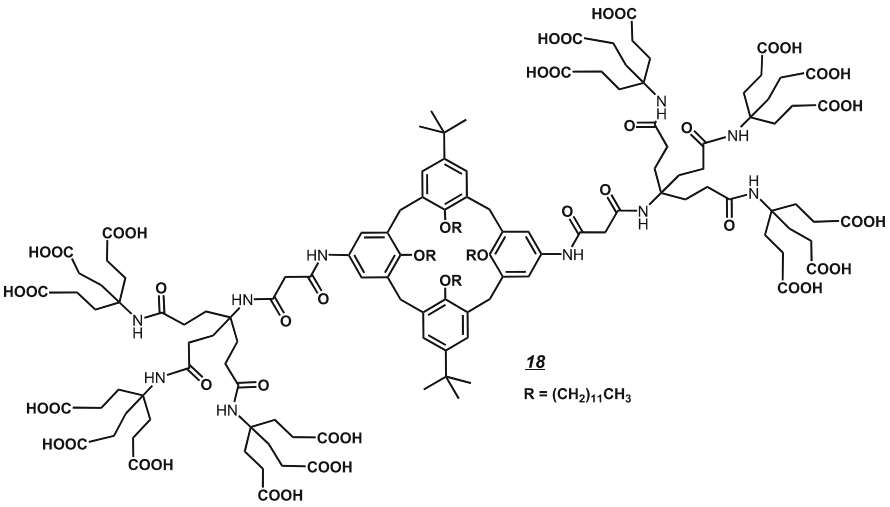

Scheme 7 Structural formula of the amphilic dendron-calix[4]arene (**18**) comprised of 18 carboxylic acid residues

or if both factors are equally important. In order to test whether monolayers generating a sufficiently high surface charge density are able to induce and stabilize metastable crystal phases at the air–water interface, the highly charged amphiphilic dendron-calix[4]arene, 5,17-di[(2-carboxyacetyl) amino]-11,23-di(*tert*-butyl)-25,26,27,28-tetradodecyloxycalix[4]arene [2]:(2-aza-3-oxopentylidyn):propanacid (**18**) was employed [101]. Indeed, crystallization of $CaCO_3$ beneath monolayers of **18** selectively led to growth of

the metastable polymorph vaterite at low surface pressure. Monolayers of **18** induce the formation of vaterite at a surface charge density corresponding to 6.7–7.2 COO^-/nm^2. On the other hand, surface charge densities in the range of 4.65–5.00 COO^-/nm^2 led to selective crystallization of aragonite, as was shown for monolayers of **16** and 5-hexadecyloxy-isophthalic acid (**11**), respectively. The formation of uniformly oriented calcite crystals with the highly polar {01.2} face oriented toward the monolayer was observed on many structurally different monolayers, all sharing similar charge densities of 2.0–2.4 COO^-/nm^2. A complete summary of the various carboxylic amphiphiles that have been used as crystallization templates and the $CaCO_3$ growth morphologies that they induce is given in Table 4.

Table 4 Correlation between area/molecule of amphiphiles used as crystallization templates and the $CaCO_3$ growth morphologies that they induce

Compound	Area/molecule		Area/molecule at which $CaCO_3$ crystals were grown [nm^2]	Charges in headgroup/ nm^2	Polymorph (pref. orientation, if any)	Refs.
	Monolayer data [nm^2]	Crystal data [nm^2]				
1	0.23–0.24 [b]	n.d.	0.22–0.23	4.35–4.44	Calcite (10.0), vaterite	[82]
2	0.26 [b]	n.d.	n.p.		(00.1)	[83]
3	0.23 [b]	n.d.	n.p.		(00.1)	[83]
6	n.p.	n.d.	$\pi = 0–5$ mN m^{-1} $\pi = 20–25$ mN m^{-1}		Calcite vaterite	[86]
8	0.50 [a]	n.d.	0.43–0.50	2.00–2.33	Calcite (01.2)	[89]
9	0.50 [b]	n.d.	0.60	3.33	Calcite (10.0)	[90]
9a	0.45 [b]	n.d.	0.40	2.50	Calcite (10.0)	
10	2.50 [b]	n.d.		1.90–2.00	Calcite (01.2), Calcite (10.0)	[91]
11	n.p.	0.43	$\pi = 10$ mN m^{-1}	4.65	Aragonite, vaterite	[92]
12	1.70–1.75 [b]	1.70	1.75–1.80	2.22–2.29	Calcite (01.2)	[93]
13	1.30–1.40 [b]	1.70	1.70–1.80	2.35–2.42	Calcite (01.2)	[94]
14	1.70–1.75 [b]	1.83	2.00–2.10	1.90–2.00	Calcite (01.2)	[95]
16	1.65–1.70 [a]	1.71				[100]
	1.80–1.85 [b]	n.d.	1.60–1.70	4.71–5.00	Aragonite, vaterite	
17	2.75–2.80 [b]	n.d.	3.30–3.50 2.60–2.70	2.29–2.44 2.96–3.08	Calcite (01.2) Calcite, vaterite	[100]
18	1.95–2.05 [b]	n.d.	2.50–2.70	6.70–7.20	Vaterite	[101]

n.d. not determined, *n.p.* not published

[a] H_2O: doubly deionized water, resistance 18.2 MΩ · cm

[b] $CaCO_3$, 9 mM

5
Formation of Tabular Aragonite Crystals via a Non-Epitaxial Growth Mechanism

As the number of investigations targeting the molecular blueprinting beneath monolayers steadily increased, a notable change of the current template model of biomineralization took place, such that the vital role of *amorphous precursors* in biologically induced mineralization processes was emphasized [102, 103]. This change in paradigm was stimulated by the discovery of thin layers of amorphous calcium carbonate preceding the formation of crystalline materials in different organisms [104, 105]. These reports – together with the fact that, to date, no monolayer model system has been able to produce the specific crystal morphology of pseudohexagonal tabular aragonite crystals found in nacre – has led us to modify the experimental conditions in monolayer investigations.

Previous studies performed using arachidic acid (**19**) or amphiphilic tricarboxyphenylporphyrin iron (III) μ-oxo dimers (**20**) had already shown that

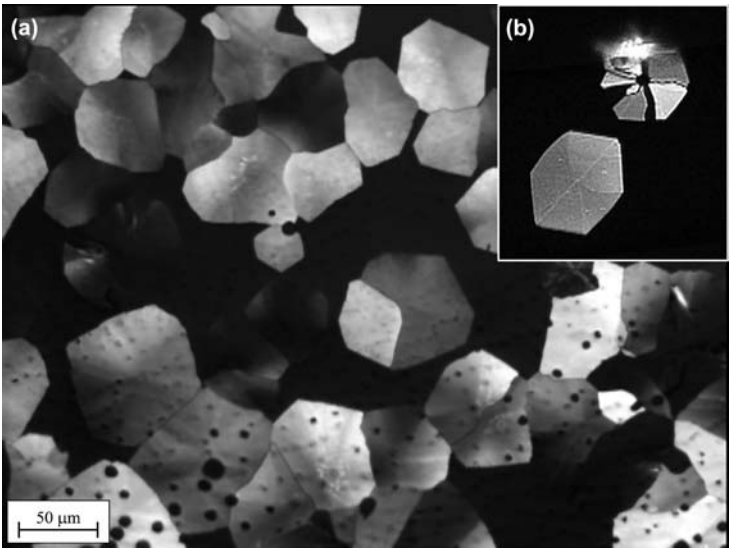

Fig. 19 **a** Polarization optical micrograph of polycrystalline calcium carbonate crystals grown from an amorphous thin film that forms beneath a monolayer of **14** when the aqueous subphase contains a growth inhibitor (polyacrylate). Holes inside the crystals are presumably due to the evolution of CO_2 bubbles from the aqueous subphase. **b** Close-up of two crystal specimens. The intact hexagonal platelet manifests sectors that might result from interpenetration twinning. The upper crystal has disintegrated into triangular sectors, the breakage presumably originating in the twinned contact planes of the crystal. Note that the pseudohexagonal shape and the twinning pattern are quite similar to those of the aragonitic platelets in biogenic nacre (Amos et al, submitted for publication)

a thin film of amorphous calcium carbonate might form below the monolayer if the subphase contains a soluble polyelectrolyte that acts as (non-specific) crystal growth inhibitor [106]. In the presence of polyacrylic acid, the fatty acid per calcium ratio is about 14–25, according to grazing-incidence X-ray diffraction measurements, and tablet morphologies of $CaCO_3$ most often resulted in the formation of calcite films [107].

Recently, the formation of single-crystalline aragonite (as well as calcite) tablets and films was accomplished by precipitating an amorphous precursor under conditions exploiting the synergistic effects of a monolayer of tetracarboxy-resorc[4]arene (**14**) and water-soluble additives, such as polyacrylic acid and/or magnesium ions (Amos et al, submitted for publication). Using appropriate concentrations of the latter, an initially amorphous film can be deposited beneath the monolayer that later crystallizes into polycrystalline films with either single-crystalline mosaic or spherulitic structure (Fig. 19a). Of particular importance is the synthesis of single-crystalline mosaic films of aragonite, which resemble the tablets of aragonite crystals in the nacreous layer of mollusc shells (Fig. 19b).

6 Conclusions

In the literature, the growth of inorganic materials below negatively charged monolayers is frequently considered to be a suitable model system for biomineralization processes. The fact that some monolayers give rise to oriented overgrowth of calcium carbonate crystals has been interpreted in terms of a geometrical and stereochemical complementarity between the arrangement of headgroups in the monolayer and the position of Ca ions in the crystal plane that attaches to the monolayer. The concept of the "molecular blueprinting" of ionic solids has partly arisen from the numerous astonishingly perfect crystal architectures found in biomineralizing organisms, the most prominent example of which is certainly provided by the "brick-and-mortar" structure of nacre. Until recently, the most widely accepted model for the emergence of nacre has suggested an epitaxy mechanism, according to which a highly ordered composite of crystal-nucleating acidic proteins and structural framework macromolecules (mostly chitin) acts as a supramolecular template matrix governing the site-selective and orientation-selective nucleation of the inorganic crystals. However, recent investigations of the structure of nacre provide strong evidence against this simple template hypothesis [108]. It turns out that the biosynthesis of an amorphous calcium carbonate precursor precedes formation of aragonite crystals. The mechanisms by which the amorphous phase is switched into a specific calcium carbonate polymorph and into crystals of particular shape are still largely unknown. However, by adapting model systems to this new paradigm, spe-

cific aspects of the complex biological growth processes might be suitably addressed.

Comparative investigations of the growth of calcium carbonate beneath monolayers of macrocyclic polyacids, for instance, have demonstrated that non-directional electrostatic parameters, such as the average charge density or the mean dipole moment of the monolayer, determine the orientation and the polymorph of the overgrowing crystals. A summary of the monolayer systems we have employed so far and the crystal morphologies they induce is given in Fig. 20.

Our results show that it is possible to control the surface charge densities in monolayers by the appropriate design of amphiphilic molecules. A polymorph switch occurs above a critical monolayer charge density at which aragonite or vaterite nucleation ensues, presumably due to a kinetically controlled precipitation process (Fig. 21a). Below this critical charge density value (for which, based on numerous monolayer investigations (Table 4), we may tentatively assign a value range of 3.5–4.5 COO^-/nm^2), calcite single crystals form. The sharply defined rhombohedral shape of these crystals and the fact that they show an island-like distribution beneath the monolayer provide a strong indication against epitaxial lattice correlations between the monolayer matrix and the incipient crystal face. Moreover, monolayers consisting of structurally

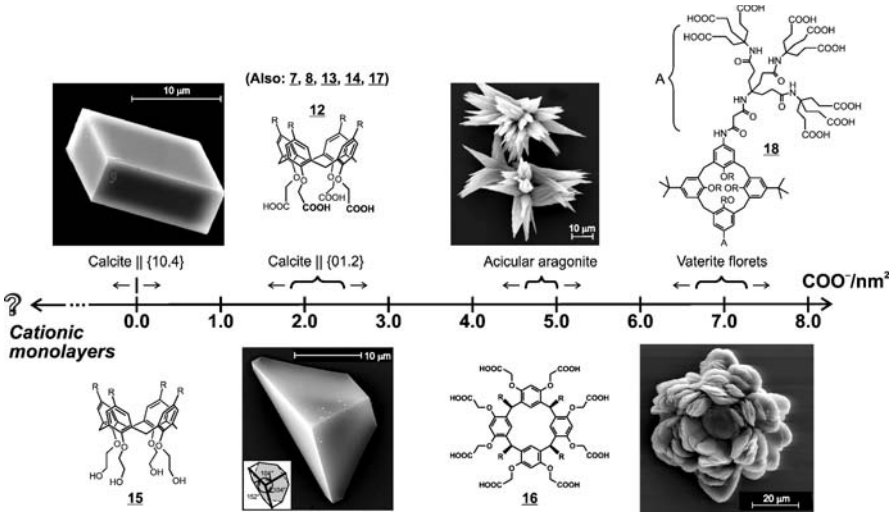

Fig. 20 Overview of macrocyclic polyacids employed in previous investigations of the growth of calcium carbonate beneath monolayers. Polyacids are arranged according to increasing (negative) charge density, which is expressed here as the number of carboxylate residues per unit area. Experimental ranges of charge density leading to a characteristic calcium carbonate crystal habit or orientation are indicated with *braces*. (Charge density values are directly gained from Langmuir isotherms)

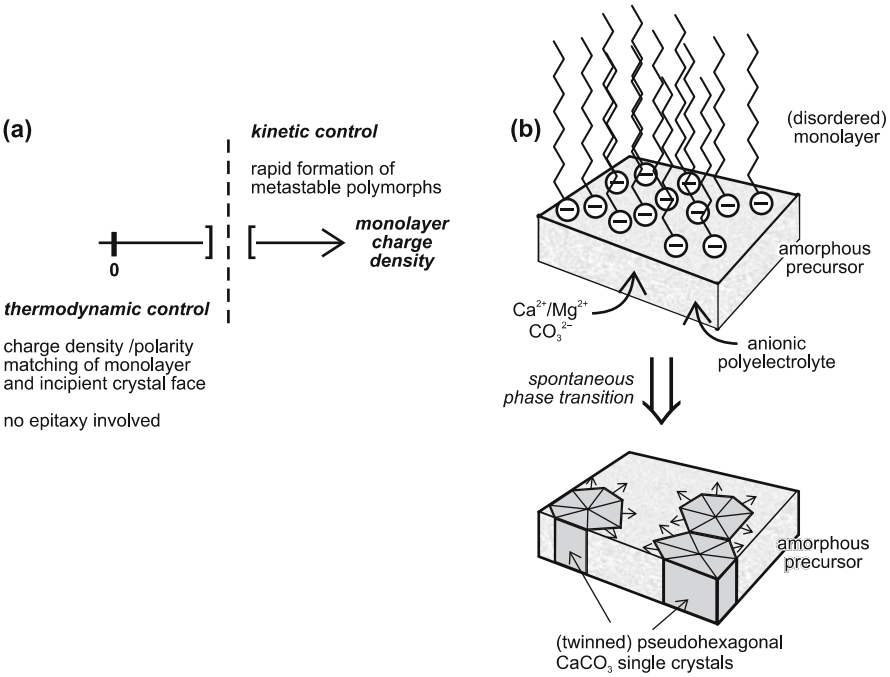

Fig. 21 **a** Scheme of charge density controlling the inorganic crystal polymorph that forms beneath the monolayer. For calcium carbonate, a switch from thermodynamically stable calcite to less-stable aragonite or vaterite occurs at a charge density ranging from 3.5–4.5 COO^-/nm^2. **b** Formation of polycrystalline thin films comprised of tabular pseudohexagonal calcium carbonate crystals via transformation of an amorphous precursor thin film. Recent investigations indicate that a similar phase transition occurs during the biological formation of nacre

very dissimilar amphiphiles often lead to identical crystal orientations, for which nucleation from the {01.2} crystal face of calcite is most often observed. We suggest that crystal nucleation occurs preferentially from this particular face because of charge density/polarity matching at the interface, considering that the {01.2} face is the most strongly polar (low-index) crystal face of the calcite crystal lattice. This hypothesis is further supported by recent modeling studies, which question the idea of stereochemical or geometrical complementarity between the monolayer and the nucleated crystal face [109, 110].

There are notable exceptions, such as monolayers of simple monofunctional surfactants, which lead to exceptional crystal growth orientations (e.g., alkyl sulfates leading to nucleation from the {00.1} crystal face or alkyl carboxylates nucleating calcite from a {11.0} face (Table 4)). However, more in-depth studies employing these simple surfactants once again have chal-

lenged the simple picture of interfacial complementarity. To give an example, the crystallization of $CaCO_3$ beneath fatty acid monolayers was studied by in-situ grazing incidence X-ray diffraction [111]. It was found that in monolayer systems of stearic acid (**1**) or arachidic acid (**19**), spread on 4.5 or 9 mM calcium carbonate solutions, there are only some four to eight surfactant molecules per calcium ion. A strict epitaxial correlation between the monolayer and the nucleated crystal would require a 1 : 1 or 2 : 1 ratio. This result demonstrates that the structure of the monolayer/crystal interface is very likely not as simple as suggested in preceding reports. Thus, it is safe to predict that there will be many more investigations in the near future targeting the fundamental mechanisms of crystal nucleation and growth beneath structurally mobile monolayers (without having to emphasize any model character that such systems may have for biomineralization processes!).

On the other hand, one of the most annoying and puzzling aspects of monolayer studies claimed as biomimetic model systems has been the fact that until very recently none of the systems has produced crystal morphologies reminiscent of aragonitic nacre, although this was implicit in the motivation of numerous studies. As we have stressed in this review, the main reason for this discrepancy is most likely an imperfect working hypothesis regarding the biological process of nacre formation itself. In fact, in recent model systems explicitly taking into account the multistepped formation process of biogenic nacre, including a phase transition from an amorphous precursor to a solid phase, many characteristic features of nacre could be reproduced in quite simple model systems [112].

Again, model systems employing monolayers as crystal growth matrices may provide novel insights into such transformations, as we have shown very recently when the aqueous phase contains a soluble polyelectrolyte (polyacrylate) and the Ca to Mg ion concentration ratio is adjusted appropriately. This system produces tabular pseudohexagonal calcium carbonate platelets, which occasionally show the characteristic crystal twinning pattern that is frequently reported for aragonite crystal platelets stemming from bivalve nacre. A shortcoming of the strategy for producing highly regular polycrystalline thin films according to Fig. 21b is the fact that the crystal texture of the film manifests significant variation from experiment to experiment (at least in our laboratory). Thus, the process requires further improvement if it is ever to be translated into a technically reliable production scheme for artificial nacre. A major leap towards this goal is certainly the development of processing strategies that lead to the deposition of *multilayered* crystal architectures. Recent progress in understanding natural biomineralization processes as well as experimental advances gained from model studies give rise to the hope that novel composite materials reminiscent of their biological counterparts might be produced at an industrial scale in the near future. It is very likely that some of these bionic materials will be constructed from totally different materials, since there is no urgent need to stick to calcium carbonate, chitin, or pep-

tides once the basic principles of biomineralization are clearly understood. The competition for attractive products has just begun [113].

Acknowledgements The authors are thankful to C.E. Krill III for proofreading the manuscript and providing critical comments. Financial support provided by the Deutsche Forschungsgemeinschaft (DFG Priority Program 1117, "Principles of Biomineralization", DFG grant Vo829/3) is gratefully acknowledged.

References

1. Weiner S, Addadi L (1997) J Mater Chem 7:689
2. Geisen M, Billard C, Broerse ATC, Cros L, Probert I, Young JR (2002) Eur J Phycol 37:531
3. Towe KM, Harper CW Jr (1966) Science 154:153
4. Gotliv BA, Addadi L, Weiner S (2003) ChemBioChem 4:522
5. Arias JL, Neira-Carrillo A, Arias JI, Escobar C, Bodero M, David M, Fernandez MS (2004) J Mater Chem 14:2154
6. Effenberger H, Mereiter K, Zemann J (1981) Z Kristallogr 156:233. ICSD no. 100676
7. de Villiers JPR (1971) Am Mineral 56:758. ICSD no. 15194
8. Meyer H-J (1969) Z Kristallogr 128:183. ICSD no. 18127
9. Effenberger H (1981) Monatsh Chem 112:899. ICSD no. 100846
10. Hesse KF, Kueppers H, Suess E (1983) Z Kristallogr 163:227. ICSD no. 31305
11. Morse JW, Mackenzie FD (1990) Geochemistry of sedimentary carbonate. Elsevier, Amsterdam, p 41
12. Lippmann F (1973) Sedimentary carbonate minerals, minerals, rocks and inorganic materials, vol 6. Springer, Berlin Heidelberg New York
13. Givargizov EI (1991) In: Oriented crystallization on amorphous substrates. Plenum, New York, p 10
14. Ward MD (2001) Chem Rev 101:1697
15. Carbone A, Prusinkiewicz P, Gromov M (eds) (2000) Pattern formation in biology, vision and dynamics. World Scientific, Hackensack NJ
16. Ball P (1991) The self-made tapestry: pattern formation in nature. Oxford University Press, USA
17. Simkiss K, Wilbur KM (1989) In: Biomineralization. Cell biology and mineral deposition. Academic, San Diego, p 230
18. Volkmer D (2000) In: Cooke M, Poole CF (eds) Encyclopedia of separation science, vol 2 (Crystallization). Academic, New York, p 940
19. Schäffer TE, Ionescu-Zanetti C, Proksch R, Fritz M, Walters DA, Almqvist N, Zaremba CM, Belcher AM, Smith BL, Stucky GD, Morse DE, Hansma PK (1997) Chem Mater 9:1731
20. Marin F, Luquet G (2004) C R Palevol 3:469
21. Belcher AM, Wu XH, Christensen RJ, Hansma PK, Stucky GD, Morse DE (1996) Nature 381:56
22. Falini G, Albeck S, Weiner S, Addadi L (1996) Science 271:67
23. Samata T, Hayashi N, Kono M, Hasegawa K, Horita C, Akera S (1999) FEBS Lett 462:225
24. Sudo S, Fujikawa T, Nagakura T, Ohkubo T, Sakaguchi K, Tanaka M, Nakashima K, Takahashi T (1997) Nature 387:563

25. Zhang Y, Xie LP, Meng QX, Jiang TM, Pu RL, Chen L, Zhang RQ (2003) Comp Biochem Phys B 135:565
26. Kono M, Hayashi N, Samata T (2000) Biochem Biophys Res Comm 269:213
27. Schen X, Belcher AM, Hansma PK, Stucky GD, Morse DE (1997) J Biol Chem 272:32472
28. Suzuki M, Murayama E, Inoue H, Ozaki N, Tohse H, Kogure T, Nagasawa H (2004) Biochem J 382:205
29. Sarashina I, Endo K (1998) Am Mineral 83:1510
30. Miyamoto H, Miyashita T, Okushima M, Nakano S, Morita T, Matsushiro A (1996) Proc Natl Acad Sci USA 93:9657
31. Marin F, Corstjens P, de Gaulejac B, de Vrind-De Jong E, Westbroek P (2000) J Biol Chem 275:20667
32. Mann K, Weiss IM, André S, Gabius H-J, Fritz M (2000) Eur J Biochem 267:5257
33. Weiss IM, Göhring W, Fritz M, Mann K (2001) Biochem Biophys Res Commun 285:244
34. Tsukamoto D, Sarashina I, Endo K (2004) Biochem Biophys Res Commun 320:1175
35. Michenfelder M, Fu G, Lawrence C, Weaver JC, Wustman BA, Taranto L, Evans JS, Morse DE (2003) Biopolymers 70:522
36. Fu G, Valiyaveettil S, Wopenka B, Morse DE (2005) Biomacromolecules 6:1289
37. Marin F, Amons R, Guichard N, Stigter M, Hecker A, Luquet G, Layrolle P, Alcaraz G, Riondet C, Westbroek P (2005) J Biol Chem 280:33895
38. Gotliv B-A, Kessler N, Sumerel JL, Morse DE, Tuross N, Addadi L, Weiner S (2005) ChemBioChem 6:304
39. Addadi L, Weiner S (1989) In: Mann S, Webb J, Williams RJP (eds) Biomineralization. VCH, Weinheim, p 133
40. Addadi L, Moradian J, Shay E, Maroudas NG, Weiner S (1987) P Natl Acad Sci USA 84:2732
41. Levi Y, Albeck S, Brack A, Weiner S, Addadi L (1998) Chem Eur J 4:389
42. Weiss IM, Renner C, Strigl MG, Fritz M (2002) Chem Mater 14:3252
43. Levi-Kalisman Y, Falini G, Addadi L, Weiner S (2001) J Struct Biol 135:8
44. Bertrand M, Brack A (1997) Origin Life Evol B 27:589
45. Weiner S, Traub W (1980) FEBS Lett 111:311
46. Weiner S, Traub W, Parker SB (1984) Proc R Soc B 304:425
47. Giles R, Manne S, Mann S, Morse DE, Stucky GD, Hansma PK (1995) Biol Bull 188:8
48. Yeh Y, Feeney RE (1996) Chem Rev 96:601
49. Davies PL, Sykes BD (1997) Curr Opin Struct Biol 7:828
50. Evans JS (2003) Curr Opin Coll Int Sci 8:48
51. Mayer G (2005) Science 310:1144
52. Wilmot NV, Barber DJ, Taylor JD, Graham AL (1992) Proc R Soc B 337:21
53. Taylor JD, Kennedy WJ, Hall A (1969) Bull Br Mus (Nat Hist) Zool Suppl 3:1
54. Chateigner D, Hedegaard C, Wenk H-R (2000) J Struct Geol 22:1723
55. Bruet BJF, Qi HJ, Boyce MC, Panas R, Tai K, Frick L, Ortiz C (2005) J Mater Res 20:2400
56. Jackson AP, Vincent JFV, Turner RM (1988) Proc R Soc London B Biol Sci 234:415
57. Wang RZ, Suo Z, Evans AG, Yao N, Aksay IA (2001) J Mater Res 16:2485
58. Jackson AP, Vincent JFV, Turner RM (1990) J Mater Sci 25:3173
59. Currey JD (1977) Proc R Soc London B Biol Sci 196:443
60. Erben HK (1974) Biomineralisation 7:14
61. Addadi L, Joester D, Nudelman F, Weiner S (2006) Chem Eur J 12:980
62. Lin A, Meyers MA (2005) Mater Sci Eng A 390:27

63. Mutvei H (1978) Zool Scr 7:287
64. Hedegaard C, Wenk H-R (1998) J Moll Stud 64:133
65. Li X, Chang W-C, Chao YJ, Wang R, Chang M (2004) Nano Lett 4:613
66. Manne S, Zaremba CM, Giles R, Huggins L, Walters DA, Belcher AM, Morse DE, Stucky GD, Didymus JM, Mann S, Hansma PK (1994) Proc R Soc London B 256:17
67. Watabe N (1965) J Ultrastruct Res 12:351
68. Wustman BA, Morse DE, Evans JS (2002) Langmuir 18:9901
69. Smith BL, Schäffer TE, Viani M, Thompson JB, Frederick NA, Kindt J, Belcher A, Stucky GD, Morse DE, Hansma PK (1999) Nature 399:761
70. Meldrum FC (2003) Int Mater Rev 48:187
71. Mann S, Heywood BR, Rajam S, Birchall JD (1998) Nature 334:692
72. Kaganer VM, Möhwald H, Dutta P (1999) Rev Mod Phys 71:779
73. Dynarowicz-Latka P, Dhanabalan A, Oliveira ON Jr (2001) Adv Colloid Interface Sci 91:221
74. Landau EM, Levanon M, Leiserowitz L, Lahav M, Sagiv J (1985) Nature 318:353
75. Weissbuch I, Lahav M, Leiserowitz L (2003) Cryst Growth Des 3:125
76. Zhang Y, Jin R, Zhang L, Liu M (2004) New J Chem 28:614
77. Wenk H-R, Van Houtte P (2004) Rep Prog Phys 67:1367
78. Kitano Y, Hood DW, Park K (1962) J Geophys Res 67:4873
79. Sohnel O, Mullin JW (1982) J Cryst Growth 60:239
80. Kitamura M, Konno H, Yasui A, Masuoka H (2002) J Cryst Growth 236:323
81. Heywood BR (1996) In: Mann S (ed) Biomimetic Materials Chemistry. VCH, Weinheim, p 143
82. Rajam S, Heywood BR, Walker JBA, Mann S, Davey RJ, Birchall JD (1991) J Chem Soc, Faraday Trans 87:727
83. Heywood BR, Mann S (1994) Chem Mater 6:311
84. Heywood BR, Mann S (1994) Adv Mater 6:9
85. Loste E, Diaz-Marti E, Zarbakhsh A, Meldrum F (2003) Langmuir 19:2830
86. Litvin AL, Samuelson LA, Charych DH, Spevak W, Kaplan DL (1995) J Phys Chem 99:12065
87. Berman A, Ahn DJ, Lio A, Salmeron M, Reichert A, Charych D (1995) Science 269:515
88. Ahn DJ, Berman A, Charych D (1996) J Phys Chem 100:12455
89. Champ S, Dickinson JA, Fallon PS, Heywood BR, Mascal M (2000) Angew Chem Int Ed 39:2716
90. Buijnsters PJJA, Donners JJJM, Hill SJ, Heywood BR, Nolte RJM, Zwanenburg B, Sommerdijk NAJM (2001) Langmuir 17:3623
91. Cavalli S, Popescu DC, Tellers EE, Vos MRJ, Pichon BP, Overhand M, Rapaport H, Sommerdijk NAJM, Kros A (2005) Angew Chem Int Ed 44:1
92. Litvin AL, Valiyaveettil S, Kaplan DL, Mann S (1997) Adv Mater 9:124
93. Volkmer D, Fricke M, Vollhardt D, Siegel S (2002) J Chem Soc Dalton Trans 4547
94. Volkmer D, Fricke M (2003) Z Anorg Allg Chem 629:2381
95. Volkmer D, Fricke M, Agena C, Mattay J (2002) CrystEngComm 4:288
96. Volkmer D, Fricke M, Gleiche M, Chi L (2005) Mater Sci Eng C 2:161
97. Lochhead MJ, Letellier SR, Vogel V (1997) J Phys Chem B 101:10821
98. Taylor DM (2000) Adv Colloid Interface Sci 87:183
99. Brockman H (1994) Chem Phys Lipids 73:57
100. Volkmer D, Fricke M, Agena C, Mattay J (2004) J Mater Chem 14:2249
101. Fricke M, Volkmer D, Krill CE III, Kellermann M, Hirsch A (2006) Cryst Growth Des 6:1120

102. Addadi L, Raz S, Weiner S (2003) Adv Mater 15:959
103. Olszta MJ, Odom DJ, Douglas EP, Gower LB (2003) Connect Tiss Res 44 Suppl 1:326
104. Weiss IM, Tuross N, Addadi L, Weiner S (2002) J Exp Zool 293:478
105. Politi Y, Arad T, Klein E, Weiner S, Addadi L (2004) Science 306:1161
106. Xu GF, Yao N, Aksay IA, Groves JT (1998) J Am Chem Soc 120:11977
107. DiMasi E, Patel VM, Sivakumar M, Olszta MJ, Yang YP, Gower LB (2002) Langmuir 18:8902
108. Nassif N, Pinna N, Gehrke N, Antonietti M, Jäger C, Cölfen H (2005) Proc Natl Acad Sci 102:12653
109. Duffy DM, Harding JH (2004) Langmuir 20:7630
110. Duffy DM, Harding JH (2004) Langmuir 20:7637
111. DiMasi E, Oltsza MJ, Patel VM, Gower L (2003) CrystEngComm 5:346
112. Volkmer D, Harms M, Gower L, Ziegler A (2005) Angew Chem Int Ed 44:639
113. BASF symposium on bioinspired materials for the chemical industry at ISIS in Strasbourg, France, 7–9 August 2006

Top Curr Chem (2007) 270: 43–72
DOI 10.1007/128_054

Published online: 5 July 2006

Self-Organized Formation of Hierarchical Structures

Hiroaki Imai

Keio University, Department of Applied Chemistry, 3-14-1 Hiyoshi, Kohoku-ku, 223-8522 Yokohama, Japan
hiroaki@applc.keio.ac.jp

Abstract Hierarchical architectures consisting of small building blocks of inorganic crystals are widely found in biominerals. Crystal growth mimicking biomineralization has been studied using various kinds of organic molecules and molecular assembly. The emergence of complex organization of inorganic crystals was observed through biomimetic approaches in aqueous solution. A wide variety of hierarchical architectures including fractals, dendrites, self-similar and helical structures were achieved in the artificial systems. Self-organized formation, with exquisite control of mass transport and the variation of surface energy with organic molecules, is essential for versatile morphogenesis of inorganic crystals similar to biominerals.

Keywords Biomineral · Nanocrystal · Self-assembly · Self-organization · Self-similarity

1
Introduction: The Hierarchy of Biominerals

Hexagonal prisms of quartz and cubic particles of table salt are typical single crystals exhibiting simple, flat surfaces. We can observe no structures

on an intermediate scale between the macroscopic geometric forms and the microscopic atomic arrays. On the other hand, dendrites, like snowflakes, have periodic branches depending on their environment in the intermediate region. In this sense, the complex forms could be defined as hierarchical structures consisting of units on various scales.

The fascinating structural design of biominerals has attracted the interest of researchers in a broad range of chemistry disciplines [1–3]. Hierarchical architectures consisting of small building blocks of inorganic crystals are often found in biominerals [4, 5]. Hard tissues of vertebrates, such as bones and teeth, usually have a three-dimensional (3D) complex structure that is hierarchically organized with hydroxyapatite nanocrystals and organic matrices, such as collagen fibers. The biosilica of a hexactinellid sponge was reported to be remarkably designed with nanometer-scaled silica that was hierarchically arranged from nanometers to macroscopic lengths [4]. Since the elaborate forms of biominerals are spontaneously produced in a living organism, biomineralization is a typical self-organized formation of hierarchical structures in an aqueous solution system at ambient atmosphere.

Recently, bridged nanocrystals with the incorporation of organic polymers were found to reside in real biominerals [6–11]. Specific macroscopic morphologies in biominerals of seashells, corals, echinoderms, and eggshells consist of the oriented architecture of nanocrystals 20–100 nm in size. Typical scanning electron microscope (SEM) and transmission electron microscope (TEM) images of a nacreous layer of Japanese pearl oyster (*Pinctada fucata*) and a spine of the sea urchin (*Echinometra mathaei* (*Blainville*)) on macroscopic and microscopic scales are shown in Fig. 1. Each biomineral represented the characteristic morphologies on a macroscopic scale. The magnified SEM and TEM images reveal the presence of the assembly of nanocrystal blocks in the microscopic structures of all the biominerals. The sizes of aragonite in the nacreous layer and calcite in the sea urchin spine were within a range of approximately 10–200 nm. Interestingly, the nanocrystals resided in various morphologies and crystal structures beyond the species barrier. These facts indicate that the integration of nanocrystals could be an important process for crystal growth in biomineralization. Moreover, nanoscale mineral bridges between two adjacent nanocrystals were acquired in TEM images (Fig. 1e). Therefore, a biomimetic approach is attracting a great deal of attention in the research fields of materials chemistry and nanotechnology as a smart technique for the fabrication of functional nanoscale materials.

Crystal growth mimicking biomineralization has been studied using various kinds of organic molecules and molecular assembly [12–22]. The emergence of complex and hierarchical architectures of inorganic crystals has been observed through various types of biomimetic processing in aqueous systems [23–26]. In this chapter, hierarchically structured crystals formed

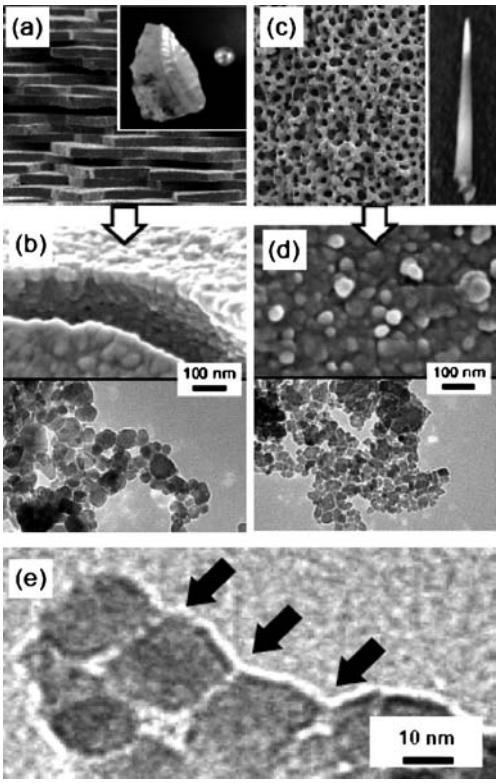

Fig. 1 Typical macroscopic shapes and microscopic structures of biominerals. **a**,**b** Nacreous layer and **c**–**e** sea urchin spine

through self-organization in solution systems are described. A careful review of previous studies on the formation of inorganic crystals exhibiting a wide variety of complex morphologies including fractals, dendrites, and self-similar structures would be helpful for the understanding of biomineralization and development of biomimetic materials processing.

2
A Hierarchy of Nonclassical Crystallization

Recently, many crystallization events, which are not categorized as classical single crystals or polycrystals, have been reported [27–35]. Figure 2 illustrates intermediate states between single crystal and polycrystal. Some of the intermediates, such as particle-mediated crystallizations called mesocrystals, are a hierarchical assembly of nanocrystals to superstructures with an ion or molecule attachment. Mesocrystals are typical examples of nonclassical crys-

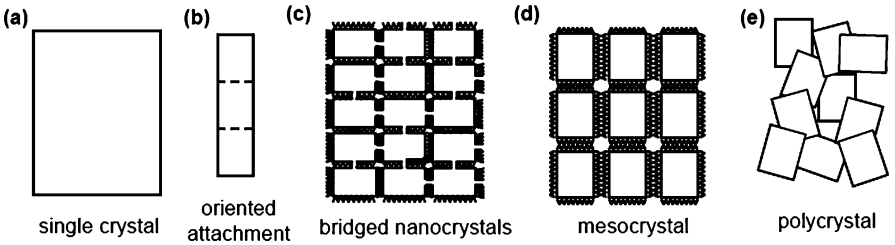

Fig. 2 Classification of intermediate states between single crystal and polycrystal. Oriented attachment and bridged crystal may be categorized as single crystal. Bridged crystal and mesocrystal are fundamentally covered with molecular species that can accept organic molecules

tallization by a modular nanobuilding-block route. They were observed as kinetically metastable species or as intermediates in a crystallization reaction leading to single crystals with typical defects and inclusions. For example, a simple system of calcite was assembled with polystyrene sulfonate (PSS), which underwent mesocrystal formation [29]. Appropriate control allows variation of the mesocrystal morphology, exposing unusual crystal faces in their superstructure. Subsequent crystallographic fusion of mesocrystals can lead to single crystals with preserved shape. Direct nanoparticle fusion according to the mechanism of oriented attachment can directly lead to single crystals. However, the controlling forces and mechanism of mesocrystal formation are largely unknown.

While the self-assembly of nanobuilding blocks into a mesocrystal may be associated with a hierarchy of biominerals, the oriented structure of biominerals could be interpreted as bridged architecture with incorporation of biopolymers. TEM images of the nanomineral bridge between two adjacent nanocrystals were acquired (Fig. 1e). Schäffer and coworkers first reported that a macroscopic mineral bridge was formed in the interlayer of mother-of-pearl [36]. Since the daughter aragonite plate is directed on the mother plate through the formation of a mineral bridge, the orientation of the *c* axis perpendicular to the plates is inherited in a late stage of growth. According to these facts, the oriented architecture of nanocrystals in biominerals is ascribed to the similar bridged-growth process. The complex morphologies of biominerals can be designed by bridged nanocrystals via the self-organized growth in association with biopolymers. A batch of bridged nanocrystals is fundamentally assigned to be a single crystal incorporating organic molecules. However, the crystallographic orientation gradually varies with nonconformity or twin formation at the nanobridges. The nanocrystals, as building blocks, realize the versatile morphological design on a macroscopic scale, especially in terms of complex or curved shapes with a smooth surface.

3
Self-Organization for Morphogenesis on Crystal Growth

Currently, "self-assembly" and "self-organization" are popularly used for spontaneous ordering, including the formation of spatial patterns and temporal oscillation [37–39]. However, the definition of these words is obscure to the general public. Self-assembly occurs near equilibrium, and the order or pattern formed via self-assembly exhibits the periodicity and the symmetry derived from the components of the system. The formation of supramolecules through hydrogen bonds and molecular aggregates, such as micelles, is categorized as self-assembly. On the other hand, self-organization, which is also called "dissipative structure", is ordering at far-from-equilibrium, and the scale of the resultant patterns is larger than that of the components.

Crystallization is the spontaneous formation of a microscopic periodic array of atoms, ions, or molecules and may be categorized as self-assembly or self-organization. The pattern formed by the crystallization is generally affected by the distance between the growth condition and the equilibrium state (i.e., the driving force for the crystallization) such as the degree of supersaturation and the supercooling (Fig. 3). Polyhedral forms are obtained through the crystal growth near the equilibrium state. Since the macroscopic shape of the polyhedrons reflects the arrangement and the symmetry of the microscopic atomic or molecular lattice, which is a component of the system, the crystallization would be categorized as self-assembly. The colloidal crystallization associated with mesocrystals may be classified as a self-assembly

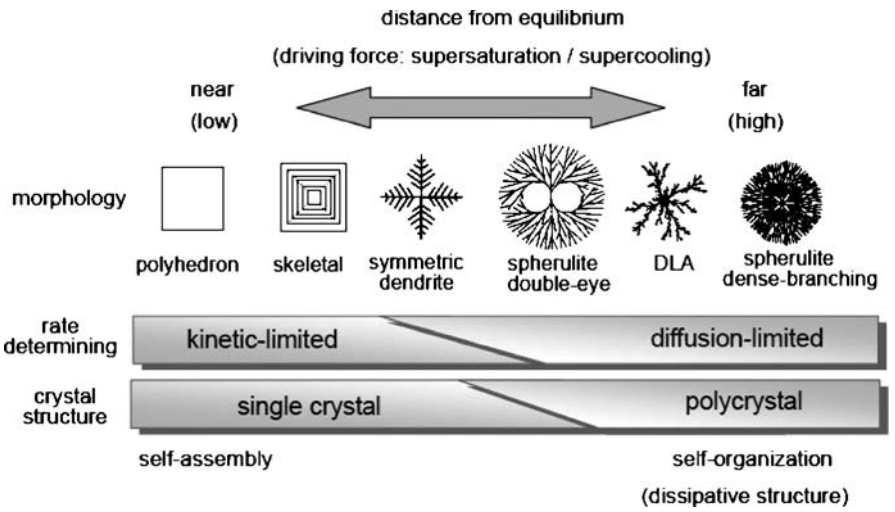

Fig. 3 Self-assembly and self-organization on morphological variation of crystals with increasing the distance from equilibrium or the driving force of crystallization

of the nanoscale components. As the driving force increases, the growth rate is governed by mass diffusion or heat transfer, and then the growing surface becomes unstable in a diffusion field. Under this condition, dendrite forms with a complicated period structure are produced by the competition between the promotion and suppression of the crystal growth. When the driving force is extremely high, the random polycrystals exhibiting spherulite and diffusion-limited aggregate (DLA) are formed with a disappearance of the crystallographic symmetry. The crystallization process of these various morphologies depending on the environment, including the driving force of the crystallization and the diffusion rate of the components, should be categorized as self-organization. Figure 4 shows the morphological transition obtained in the Monte Carlo simulation of a crystal growth from a lattice gas [40]. The time evolution of faceted and dendritic shapes is depicted at different driving forces.

A systematic variation of crystal morphology was experimentally demonstrated by varying the density of the gel matrix [41] (Fig. 5). The morphological evolution of the inorganic crystals ($Ba(NO_3)_2$, NH_4Cl, H_3BO_3, $K_2Cr_2O_7$) was observed in various kinds of organic gel media (agar, gelatin, pectin, and poly(vinyl alcohol)). As the gel density increased, the morphology grown in the gel matrix changed remarkably from polyhedral single crystals exhibiting specific habits into dendritic forms consisting of irregularly branched polycrystalline aggregates, regardless of the sorts of inorganic compounds and gelling agents. The evolution from polyhedrons into dendrites via skeletal forms is ascribed to an increase in the influence of diffusion of the solutes on the crystal growth. Since gel media generally suppress the mobility of ions, densification of the media decreased the apparent diffusion rate of the solutes and finally promoted the formation of diffusion-controlled morphologies including skeletal, dendritic, and branched forms.

Under conditions of a low degree of supersaturation or a low gel density, polyhedral shapes are formed through self-assembly. The morphogenesis of the geometric shapes is restricted because they are thermodynamically stable.

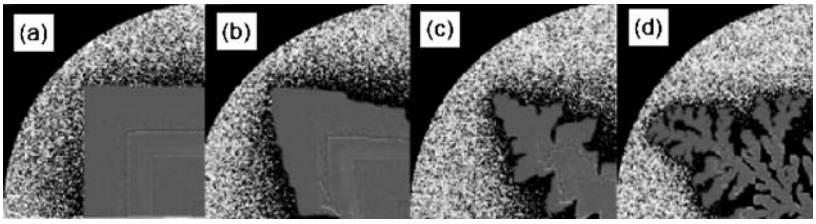

Fig. 4 Morphological transition obtained in the Monte Carlo simulation of crystal growth from a lattice gas. The morphology varied from a faceted shape (**a**) into dendritic form (**c**,**d**) with increasing the driving force of the crystallization. Reproduced from [40] with permission of the American Institute of Physics

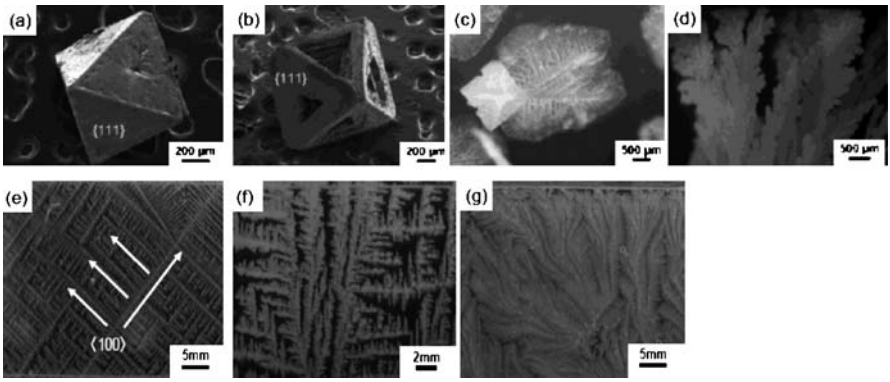

Fig. 5 A variation of crystal morphology demonstrated by varying the density of the gel matrix. The morphology of $Ba(NO_3)_2$ grown in agar was changed from regular octahedron (**a**) into skeleton (**b**), regular dendrite (**c**), and disordered dendrite (**d**) with increasing the gel density. The dendritic morphology of NH_4Cl grown in agar varied from a regular form (**e**) into an irregularly branched one (**g**) with increasing the gel density. Reproduced from [41] with permission of the American Chemical Society

On the other hand, the orderliness and controllability of random aggregates are quite low under conditions of a high degree of supersaturation or a high density of gel matrix. Self-organization that is induced under an intermediate condition would produce various complex and hierarchical structures by the integration of unit crystals with the combination of appropriate order and flexibility. The emergence of the self-organization by a balance between the crystal growth and the mass transport with gel matrix would be an essential factor for the control of the morphogenesis mimicking biomineralization.

4
Self-Organization of Branching Morphologies

4.1
Diffusion-Limited Aggregate and Fractal Crystals

Hyperbranched structures of DLA are one type of hierarchical architectures formed by self-organization under nonequilibrium conditions. The formation of DLA is, in a way, controlled by the possibility of particles reaching the cluster. A fluffy shape with many branches like trees occurs during the diffusion of a particle through the solution. The geometric characterization of DLA is self-similarity, which is an aspect of fractals. For the loosely aggregated clusters, these exponents form fractal numbers, somewhere between 2 (2D-areas) and 3 (dense 3D-buildings). Generally, DLA is found naturally in nonliving (mineral deposition, snowflake growth, lightning paths, viscous

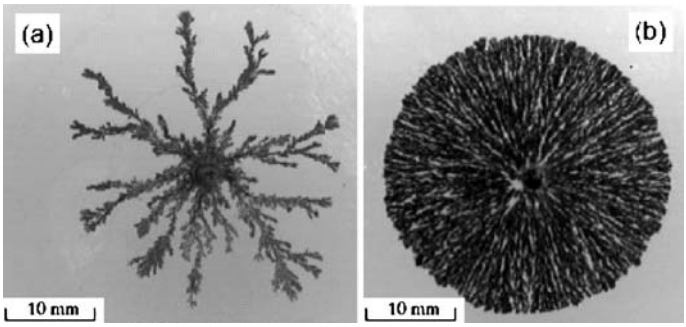

Fig. 6 DLA-like (**a**) and dense branching (**b**) morphologies of zinc electrodeposits grown in flat horizontal cells. Reproduced from [42] with permission of the American Institute of Physics

fingering) or living (corals, bacteria colonies) forms. Moreover, the hierarchical patterns in chemical systems are promising candidates for the design and fabrication of new functional nanomaterials showing a distinct size, shape, and chemical functionality. It is challenging to develop simple and novel synthetic approaches for building hierarchically organized architectures of various systems.

There are many experimental studies of fractal objects as aggregates of crystals grown by electrochemical deposition in solution. As shown in Fig. 6, zinc metal trees were obtained from an electrolyte consisting of a solution of a metallic salt in a 2D cell [42]. The morphologies of the resultant crystals vary, depending on the conditions such as applied voltage and ion concentration. While DLA is grown with a very low voltage and low concentration, dense radial or dense branching morphologies within a clearly defined circular envelope were deposited at low concentrations and at higher applied voltages. These results suggest that the branching morphologies grown under diffusion-controlled mass transport are highly sensitive to the environment of the crystal growth.

4.2 Symmetric Dendrites

Stellar snowflakes are a typical symmetric dendrite. In a diffusion field, small bumps on the surface of a growing crystal develop into large branches, and bumps on the branches become side branches. When the branching instability applies itself to a growing crystal, the result is the formation of a dendrite. This instability plays a major role in producing the complex shapes of crystals. The growth of dendritic crystals depends on a balance between faceting and branching due to the instability. Faceting tends to make simple flat surfaces, while branching tends to make more complex structures. The interplay

between faceting and branching is a delicate one, depending strongly on the conditions of the crystal growth. Commonly, the influence of branching on the formation of symmetric dendrites is smaller than that on the growth of DLA and dense branching morphologies. The formation of symmetric dendrites has focused on single-crystal growth. Phase-field simulations showed that the perturbation of the growth forms by heterogeneities yields a rich variety of polycrystalline growth patterns [43] (Fig. 7). Similar crystallization patterns are also found in thin polymer films with particulate additives and pure films with high supercooling. This fact suggests that the morphological transition from symmetric dendrites to dense branching morphologies is ascribed to the static and dynamic heterogeneity on the crystal growth. The morphological variation from symmetric dendrites into random branching morphologies was experimentally demonstrated by crystal growth of NH_4Cl in agar gel media [41], as shown in Fig. 5. This variation is ascribed to an increase in the gel density causing a decrease in the diffusion rate of the solute.

Recent reports on particular dendritic morphologies of sulfides, oxides, carbonates, and metal crystals formed in solution systems are described here. Hierarchical eight-arm, star-shaped PbS single crystals were synthesized by the controlled release of sulfide ions from thioacetamide in aqueous solutions of lead acetate and acetic acid (Fig. 8a) [44]. The unique star-shaped PbS crystals have eight symmetric arms, each of which shows a trident-like, dendritic structure and consists of parallel PbS nanoleaflets. Novel hierarchical HgS dendrites were synthesized by hydrothermal treatment of a mercury–thiourea complex (Fig. 8b) [45]. The individual HgS dendrite consisted of a long central trunk with secondary and tertiary sharp branches, which preferentially grew parallel to the (001) plane. A nanoscale dendrite of Bi_2S_3 was produced by a biomolecule-assisted approach under microwave–hydrothermal conditions (Fig. 8c,d) [46]. Dendritic nanostructures of magnetic Fe_2O_3 were synthesized by the hydrothermal reaction of $K_3[Fe(CN)_6]$ in an aqueous solution at suitable temperatures (Fig. 8e) [47]. Single crystals of calcite exhibiting a morphology of well-defined eight-armed stars, which evolved from original rhombohedral calcite crystals, were produced

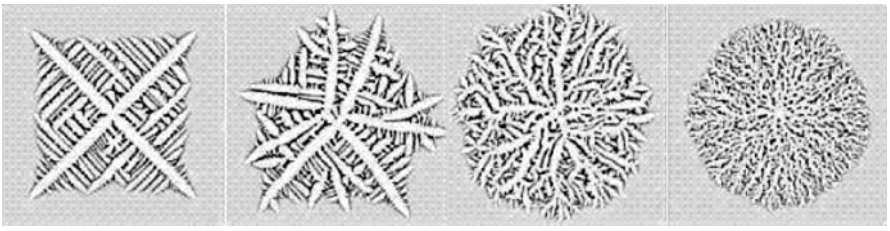

Fig. 7 Phase-field simulations of the growth forms with heterogeneities. Reproduced from [43] with permission of Nature Publishing

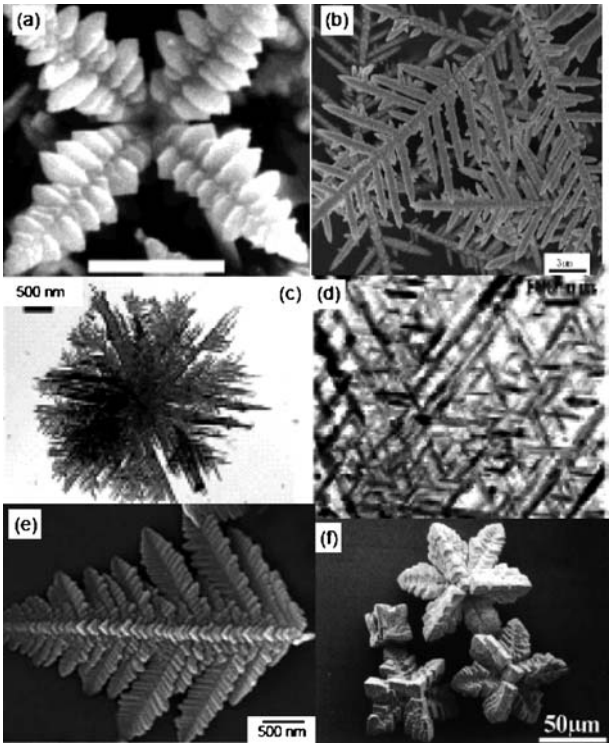

Fig. 8 A wide variety of dendritic morphologies of inorganic crystals grown in aqueous solutions: **a** star-shaped PbS [44], **b** hierarchical HgS dendrites [45], **c**,**d** Bi_2S_3 [46], **e** magnetic Fe_2O_3 [47], and **f** eight-armed stars calcite [48]. Reproduced from [44–48] with permission of the American Chemical Society, Wiley, and the Royal Society of Chemistry

by crystallization of $CaCO_3$ in agarose gels (Fig. 8f) [48]. The formation of the symmetric branching morphologies generally requires appropriate conditions for the achievement of a suitable balance between the mass transport and the reaction rate.

Recently, elaborately structured dendritic crystals have been reported to be spontaneously formed in oscillatory electrodeposition. The zinc dendrites changed their shape periodically in synchronization with the potential oscillation from thick hexagonal wafers on the negative potential side to thin maple-leaf-like wafers on the positive potential side (Fig. 9) [49–51]. Well-ordered tin latticeworks, standing perpendicular to the substrate, are formed through cooperation of various processes with long-range spatiotemporal synchronization (Fig. 9) [52]. A mechanism was proposed to explain the oscillation and the dendrite formation by taking into account coupling of autocatalytic crystal growth, in close relation with the surface instability, and

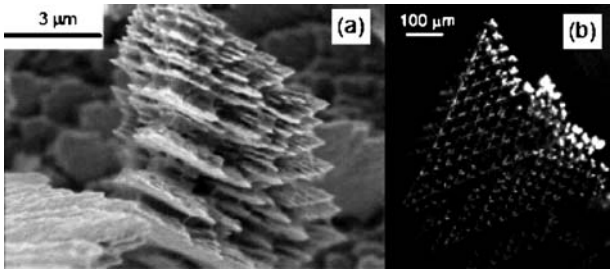

Fig. 9 A maple-leaf-like zinc wafer (**a**) [49–51] and well-ordered tin latticeworks (**b**) [52]. Reproduced from [49–52] with permission of the Chemical Society of Japan and the American Chemical Society

autocatalytic surface oxidation at the closely packed crystal faces leading to surface passivation. These cases elaborately controlled the branching morphologies with spontaneous oscillation of the growth modes coupled with electrochemical reactions.

4.3
Spherulites with Double Eye and Dumbbell Structures

In polymeric spherulites with the lamellae radiating from the core, the lamellar orientation is globally random. However, a sheaflike structure with a so-called dual eye-pocket has been frequently observed in the spherulitic growth of other polymeric materials [53]. The lamellar branching and splaying can occur from a nucleus that contains a single lamella forming the sheaflike texture (Fig. 10a,b). The spherulites with a dual-eye structure are categorized as an intermediate form between faceted crystals and dense branching morphologies (Fig. 3). Although the main lamellae grow in some preferential crystallographic axes, the side branching in a spherulite is noncrystallographic. The initial nuclei grow into rectangular shaped lamellae, reflecting the crystallographic axes of the crystals. These lamellae tend to be stacked into lamellar bundles that transform into the sheaflike structure before emerging as a dense lamellar branching morphology. Some spherulites show anisotropic nuclei with a dual eye-pocket appearance at the core. The duel-eye structures were also formed with an inorganic crystal in a solution system. As shown in Fig. 10c,d, a hierarchically ordered inorganic–organic composite superstructure with periodic orientation of a hexagonal primary fluoroapatite nanocrystal was formed from an elongated, hexagonal–prismatic fluoroapatite in a gelatin gel. The central part of the spheres is characterized by a torus-shaped cavity generated by the fractal growth mechanism [54–56]. Peanut and dumbbell structures are interpreted as an intermediate between bundles of rods and spherulites with the duel-eye structure. The morphogenesis from rod to spherulite via dumbbell structures was observed in the

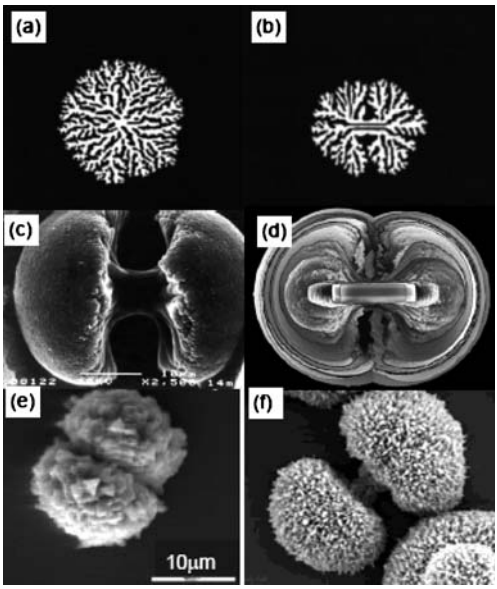

Fig. 10 Duel eye-pocket structures or dumbbell-shaped morphologies; phase filed simulations of branching morphologies without (**a**) and with (**b**) a dual eye-pocket texture at the core of polymer spherulite [53], dumbbell-shaped aggregate of fluorapatite-gelatin composite (**c**,**d**) [54–56], $CaCO_3$ (**e**) [57] and $BaCO_3$ (**f**) [58]. Reproduced from [53–58] with permission of the American Institute of Physics, Wiley and the American Chemical Society

case of $CaCO_3$ and $BaCO_3$ under the control of double-hydrophobic block copolymers (DHBCs) [57, 58] (Fig. 10e,f). These results show that polymer-controlled mineralization is a versatile step toward crystal morphogenesis between DLA and symmetric dendrites.

5
Self-Organization of Novel Morphologies

5.1
Crystals with Self-Similarity

Recently, a variety of nondendritic complex morphologies exhibiting partial self-similarity, but not real fractals with a noninteger dimension, have been reported. The shape which partially contains smaller copies of itself was prepared in the presence of various additives, such as amphiphilic agents and organic and inorganic polymeric species. Therefore, the specific morphological features could be ascribed to the reclusive suppression of the crystal growth with the adsorption of the additives on different scales.

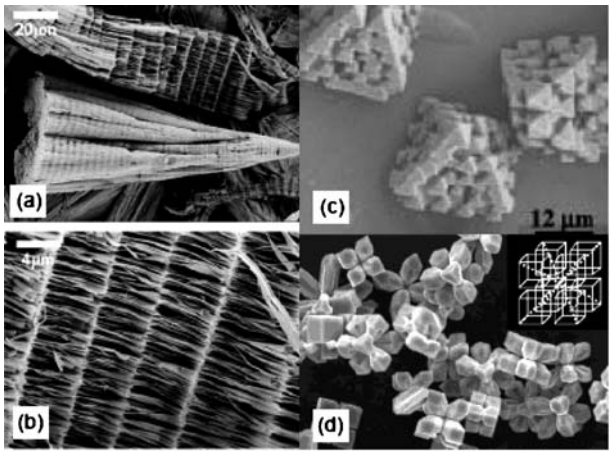

Fig. 11 Self-similar morphologies: **a**,**b** funnel-like $BaCrO_4$ superstructures produced by using polyacrylate [59], **c** microscopic polyhedral mesophase crystals prepared from a hybrid organic silane [60], and **d** multipod framework of Cu_2O microcrystals [61]. Reproduced from [59–61] with permission of the American Chemical Society and Wiley

Highly ordered funnel-like $BaCrO_4$ superstructures with a complex form showing a self-similar growth pattern were produced by using polyacrylate as a structure-directing agent in the crystallization process (Fig. 11) [59]. The hierarchical structures are deduced to be achieved through the self-organized formation by the modulation of the crystal growth with the adsorption of inorganic and organic soluble agents. Hierarchical crystals with an open structure were also reported to be constructed by microscopic polyhedral mesophase crystals prepared from a hybrid organic silane along with cationic surfactant [60]. Novel hierarchical and self-similar crystals were spontaneously formed by multiple and self-similar growth based on an edge-sharing mode (Fig. 11). A novel multipod framework of Cu_2O microcrystals was prepared in a solution phase [61]. Faceted microcrystal subunits with simple cubic or face-centered cubic lattices have been organized with the creation of intracrystal porosity and crystal self-amplification.

Hierarchical self-similar morphologies were frequently observed in the crystal growth of carbonates in silica gel containing a high pH solution (Fig. 12) [62]. A hierarchical calcite consisting of three-pointed stars with sizes ranging from 100 nm to 100 μm was grown in silica gel. The self-organized formation of calcite was attributed to the crystal growth in a supersaturated solution with a gradual increase in the influence of silicate anions. Symmetric dendrites of $BaCO_3$ grown in the presence of silicate anions were found to be composed of small hexagonal plates ($\sim$ 10 μm) consisting of nanoscale subunits smaller than 100 nm. These nanoscale units were covered with silicate. Figure 13 shows the growth process of the hierarchical calcite

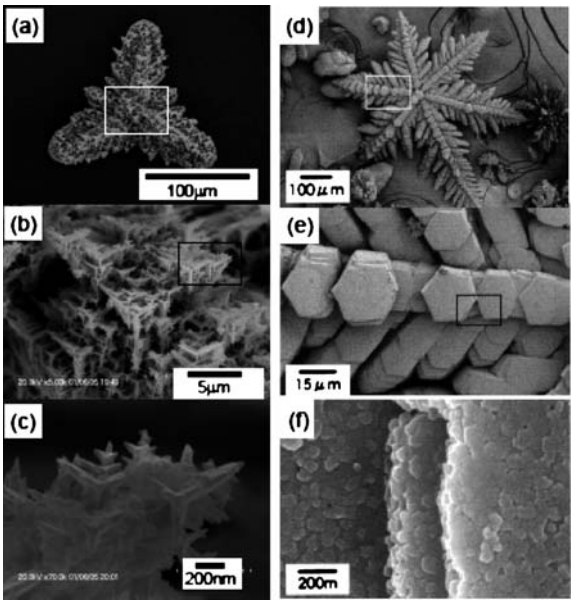

Fig. 12 Self-similar morphologies of calcite $CaCO_3$ (**a**–**c**) [62] and $BaCO_3$ (**d**–**f**) grown in silica gel at pH 10.5. Reproduced from [62] with permission of the Royal Society of Chemistry

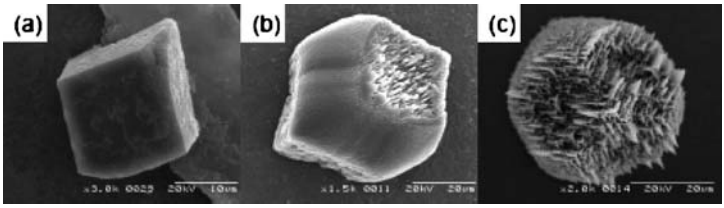

Fig. 13 Time-dependent evolution of the self-similar morphologies of calcite $CaCO_3$ grown in silica gel: **a** 1 h, **b** 6 h, and **c** 12 h. Reproduced from [62] with permission of the Royal Society of Chemistry

in silica gel. Further growth of three-pointed stars on a rhombohedral form produced the hierarchical architecture. It suggests that the self-organized formation of the self-similar structures may be categorized as the variation of dendritic growth mode under diffusion-controlled conditions.

5.2 Helical Crystals

Helical and spiral architectures, which are fascinating shapes exhibiting chirality, are observed on various scales in nature. Macroscopic helical mor-

phologies were observed with organic molecules [63, 64], polymers [65, 66], and inorganic materials [67–84] without microscopic chirality. In recent years, new families of helical shapes of inorganic crystals have been discovered for barium sulfate [65, 66], calcium [69], barium and strontium carbonates [70–73], potassium dichromate [74–77, 83], manganese oxide [78], boric acid [83], and potassium sulfate [84]. These helical morphologies were categorized as hierarchical structures because the twisted architectures were composed of smaller crystal units.

García-Ruiz and coworkers have reported a series of interesting studies on the various strange morphologies of alkali-earth carbonate crystals formed in silica gel [70, 71]; in particular, curved sheets and twisted ribbons of strontium and barium carbonates were fantastic and different from the crystallographic symmetry (Fig. 14a). They described the aggregates showing the unusual morphologies as a composite of the carbonate crystals surrounded by a silicate membrane. The formation of the shapes was attributed to the results of the interplay between localized crystal growth and inhibition at the fluid–solid interface. Strontium carbonate grown in silica gel showed a variety of complex morphologies including sheets and spirals associated with biogenetic products. The noncrystallographic architecture had a hierarchical structure consisting of nanoscale needle-like building blocks enveloped with a silicate sheath. By monitoring the time-dependent growth, a spherical cluster of the fibrous crystals was transformed into the highly ordered morphologies having strange outgrowths with helical structures in the pro-

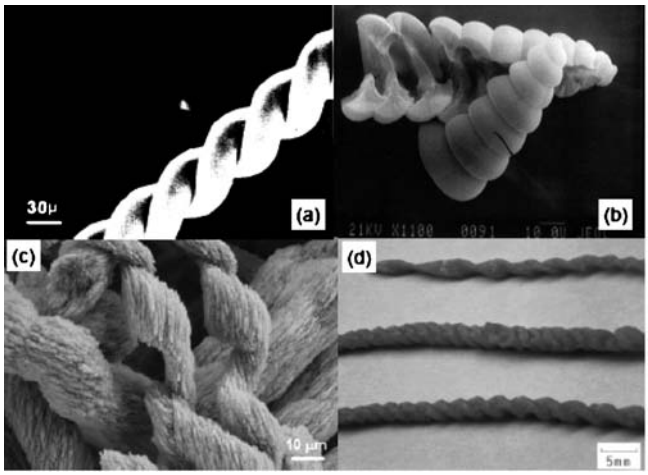

Fig. 14 Various types of helical morphologies of inorganic crystals: **a** $BaCO_3$ grown in silica gel [70, 71], **b** polyelectrolyte-mediated $CaCO_3$ [69], **c** $BaCO_3$ nanocrystals prepared in the presence of racemic DHBCs [73], and **d** $K_2Cr_2O_7$ produced in gelatin [74–77]. Reproduced from [69–71, 73–77] with permission of Elsevier, Dr. H. Cölfen, and the Physical Society of Japan

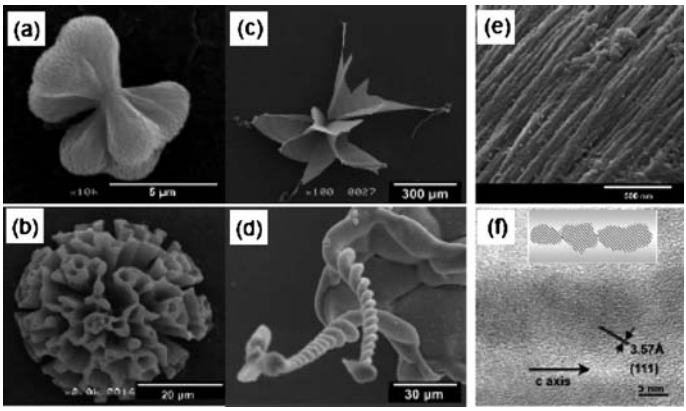

Fig. 15 Time-dependent growth of $SrCO_3$ in silica gel at pH 10.5: **a** 0.5 h, **b** 2 h **c**,**d** 72 h. Enlarged SEM (**e**) and TEM (**f**) images of fibrous units of the helical structure. Reproduced from [72] with permission of Elsevier

gressive stages as shown in Fig. 15. The unusual morphologies were achieved with a reduction of the subunit size and restriction of the growth direction by selective adsorption of silicate anions on the specific crystal surfaces of the carbonate crystals. In this sense, the helical architecture would be produced by a preferential growth mode in branching morphologies. Similar helical morphologies were also generated by a polyelectrolyte-mediated crystallization of calcium carbonate [69] (Fig. 14b). The formation of helices of $BaCO_3$ nanocrystals was performed in the presence of racemic DHBCs [73]. In this case, a helical alignment can be induced by racemic polymers through selective adsorption on a specific face of the nanocrystals (Fig. 14c).

Matsushita et al. first found that helical potassium dichromate ($K_2Cr_2O_7$) crystals were grown in gelatin gel [74–77] (Fig. 14d). Then, helical morphologies were reportedly grown with triclinic crystals (H_3BO_3, $K_2Cr_2O_7$, and $CuSO_4 \cdot 5H_2O$) in various kinds of gel matrices [41, 83] (Fig. 16). The essence of the formation of the chiral architecture from achiral components is the rotated accumulation of tilted units under conditions of diffusion-limited growth. Since helical morphologies consisting of tilted plates were achieved with monoclinic potassium sulfate, the triclinic crystal structure is not always required for the formation of a twisted assembly of tilted-growth units. The backbone of the unique architectures was composed of twin crystals twisted with a constant angle. DLA-like branching morphologies were obtained in a dense gel, whereas faceted crystals were grown in loose media. Thus, the helical structures were formed under an intermediate condition between faceted crystals and DLA (Fig. 17). As shown in Fig. 15, the helical architecture of $SrCO_3$ was produced at the top of the projections formed by further outgrowth from a spherulite [72]. Figure 18 shows the morphological variation of K_2SO_4 grown with PAA from tilted columns into helical structures with an in-

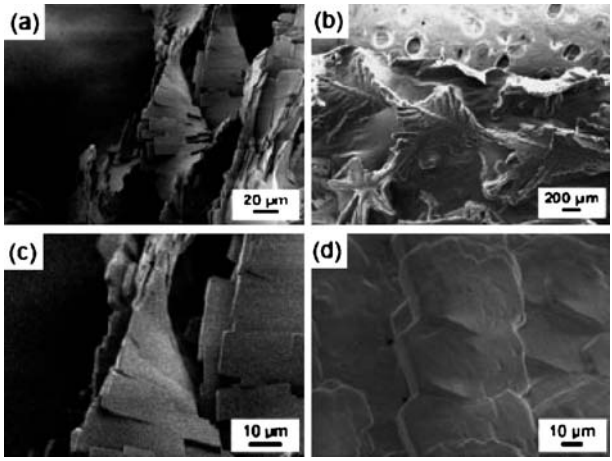

Fig. 16 Helical morphologies of $K_2Cr_2O_7$ (**a**,**b**) and H_3BO_3 (**c**,**d**) in gelatin and agar, respectively. Reproduced from [83] with permission of the American Chemical Society

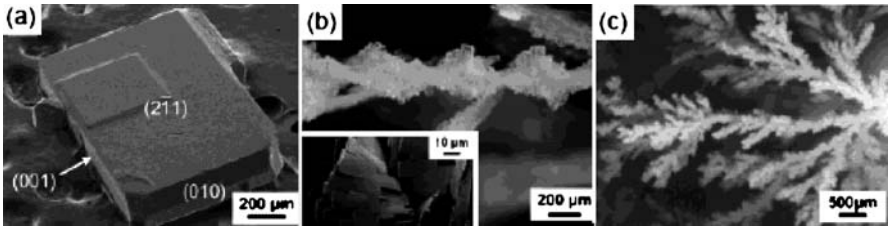

Fig. 17 Morphological variation of $K_2Cr_2O_7$ grown in gelatin gel. The morphology was changed from a regular plate (**a**) into helical (**b**), and branching structures (**c**) with increasing the gel density. Reproduced from [41] with permission of the American Chemical Society

crease of PAA concentration [84]. These facts suggest that the self-organized formation of the helical structures may be categorized by the variation of dendritic and branching growth modes under appropriate diffusion-controlled conditions. The emergence of the macroscopic chiral morphology from achiral components is attributable to the twisted assembly of tilted units under diffusion-controlled mass transport.

Right-handed helices were predominantly obtained in a gel matrix consisting of biological macromolecules, whereas almost the same number of right- and left-handed structures was produced in artificially synthesized polymers, such as poly(acrylic acid) and poly(vinyl alchohol). A novel type of morphological chiral tuning of inorganic helical crystals was achieved through stereochemical recognition of organic molecules [85]. The proportion of the right- and left-handed helices was precisely tuned with the addition of a specified amount of chiral molecules, such as D- and L-glutamic acids. The chiral

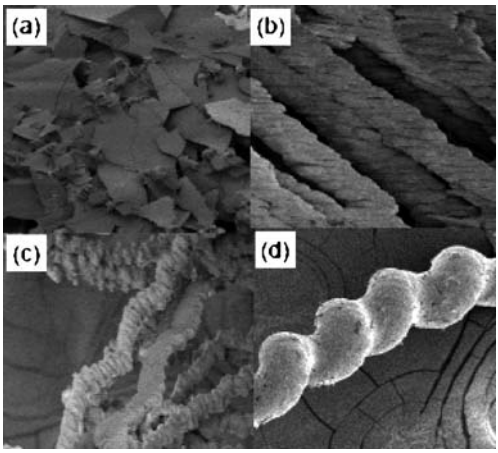

Fig. 18 Morphological evolution of K_2SO_4 with increasing PAA concentration: **a** thin plates, **b** tilted columnar assembly, **c** zigzag architecture, **d** helical morphologies. Reproduced from [84] with permission of the American Chemical Society

molecules recognized the enantiomeric surface of the triclinic crystal and then changed the growth behavior of the helical morphology. As a result, the microscopic chiral information, at a molecular level, was amplified into the macroscopic helices consisting of inorganic achiral components.

6
Oriented Architectures Consisting of Small Building Blocks

6.1
Calcium Carbonate

As mentioned in the previous section, biominerals are fundamentally constructed with building blocks on several scales. The oriented architecture in biominerals is ascribed to bridged nanocrystals with the incorporation of biopolymers. The crystal growth mimicking biomineralization would be achieved by self-organized formation of bridged nanocrystals using various kinds of organic molecules. Since calcium carbonate ($CaCO_3$) is one of the most popular biominerals, a wide variety of morphologies of the carbonate crystals have been demonstrated using various organic molecules and templates. A typical approach is habit modification leading to the morphological evolution of precipitates using polyelectrolytes [86]. The rigid templates and patterned molds are used for the production of a porous carbonate mimicking biogenic structures [87–89]. This section reviews recent research on the self-organization of hierarchical structures of $CaCO_3$ using various organic molecules.

Various kinds of hierarchical calcium carbonate crystals have been prepared in the presence of organic additives, as shown in Fig. 19. Macroscopically faceted morphologies were found to be composed of small grains (Fig. 19a) [90]. Hexagonal forms of vaterite with intracrystalline gelatin were obtained from the hydrothermal reaction between calcium nitrate and urea in the presence of gelatin (Fig. 19b) [91]. Although the overall morphology

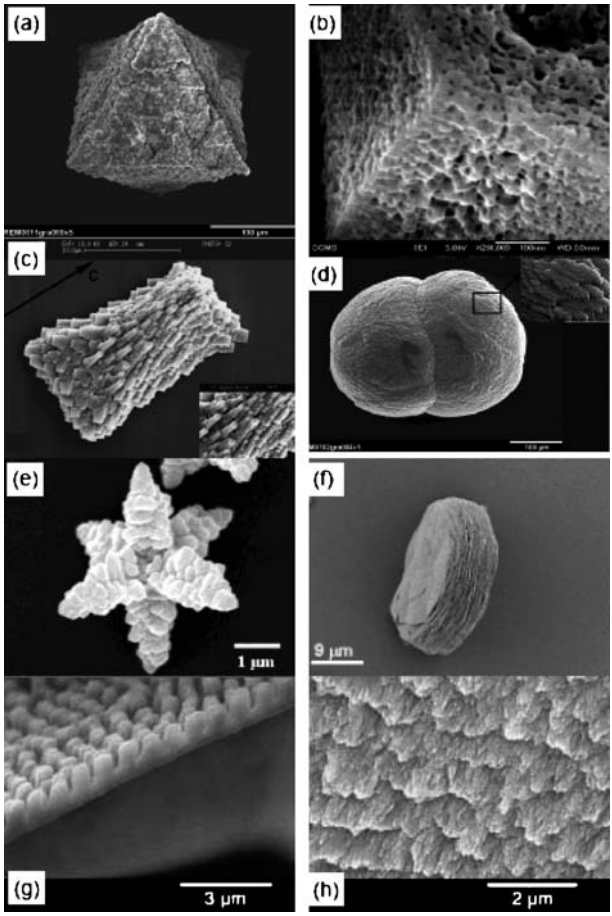

Fig. 19 Wide variety of oriented architectures consisting of $CaCO_3$ nanocrystals: **a** faceted morphologies composed of small grains [90], **b** hexagonal forms of vaterite with intracrystalline gelatin [91], **c** hierarchical calcite grown in the presence of acidic glycoproteins [92], **d** barrel-shaped calcite particles obtained in gelatin [90], **e** star-shaped $CaCO_3$ crystals with phosphotungstic acid [93], **f** calcite pancakes formed using DHBCs [94], **g**,**h** regular surface-relief structures of $CaCO_3$ on a hydrophobically modified polysaccharide in the presence of PAA [95]. Reproduced from [90–95] with permission of the American Chemical Society, Wiley and the Royal Society of Chemistry

obeys the single-crystal nature, the hexagonal forms consisted of a nanocrystal aggregation. Hierarchical calcite was grown in the presence of acidic glycoproteins isolated from adult spines of sea urchin (Fig. 19c) [91]. Barrel-shaped calcite particles showing submicron terraces assigned to the {10–14} planes were obtained in gelatin gel although the concentric structure was formed through a radial growth from a central nucleation site (Fig. 19d) [90]. Star-shaped $CaCO_3$ crystals were created by the reaction of an aqueous solution of phosphotungstic acid and Ca^{2+} ions with CO_2 (Fig. 19e) [93]. Calcite pancakes were formed using a double-hydrophilic block copolymer (Fig. 19f) [94]. Regular surface-relief structures of $CaCO_3$ crystals with submicrometerscale periodicity were formed from solution on the thin matrix of a hydrophobically modified polysaccharide in the presence of poly(acrylic acid) (PAA) (Fig. 19g,h) [95]. These hierarchical structures are attributable to polymer- or complex-mediated self-organization. On the other hand, the morphogenesis in gelatin gel was attributed to the physical growth environment on the basis of our previous work and the results of other groups. Moreover, hierarchical structures were reported in the absence of organic molecules [96]. The formation mechanism of the elaborate structures in solution systems is still a mystery.

The influence of the concentration and the molecular weight of PAA on the morphological evolution of $CaCO_3$ was systematically investigated in order to clarify the performance of the polymeric molecules [97]. While the addition of a small amount of low molecular weight PAA resulted in the formation of faceted calcite surrounded by rough surfaces (Fig. 20a), round crystals were obtained with increasing the concentration of the PAA molecule (Fig. 20b). Small triangular calcite grains of less than 1 μm, which were arranged with the same orientation, were found on the round crystals. The similarity of the nanostructures and biominerals was investigated as a prime example of biomineralization [8]. Planar films were formed on a glass substrate with a large amount of high molecular weight PAAs. Especially, the combination of low and high molecular weight PAAs produced lozenge-shaped calcite films with definite edges obtained in a solution (Fig. 20c,d). Although the lozenge-shaped films exhibited regular crystallographic habits, small grains less than 100 nm were observed on the surface. Low molecular weight PAA weakly suppressed the regular crystal growth and miniaturized calcite grains as a capping agent. The specific interaction is ascribed to the similarity of the distance of carboxy groups of a PAA molecule to that of carbonate anions on the {10–14} plane of $CaCO_3$. The oriented architectures are suggested to be composed of bridged crystals. High molecular weight PAA drastically decreased the grain size as a strong capping agent and promoted the formation of thin films. The array of PAA on the solid surface induced 2D growth of $CaCO_3$ crystals. Subsequent overgrowth of PAA-mediated $CaCO_3$ films was performed in a freshly prepared calcium chloride aqueous solution without PAA [98]. The planar morphology of the films evolved into 3D forms with

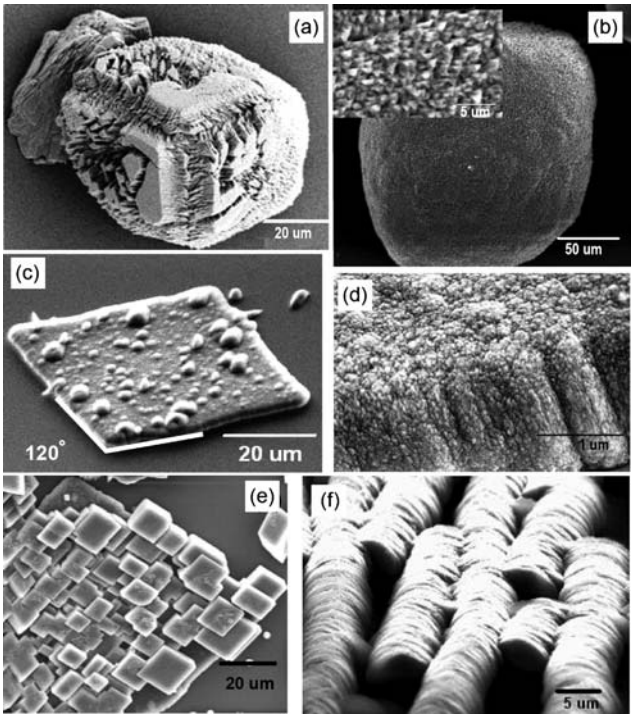

Fig. 20 Wide variety of oriented architectures consisting of $CaCO_3$ nanocrystals with PAA: **a** faceted calcite with rough faces and **b** round calcite grown with a low molecular weight PAA, **c**,**d** lozenge-shaped films consisting of oriented nanocrystals grown with the combination of low and high molecular weight PAAs, the array of rhombohedral calcite blocks (**e**) and high-aspect thin walls of vaterite (**f**). Reproduced from [97] with permission of the American Chemical Society

the subsequent growth. The evolution of the morphology was clearly dependent on the polymorphs and crystallographic orientation of the base films, as shown in Fig. 20e,f. The array of rhombohedral calcite blocks and high-aspect thin walls of vaterite were produced on the specific basal films. Fundamentally, the crystal structure of the daughter crystals was inherited from the basal films, regardless of the condition of the precursor solution.

Hollow morphologies of $CaCO_3$ were reported to be composed of small units. Crystallization of calcium carbonate in the presence of a polycarboxylate in the formation of microtrumpets was composed of nanocrystalline calcite (Fig. 21a) [99]. Since DHBCs temporarily stabilize $CaCO_3$ nanocrystals, tunable complex shuttlecock and other superstructures are formed, which are aggregates of $CaCO_3$ vaterite nanoparticles (Fig. 21b) [100]. Simple templates such as gas bubbles can already be used to generate complex crystal aggregate morphologies in a crystallization reaction occurring at the air–solution interface. Porous $CaCO_3$ microparticles were synthesized using

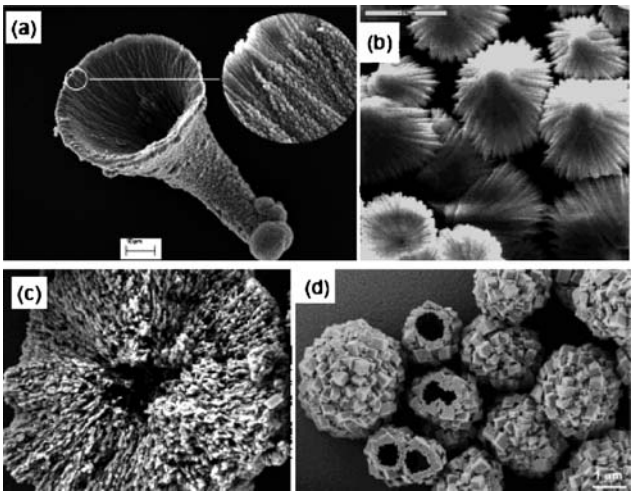

Fig. 21 Hollow and porous morphologies of $CaCO_3$ consisting of small units: **a** microtrumpet [99], **b** shuttlecock [100], **c** porous microparticles synthesized with polyelectrolyte layer-by-layer assembly [101], **d** hollow particles consisted of the calcite rhombohedral subunits grown with DHBCs [58]. Reproduced from [58, 99–101] with permission of the American Chemical Society and the Royal Society of Chemistry

polyelectrolyte layer-by-layer assembly of two oppositely charged polyelectrolytes (Fig. 21c) [101]. Calcium carbonate core dissolution resulted in the formation of polyelectrolyte microcapsules with an internal matrix consisting of a polyelectrolyte complex. Well-defined crystals with sizes ranging from microscale to mesoscale and complex higher-order superstructures, such as hollow spheres, were obtained by different strategies for various metal carbonate minerals such as $CaCO_3$, $BaCO_3$, $CdCO_3$, $MnCO_3$, and $PbCO_3$ using DHBCs (Fig. 21d) [58]. The polymer-controlled mineralization, with a strong selective interaction between the functional groups of DHBCs and crystals, is a versatile step toward crystal morphogenesis. Complex $BaCO_3$ superstructures were generated by using poly(sodium 4-styrenesulfonate) and poly(allylamine hydrochloride) as structure-directing agents in the mineralization process [102]. More complex macroporous superstructures could be generated by cooperative templating effects of the molecular template and a foreign static template such as air bubbles.

Aragonite occasionally precipitated in silica gel, whereas calcite was dominantly produced under this condition. Although hexagonal rods, which are a regular form of aragonite, were obtained in the absence of silicate, coral-like porous morphologies with a nanoscale cellular framework (Fig. 22) were found in the presence of silicate anions at pH 10.5 [103]. Platy units of aragonite in the porous structures were individually covered with silicate envelopes. These results suggest that various morphologies were constructed by

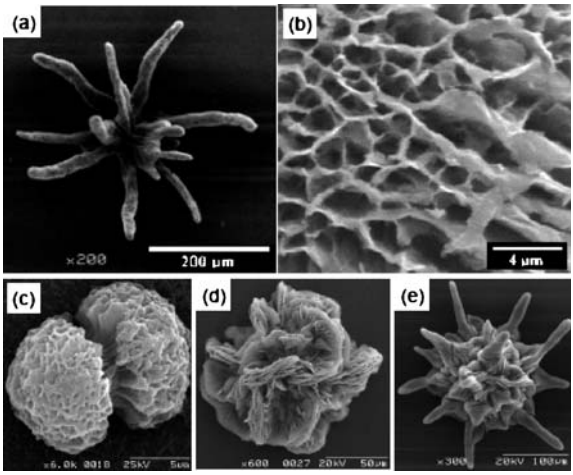

Fig. 22 Coral-like porous morphologies with nanoscale cellular framework found in the presence of silicate anions at pH 10.5. An enlarged SEM (**b**) image of a projection of a coral morphology (**a**). The particular shape was formed from a dumbbell-shaped spherulite (**c**) via intermediate morphologies (**d**,**e**). Reproduced from [103] with permission of Elsevier

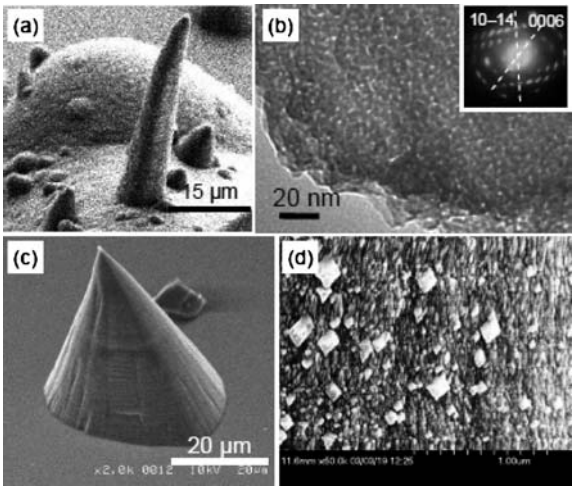

Fig. 23 Calcite spines (**a**,**b**) and cones (**c**,**d**) composed of small PAA-mediated grains with a preferred crystallographic orientation were obtained in a binary system of low and high molecular weight PAAs. Reproduced from [104] with permission of the American Chemical Society

sequential, bridged growth of carbonate crystals in cooperation with inorganic polymeric anions. The presence of silica gel could exhibit a matrix effect for a diffusion-controlled mass transport.

Structural analogs of biominerals (such as calcite spines and cones) composed of small PAA-mediated grains with a preferred crystallographic orientation, were obtained in a binary system of low and high molecular weight PAAs [104]. Spines were grown on the previously deposited pedestals in the latter stage (Fig. 23). According to SEM and TEM observations, the spines were found to consist of small bridged grains of 10–20 nm in diameter. Various types of tapering morphologies, such as cones and hollow horns, were produced under similar conditions. These tapering structures also consisted of small oriented grains. Although similar morphologies have reportedly been produced by self-assembly of $BaCrO_4$ and $BaSO_4$ nanofibers [59, 105–109], the formation mechanism is still unclear. Tentatively, the bridged growth of the oriented grains is suggested to require the presence of a specific diffusion field around the basal crystals. The formation of tapering morphologies is attributable to the preferential 3D assembly of the small building units along the specific directions under diffusion-controlled mass transport.

6.2 Other Materials

Hard tissues in vertebrates, such as bones and teeth, are a three-dimensionally oriented assembly of nanoscale hidroxyapatite (HAp) with a hierarchical architecture. As a first step towards the design and fabrication of biomimetic bonelike composite materials, a template-driven nucleation and mineral growth process was developed for the high-affinity integration of hydroxyapatite with a poly(2-hydroxyethyl methacrylate) (pHEMA) hydrogel scaffold [110]. A mineralization technique was developed that exposes carboxylate groups on the surface of cross-linked pHEMA, promoting high-affinity nucleation and growth of calcium phosphate on the surface. A designed hierarchical structure was made by the self-assembly of nanofibrils of mineralized collagen resembling an extracellular matrix [111]. The collagen fibrils were formed by the self-assembly of collagen triple helices. HAp crystals grew on the surface of these fibrils in such a way that their *c* axes were oriented along the longitudinal axes of the fibrils. The mineralized collagen fibrils aligned parallel to each other to form mineralized collagen fibers. This template-driven mineralization technique provides an efficient approach toward bonelike composites with high mineral–hydrogel interfacial adhesion strength. Hierarchically organized nanostructures of HAp were produced using a novel preparation route through the topotactic transition of dicalcium phosphate dihydrate (DCPD) prepared in gelatin gel (Fig. 24) [112]. A nanoscale texture of dicalcium phosphate (DCP) was formed by the dehydration of DCPD. A three-dimensionally oriented framework of HAp consisting of ca. 20 nm grains was prepared by rapid hydrolysis of the nanotextured DCP with a sodium hydroxide solution.

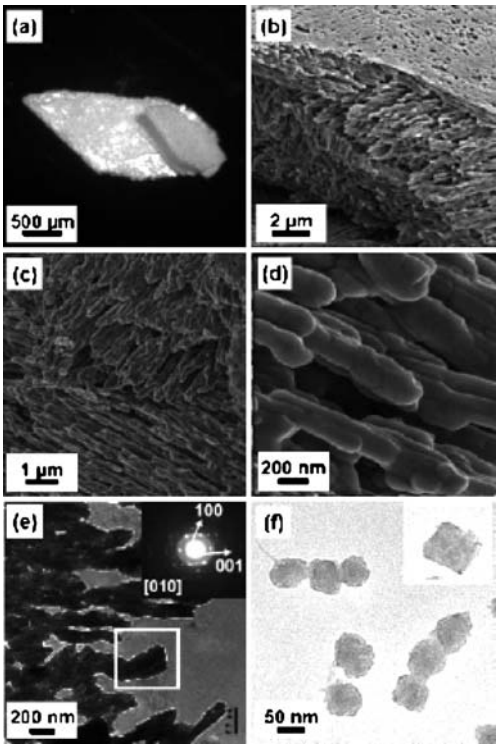

Fig. 24 Hierarchically organized dicalcium phosphate (DCP): an optical micrograph (**a**), SEM images (**b**,**c**,**d**) and TEM images (**e**,**f**). The *inset* of **e** is an electron diffraction pattern for the rectangle area. Reproduced from [112] with permission of the American Chemical Society

A novel type of hierarchically organized superstructure emerged from an exquisite association of inorganic crystals and organic polymers through simple biomimetic crystallization. Potassium sulfate (K_2SO_4) was prepared in an aqueous solution containing PAA with evaporation of water [113]. The resultant superstructure consisting of K_2SO_4 and PAA was hierarchically organized on five levels from nanoscopic to macroscopic. Figure 25 shows a FESEM image and the schematic representation of the macroscopic lattice architecture (tier 1), columns between plates (tier 2), platy units in the columns (tier 3), granular subunits inside of a unit (tier 4), and crystallites with the same orientation in a subunit (tier 5). A hierarchically organized architecture on multiple scales was also generated from potassium hydrogen phthalate crystals and PAA with an exquisite association of polymers on crystallization. In accordance with these two model cases, the concept for crystal growth can be applied to the generation of a hierarchically organized architecture regardless of whether organic or inorganic materials are used. These findings shed light on the nature of hierarchical crystal growth in various

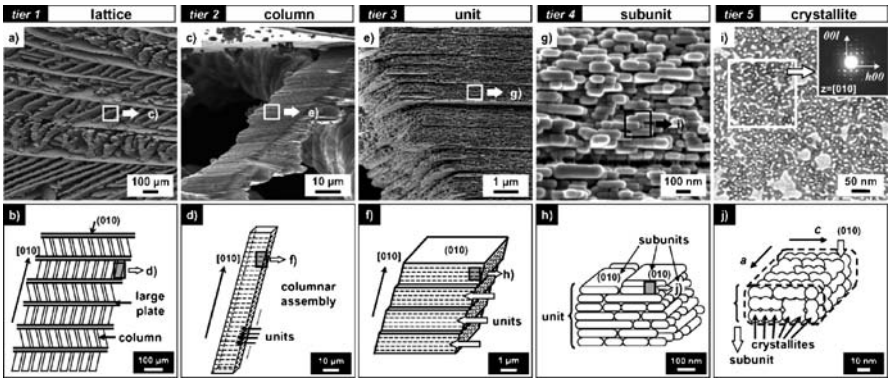

Fig. 25 Hierarchical architecture of K_2SO_4 grown with PAA: **a**,**b** the macroscopic lattice architecture (tier 1), **c**,**d** columns between plates (tier 2), **e**,**f** platy units in the columns (tier 3), **g**,**h** granular subunits inside of a unit (tier 4), and **i**,**j** crystallites with the same orientation in a subunit (tier 5). Reproduced from [113] with permission of Wiley

biominerals, such as bone and mother-of-pearl. Furthermore, tailoring the combination of crystals and polymers could realize various hierarchically organized materials with emergent properties that are unattainable with the individual components.

7
Conclusions: Self-Organization for Hierarchical Structures

A wide variety of examples of the formation of hierarchical architectures in artificial systems mimicking biomineralization have been reviewed here. The morphological evolution of inorganic crystals on several scales is fundamentally induced by self-assembly at the atomic level and self-organization at microscopic and macroscopic levels. The macroscopic self-organization of crystal growth could be achieved by a balance between the driving force of crystallization and the surface energy of the crystals. Consequently, the multiscale structures are precisely modulated by the combination of the capping and template effects with organic and/or polymeric species. A similar strategy would lie in bioinorganic superstructures that are directed by controlled crystallization with the assistance of biological molecules and polymers. In biomineralization, the macroscopic morphology could be constructed through the sequential growth of bridged nanocrystals with biological polymers. In artificial systems, the bridged nanocrystals covered with organic molecules were achieved by polymeric agents exhibiting specific interaction with inorganic crystals. The properties of both single crystals and organic–inorganic composites reside in the bridged nanocrystals having an

oriented architecture. Furthermore, the bridged architecture may be suitable for the formation of various types of complex morphologies, with a batch of nanocrystals having the same crystallographic orientation. Unconformity and twinning at the bridges could induce further morphological evolution in the macroscopic shapes. Many types of morphogenesis were observed under diffusion-controlled mass transport in a gel matrix. Convection-free matrices of gel and viscous liquid easily promote self-organized growth, with a diffusion-controlled growth mode through the suppression of mass transport. Various hierarchical architectures exhibiting complex macroscopic shapes, such as helical and tapering forms, can be realized when these versatile effects of the organic and/or polymeric species are exquisitely combined on the crystal growth.

Traditional technology of crystal growth has been mainly focused on the top-down fabrication of homogeneous, large-sized single crystals. On the other hand, the life ability inspires a bottom-up chemical approach to various hierarchical architectures consisting of nanomaterials and nanostructures. In an artificial system mimicking biomineralization, self-organized formation (with exquisite control of mass transport and the variation of surface energy with organic molecules) was essential for versatile morphogenesis of various inorganic crystals in solution systems. The formation process through self-organization is highly suggestive of a new paradigm for advanced material processing. The general concept of bridged nanocrystals would be applicable as a novel type of inorganic crystal and for inorganic–organic nanocomposite materials. Therefore, self-organization of hierarchical architectures would create a novel route in materials chemistry and nanotechnology as a smart technique for the fabrication of functional nanoscale materials. Moreover, an improved understanding of the formation of fractals and self-similar structures holds promise for the further development of chemical, biological, and materials sciences.

References

1. Mann S (1988) Nature 332:119
2. Mann S (2001) Biomineralization: principles and concepts in bioinorganic materials chemistry. Oxford University Press, New York
3. Lowenstam H, Weiner AS (1989) On biomineralization. Oxford University Press, Oxford, England
4. Aizenberg J, Weaver JC, Thanawala MS, Sundar VC, Morse DE, Fratzl P (2005) Science 309:275
5. Sumper M, Brunner E (2006) Adv Funct Mater 16:17
6. Li X, Chang WC, Chao YJ, Wang R, Chang M (2004) Nano Lett 4:613
7. Takahashi K, Yamamoto H, Onoda A, Doi M, Inaba T, Chiba M, Kobayashi A, Taguchi T, Okamura T, Ueyama N (2004) Chem Commun, p 996
8. Sethmann I, Putnis A, Gransmann O, Löbmann P (2005) Am Mineral 90:1213

9. Sethmann I, Hinrichs R, Wörheide G, Putnis A (2006) J Inorg Biochem 100:88
10. Oaki Y, Imai H (2005) Angew Chem Int Ed 44:6571
11. Oaki Y, Imai H (2006) Small 2:66
12. Kato T, Sugawara A, Hosoda N (2002) Adv Mater 14:869
13. Kato T, Amamiya T (1999) Chem Lett 28:199
14. Kato T, Suzuki T, Irie T (2000) Chem Lett 29:186
15. Sugawara A, Kato T (2000) Chem Commun, p 487
16. Hosoda N, Kato T (2001) Chem Mater 13:688
17. Sugawara A, Ishii T, Kato T (2003) Angew Chem Int Ed 42:5299
18. Hosoda N, Sugawara A, Kato T (2003) Macromoecules 36:6449
19. Zhang S, Gonsalves KE (1998) Langmuir 14:6761
20. Heywood BR, Mann S (1992) J Am Chem Soc 114:4681
21. Xu G, Yao N, Aksay IA, Groves JT (1998) J Am Chem Soc 120:11977
22. Gower LB, Odom DJ (2000) J Cryst Growth 210:719
23. Cölfen H (2003) Curr Opin Colloid Interface Sci 8:23
24. Yu SH, Cölfen H (2004) J Mater Chem 14:2124
25. Cölfen H, Mann S (2003) Angew Chem Int Ed 42:2350
26. Mann S (2004) Chem Commun, p 1
27. Cölfen H, Antonietti M (2005) Angew Chem Int Ed 44:5576
28. Wohlrab S, Pinna N, Antonietti M, Cölfen H (2005) Chem Eur J 11:2903
29. Wang XT, Cölfen H, Antonietti M (2005) J Am Chem Soc 127:3246
30. Penn RL, Banfield JF (1998) Science 281:969
31. Penn RL, Banfield JF (1999) Geochim Cosmochim Acta 63:1549
32. Polleux J, Pinna N, Antonietti M, Niederberger M (2004) Adv Mater 16:436
33. Pacholski C, Kornowski A, Weller H (2002) Angew Chem Int Ed 41:1181
34. Liu B, Yu SH, Li L, Zhang F, Zhang Q, Yoshimura M, Shen P (2004) J Phys Chem B 108:2788
35. Niederberger M, Krumeich F, Hegetschweiler K, Nesper R (2002) Chem Mater 14:78
36. Schäffer TE, Ionescu-Zanetti C, Proksch R, Fritz M, Walters DA, Almqvist N, Zaremba CM, Belcher AM, Smith BL, Stucky GD, Morse DE, Hansma PK (1997) Chem Mater 9:731
37. Kondepudi DK, Prigogine I (1998) Modern thermodynamics – from heat engines to dissipative structures. Wiley, New York, p 427
38. Epstein IR, Pojman JA (1998) An introduction to nonlinear chemical dynamics – oscillations, waves, patterns, and chaos. Oxford University Press, Oxford, England
39. Ben-Jacob E, Garik P (1990) Nature 343:523
40. Saito Y, Ueta T (1989) Phys Rev A 40:3408
41. Oaki Y, Imai H (2003) Cryst Growth Des 3:711
42. Ní Mhíocháin TR, Coey JMD (2004) Phys Rev E 69:061404
43. Gránásy L, Pusztai T, Börzsönyi T, Warren JA, Douglas JF (2004) Nat Mater 3:645
44. Ma Y, Qi L, Ma J, Cheng H (2004) Cryst Growth Des 4:351
45. Chen X, Wang X, Wang Z, Yang X, Qian Y (2005) Cryst Growth Des 5:347
46. Lu Q, Gao F, Komarneni S (2004) J Am Chem Soc 126:54
47. Cao M, Liu T, Gao S, Sun G, Wu X, Hu C, Wang ZL (2005) Angew Chem Int Ed 44:4197
48. Yang D, Qi L, Ma J (2003) Chem Commun, p 1180
49. Nakanishi S, Fukami K, Sakai S, Nakato Y (2002) Chem Lett 31:636
50. Fukami K, Nakanishi S, Sakai S, Nakato Y (2003) Chem Lett 32:532
51. Fukami K, Nakanishi S, Tada T, Yamasaki H, Sakai S, Fukushima S, Nakato Y (2004) J Electrochem Soc 152:C493

52. Nakanishi S, Fukami K, Tada T, Nakato Y (2004) J Am Chem Soc 126:9556
53. Xu H, Keawwattana W, Kyua T (2005) J Chem Phys 123:124908
54. Kniep R, Busch S (1996) Angew Chem Int Ed Engl 35:2624
55. Busch S, Schwarz U, Kniep R (2001) Chem Mater 13:3260
56. Busch S, Schwarz U, Kniep R (2003) Adv Funct Mater 13:189
57. Yu SH, Cölfen H, Hartmann J, Antonietti M (2002) Adv Funct Mater 12:541
58. Yu SH, Cölfen H, Antonietti M (2003) J Phys Chem B 107:7396
59. Yu SH, Antonietti M, Cölfen H, Hartmann J (2003) Nano Lett 3:379
60. Tian ZR, Liu J, Voigt JA, Mckenzie B, Xu H (2003) Angew Chem Int Ed 42:414
61. Chang Y, Zeng HC (2004) Cryst Growth Des 4:273
62. Imai H, Terada T, Yamabi S (2003) Chem Commun, p 484
63. Lindsell WE, Preston PN, Seddon JM, Rosair GM, Woodman AJ (2000) Chem Mater 12:1572
64. Yang W, Chai X, Chi L, Liu X, Cao Y, Lu R, Jiang Y, Tang X, Fuchs H, Li T (1999) Chem Eur J 5:1144
65. Liu J, Zhang F, He T (2001) Macromol Rapid Commun 22:1340
66. Barteczak Z, Argon AS, Cohen RE, Kowalewski T (1999) Polymer 40:2367
67. Li M, Mann S (2000) Langmuir 16:7088
68. Hopwood JD, Mann S (1997) Chem Mater 9:819
69. Gower LA, Tirrell DA (1998) J Cryst Growth 191:153
70. García-Ruiz JM (1985) J Cryst Growth 73:251
71. García-Ruiz JM, Hyde ST, Carnerup AM, Christy AG, Van Kranendonk MJ, Welham NJ (2003) Science 302:1194
72. Terada T, Yamabi S, Imai H (2003) J Cryst Growth 253:435
73. Yu SH, Cölfen H, Tauer K, Antonietti M (2005) Nat Mater 4:51
74. Suda J, Matsushita M (1995) J Phys Soc Jpn 64:348
75. Suda J, Matsushita M, Izumi K (2000) J Phys Soc Jpn 69:124
76. Suda J, Nakayama T, Matsushita M (1998) J Phys Soc Jpn 67:2981
77. Suda J, Matsushita M (2004) J Phys Soc Jpn 73:300
78. Giraldo O, Brock SL, Marquez M, Suib SL, Hillhouse H, Tsapatsis M (2000) Nature 405:38
79. Wang ZL, Kong XY, Ding Y, Gao P, Hughes WL, Yang R, Zhang Y (2004) Adv Funct Mater 14:943
80. Kong XY, Wang ZL (2003) Nano Lett 3:1625
81. Yang SM, Sokolov I, Coombs N, Kresge CT, Ozin GA (1999) Adv Mater 11:1427
82. Kim WJ, Yang SM (2001) Adv Mater 13:1191
83. Imai H, Oaki Y (2004) Angew Chem Int Ed 43:1363
84. Oaki Y, Imai H (2005) Langmuir 21:863
85. Oaki Y, Imai H (2004) J Am Chem Soc 126:9271
86. Estroff LA, Incarvito CD, Hamilton AD (2004) J Am Chem Soc 126:2
87. Park RJ, Meldrum FC (2002) Adv Mater 14:1167
88. Aizenberg J, Muller DA, Grazul JL, Hamann DR (2003) Science 299:1205
89. Ha YH, Vaia RA, Lynn WF, Costantino JP, Shin J, Smith AB, Matsudaira PT, Thomas EL (2004) Adv Mater 16:1091
90. Grassmann O, Müller G, Löbmann P (2002) Chem Mater 14:4530
91. Zhan J, Lin HP, Mou CY (2003) Adv Mater 15:621
92. MacKenzie CR, Wilbanks SM, McGrath KM (2004) J Mater Chem 14:1238
93. Rautaray D, Sainkar SR, Sastry M (2003) Langmuir 19:10095
94. Chen SF, Yu SH, Wang TX, Jiang J, Cölfen H, Hu B, Yu B (2005) Adv Mater 17:1461
95. Sugawara A, Ishii T, Kato T (2003) Angew Chem Int Ed 42:5299

96. Gehrke N, Cölfen H, Pinna N, Antonietti M, Nassif N (2005) Cryst Growth Des 5:1317
97. Kotachi A, Miura T, Imai H (2004) Chem Mater 16:3191
98. Kotachi A, Miura T, Imai H (2006) Chem Lett 35:204
99. Mukkamala SB, Powell AK (2004) Chem Commun, p 918
100. Rudloff J, Cölfen H (2004) Langmuir 20:991
101. Volodkin DV, Petrov AI, Prevot M, Sukhorukov GB (2004) Langmuir 20:3398
102. Yu SH, Cölfen H, Xu AW, Dong W (2004) Cryst Growth Des 4:33
103. Imai H, Terada T, Miura T, Yamabi S (2002) J Cryst Growth 244:200
104. Miura T, Kotachi A, Oaki Y, Imai H (2006) Cryst Growth Des 6:612
105. Qi L, Cölfen H, Antonietti M, Li M, Hopwood JD, Ashley AJ, Mann S (2001) Chem Eur J 7:3526
106. Qi L, Cölfen H, Antonietti M (2000) Angew Chem Int Ed 39:604
107. Qi L, Cölfen H, Antonietti M (2000) Chem Mater 12:2392
108. Cölfen H, Qi L, Mastai Y, Börger L (2002) Cryst Growth Des 2:191
109. Yu SH, Cölfen H, Antonietti M (2002) Chem Eur J 8:2937
110. Song J, Saiz E, Bertozzi CR (2003) J Am Chem Soc 125:1236
111. Zhang W, Liao SS, Cui FZ (2003) Chem Mater 15:3221
112. Furuichi K, Oaki Y, Imai H (2006) Chem Mater 18:229
113. Oaki Y, Imai H (2005) Adv Funct Mater 15:1407

Top Curr Chem (2007) 270: 73–125
DOI 10.1007/128_053

Published online: 22 July 2006

Fluorapatite-Gelatine-Nanocomposites: Self-Organized Morphogenesis, Real Structure and Relations to Natural Hard Materials

Rüdiger Kniep (✉) · Paul Simon

Max-Planck-Institut für Chemische Physik fester Stoffe, Nöthnitzer Str. 40,
01187 Dresden, Germany
kniep@cpfs.mpg.de

Abstract The biomimetic system fluorapatite-gelatine (in aqueous solutions) is perfectly suited for the study of biomimetic steps closely related to steps in osteo- and dentinogenesis. Although representing a relatively low level of complexity, the biomimetic system still includes all aspects of complexity, such as metastability, self assembly, self-similarity, fractals, pattern-formation, hierarchy, and others. The present review is focused on the morphogenesis and real structure of fluorapatite-gelatine-nanocomposites and is structured in a sequence from macroscopic/bulk-properties to mesoscopic and finally microscopic observations, in part also supported by atomistic simulations. The field encompasses a large variety of components reaching from basic science to applications.

Keywords Applications · Atomistic simulations · Electrical dipole fields · Fluorapatite · Gelatine · Morphogenesis · Nanocomposites

1 Introduction

The biomimetic system fluorapatite-gelatine bears strong resemblance to the biosystem hydroxyapatite (HAP)-collagen which plays a decisive role in the human body (vertebrates in general) as functional material in the form of bone [1, 2] and teeth [3, 4]. In the bio-systems, the hierarchical and self-similar organization of nanocomposite structures is of prominent relevance [5–8], with HAP-protein (collagen) nanocomposite structures dominated by a close orientational relationship between the triple-helical collagen molecules (arranged in the form of fibrils) and the HAP nanocrystals which first nucleate in the gaps between neighboring protein molecules. In these arrangements, the crystallographic *c*-axes of the HAP nanocrystals are oriented parallel to the longitudinal direction of the fibrils [9, 10].

As the development of bone and teeth proceeds during processes of high complexity involving metabolisms and cell activities of living system, it was a consistent decision to clearly reduce the level of complexity by restricting the investigations to water-soluble gelatine (denatured collagen) and aqueous solutions of the appropriate ions needed for the formation of apatite. The biomineralization process is then mimicked by a double diffusion system in which the ions migrate into a gelatine gel from opposite reservoirs containing solutions of calcium and phosphate/fluoride, respectively. The mobility of the protein (gelatine) in the gel thereby eases rearrangements of the protein fibers during processes of self-organization.

1.1 Basic Idea and Conception

The chemical system under consideration raised great hopes as being representative of a materials combination that had been optimized during the processes of evolution, and which would allow us to gain deeper insight into the

general principles of biomineralization (the formation of inorganic/organic nanocomposites). This task is a real challenge and has to be tackled on all length scales accessible by various methods of investigation. Therefore, the present review is structured in a sequence from macroscopic/bulk-properties to mesoscopic and finally microscopic observations. We are still far away from a perfect understanding of all the experimental indications obtained so far, but it has already become clear that the first steps in this direction have been taken showing promising future trends. The field encompasses all the components from basic science to applications. With respect to materials properties and applications an increasing interest is clearly reflected by the presently increasing number of publications dealing with apatite-gelatine composites [11–14].

Also from the point of view of fundamental research the chemical system under consideration is of significant relevance. First of all, it calls for the combination of scientific aspects from various fields, such as: chemistry, physics, crystallography, mineralogy, biology, zoology, microbiology, paleontology, medicine, pharmacy, theory, atomistic simulations, and others. This (incomplete) list clearly draws a path back to the initial material science ("Naturforschung") including even aspects of philosophy and arts. Placing the focus on materials only, the system still remains of great interest, because all aspects of complexity are included: Metastability, self-organization (self-assembly), self-similarity, fractals, pattern formation, hierarchy, transfer of information, and others. As the morphogenetic process in the apatite-gelatine system proceeds at biological time scales (days/weeks), general problems concerning the isolation and investigation of the different stages of development of the composite aggregates do not appear. To summarize the given statements and to clarify the focus of the present review [15–25]: The system apatite-gelatine is perfectly suited for obtaining deeper insight into the processes of self-organization, and can help in learning the essentials in the formation of inorganic–organic nanocomposites of biological relevance.

1.2 Restriction to FAP-Composites

In order to closely mimic the bio-systems of bone and teeth the inorganic component should be involved in the form of hydroxyapatite (HAP), which most certainly when compared to the hard tissues of vertebrates is far away from the ideal stoichiometric composition $Ca_5(OH)[PO_4]_3$. Besides Ca-deficiency and the presence of hydrogenphosphate groups [26], carbonate substitution is common as well as substitution by other foreign ions [27]. Substitution ($OH_{1-x}F_x$) by formation of members ("parts") of the solid-solution series between HAP and FAP [28] is of overriding importance because of dramatic effects concerning control and change of the apatite morphology. This effect has recently been investigated in some detail [21, 29]. Moreover, the

chemical systems without addition of fluoride tend towards the formation of other calcium phosphates such as octacalcium phosphate. The influence of fluoride on phase formation and morphology of calcium phosphate-gelatine composites grown by the double diffusion technique [21] is clearly demonstrated by the SEM images shown in Fig. 1. From this it becomes evident that the "most clearly" structured aggregate is represented by the notched sphere consisting of the FAP composite. Even its surface structure is dominated by sub-individuals which are clearly made out and distinguished. This kind of overall structuring allows unimpeded positional orientation in/on such kinds of aggregate and makes attempts in the direction of the interpretation of morphogenetic details easier, even from a crystallographic point of view. In other words, "things" become easier with the FAP-gelatine nanocomposites, and at the same time the large and still unexplored fields of HAP- and OCP-composites and their morphogenesis are demonstrated.

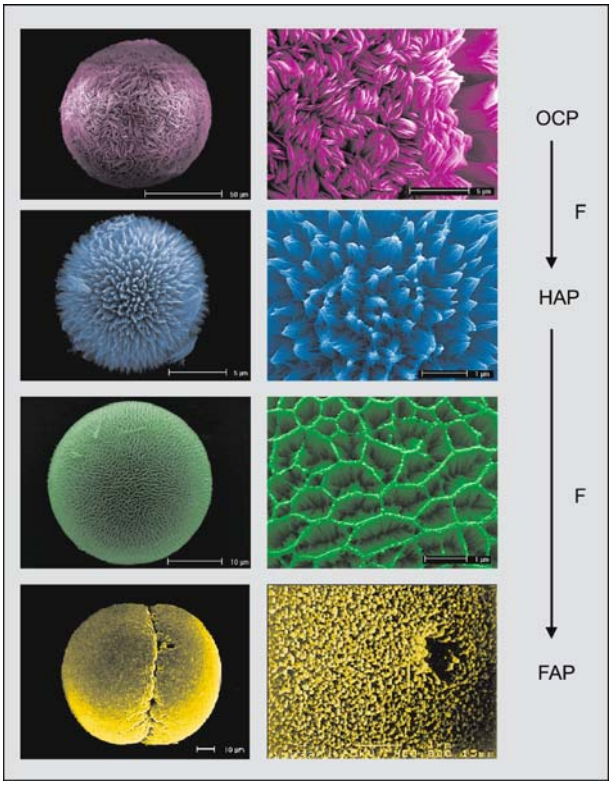

Fig. 1 Influence of fluoride on phase formation and morphology of calcium phosphate-gelatine-nanocomposites grown by the double-diffusion technique. SEM images. OCP = Octacalcium phosphate. The surface structures change with increasing amounts of fluoride (*right panel* from *top* to *bottom* starting with [F] = 0) in the solutions and in the composites [21]

2 Experimental (Double Diffusion and Liesegang Bands)

The growth of fluorapatite-gelatine-nanocomposite aggregates is carried out in U-tubes (Fig. 2) according to the double diffusion technique [30], which is normally used for the growth of crystals of compounds with low solubility [31]. In general, the gel takes over the control of the ion diffusion only, and is not actively involved in the crystallization processes. During the growth of apatite within a gelatine gel matrix the situation is completely different: The gelatine molecules interact with the ions in solution in such a way that they provide nucleation positions for nanoapatite and, in this way, give rise to the formation of a nanocomposite scenario which then becomes the master control of the processes of self-organization and pattern formation including dramatic activities in reorganization of the gel-matrix.

Within periods of days to weeks the nanocomposite aggregates form inside the gel-matrix in periodically arranged growth areas, the so-called Liesegang

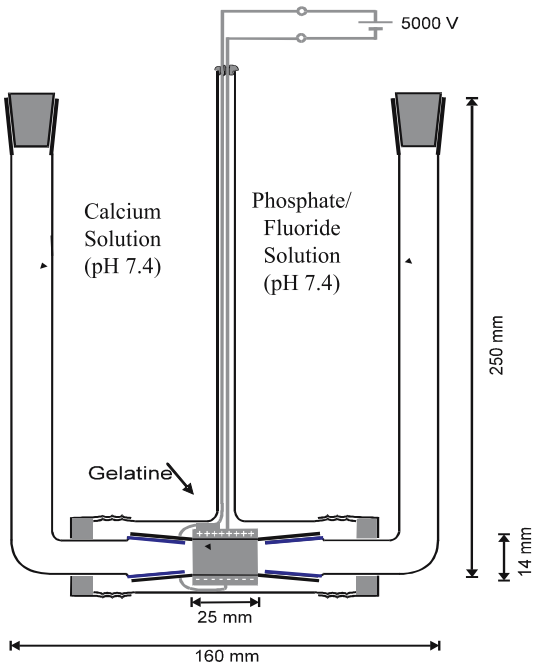

Fig. 2 Growth chamber [17] (double diffusion technique) including the facility for application of an external electric field (5000 V/1.4 cm; D. C. conditions) as discussed in Sect. 7.2; the electrodes are placed on opposite sites of the horizontal glass tube which contains the gelatine plug; to prevent contact with moisture the electric circuit is protected by an outer glass envelope; the equipment is suitable for use in thermostats operating with water

bands (Fig. 3) [15, 16, 21, 32, 33]. In order to isolate the aggregates from the gel the gelatine plug is cut into slices containing the different Liesegang bands. To isolate the solid composite aggregates, the slices are washed several times with hot water and centrifuged. The local positions of the Liesegang bands relative to the calcium- and phosphate-fluoride-source are of essential importance because of pre-structuring effects of the gelatine (Sect. 6). The Liesegang bands are described as C, M and P, respectively (Fig. 3) and contain the composite aggregates formed during two different kinds of morphogeneses (Sect. 3), called fan-like and fractal-type developments.

In a typical double diffusion experiment [18, 19, 21] pig skin gelatine (300 bloom, Aldrich) is heated together with water (gelatine concentration maximum 15%) with stirring for a few minutes in a water bath (after acidification with glutamic acid or 2 N HCl). The central tube of the diffusion cell (Figs. 2 and 3) is filled with the hot gelatine and left at room temperature in a vertical position until gelation is finished (e.g. 24 h). The L-shaped tubes are then attached to the central gel-tube, filled with the aqueous solutions. (e.g.: 0.133 m $CaCl_2$ and 0.08 m Na_2HPO_4/0.0027 m KF), and closed with ground-glass stoppers. Both solutions were previously adjusted to the physiological pH of 7.4 with α,α,α-tris(hydroxymethyl) methylamine/HCl. The diffusion experiments are carried out between 25 °C and 30 °C (thermostat).

Variation of parameters is possible within defined limits [19]. For the fluorapatite-gelatine composites the maximum gelatine-concentration is 15 wt. %, otherwise additional CaF_2 is formed. The maximum pH of the aqueous gel at the beginning of the double diffusion should not exceed the value of 6, otherwise a microcrystalline FAP-precipitate is formed and the fractal growth is suppressed. Studies on the time-dependence of the growth result in

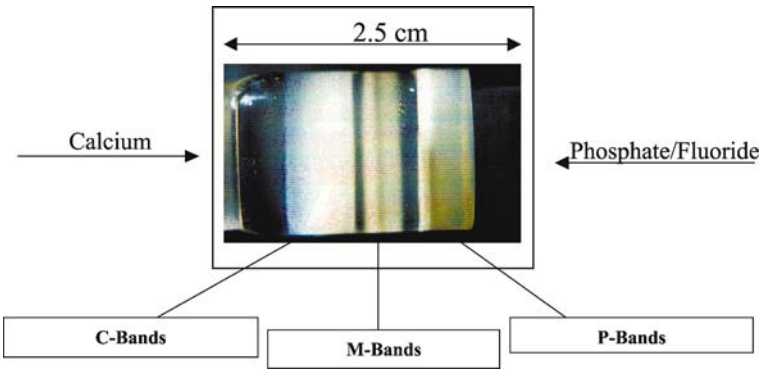

Fig. 3 Periodic growth of calcium phosphate–gelatine-composites (formation of Liesegang bands) within a gelatine gel plug by application of the double diffusion technique (*top*: photograph of the reaction tube) [15, 16, 21, 32]. The bands are described as C, M and P, respectively, showing their positions in the (*horizontal*) diffusion tube (C = bands close to the calcium source, M = middle bands, P = bands close to the phosphate(fluoride) source)

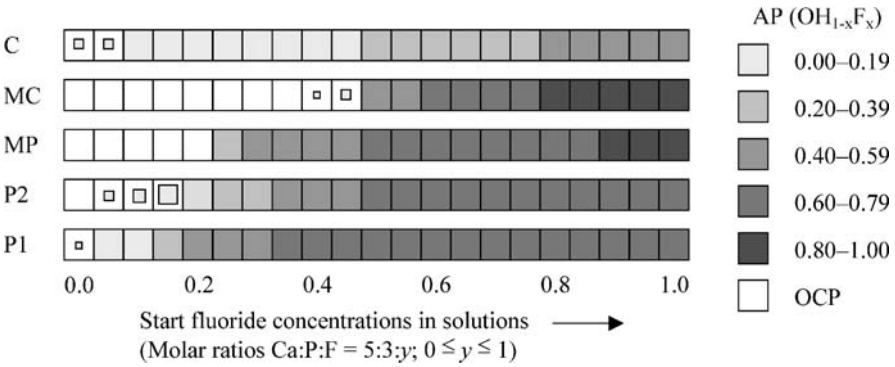

Fig. 4 Calcium phosphate phases grown by double diffusion in gelatine-gel. Identification of crystalline phases by powder X-ray diffraction. Appearance of the phases OCP (octacalcium phosphate) and AP (apatite) in C-, M- and P-bands, respectively, after a growth period of three weeks at constant temperature (25 °C). Variable: starting fluoride concentration y (molar ratio P : F = 3 : y; $0 \leq y \leq 1$) in the phosphate/fluoride solution. The substitution parameter x ($OH_{1-x}F_x$) in the AP-phase was determined by refinement of the lattice parameters and application of Vegard's rule (continuous solid solution series between HAP and FAP [28]). The color scale represents x-ranges of substitution ($OH_{1-x}F_x$) in the AP phase

the finding that a three-week period is optimum concerning size and yield of the composite aggregates.

The influence of the fluoride concentration on phase formation and morphology in the course of the double diffusion experiments was only recently investigated in detail [21]. The results concerning phase formation are summarized in Fig. 4. Together with the statements concerning morphogenetic aspects (Sect. 1.2) it becomes clear again, why the present review is restricted to the F-rich composite only.

3
Form-Development (Macroscopic Length-Scale)

The morphogenesis of fluorapatite-gelatine nanocomposite aggregates proceeds from hexagonal-prismatic seeds, via dumbbell-shaped states, to spherical particles with a characteristic notch. Phenomological aspects can be best clarified by SEM-investigations on as-grown aggregate states as well as on fragments with various orientations with regard to the symmetry of aggregate development. From that first simulation models for general growth principles can be derived and continuously tested by additional findings obtained by other (more detailed) experimental observations as well as by theoretical investigations.

Particularly, the composite aggregates belonging to the fractal growth series [obtained from P-(and M-) bands; see Sect. 2] impressively illustrate the overall complexity of the system including the principles of self-similarity and hierarchy even on the macroscopic length-scale (Fig. 5). This kind of morphogenesis clearly exceeds the form developments known from pure inorganic systems, such as sheave-bundles, dumbbells, and spherulites (ontogenesis of minerals) [34], and has its origin in the intrinsic structure of the composite on the nanoscale level.

The secret of the pattern formation is then put down to the nanoscale-interactions between the organic and the inorganic components of the composite and in consequence the morphogenesis is controlled by the resulting and developing chemical and physical properties. As the general rule "The Principle of Continuous Development in Nature" also holds for composite and non-composite materials, even related shapes of solid aggregates do not exclude each other, but will have their morphogenetic origin in different growth principles. On the other hand, the more complex chemical system will be able to develop patterns of higher complexity, and this is, for example, what biominerals are representative for. The hierarchical composite pattern shown in Fig. 5 will hardly be obtained from a pure inorganic system, even if splitting of sub-crystals by incorporation of impurities [34] or "kayak"-like sub-specimens [35] (also known as spindle-individuals [36]) and their intergrowths are assumed. The real challenge in connection with complexity is provided by biomimetic nanocomposite systems and their basic morphogenetic principles.

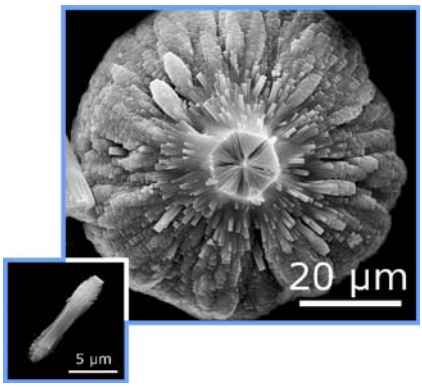

Fig. 5 Self-similarity and hierarchical pattern formation by fractal growth of fluorapatite-gelatine nanocomposites (SEM images) [24]. *Main picture*: half of a dumb-bell aggregate viewed along the central seed axes. *Small picture*: Central seed exhibiting tendencies of splitting at both ends ("small" dumb-bell). The development from "small" to "large" dumb-bells implies a remarkable reduction of shape information, in which only the club-motif is transmitted

3.1
Fractal and Fan-Like Morphogenesis

As mentioned earlier (Sect. 2), the nanocomposite aggregates grown by double-diffusion into a gelatine gel-matrix appear within so-called Liesegang bands, named as C, M and P, respectively (Fig. 3 in Sect. 2). A fractal growth mechanism (first reported in 1996) [15, 16] dominates in the P (and M) bands, whereas a fan-like growth mechanism (first reported in 2006) [24] preferentially occurs in the C bands. Phenomological aspects and the simulation model for the fractal series will be described first. Details concerning the inner architecture of the fractal composite aggregates are given in Sect. 3.2.

The fractal growth mechanism starts with elongated hexagonal-prismatic seeds up to 30 μm in length (critical aspect ratio $\approx 3:1$). Progressive stages of self-assembled (non-crystallographic) upgrowths of needle-shaped prisms at both ends of the seed (fractal branching) lead to dumbbell-shaped aggregates (Fig. 6) which complete their shapes by successive and self-similar upgrowths to give notched spheres after about the 10th fractal generation.

The morphogenesis from a needle-shaped seed of about 10 μm in length to a spheroaggregate of about 60 μm in diameter takes approximately one week. The fractal growth and architecture is controlled by two non-crystallographic parameters, which were derived from SEM images at different growth stages: (1) the maximum aperture angle between the long axis of the seed and the needle-axes of the units of the following generation is $45° \pm 5°$; (2) subsequent generations scale down in their lengths by a factor of ≈ 0.7. On the basis of these two limiting conditions the fractal model of a just-closed sphere is shown in Fig. 7 (2D-simulation with the umbrella-tree model [37]; crossing of individual crystals suppressed). The simulated surface of the spheroaggregate consists of very small needlelike units, an observation which is consistent with the SEM images (mean diameter < 0.1 μm for the surface prisms of a just-closed sphere; see also Fig. 8). Inside the spherocrystal a torus-shaped cavity is formed around the elongated seed (Sect. 3.2 for more details). A similar architecture is generated by the geometrical model of a splitting needle at constant growth rate and constant splitting rate [38].

Selected stages of the fractal morphogenesis (SEM images), together with more detailed 3D-simulations [39] are shown in Fig. 9, and reveal good agreement in structural shapes.

A second fan-like growth pattern [24] preferentially occurs in the C-bands and is shown in Fig. 10 (vertical rows on the left-hand sides; the fractal series is shown in the vertical rows on the right-hand sides). Both principles involve the initial formation of a hexagonal prismatic seed and develop via dumbbell-like structures to spheres. Distinguishing the two form developments is hence far from trivial and requires the knowledge of specific morphological criteria.

The two different morphogeneses are illustrated by a series of six subsequent growth states. The morphological key differences are discussed on

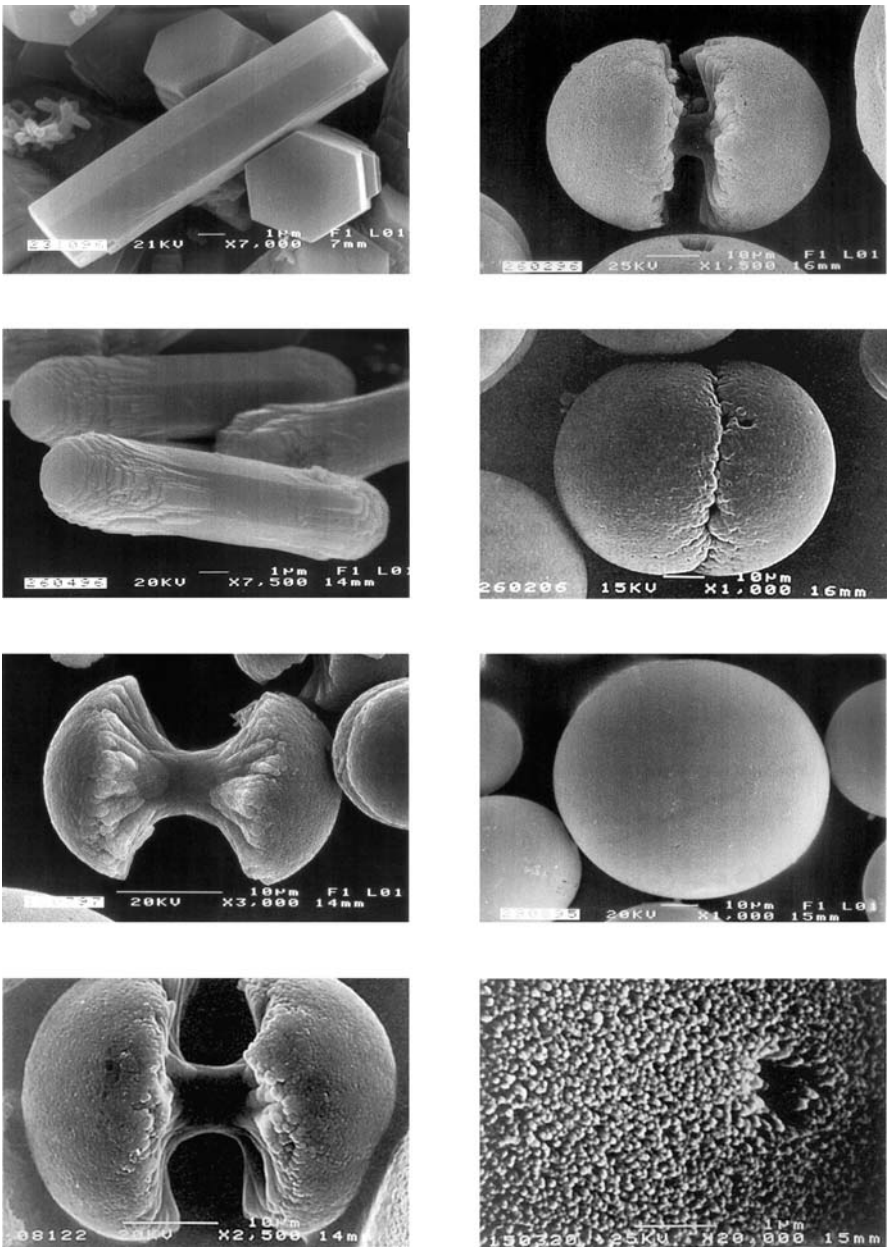

Fig. 6 Selected sequence of SEM images of progressive stages of self-assembled (hierarchical) growth of fluorapatite-gelatine nanocomposite aggregates (morphogenesis) [17, 22]: from an elongated hexagonal-prismatic seed (*top left*) through dumbbell shapes to spheres; the surface of a just-closed sphere also consists of needlelike units (*bottom right*) following the general principles of self-similarity

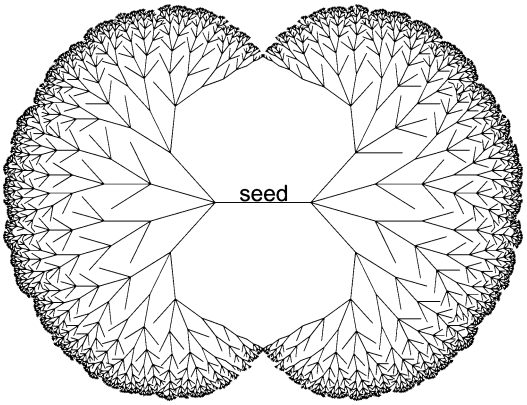

Fig. 7 2D-simulation of a just-closed fluorapatite spheroaggregate [17]; fractal model (seed plus 10 generations) assuming a fourfold splitting in each generation (in fact, orders of non-crystallographic branching can be higher); maximum opening angle 48°, scale down factor 0.7; crossing of individuals is suppressed by particular rules following real growth conditions: (1) all individuals have the same growing speed; (2) members of higher generations are suppressed, if they cross members of a lower generation; (3) if members of the same generation reach the crossing point at the same time, it is a random decision which one is deleted; if crossing is "non-symmetric", the individual reaching the crossing point first is favored; (4) to simulate diffusion-inhibition inside the growing dumbbell area all individuals with an angle greater than 160° relative to the seed are deleted. The fine-structure of the fractal surface reminds of a cauliflower pattern consisting of bundles of subunits (see ESEM image in Fig. 8)

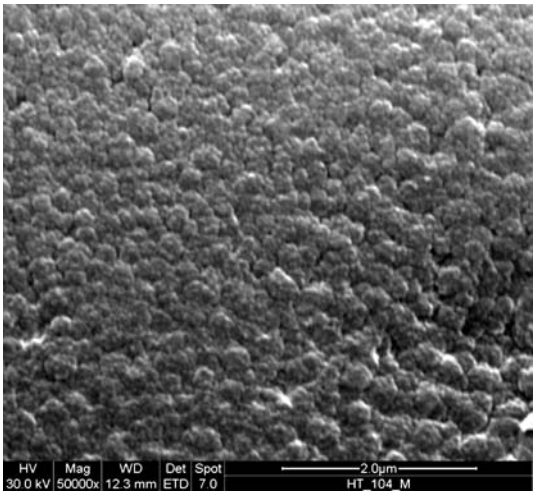

Fig. 8 ESEM image of the surface of a freshly prepared fractal composite sphere showing a cauliflower-like arrangement representing bundles of subunits of the last fractal generation (Fig. 7). By comparison with the surface image given in Fig. 6 it becomes evident that drying and ageing slightly affects the images of the composite samples

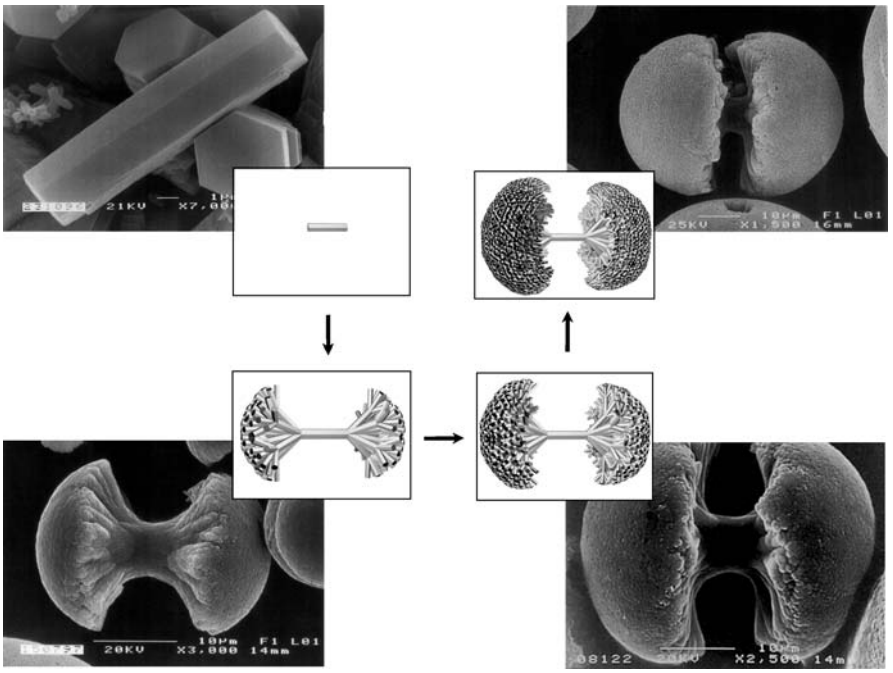

Fig. 9 Selected states of the fractal morphogenesis (SEM images) together with 3D-simulations (*from top left anticlockwise*: seed, seed + 2, seed + 3 and seed + 4 generations)

the basis of the fan-like series: The central hexagonal prismatic seed exhibits a more compressed habit with an aspect-ratio of about 2 : 1. The fan-like development evolves from a common (central) plane perpendicular to the hexagonal axis of the seed. The following structural units exhibit a wedge-like shape with the size of their basal faces increasing during the growth process. The small opening angle of the "prism-faces" against the central axis already indicates an inner structure with a radial arrangement of sub-individuals. The individual units growing on or out of the prismatic seed are separated by planar faces and straight edges. Bent shapes as characteristic for biological systems and also observed in the fractal growth series do not occur. The surfaces of the dumbbells and spheres are characterized by a coarse hexagonal tiling reflecting the basal faces of the individuals arranged to the fan-like aggregate. In the fractal growth series, however, the surface structures of the dumbbells and spheres become smaller and smaller (Figs. 6–9). Both final growth states result in notched spheres. However, while the sphere-aggregates grown via the fractal growth mechanism exhibit a toroidal cavity around the seed, (Sect. 3.2) the fan-like spheres are completely filled in the vicinity of their "intergrowth"-plane. This observation is directly related to the absence of a "free bridge" in the center of the growing fan-like aggregates (see

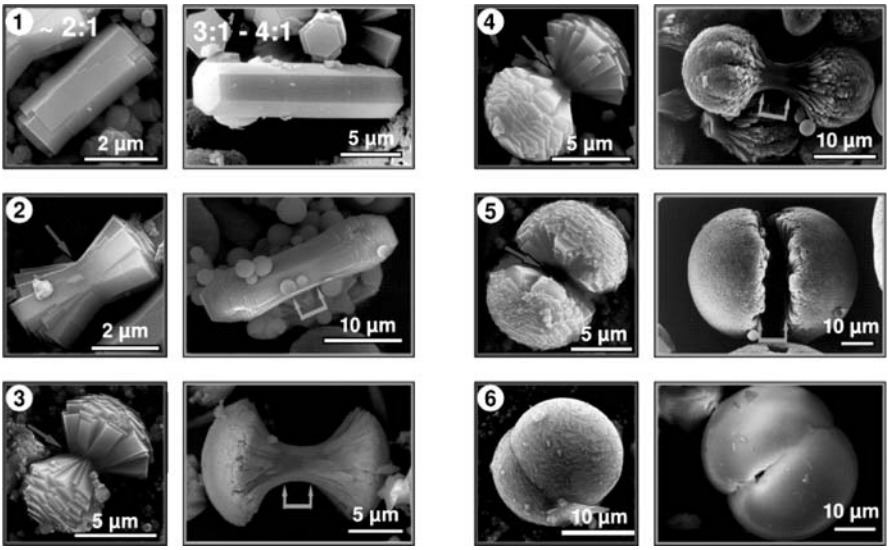

Fig. 10 SEM images illustrating subsequent states (1–6) of the morphogeneses of fluorapatite-gelatine nanocomposites for fan-like (vertical rows on the left-hand side) and fractal (vertical rows on the right-hand side) growth mechanisms [24]. The *arrows* indicate the growth plane and the "free bridge" respectively, see text for details

arrows in Fig. 10). To summarize all the observations made, the main differences between the two types of morphogeneses (fan-like and fractal) may be characterized in terms of "crystallographical" (straight, hard) and "biological" (bent, soft), respectively. In Sect. 6 it is shown that pre-structuring of the gelatine-gel by ion-impregnation (Calcium → C-bands; phosphate → P-bands) is held to be a responsible factor for the two different principles of form development.

3.2 Fracture Properties and Inner Architecture

The fracture properties as well as the fracture patterns of the fractal nanocomposite aggregates (Sect. 3.1) should not only reflect their inner (nano)structure ("principle of correspondence") but should also be consistent with the growth model and the resulting inner architecture.

The fracture area of a seed perpendicular to the hexagonal axis shows an overall radial structure (Fig. 11a,b) completely different to the fracture surface of a pure apatite single crystal (Fig. 11c,d; hydrothermally grown mineral) with a glass-like structure without any preferred pattern. This observation already led to the assumption [19] that the composite seed represents some kind of an ordered nano-superstructure which may explain the specific structure of the fracture area (Sect. 5).

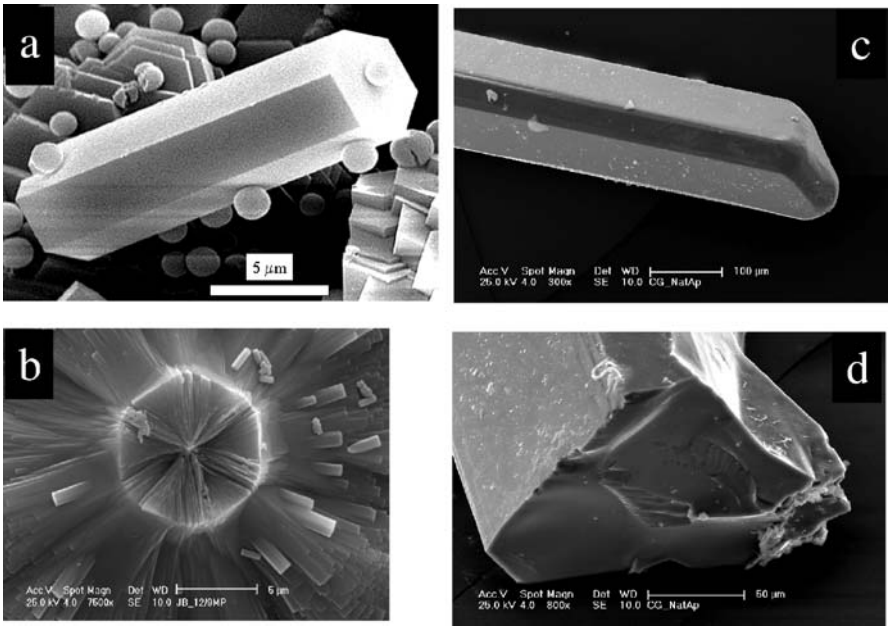

Fig. 11 **a** SEM image of a virgin fluorapatite-gelatine-composite seed. **b** SEM image of the fracture area of a central seed of a fractal composite aggregate. The fracture surface is dominated by a highly structured pattern. **c,d** SEM images of an elongated prismatic apatite crystal (hydrothermally grown mineral) and the fracture surface perpendicular to the prism-axis (glass-like structure without any preferred pattern)

Actually, the situation develops in a much more complex manner as indicated in Fig. 12, where the central seed area is highlighted by the white hexagon. The regions outside the hexagon represent areas of higher hierarchy and are structured between platy and more compact appearance. This scenario of complexity will be discussed in Sects. 6.2 and 7.2.

In the course of the fractal morphogenesis of the composite aggregates a torus-shaped cavity around the central seed is formed (Sect. 3.1). The torus-shaped cavity is shown in Fig. 13 (left) and makes clear that the cross section of the cavity is characterized by a hexagonal shape [21]. This observation is in total agreement with the fractal growth and clearly supports the model as can be seen from the 2D-simulation (Fig. 13, right).

Compared with the fractal 2D-simulation given in Sect. 3.1 (Fig. 7), where splitting exclusively takes place at the outer ends of the previous generations (especially the seed), the modified simulation takes into consideration that "upgrowth" on the seed is actually observed "below" its ends and is shifted into the direction of the center of the seed (Sects. 6.2 and 7.2). In this way, also the equatorial notch of the sphere becomes less dominant (compared with the simulations given in Sect. 3.1, Fig. 7) which is in full agreement with

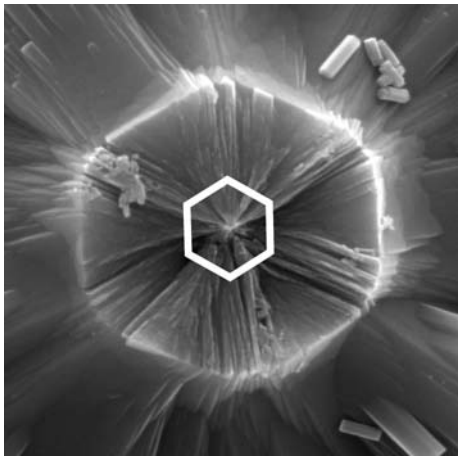

Fig. 12 Enlarged image of the central fracture area from Fig. 11b. The virgin seed (Fig. 11a) only extends inside the *white hexagon*. For further details see text (Sects. 6.2 and 7.2)

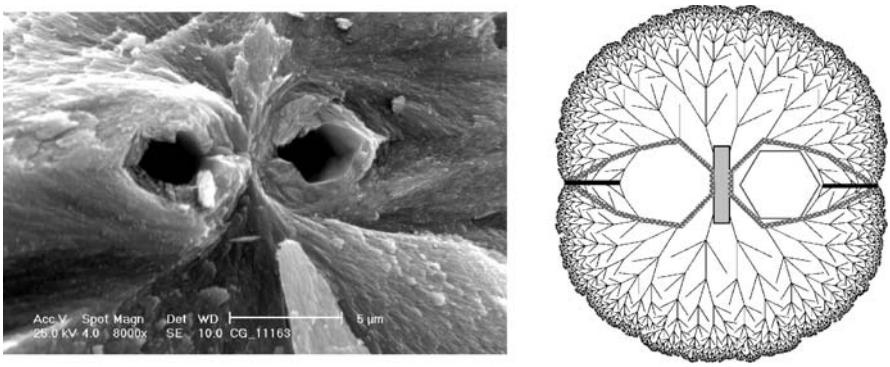

Fig. 13 Torus-shaped cavity around the seed in a closed sphere of the fractal morphogenesis. The SEM image (*left*) clearly shows the hexagonal cross section of the cavity which impressively supports the (modified: see text) 2D simulation model (*right*)

the experimental observations. Furthermore, the hexagonal shape of the cross section of the cavity around the seed becomes evident, as well as the join between the two half spheres and the brow-like structure (Fig. 13, right) around the cavity.

Finally, it should be pointed out that the overall growth-orientation within a fractal composite sphere, in plane with the hexagonal axis of the seed, shows remarkable correspondence to the orientation of electric field lines around a permanent dipole (Fig. 14) [17]. This correlation will be discussed in Sect. 7 in more detail.

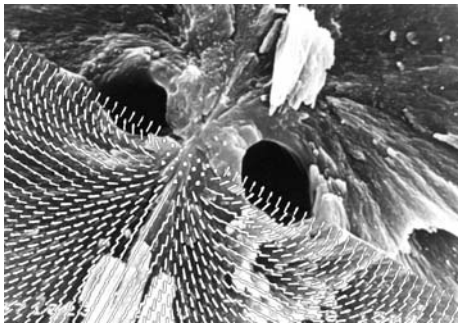

Fig. 14 SEM image of a fractal composite sphere broken parallel (*in plane*) to the long seed axis combined with the calculated shape of electric field lines around a permanent dipole (*field lines* reduced to only one half of the complete fracture area)

3.3
Core/Shell Assemblies

The surface of a just-closed (and notched) sphere of the fractal composite series (Sect. 3.1) is covered with small elongated units as shown in Fig. 15a. These small prismatic units seem to act as nucleation centers for the growth of a shell on top of the fractal core. The shell is built up of needle-shaped rods (Fig. 15b) oriented perpendicular to the core-surface and nearly parallel to each other (radial growth with only a small opening angle). A core/shell assembly is presented in Fig. 16a with the fractal core showing its characteristic equatorial notch [17, 18]. The core/shell interface represents an area of decreased stability against thermal and/or mechanical treatment. In fact, the

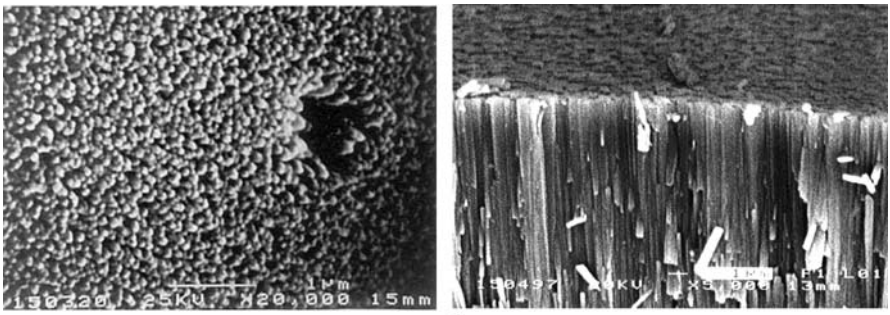

a b

Fig. 15 **a** Surface image of a just closed fluorapatite-gelatine nanocomposite sphere. **b** Arrangement of elongated prisms in the outer shell of the spheroids originating from a second growth mechanism. The prisms are almost parallel and bear a close resemblance to the arrangement of elongated prism bundles in enamel [40]

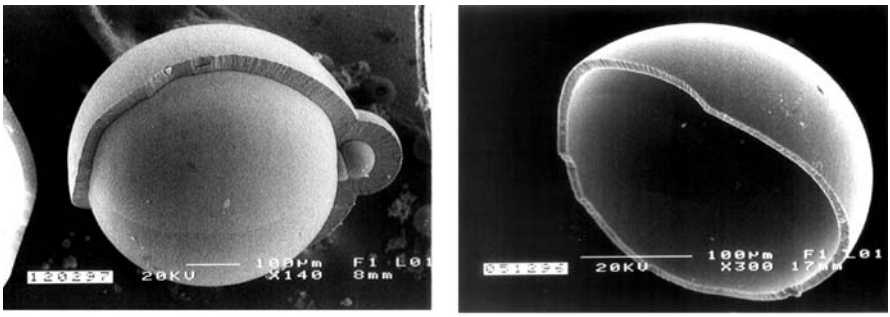

a b

Fig. 16 SEM images of a core/shell assembly. **a** Shell partly removed, free core; **b** Core removed from the shell

core is easily removed from the shell (Fig. 16b). In summary, the core and shell assemblies bear a strong resemblance to the complex organization of teeth (dentin and enamel) [40]. This relation will be discussed in Sect. 8.

4
Overall Characterization of the Fractal Composite Aggregates

The results reported in this section (4.1–4.4) were obtained using samples that were prepared well within the optimum stability region of the fractal particles, i.e., the fluorapatite-gelatine composites were grown in aqueous gels with about 10 wt. % gelatine and a starting pH between 2 and 5. The molar ratio of the educt solutions was adjusted to $Ca/P(PO_4^{3-}/HPO_4^{2-})/F = 5 : 5 : 1$, and the diffusion process was allowed to continue for three weeks. To isolate the aggregates from the surrounding gel, the gelatine plug was divided into particular bands and each one was added to 20 ml of ion-free water, heated to 40 °C, and centrifuged. After repeating this procedure five times the composite particles were almost free from attached gelatine.

4.1
X-Ray Diffraction

X-ray diffraction experiments on single individuals were performed using the high brilliance of a synchroton radiation source [19]. The macroscopic aggregates that are formed in the early stages of the morphogenesis and that are isolated from the gel are hexagonal prismatic seeds. The results of the diffraction investigations indicate that these particles exhibit scattering properties which are representative for single crystals (Fig. 17a). The sharp Bragg reflections evidence a three-dimensionally periodic arrangement of the fluorapatite component within the composite. Aiming to determine the crystal

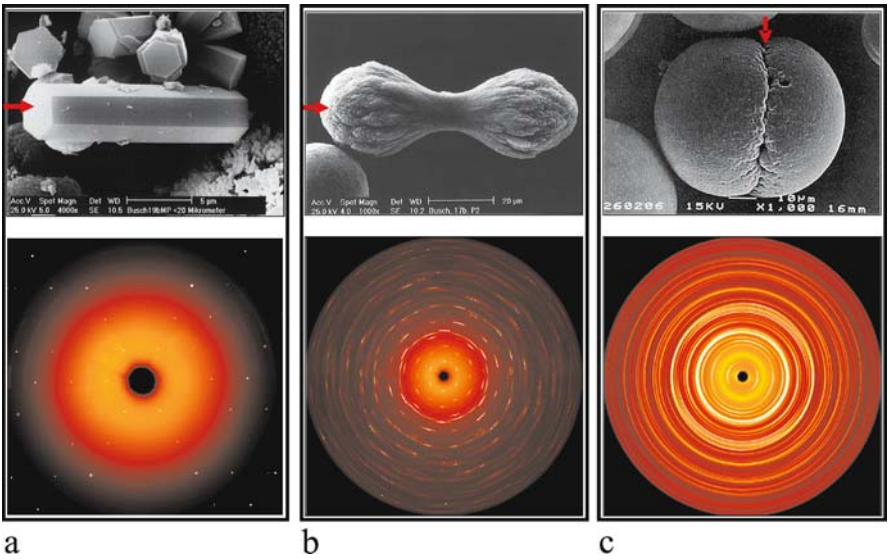

Fig. 17 SEM images of different growth stages from seed to sphere together with the corresponding diffraction patterns recorded using a synchrotron radiation source. *Red arrows* indicate the direction of the incident X-ray beam: **a** hexagonal prismatic seed (only the central part of the diffraction pattern is shown, **b** dumbbell stage, **c** just-closed sphere. See text for further explanations

structure of a hexagonal prismatic seed, a data set of a single particle (5 μm × 5 μm × 20 μm) was collected. Peak positions and intensities do not show indications of significant deviations from hexagonal symmetry or the formation of a superstructure in the composite particle. Thus, the atomic arrangement of fluorapatite was refined using the determined peak intensities [41]. Parameters of the measurement and refinement results are given in Tables 1 and 2. Thus, the refinements of the diffraction data do not allow a conclusive statement about a calcium deficiency of the inorganic component in the seed particles.

With proceeding growth of the particles, the scattering spots broaden and change into sickle-shaped maxima for dumbbell-shaped aggregates (Fig. 17b). This broadening continues with progressing growth of the particles, and for those individuals that complete the morphogenesis to a closed sphere diffraction patterns were observed consisting of almost complete powder rings (Fig. 17c). The correlation of growth state and diffraction patterns indicate the change of particle orientation during the fractal morphogenesis. Successive skewing of the following generations with respect to the alignment of the seed leads to a nearly overall isotropic distribution of particle orientations within the closed spheres resulting in moderately textured powder rings as diffraction patterns.

Table 1 Parameters of the data collection and refinement of a single hexagonal prismatic fluorapatite-gelatine composite seed measured using synchrotron radiation. The number of refined parameters includes an anisotropic description of atomic displacements. The sample to detector distance was not calibrated as lattice parameters were calculated from powder data [42]

Crystal habitus	Hexagonal prismatic 5 μm × 5 μm × 20 μm
Space group	$P6_3/m$
Formula units per unit cell	$Z = 2$
Lattice parameters	$a = 931.1(5)$ pm
	$c = 688.5(4)$ pm
Wavelength used for data collection	$\lambda = 51.66$ pm
Number of measured/unique reflections	2148/477
R_{eq}	0.0895
Measured range	$-12 < h < 12$, $-12 < k < 11$, $-9 < l < 9$
Number of reflection used for refinement $I > 2\sigma(I)$	413
Program used for refinements	SHELXL-97 [41]
Crystal structure refinement	Full matrix least squares on F^2
Number of refined parameters	39
$R(F^2)$, $wR(F^2)$, GOOF	0.038, 0.094, 1.01

Table 2 Refined positional and isotropic displacement parameters of the inorganic component (FAP) of a hexagonal prismatic fluorapatite-gelatine composite seed. The isotropic displacement parameter U_{eq} is defined as 1/3 of the orthogonalized U_{ij}-tensor

	x/a	y/b	z/c	U_{eq} [pm^2]
Ca(1)	0.24259(9)	–.00752(9)	0.25	103(3)
Ca(2)	0.66667	0.33333	–.0016(1)	115(3)
F	0.0	0.0	0.25	28(1)
P	0.3977(1)	0.3691(1)	0.25	57(3)
O(1)	0.3256(4)	0.4835(3)	0.25	109(6)
O(2)	0.5862(3)	0.4662(3)	0.25	140(6)
O(3)	0.3415(3)	0.2572(2)	0.0704(3)	160(5)

The possibility of investigating single particles that are typical for specific development stages enables us to determine growth state-dependent lattice constants and, thus, to gain an impression of the homogeneity of the chemical composition during the growth process. Figure 18 shows lattice parameters determined by X-ray diffraction of the different types of individual aggregates sorted by their state of morphogenesis [42]. For comparison, the range of values for pure hydroxyapatite, fluorapatite, and enamel (carbonate-containing apatite) are indicated; the variation of lattice param-

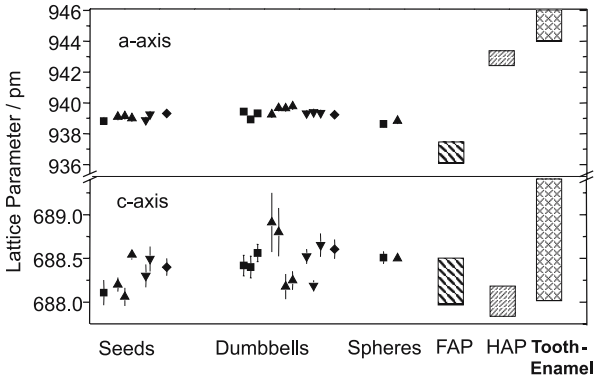

Fig. 18 Lattice parameters as refined by least squares fits to experimental *d*-values obtained by X-ray diffraction experiments on single particles belonging to successive growth stages of the composite [42]. Each variety of the symbols corresponds to a different particle of a certain type. Groups of the same symbol within one type are due to experiments with one particle in different orientations relative to the incident beam. *Error bars* are shown as *vertical lines* if they were determined to be larger than the size of the symbol. The data clearly show that both lattice parameters *a* and *c* are not affected significantly by the stadium of the fractal morphogenesis. For comparison, the range of lattice parameters of the *a*- and *c*-axes of inorganic hydroxyapatite (HAP), fluorapatite (FAP) and tooth enamel are indicated by shaded *vertical areas* [44–49]

eters is attributed to differences in the chemical composition of the samples [43–46]. The data shows that the *a*-axis is more sensitive to composition changes than the *c*-axis, and thus only the values found for *a* are considered as a suitable means for detecting partial substitution within the inorganic composite-component. Refinements of lattice parameters of ten different particles in development stages ranging from seeds to closed spheres result in the same average parameter value ($a = 939.1(5)$ pm) for all kinds of aggregates. The measurements show no evidence of alterations of the lattice parameter and thus of changes in the chemical composition of the particles during the growth process.

4.2 Thermal Decomposition

Decomposition of the composite with increasing temperature was investigated by thermogravimetry (TG) methods. Coupling of thermogravimetry with mass-spectroscopy (MS) allows a correlation of the weight loss to specific degradation products. Figure 19 shows a typical DTG/TG diagram of a composite sample with particle sizes between 140 μm to 200 μm in comparison with powdered single-phase natural fluorapatite [19]. While the weight loss of the abiogen mineral is negligible within the precision of the method, the data for the composite clearly indicates a stepwise weight loss. The first

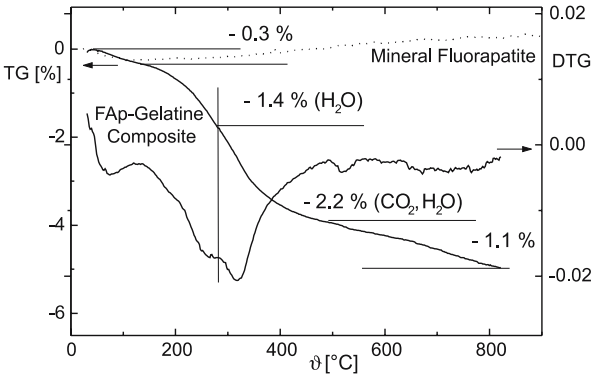

Fig. 19 Relative mass loss $\Delta m/m \times 100$ (TG) and its first derivative (DTG) in dependence from the sample temperature, ϑ, of the mineral fluorapatite (*dotted line*) and pure FAP-gelatine composite spheres with diameters ranging from 140 μm to 200 μm. Samples were heated in air with an increase of temperature corresponding to 10 °C/min. Attributions of weight losses to certain compounds resulting from a joined mass spectroscopic investigation are indicated in *brackets*. The overall relative weight loss of the composite in the investigated temperature range amounts to about 5 wt. % and occurs stepwise: The first step is attributed to the loss of adsorbed water, the second one to a desorption of constitutional water and the third one to the thermal decomposition of gelatine into water and carbon dioxide. Further weight decrease is attributed to complete oxidation of gelatine at higher temperatures

step is finished at 150 °C (weight loss: 0.3–1.0 wt. %) and is interpreted as the loss of adsorbed water. The second step is finished at 280 °C and is in analogy to tooth enamel attributed to the loss of constitutional water. For tooth enamel the loss of chemical bound water is explained with the reaction: $2HPO_4^{2-} \rightarrow P_2O_7^{4-} + H_2O$ [48]. The third step with its maximum at 324 °C is characterized by a release of fragments with molecular masses of 18 and 44, respectively. They are attributed to degradation products of the incorporated gelatine (water and carbon dioxide). With further increases of temperature a slight and almost steady decrease of the sample weight is observed that is not distinctive enough to be attributed to a special product of decomposition via mass spectrometry. The optical behavior of the particles during heating in air leads to the assumption that the weight loss above 300 °C is correlated to further protein decomposition (Fig. 20). Applying a heating rate of 30 °C/min the color immediately changes from translucent/pale-blue (Fig. 20a) to yellow at 300 °C (Fig. 20b) and intensifies parallel to a beclouding of the spheres. The particles turn reddish-brown at 360 °C (Fig. 20c). Around 550 °C the particles appear silvery (Fig. 20d) because the gelatine is mainly decomposed to carbon and water. Further heating to 1000 °C changes the color to dull-white (Fig. 20e) indicating that the carbon has been removed completely from the samples due to oxidation to CO and CO_2.

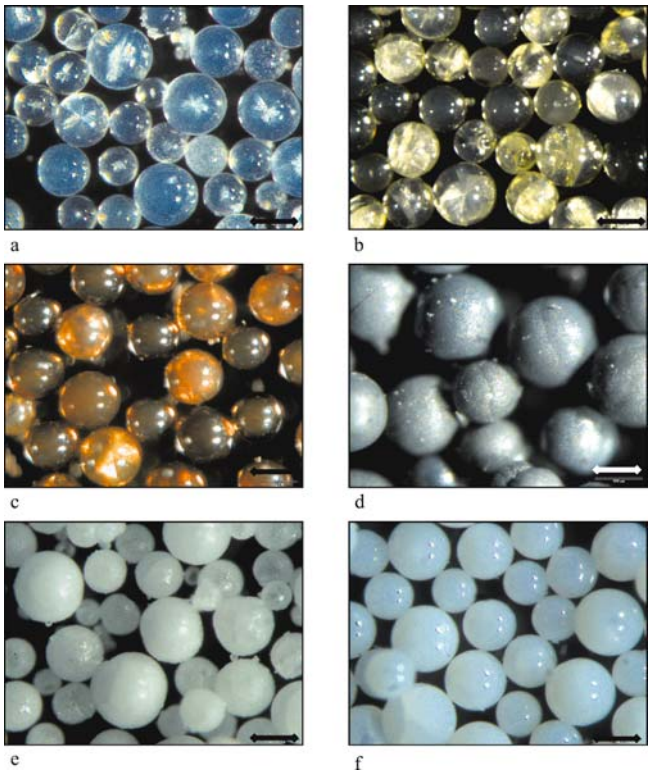

Fig. 20 Photographs of composite spheres heated to different temperatures under an optical microscope using a temperature increase of 30 °C/min. *Scale bars* in the *lower right* correspond to 100 μm: **a** room temperature, **b** 250 °C, **c** 400 °C, **d** 700 °C, **e** 1000 °C. The decomposition of the gelatine is accompanied by a color change from *translucent* over *yellow* to *red*, *black* and finally to *white*. **f** Treatment of the aggregates with boiling water for seven days leads to a loss of translucency

4.3 Chemical Composition

The analysis of the real amount of the organic component belonging to the composite system only, and the abstraction from the gelatine occluded in cavities and fissures as well as adhering to the surfaces of the individuals is far from trivial and needs a lot of detailed preparations and investigations [19]. Furthermore, the characteristic property of the inorganic constituent of the composite is the ability to replace its components by a large variety of chemically related ions [50, 51]. Thus, the composition of fluorapatite also depends on the constituents of the mother liquor during particle growth, and differs pronouncedly from the idealized formula $Ca_5(PO_4)_3F$. Additionally, the ability of the apatite structure to form vacancies complicates precise analyses.

The analytical problem under consideration in this section is a real challenge and is therefore discussed in more detail.

Figure 21 visualizes the Ca/P ratio of fluorapatite-composites grown at different pH-values of the starting gel. The results indicate that the calcium deficiency of the inorganic component of the composite is clearly dependent on the acidity of the starting gel. The calcium deficiency of fluorapatite (FAP) grown at low starting pH-values (pH 2: Ca/P = 1.53(2), idealized FAP: Ca/P = 1.67) is paralleled by the replacement of phosphate by hydrogenphosphate to keep the charge balance of the inorganic phase. The presence of the protonated species HPO_4^{2-} can be evidenced by infrared spectroscopic investigations. As-grown composite samples show a band at 865 cm^{-1} in their absorption spectra (Fig. 22) that is attributed to the P – OH stretching vibration υ_5 [52].

Within the accuracy limits of the fluoride determination by means of an ion-sensitive electrode, the content of 3.7(1) wt. % does not evidence a partial substitution of fluoride by hydroxide in the fluorapatite-gelatine composites (idealized FAP: 3.8 wt. %). Thus, infrared spectroscopy was used as a more sensitive method to detect small amounts of OH^-. The infrared spectrum of the as-grown composite shows a weak band at approximately 3570 cm^{-1} which is attributed to the OH^--stretching vibration (Fig. 22) [52, 53]. However, this assignment is precarious since in the same frequency range a broad and intense absorption band of water is observed. In order to reduce this background peak the composite was dried by heating the samples to 600 °C.

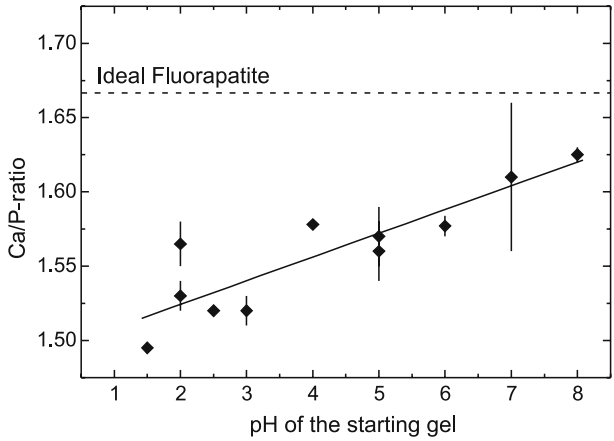

Fig. 21 Ca : P-ratio of composite particles grown at different pH-values of the starting gel. The *solid line* corresponds to a least squares fit of a linear function to the experimental data. The data clearly indicate a linear correlation between calcium deficiency of the inorganic composite component and the acidity of the gel. Each data symbol represents the average value of three determinations. *Error bars* are shown as *vertical lines* if larger than the size of the symbol. The *dashed line* indicates the calculated value for ideal fluorapatite

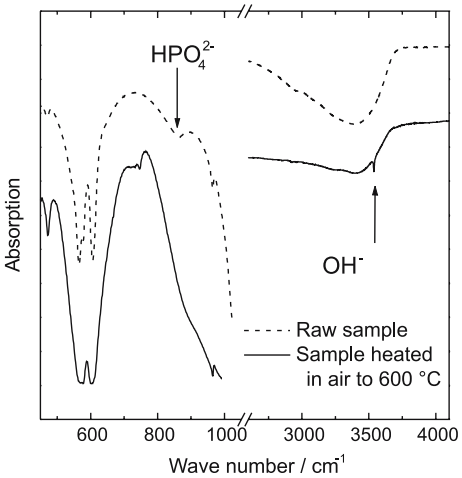

Fig. 22 IR-spectra of composite aggregates before and after drying at 600 °C. The weak band at 3570 cm^{-1} is attributed to the OH^--stretching mode and becomes clearly visible only after water has been removed from the sample. The band at 865 cm^{-1} is attributed to the HPO_4^{2-}-stretching mode and disappears after the heating procedure. See [52, 53] for assignment of the bands

The remaining weak, but sharp band with a full width at half maximum (FWHM) of 7(2) cm^{-1} is taken as an indication of the presence of a small amount of hydroxide ions (less than 10% of the fluoride ions are replaced) in the fluorapatite. Freud et al. [53] reported the appearance of a sharp OH-stretching band at 3540 cm^{-1} (FWHM: 9 cm^{-1}) for an inorganic apatite with 5% of F^- replaced by OH^--ions. Samples with 25% of F^- replaced by OH^- showed a peak with a FWHM of about 30 cm^{-1}.

Summing up the results of the different analyses, the composition of the inorganic component of the composite corresponds to $Ca_{5-x/2}(PO_4)_{3-x}(HPO_4)_x(F_{1-y}(OH)_y)$, $x = 0.82$, $0 < y \leq 0.1$, if it is assumed that the positions of ions with a single negative charge are fully occupied by fluoride or hydroxide and that the calcium deficit is completely compensated by a replacement of PO_4^{3-} with HPO_4^{2-} to maintain the charge balance.

Next, the carbon content of pure and dried gelatine was determined experimentally to correspond to 44 wt. % [19]. On the basis of this value, the typically found carbon content of 1.0(1) wt. % in the case of the composite samples corresponds to 2.3 wt. % gelatine. In order to specify whether the organic component is distributed homogeneously in the composites, spheres with a diameter between 140 μm and 200 μm were ground carefully and sorted by size by means of sieving. Aiming to remove the fraction of gelatine which is not tightly embedded in the inorganic component, these samples were washed three times for 30 min with water heated to three selected temperatures. Figure 23 shows the carbon content for different particle sizes after

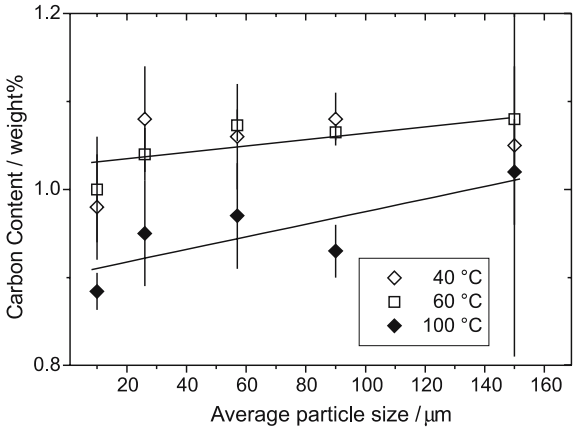

Fig. 23 Carbon content of the composite particles mechanically mortared to different particle sizes and treated with an excess of water at three selected temperatures. Each data symbol represents the average value of three determinations. *Error bars* are shown as *vertical lines* if larger than the size of the symbol. Inclined *solid lines* show the results of least *squares* fits of linear functions to the experimental data. Samples heated to 40 °C and 60 °C both show an increase of the carbon content of about 10% with ascending particle size. The samples treated at 100 °C exhibit a steeper increase at absolute values which are approximately 20% smaller indicating that most of the organic molecules are shielded within the inorganic component. *Solid lines* correspond to least squares fits of linear functions to the experimental data

repeated washing. The results of least square fits to the experimental data show that the slopes and axes intercepts for samples treated at 40 °C and 60 °C are identical within the limits of error indicating that the carbon content of both sample series decreases by about 10% with descending particle size. The samples washed at 100 °C exhibit a steeper decrease at absolute values which are approximately 20% smaller. The data indicate that only a small fraction of the gelatine is removed by reducing the particle size mechanically to approximately 10 μm and treating the samples with hot water for 1.5 hours. However, the storing of unmilled composite particles in boiling water for seven days decreases the carbon content to 0.37(3) wt. %. This finding indicates that the loss of gelatine is also kinetically controlled and probably affected by particle-reorganization (Ostwald-ripening). Grinding of a sample in an agate ball mill down to particle sizes of about 60 nm causes a similar reduction of the carbon content [carbon analysis: 0.35(5) wt. %] after a treatment with boiling water for two days. Thus, a significant part of the organic component is shielded within composite particles realizing grain sizes smaller than 60 nm.

Several attempts were undertaken to free the particles from the organic component without destroying the architecture of the inorganic phase. A repeated treatment with H_2O_2 dissolves only gelatine in the border area of the particles but the content of incorporated protein molecules is only reduced to

about 75% of the value determined for water-cleaned particles. Treating the composites for a week with water heated to 95 °C leads to a beclouding and color change to milky white (Fig. 20f) while the carbon content is reduced to 0.37(3) wt. %. Similar to the boiling process which induces a partial loss of the protein and therefore a clouding of the particles, a treatment with aqueous NaOCl solution can reduce the carbon content down to 0.20(5) wt. %. To interpret the observation that the organic component is not removed completely it is assumed that the residual part of the organic material is protected against oxidation inside apatite-rich composite particles. A similar phenomenon is known for sea urchin spines where skeleton macromolecules are occluded inside magnesium-bearing calcite crystals [54, 55].

As a summary, the average composition of fluorapatite-gelatine composites grown in aqueous gels with about 10 wt. % gelatine, a starting pH between 2 and 5 using a molar ratio of the educt solutions corresponding to $Ca : P\ (PO_4^{3-}/HPO_4^{2-}) : F = 5 : 5 : 1$ with the diffusion process continuing three weeks is given by:

$$Ca_{5-x/2}(PO_4)_{3-x}(HPO_4)_x(F_{1-y}(OH)_y) \cdot 2.3(3)\ \text{wt. \% gelatine}$$
$$x = 0.82, \quad 0 < y \leq 0.1\ .$$

The chemical composition of the composite should also be reflected in its density. The calculated density of the inorganic component corresponds to 2.98 g/cm^3 using the experimentally determined lattice parameters (Table 1) and the average chemical composition of the fluorapatite-gelatine composites according to the formula given above with $x = 0.82$ and $y = 0$. Because of the calcium-deficiency and the change of lattice parameters compared to pure fluorapatite this value is smaller than the density of pure mineral FAP which is calculated to correspond to 3.20 g/cm^3 using the lattice constants $a = 936.7(1)$ pm and $c = 688.4(1)$ pm [44], and an assumed ideal composition. The expected value for a composite composed of 95 wt. % calcium-deficient fluorapatite and 5 wt. % aqueous gelatine, with the density for water and gelatine being estimated to be equal to 1.0 g/cm^3, is 0.95×2.98 g/cm^3 + 0.05×1 g/cm^3 = 2.88 g/cm^3. A sample that contains spheres with diameters ranging from 140 μm to 200 μm yields a value of 2.78(1) g/cm^3 using a He-gas-pycnometer. Taking into account the necessary approximations to calculate a theoretical density and considering the experimental error, both values correspond satisfactory. Oxidation of the organic component with aqueous H_2O_2 or NaOCl solution leads to an increase of the density to 2.90(1) g/cm^3 for samples with 0.5(1) wt. % gelatine (corresponding to 0.20(5) wt. % carbon). The increase in density is consistent with a loss of parts of the lightweight gelatine-fraction.

The findings indicate that the results of chemical analyses and those of the density determinations are consistent. Moreover, the values found for composite aggregates are in good agreement with estimations on the basis of the

analytically determined gelatine (carbon) content assuming that the density of the polypeptides remains constant when incorporated into the composite. Accordingly, samples with a reduced gelatine content show an increase in density.

4.4 Decalcification

During treatment of nanocomposite spheres with EDTA (0.25 N, pH = 7) the first observation is that they lose their opalescence and turn pale white. The second and even more interesting observation is that in case of core/shell assemblies (Sect. 3.3) dissolution starts within the core and spreads out to the shell, thereby running through continuous stages of apatite hollow-spheres filled with residual gelatine [17, 18]. This situation is shown in Fig. 24, which represents hollow hemispheres broken from spheres at different stages of dissolution. In the first stage of the dissolution process the seed within the core is only weakly affected; the later generations of the fractal core are obviously

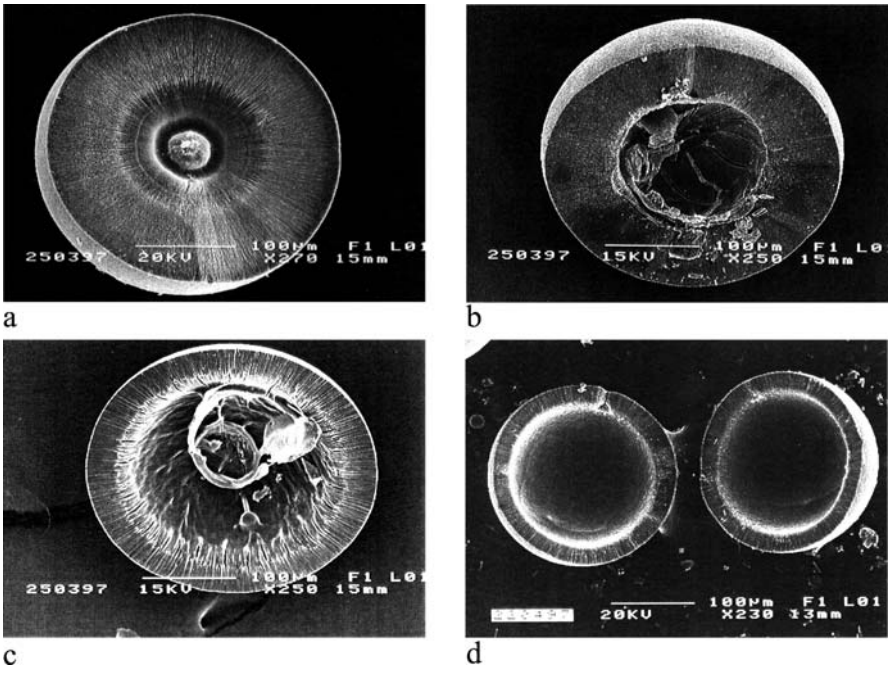

Fig. 24 Dissolution of nanocomposite core/shell assemblies in EDTA as a solvent; SEM images of hollow hemispheres broken from spheres after treatment with EDTA for 24 h (**a**), 48 h (**b**), 72 h (**c**) and 96 h (**d**); picture **d** represents the two hollow hemispheres of the same individual; due to shrinking effects during the preparation for SEM investigations (drying) the residual gelatine inside the core loses its original (biomimetic) structure

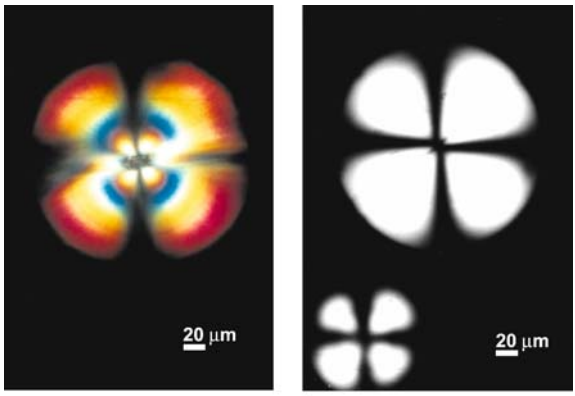

Fig. 25 Light microscopic image of a typical **a** synthesized fluorapatite-gelatine nanocomposite sphere and **b** a completely decalcified gelatine residue of 125 μm diameter using a polarization microscope (crossed polarizers)

dissolved first (a). After the core has been completely dissolved the attack of the solvent extends to the shell structure and the dissolution progresses leading to a decrease of the wall thickness and an increase of the cavity area (b–d). Finally, the complete sphere is dissolved and an exact copy of the original morphology remains in the form of the gelatine residue (a jellyfish-like sphere).

The gelatine residues show basically the same anisotropic optical behavior (Brewster cross) as primary composites (Fig. 25a), with the only difference being the lack of interference colors in the case of the gelatine sphere (b) due to the loss of the inorganic material. As a conclusion, already this observation of similar optical properties can be taken as an indication that there is an interdependence of the orientation of the apatite nanoparticles and the alignment of the polypeptide molecules in the composite.

The early stages of the dissolution process of the composite core/shell assemblies show close similarities to the early effects of caries [56]. Details concerning this relationship will be discussed in Sect. 8.

5
The Virgin Composite Seed (Fractal Series)

The content of this section is focussed on the inner architecture and real structure of the central fluorapatite-gelatine nanocomposite seed which already has the potential for subsequent fractal morphogenesis. In order to classify a seed as a *virgin* specimen its morphology should be characterized by a perfect hexagonal-prismatic habit without any indication for additional

face-steps. In the case that additional face steps are indicated, the seed already develops a state of higher inner hierarchy and is then called a *mature* seed, although conventional diffraction techniques (X-ray) do not show significant differences between the two states. These complex interrelations will be discussed in more detail in connection with Sects. 6 and 7.

5.1 Nano-Structuring

It has already been shown that the fracture area of a central hexagonal seed is characterized by a radial structure surrounded by more plate-like structures (Figs. 11 and 12 in Sect. 3.2). The fracture pattern observed for the composite is in sharp contrast to the glass-like fracture behavior of pure apatite crystals and is, thus, taken as an indication [19] of an ordered nanosuperstructure in the composite (Sect. 5.2). Characterization of unbranched seeds having a perfect hexagonal shape by X-ray diffraction gives sharp Bragg reflections. A crystal structure model of apatite was refined using the X-ray intensity data (Sect. 4.1). However, TEM images of a seed cut parallel to [001] show clear evidence of an ensemble of elongated nanosubunits following the principles of self-similarity i.e., in parallel to each other and with their long axes parallel to the *c*-axis of the seed (Fig. 26a). The diameters of the elongated subunits are between 10–15 nm and multiples thereof; their lengths are several hundred nanometers, or more. TEM images of ultra-thin slices of the central seed cut perpendicular to the *c*-axis show a homogenous nano-scale pattern with grain boundaries representative of a hexagonal material, and particle diameters ranging between 10–15 nm and multiples thereof (Fig. 26b).

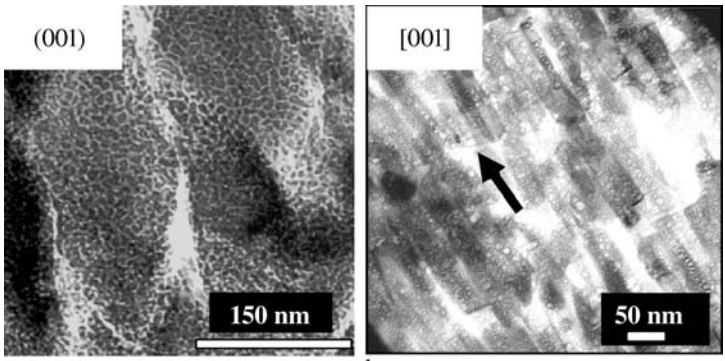

Fig. 26 Nano-structuring of the seeds of the fractal aggregates of fluorapatite-gelatine-nanocomposite. **a** TEM image of an ultra thin slice of a seed oriented parallel to [001]: the parallel arrangement of elongated subunits follows the principles of self-similarity. **b** TEM image of an ultra thin slice oriented perpendicular to [001]: the nano-structure with its grain boundaries corresponds to a hexagonal material

Together with the chemical composition of the composite (Sect. 4.3) the structural facts already given point to an inorganic–organic hybrid material which may be grown by a non-classical crystallization process (formation of so-called "mesocrystals") [57, 58]. This picture will be taken up in Sects. 5.2 and 5.3 in terms of a strongly mosaic-controlled nano-superstructure.

5.2
Real- and Superstructure

The significant and representative nano-structures in ultra-thin cuts of the seed (Sect. 5.1) are caused by the cutting procedure and represent areas of structural weaknesses within the nano-ensemble. Structural weaknesses in the composite structure may also be increased and clarified by shrinking effects during drying. Both phenomena may act in a cooperative way making it possible to clearly observe the nano-structuring of the composite in ultra-thin cuts. To avoid these effects caused by mechanical stress during the (conventional) cutting procedure the Focussed Ion Beam technique (FIB) has to be used.

High-resolution TEM micrographs of the [001] zones of the composite seed (FIB preparation) and an abiogen apatite mineral (ultramicrotome cut) were recorded. Because of the larger thickness of the FIB samples (100–200 nm) the quality of the high-resolution images of the composite seed (Fig. 27) is clearly reduced. The corresponding Fast Fourier Transform (FFT) (inset Fig. 27) shows the characteristic hexagonal pattern with reflections not

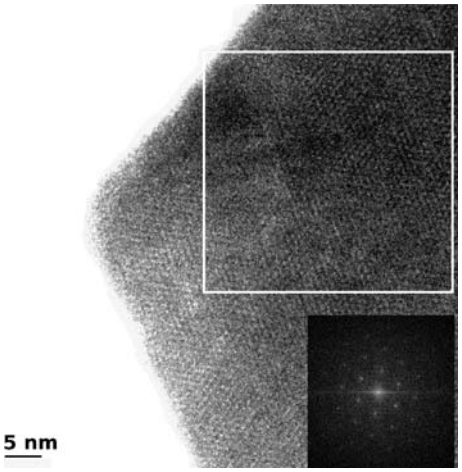

Fig. 27 High-resolution electron micrograph of a composite seed (FIB preparation) viewed along [001]. The FFT (*inset bottom right*) is characterized by hexagonal symmetry. Structural disorder of the composite (defects, mosaic structure) is indicated by diffuse reflections and by vanishing of higher order peaks

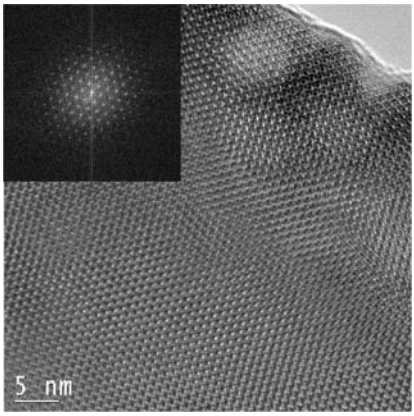

Fig. 28 High-resolution electron micrograph of an abiogen apatite mineral from Jumilla, Spain, viewed along [001]. The FFT (*inset*) is characterized by hexagonal symmetry and sharp reflections up to the 7th order

higher than to the 3rd order. The high-resolution image of the abiogen apatite mineral (Fig. 28) is of a very good quality. Because of the excellent long-range orientation of the crystal the hexagonal FFT pattern is characterized by sharp reflections up to the 7th order (inset Fig. 28).

The original shape of the composite seed is clearly preserved in the FIB sample (angle of 120° between prism-faces, Fig. 27). An overall periodic hexagonal pattern is representative of the composite structure, an observation which is consistent with the X-ray pattern of macroscopic seed specimens which consists of sharp Bragg reflections (Sect. 4.1, Fig. 17a).

In order to identify defects, dislocations or other peculiarities of the real structure of the composite seed a filtered and enhanced image of the white frame area of Fig. 27 was generated (Fig. 29). The main interest was focused on areas which may be affected (controlled) by the organic component

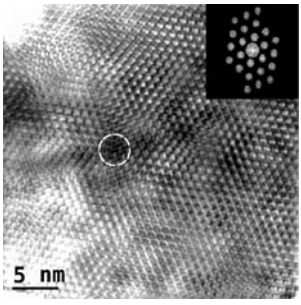

Fig. 29 Filtered and enhanced view of the white frame area of Fig. 27. The *inset* represents the mask used for the filter process (reflections observed). The overall hexagonal pattern is significantly broken inside the area of the *white circle*. For further details see text

of the composite which is assumed to take part in the composite seed as triple-helical macromolecules. A general structural correlation of the organic and inorganic components was already indicated by TEM images of Pt/C replicas of freeze-fractured shock-frozen and partially decalcified composite samples [18], where a parallel orientation of the long (hexagonal) axes of fluorapatite and the long axis of polypeptide fibers was observed (Fig. 30). Applied to the present investigation, the orientation of the macromolecules is assumed to be parallel to [001] of the composite seed and only their cross-sections should affect the TEM images which in the case of single triple-helical molecules means areas of about 1.5 nm in diameter.

Besides shagreen-like contrasts a clear structural defect in the overall hexagonal pattern of Fig. 29 is marked by the white circle with a diameter of 3.3 nm. The central area of the circle is assumed to consist of a calcified triple-helical macromolecule (cross-section) acting as a nucleation center for the surrounding apatite and supplying the motif of the apatite crystal structure extending around the area of nucleation. This situation is sketched and visualized in Fig. 31 with the (colored) dots representing the roughly hexagonal arrangement being directly taken from the bright-spot pattern of the filtered TEM image of Fig. 29. The blue, red, and green domains do not match perfectly and are characterized together by a significant mosaic structure. At the outer borders the defects are already healed which is indicated by the black hexagonal pattern matching the red and the green domains. Although the grey pattern inside the (yellow) nucleation area is taken as a 1 : 1 image from Fig. 29 it should not be discussed here.

At mesoscopic magnification preferred orientations (consistent with the hexagonal symmetry) in the TEM images of cross sections of the composite seeds become visible by careful tilting (6–8°) from the [001] orientation

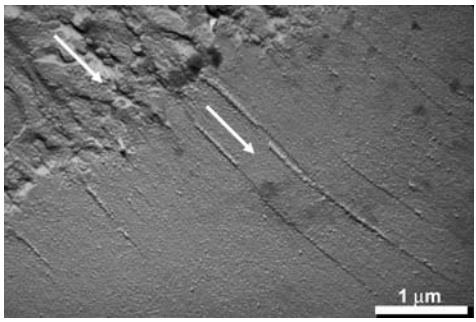

Fig. 30 TEM-image of a Pt/C-replica of a freeze-fractured shock-frozen particle: Decalcified composite sphere in the borderline region of partly and completely decalcified areas (Sect. 4.4). *Top left*: Apatite replica, *bottom right*: replica of the gelatinous residue. The fiber-like structures discernible in the completely decalcified region are attributed to gelatin skins consisting of condensed fibrils. The direction of the hexagonal axis of the inorganic component is indicated by *arrows*

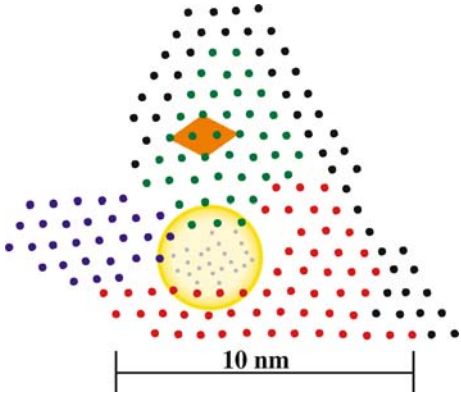

Fig. 31 Sketch [(001) plane] of the structural model of the apatite mosaic structure initiated by a calcified triple-helical macromolecule (*yellow area*) and extending around this center. *Red*, *blue* and *green* periodic domains do not match perfectly. The roughly hexagonal arrangement of (*colored*) *dots* is directly taken from the bright-spot pattern of Fig. 29. One apatite unit cell is given by the *orange area*. For further details see text

and by applying a defocus of about 1.4 μm [20, 23]. The FFT of such TEM micrographs is characterized by (100) reflections of apatite and diffuse streaks around the primary beam with a periodicity of about 5 nm and multiples of this value (Fig. 32). In order to exclude the possibility that the superstructure streaks of the composite being simply generated by any apatite lattice just by tilting from [001] and applying a defocus TEM investigations were performed on an abiogen apatite mineral [20]. There is no hint for preferred structure formation in the bright-field image and the FFT does not show additional (diffuse) reflections besides (100).

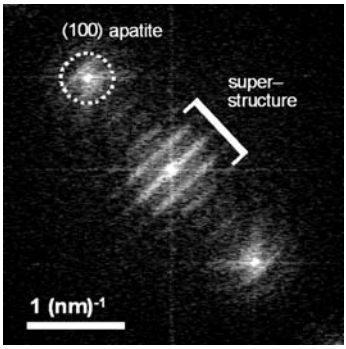

Fig. 32 Superstructure of the central composite seed caused by mineralized gelatine triple-helices observed in the FFT of TEM high-resolution micrographs as diffuse streaks around the primary beam with a periodicity of about 5 nm and multiples of this value. For further details see text

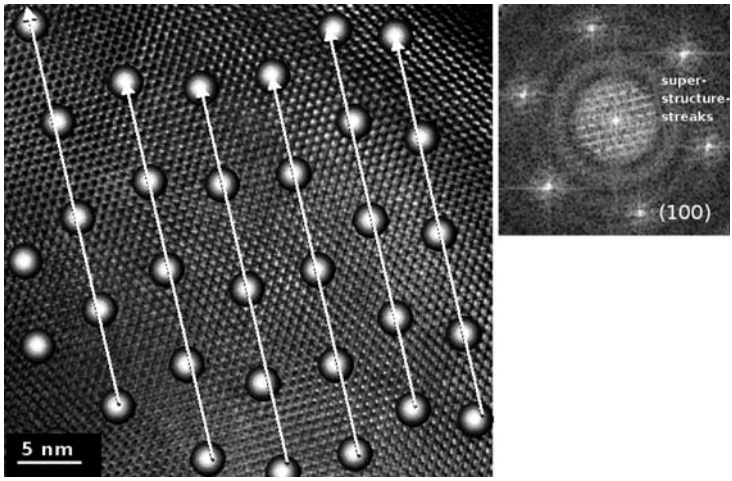

Fig. 33 Simulation of superstructure streaks in the FFT along [001] (*top right*) by a superstructure model (*left*) based on a matrix of the hexagonal pattern of abiogen apatite (Fig. 28) superimposed by a random array of linear sphere chains with 10 nm periodicity, 3 nm in diameter and an overall parallel orientation of randomly arranged chains [20]. For further details see text

As can be seen from Fig. 33 superstructure streaks in the FFT together with reflections (100) along [001] are simulated by a matrix of the hexagonal pattern of abiogen apatite superimposed by a random array of spheres (chains with 10 nm periodicity and an overall parallel orientation). The spheres (better to say: circles) are chosen with a diameter of 3 nm representing little more than the nucleation area containing the macromolecule (Figs. 29 and 31). The shading of the circles simulates the transition from the mosaic structure to the regular model. Although this simplified model is only a first approach to the nature of the composite seed the result of the FFT simulation is not far from reality. On the other hand, the area of the unaffected "apatite matrix" seems to be over represented. This is only one point which should be taken into consideration in future simulations.

5.3
Complex Inner Architecture (Summary, Sketch)

The entirety of the experimental observations (Sects. 3.2, 4.1, 5.1 and 5.2) concerning the virgin composite seed is consistent with a scenario presented schematically in Fig. 34 which gives an impression of the inner architecture of the seeds as consisting of a parallel rod-stacking of elongated nano-composite units oriented with their long axes parallel to [001]. The structural arrangement of the ribbons of hexagons (red in Fig. 34, top middle) is consistent

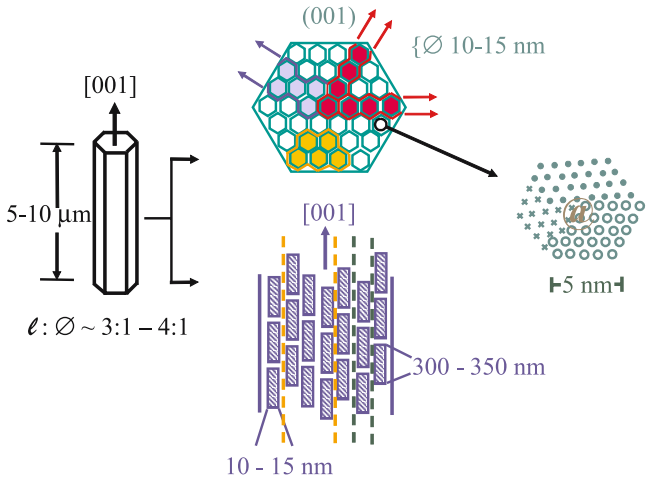

Fig. 34 Sketch representing and summarizing the experimental observations of the structure and inner architecture of the fluorapatite-gelatine nanocomposite seeds. Concordance: (*left*) elongated hexagonal-prismatic habit of the seed (Figs. 6, 9–11, 17 *top left*); (*middle bottom*) parallel rod stacking of self-similar elongated nano-subunits along [001] as well as "accidental" variations in rod-clustering caused by the cutting procedure (Fig. 26a); (*middle top*) nano-structure in (001) with grain boundaries representative for a hexagonal material as well as variations in "accidental" clustering caused by the cutting procedure (Fig. 26b); (*middle top* and *bottom*) fracture patterns of the seed characterized by a radial structure with tendencies to plate-like orientation (Fig. 12); (*right*) nano-mosaic structure nucleated by a central gelatine macromolecule (Figs. 29, 31)

with the high-resolution TEM investigations as well as with the observation of a diffuse superstructure with a spacing of about 5 nm and multiples of this value. The caption of Fig. 34 gives more detailed information concerning interpretation and concordance with experimental data.

6
Ion-Impregnation (Pre-Structuring) of the Gelatine-Gel

The two types of morphogeneses (fan-like and fractal; Sect. 3.1) exhibit a close correlation to the local areas of composite formation within the gelatine-gel plug (C-, M- and P-bands, respectively; Fig. 2 in Sect. 2). Because of this, it appeared to be reasonable to assume that this phenomenon is related to pre-structuring effects of the gelatine gels prior to the composite formation in the double diffusion cells [24]. In this picture the different growth mechanisms depend on whether the gelatine gels are impregnated with calcium or phosphate ions, first.

6.1
Stiffness against Flexibility

Recent AFM investigations into the formation of micro-cracks in bone and the corresponding healing processes as well as observations concerning the stress-strain behavior of collagen revealed that the presence of calcium ions accounts for stiffening of the organic matrix [59–61]. This effect was postulated to originate from the formation of ionic bonding between the calcium ions and charged groups of the collagen molecules. As a clear evidence for this assumption is yet missing, we decided to further elucidate this question during our studies in the biomimetic morphogenesis of the fluorapatite-gelatine composites in the C-bands which are located close to the calcium ion source.

The two different types of morphogeneses have already been described in Sect. 3.1 in detail (Fig. 10), and it was also pointed out that the fan-like series may be characterized in "crystallographic" (straight, hard) terms, which should be reflected in the inner composite architecture. In fact, TEM investigations (Fig. 35) indicate stiffness and rigidity of the organic component of the composite. The gelatine fibrils run as straight lines without orientational changes through the composite individuals. Inside each individual the fibrils

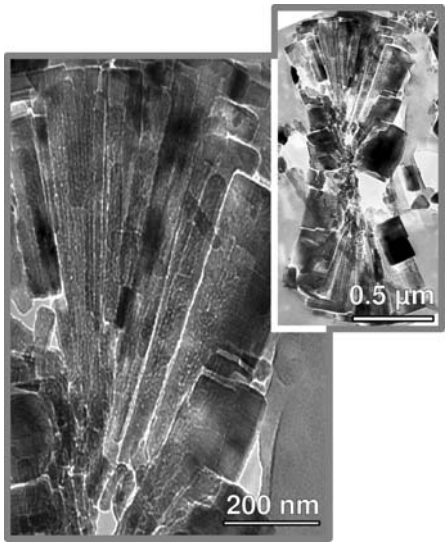

Fig. 35 TEM images of a fluorapatite-gelatine nanocomposite individual exhibiting first states of branching in the fan-like growth series (state 2 in Fig. 10, *left-hand side*). Cuts prepared by ultramicrotomy. *Inset*: Overview of the fan-like grown individual. *Main picture*: Enlarged section of an aggregate of wedge-like individuals. The *dotted straight* structures with a small opening angle are the (calcified) organic component of the composite (gelatine)

seem to start from a single common origin and are arranged in a fan-like manner exhibiting only small opening angles. Details of this kind of growth mechanism are as yet unknown as detailed analyses of the structure of the central intergrowth-plane (arrows in Fig. 10, Sect. 3.1) are missing. To date, merely a pronounced radial structure of the intergrowth-plane was identified similar to the pattern found in the fracture area of a seed from the fractal growth series (Fig. 12 in Sect. 3.2).

In contrast to the fan-like series the fractal growth series can be well characterized in "biological" (bent, soft) terms. SEM investigations related to the fractal series have already shown (Fig. 12 in Sect. 3.2) that the origin of the development of the new generation lies deep inside a growing seed, even if the outer shape of the individual reveals only weak indications for the start of "splitting" (state 2 in Fig. 10; Sect. 3.1). It became clear from these observations that for the fractal series "splitting" is better described as an outgrowth-phenomenon (instead of "upgrowth") which is clearly seen in Fig. 36 (top right). The "native" seed area (state 1 in Fig. 10) is smaller than the central area highlighted by dotted borderlines (Fig. 36, top right) and the developing new generations come out of the core region like a blossom. These bent patterns are correlated with the orientation of gelatine fibers which seem to mark the boundaries of the development of the "new" individuals.

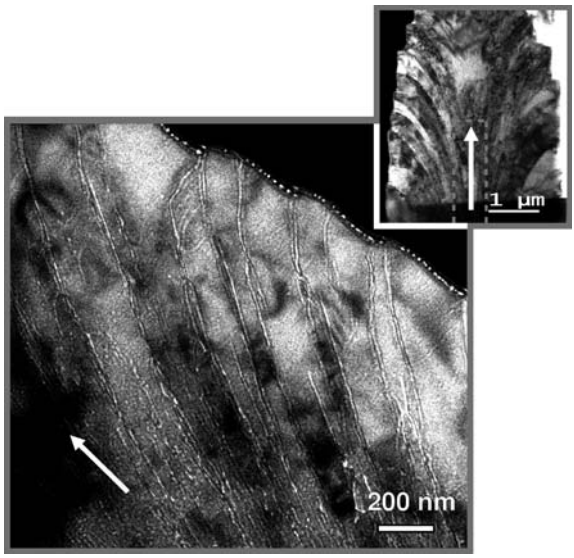

Fig. 36 TEM images of a fluorapatite-gelatine nanocomposite exhibiting first tendencies for branching in the fractal growth series (growth state 2 in Fig. 10, *right-hand side*). Cuts prepared by focused ion beam (FIB). *White arrows* indicate the direction of the hexagonal *c* axis of the central prismatic seed. *Inset*: Overview of one half of a prismatic seed with blossom-like development of a new generation. *Main picture*: Gelatine fibrils with bent structures along the growth directions of the new developing generation

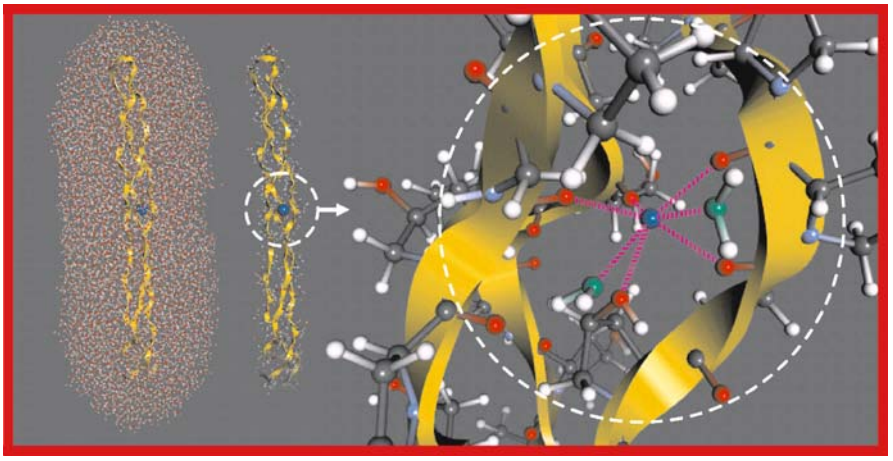

Fig. 37 *Left*: Model of a triple-helical polypeptide including a solvent shell (about 5000 water molecules) of 1.2 nm minimum thickness together with one attached (included) calcium ion. *Yellow* ribbons represent the backbones of the three peptide strands of the protein fiber. *Middle*: Same model without solvent molecules. *Right*: Focus on the binding site. Calcium forms ionic bonds (*purple dashed lines*) to carbonyle oxygen atoms of the protein ($d_{Ca\cdot\cdot O} \approx 2.3$ Å). Further ionic interactions involve oxygen atoms (*highlighted in green*) of neighboring water molecules ($d_{Ca\cdot\cdot O} \approx 2.7$ Å). (H: *white*, O: *red*, C: *grey*, N: *light blue*, Ca: *dark blue*)

Atomistic computer simulations were performed [24] in order to explore interactions of aqueous solutions of calcium- or phosphate-ions with a collagen molecule as well as possible conformational effects on the triple-helical protein. The fiber proteins were described by an all-atom model of three $(Gly\text{-}Pro\text{-}Hyp)_{12}$ polypeptide strands and empirical potential energy functions were used to model the interactions of the triple-helix with the water molecules and the ions [62, 63]. Using a recently developed algorithm for the identification of adsorption sites [64, 65] a series of 100 independent aggregation experiments was performed for each ionic species. From this a small number of characteristic binding positions could be isolated. The latter were found to dramatically depend on the associated ion species. The calcium ions form ionic bonds to the oxygen atoms of the carbonyle groups of the polypeptide backbone and to the side-chains of proline and hydroxyproline (Fig. 37). Although calcium association may cause the opening of some of the hydrogen bonds interconnecting the peptide strands of the triple-helix, only a marginal effect on the overall fiber structure is observed which causes only small configurational changes of very local nature. For the phosphate ions a completely different picture is observed. In contrast to the calcium ions, the phosphate ions are preferentially associated laterally. This process involves the formation of two to three hydrogen bonds with hydroxyproline side-groups and partially also with amino groups. In the case of phosphate binding by only a few

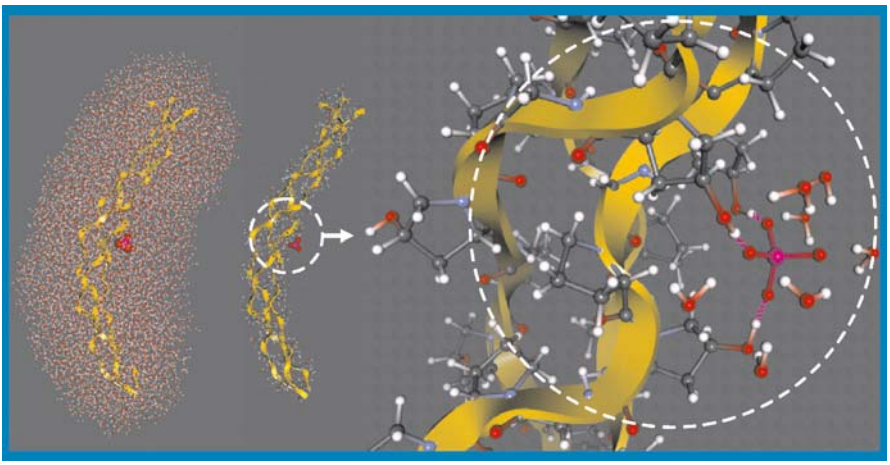

Fig. 38 Same as Fig. 37, but illustrating the association of a phosphate ion. For better orientation only the hydrogen bonds of the phosphate ion to the protein fiber ($d_{O\cdot\cdot H} \approx 1.3$ Å) are depicted (*purple lines*). Though three hydroxyproline–phosphate bonds are formed, only two strands of the triple-helix are involved. This imbalance causes tensile stress to the right side of the fiber, while the left side is less affected. As a consequence, the previously straight polypeptide is bent. (H: *white*, O: *red*, C: *grey*, N: *light blue*, P: *purple*)

hydrogen bonds the fiber structure usually remains unaffected. However, in about 50% of the simulation runs phosphate aggregation caused heavy deformations of the polypeptide. Such a situation is illustrated for PO_4^{3-} ion association in Fig. 38. The protein fiber exhibits a bent structure which originates from the local formation of three hydrogen bonds to the phosphate ion. Such tendencies for bending the polypeptide are also observed for HPO_4^{2-} ion aggregation.

The electrostatic repulsion of the incorporated calcium ions favors a straight arrangement of the fiber protein in which the binding sites are at maximum separation. The triple-helix hence experiences a stiffening effect. In the P bands an analogous tendency results from the Coulomb repulsion of the phosphate ions associated to the protein fiber. However, this effect competes with the local bending situation originating from the lateral take up of the phosphate group (Fig. 38). This combination of phenomena with opposite effects is expected to considerably increase the conformational complexity of the triple helices and implies a large number of favorable structures of protein fibers impregnated with phosphate ions which may account for an enhanced flexibility and bent structures of the (calcified) organic component of the composite (Fig. 36).

The results of the molecular dynamics simulations fully support the experimental observations for the fan-like and the fractal morphogeneses. The form development of the fluorapatite-gelatine composites is controlled by

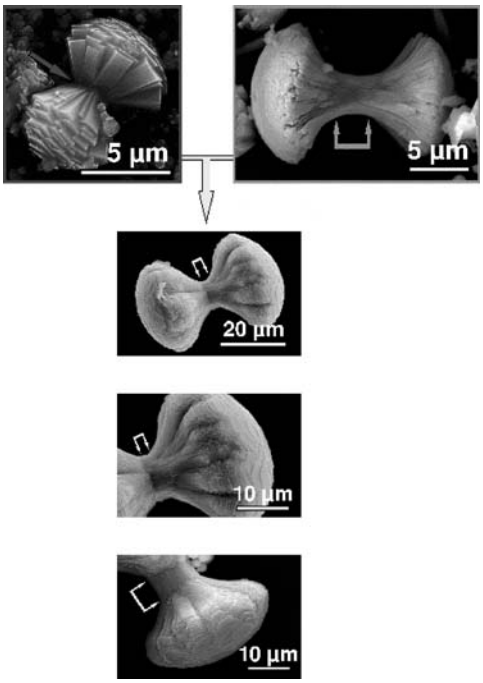

Fig. 39 SEM images of fluorapatite-gelatine composites in dumb-bell morphology (states 3 in Fig. 10). Aggregates formed via the fan-like (*top left*) and the fractal (*top right*) growth mechanism, respectively. The *vertical* series represents transitional growth states, resulting from a mixture of both archetypes in various dumb-bell developments and surface tilings. The *arrows* indicate the intergrowth plane and the free bridges, respectively

both, the self-organized growth of the inorganic (nanoapatite)/organic (gelatine) composite and the structural pretreatment of gelatine by ion impregnation. As the latter takes a decisive role, it may involve two competing effects resulting in various intermediate forms as illustrated in Fig. 39. Such aggregates are preferentially found in the M-bands and depend on the growth state and the local supply of ions (the migration of calcium ions into the gelatine gels is faster compared with the phosphate ions).

6.2
The Effect on Form Development (Mature Seed and Hierarchy, Fractal Series)

The initial stages of the fractal growth series comprise micrometer-sized hexagonal-prismatic seeds (central three individuals in Fig. 40) which develop in subsequent growth stages via dumbbells to closed spheres with an equatorial groove (Sect. 3).

The nano-structured inner architecture of a virgin seed was discussed in Sect. 5 and is characterized by a parallel arrangement of self-similar

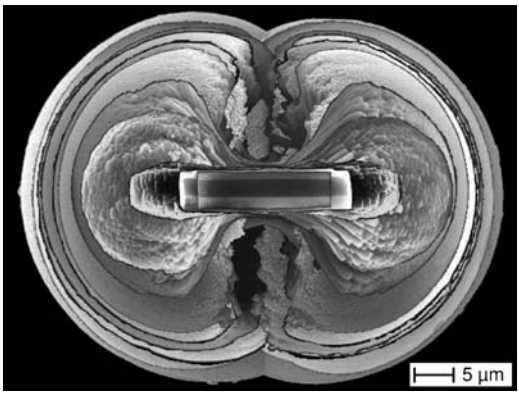

Fig. 40 Superposition of growth stages of fractal fluorapatite-gelatine nanocomposite aggregates (scanning electron microscopy images). The morphogenesis starts with an elongated hexagonal prismatic seed (virgin seed, see Sect. 5) which develops via outgrowth areas at both ends (*central third individual*, mature seed, see Fig. 41)

hexagonal-prismatic nano-rods of a highly mosaic controlled nano-apatite collective nucleated at central triple-helical gelatine macromolecules. A mature composite seed showing evidence for the start of "splitting" is presented in Fig. 41. The individual is still characterized by central prism faces giving the impression that the initial faces of the virgin seed are still present without significant changes.

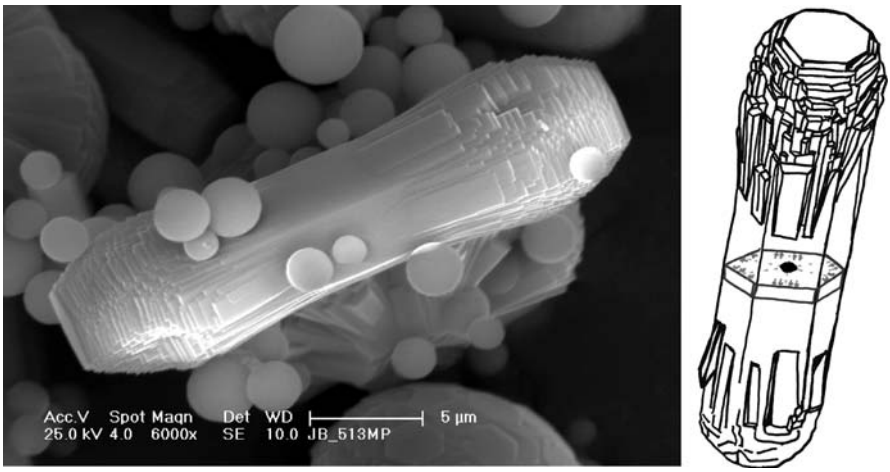

Fig. 41 SEM image of a mature seed with clear indications for the start of "splitting" by development of face steps on the prism faces near the basal planes (*left*). Schematic 3D representation of the mature seed with the central slice indicating the region of the virgin seed being restricted to the *central black spot area* only (*right*); see also Fig. 12 in Sect. 3.2

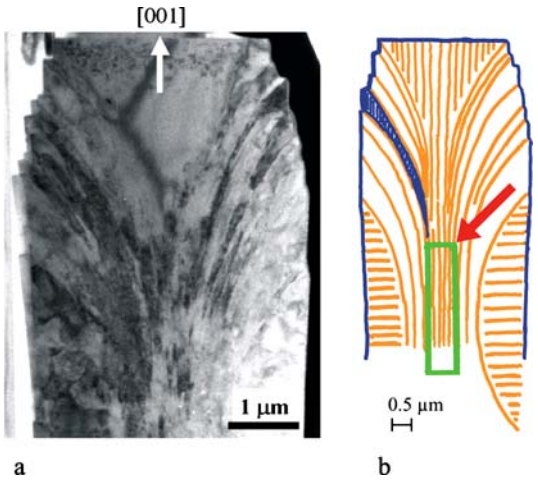

Fig. 42 **a** TEM overview image of part, (ca. one half) of a "nearly splitting" seed; cut parallel [001] (*white arrow*). The outgrowth-area for the next (the 1st) generation is clearly indicated by the contour-steps on the prism-faces near the basal plane. **b** Schematic representation of **a** showing the hierarchical arrangement of gelatine triple-helices and fibrils (*orange*) within a mature seed specimen before "real splitting". Virgin seed: *green bordered area*. At the corners of the virgin seed branching is in preparation. The area with highest tendency for branching effects is marked with a *red arrow*. For further details concerning the preparation of branching see Sect. 7.1

This assumption is only true for the three-dimensional arrangement of the nano-apatite collective but not for the organic component, which in the case of the fractal growth series with the more or less flexible gelatine arrangements (pre-impregnation by phosphate) develops to clearly bent structures inside a mature seed (Fig. 36). Figure 42a shows a TEM overview image of part (ca. one half) of a mature seed cut parallel to [001] already indicating the outgrowth-area for the next generation by the contour-steps on the prism faces close to the basal plane. This morphogenetic state is best described as a state that prepares for the outgrowth of the following generation. At this point a next and higher level of hierarchy occurs by oriented bundling of gelatine macromolecules and formation of microfibrils which stretch out of the volume with bent cone-like patterns. The total complexity of this new hierarchical pattern formed by the organic component around the central virgin seed is schematically presented in Fig. 42b and needs detailed future investigations for deeper understanding of the self-organization processes. It seems, however, to be clear at present that intrinsic electric fields and their development during composite morphogenesis play a decisive role and assume control of the morphogenetic steps (Sect. 7).

7
Electrical Fields (Fractal Series)

As early as in 1999, a possible influence of intrinsic electric fields on the fractal morphogenesis of fluorapatite-gelatine nanocomposite aggregates was discussed [17]. Model calculations of the electric fields around simulated (schematic) seed- and dumbbell-states were carried out, whereas detailed knowledge of the inner structure of these growth stages was not available at that time. On the other hand, the overall growth-orientation inside the fractal composite spheres (Sect. 3.2) was already seen to be closely related to the orientation of electric field lines around a permanent dipole (Fig. 14). The influence of electric fields on other relevant biological systems could be also proved. In 1996, Yamashita et al. demonstrated that the growth rate of bone-like layers can be affected by surface polarization of hydroxyapatite (HAp) or ferroelectric $BaTiO_3$ substrates by an applied external electric field [66]. This observation has a large impact for bone implantation because there is lively interest to induce apatite mineralization on synthetic substrates and to stimulate bone adhesion on the implant [67]. Also, the piezoelectric effect of bone was used by applying external electric fields in order to improve the bone healing processes. Inside bone and tendon, collagen fibrils are arranged parallel to their long axes. The triple-helical molecules exhibit point group 3 and can be both piezo- and pyroelectric. The generation of electric fields caused by mechanical stress is attributed to the piezoelectric effect of collagen, whereas pyroelectricity proved to be low [68]. Fluorapatite features the centrosymmetric crystal class 6/m, therefore neither piezo- nor pyroelectricity can be considered. However, Yamashita et al. showed that in the case of hydroxyapatite, polarizability is evoked by a reorientation of the dipole moments of the OH^- ions within the structural channels. In this way, accelerated crystal growth was observed on polarized HAp surfaces [66].

Recently, single-molecule manipulation by means of scanning tunneling microscopy on biopolymers was reported by using electrical fields and conductivity switching. The helical structure and molecule length of a peptide bundle could be varied by application of an external field, the variation arose through the interaction of the field with the large dipole moment of the helix [69].

7.1
Intrinsic Dipole Fields

The observations summarized in Sect. 7 together with the experimental data on fluorapatite-gelatine nanocomposites presented in Sects. 2–6 provided the basis for more detailed investigation into the influence of intrinsic electric fields on the morphogenesis and morphology of these aggregates [25]. The efforts were focussed on the virgin composite seed (Fig. 40, central hexagonal prism), since it represents the initial and thus the fundamental growth step

during the morphogenesis. The nanocomposite seed itself already consists of a self-similar and hierarchical inner nano-structure described in Sect. 5: Actual TEM investigations show, that mineralized triple-helices form a 3D-framework and that these protein macromolecules within the composite seed are in parallel orientation with the long axis of the composite seed which is the crystallographic *c*-axis of the highly mosaic-controlled apatite specimen. Assuming that the triple-helices exhibit opposite charges at their ends, and by adding up all these microscopic dipoles a macroscopic electric dipole of the composite system is formed. This could have an important or even a decisive influence on further growth steps and thus on the fractal morphogenesis.

Electron holography was chosen in order to image the electric fields around a virgin seed. This method allows to record both phase and amplitude of the image wave. The phase holds information which is lost in the amplitude images (corresponding to conventional images). The electrical potential distribution integrated along the beam direction produces a phase shift of the incident electron wave that is registered by means of an interferogram. Thus, electron holography offers the unique opportunity to visualize, for example, electric or magnetic micro- and nanofields [70, 71].

In Fig. 43a, a conventional TEM micrograph of a hexagonal prismatic seed with the typical aspect ratio close to 3 : 1 is shown. Only the silhouette of the seed is visible, whereas the phase image (eight-times boosted) clearly shows the electric potential distribution around the seed (Fig. 43b). The observed

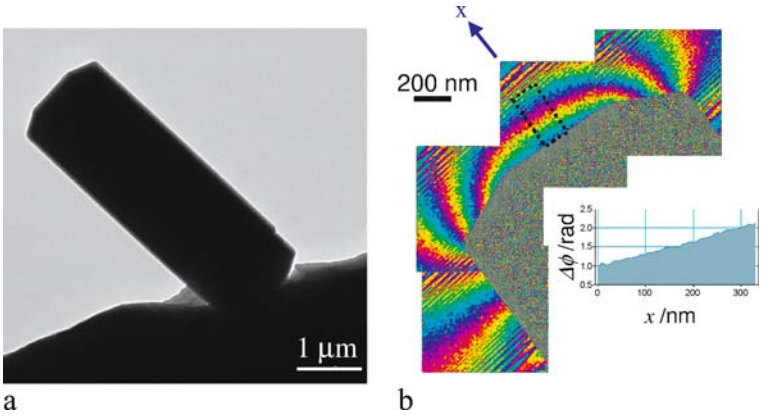

Fig. 43 Hexagonal-prismatic fluorapatite-gelatine nanocomposite seed; **a** conventional TEM micrograph. **b** Retrieved phase image of an electron hologram (eight-times boosted, composed of four single images) exhibits the electric potential distribution around a seed. Color code denotes a phase shift of 2π from *green* to *green*. Fresnel fringes of the interferograms appear as striation patterns at the corners of the phase images. The observed projected potential corresponds to a mesoscopic dipole. The phase profile (depicted for the rectangle with dotted border in the main picture) at the basal plane reveals a phase increase of about 1 rad per 300 nm

projected potential strongly resembles a macroscopic dipole. The phase profile is taken from the area marked by a dotted borderline at the basal plane and shows a phase increase of about 1 rad per 300 nm (Fig. 43b, inset). This finding corresponds to about 0.13 times the polarization observed inside $BaTiO_3$ ($P = 0.26\ C\,m^{-2}$, $\varepsilon_r \sim 1700$).

In order to check the assumption that the macro dipole is built-up by an assembly of elementary dipoles at the nanometer scale model calculations were performed. The model is based on the assumption of all dipoles being aligned parallel to the *c*-axis of the composite seed (Fig. 44a, arrows within the seed). Thereby, the hypothesis was adopted that each triple-helical gelatine molecule shows an idealized protonation state, i.e. all the *N*-termini are completely protonated and all the *C*-termini are deprotonated. The lengths of the fiber proteins and their vertical spacings were chosen according to TEM micrographs (Sect. 5). Contour plots of the phase shift calculated on the base of this structural model are shown in Fig. 44a, in which each isoline corresponds to a phase shift of 2π. The comparison with experimental data (Fig. 43b) gives a qualitative and direct agreement to the computer model.

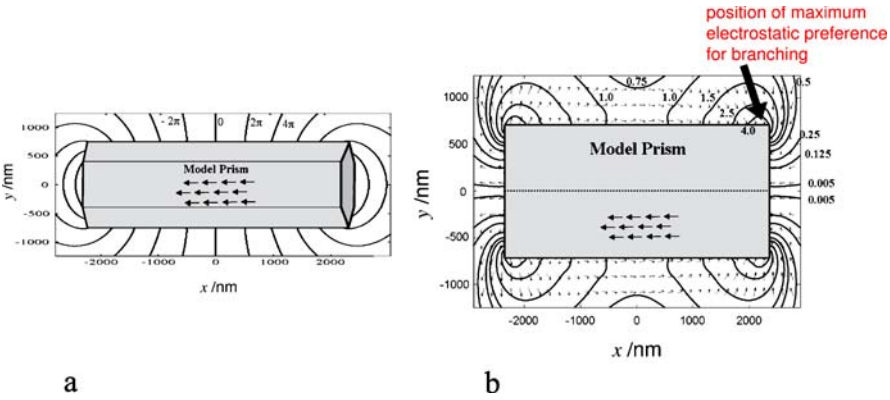

Fig. 44 **a** Simulation of the phase image around a nanocomposite seed based on an ideal arrangement of nano-dipoles. The model is constructed of triple-helices in parallel orientation along [001] within the seed. Triple-helices represent dipoles and are depicted as *arrows*; schematic representation. For further details see text. The contour plot of the phase shift shows a good qualitative agreement with the electron holographic experimental data (Fig. 43). **b** Calculation of preferred orientation of the triple-helices attaching from the gel and energy isolines around a composite seed in aqueous solution. The energy isolines ($kJ\,mol^{-1}$) indicate where and "how" neighboring macromolecules from the gel are attached to the seed (*small arrows* indicate the preferred orientations of the macromolecules). Largest divergence is produced at the corners, especially at the prism faces near the basal planes of the seed (*black arrow*). At these positions, there is also the strongest tendency for triple-helices from the gel to adopt a different orientation with respect to the hexagonal *c* axis and thus providing evidence of making preparations for branching at both ends of the seed (beginning of fractal outgrowths, see Sect. 6.2)

Therefore, in principle, the assumption of a nano-dipole model seems to be reasonable. However, a quantitative analysis yields that the phase shift of the model calculations compared with measured values is overestimated by a factor of 8. A possible reason for this could be a deviation from idealized protonation/deprotonation states of the $-NH_3^+$ and $-COO^-$ functional groups. Another source of error could be given by the estimated values for the length of the collagen molecules and the lateral spacing between them (Sect. 3). Finally, some triple-helices may adopt an antiparallel orientation with respect to each other and thus, some electric dipoles may be neutralized. However, these discrepancies between observed and calculated patterns do not change the qualitative truth of the character of the contour plot. A quantitative agreement can be achieved by a global scaling parameter of 1/8. This factor comprehends microscopic aberrations by averaging and thus, provides a model with mesoscopic resolution which is quantitatively correct.

Assuming an effective dipole moment of $1/8\ e \times 300\ nm$ for every triple-helix, we constructed an energy profile which displays the local preferred position and orientation of triple-helices coupling out of the aqueous gel onto the surface of the seed. Thereby, the dielectric effect of the medium $\varepsilon_r = 78$ (water) was assessed. Certainly, this value features an upper limit since the dielectricity number of apatite of about 8 is significantly lower. Small arrows in Fig. 44b exhibit the energetically most preferred take-up orientations, exclusively based on Coulomb interactions of the dipole model. The energy difference concerning the orientation and the alignment within the seed is given by means of isopotential lines. Most of the triple-helices in solution (in the surrounding gel, see Sect. 2) prefer a different orientation than those within the seed. This tendency is mostly pronounced at the prism faces in the vicinity of the basal plane. The energy difference between the orientation parallel [001] and the preferred (new) arrangement amounts to at least 4 kJ mol^{-1}. During the formation of the composite the surrounding solvent (water) will be replaced by apatite and hence, the dielectric effect is decreased by a factor of about 1/10 and the energy difference can be estimated up to 40 kJ mol^{-1}.

7.2
Effect of External Fields during Morphogenesis

Experimental indications for the significance of intrinsic electric dipole fields assuming control of the morphogenesis of the fractal nanocomposite aggregates were also obtained by using the growth-chamber shown in Fig. 2 (Sect. 2) including the equipment for application of an external electric field (5000 V/1.4 cm, D.C. conditions). The idea was [17] to influence fractal branching of the growing aggregates, and, in fact, "splitting" of the seeds (area of maximum electrostatic preference for branching at the prism faces near the basal planes; Fig. 44, Sect. 7.1) is predominantly affected by the external field (Fig. 45). Instead of self-similarly shaped units with more or less

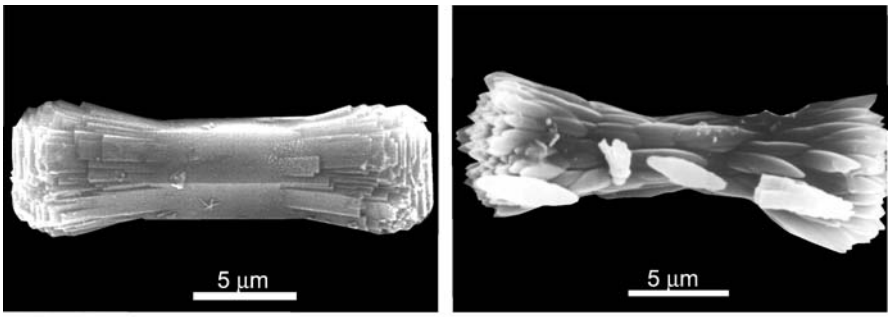

Fig. 45 SEM images of mature composite seeds showing the start of "splitting" **a** without an external field **b** with an applied external field (5000 V/1.4 cm)

well-developed prism and basal planes (Fig. 45a), the appearance of a new generation under the influence of an external electric field is nearly suppressed and the growing subunits are characterized by sharpened and bent faces (Fig. 45b). Moreover, the growing rate of the composite aggregates is significantly diminished when using an external field.

By taking into account the relevant literature data (Sect. 7) and the experimental results discussed in this section it becomes evident that intrinsic dipole fields play an important role during composite formation of polar biomacromolecules with inorganic materials on the nano-scale. This could be one of the "secrets" of biomineralization.

8
The Biomimetic Composite in Relation to Natural Hard Materials

Teeth are known to be the hardest calcium phosphate-based biomaterial produced by vertebrates. Moreover, they show an impressive high elasticity. The reason for this remarkably high mechanical stability is their inorganic–organic composite nature and the hierarchically structured, complex organization of minute (nano-) apatite crystals together with protein molecules.

Every human tooth consists of a crown (corona dentis) and one or more roots (radix dentis) which fix the tooth in the alveoli. The hard connective tissue of teeth can be subdivided into enamel (covering the crown), dentine (main inner part of the teeth), and tooth cement (covering the roots). Mature enamel consists of 95 wt. % apatite, $\sim$ 3 wt. % protein and 2 wt. % water [72–75]. Apart from the fact that the biomimetic apatite-gelatine-nanocomposite under consideration in the present contribution contains fluorapatite as the inorganic component (Sect. 1.2), the chemical composition of the composite is close to that of the mature enamel (Sect. 4.3). The structure

of tooth enamel consists of highly ordered crystal bundles, so-called enamel prisms. This structure is closely related to the almost parallel prism-structure of the outer shell area of the biomimetic core/shell assemblies (Fig. 15b in Sect. 3.3). Moreover, the prism-diameter is approximately the same for enamel (26–68 nm) [76] and the in-vitro grown composite (50–100 nm). In contrast to human enamel, the apatite crystals in human dentine are significantly smaller and less ordered, and the amount of the organic component is significantly higher (close to that of bone). Summarizing the structural aspects of human teeth, we have the outer enamel-area with a compact arrangement of prismatic subunits followed by the inner dentine-area with smaller crystals and lower ordering. This hierarchical architecture closely resembles the core/shell assemblies of the fluorapatite-gelatine nanocomposite consisting of the fractal core and the radial (almost parallel) arrangement of prismatic subunits in the shell (Sect. 3.3).

It is well known, that acid-attacks to teeth lead to subsurface demineralization processes which means the formation of caries lesions. When a lesion proceeds to the enamel-dentine junction, enamel loses its surface continuity and the hole spreads out into the softer dentine. It was shown that the effect of EDTA on enamel is similar to weak acids as its corrosive effects on extracted teeth produces caries-like lesions [77]. In the case of the biomimetic core/shell composite assemblies, the dissolution is rather similar during treatment with EDTA (Sect. 4.4): First, the spheres lose their opalescence and turn pale white, a process which corresponds to the formation of white spots in enamel [78] and the reason for this behavior is the development of small channels in the apatite surface that is accompanied by an alteration of the optical behavior and a "softening" of the material. The dissolution of the core/shell composite spheres proceeds via different steps of hollow spheres and corresponds to

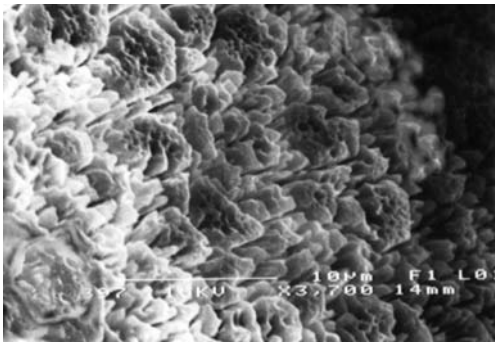

Fig. 46 Surface of a fluorapatite-gelatine composite aggregate in the stage of a hollow sphere (Fig. 16b) after EDTA attack. The surface is softened because of partial dissolution of apatite. Analogous to dental caries, the solvent reaches the interior of the sphere through these channels and the EDTA attack affects the fractal core

the undermining of caries attacks. Figure 46 shows a typical SEM image of a hollow sphere illustrating the "softening" of the shell material (enamel in the case of teeth).

Referring back to the introductory section (1.1 Basic Idea and Conception) it becomes clear: The apatite-gelatine system is perfectly suited to obtaining deeper insight into the processes of self-organization, and can help in learning about essentials in the formation and the properties of inorganic–organic nano-composites of biological relevance.

9 First Applications

The close chemical and structural relation of the biomimetic composite to the natural hard material in the form of the teeth (Sect. 8) as well as all the observations made concerning the dramatic processes of self-organization in the chemical system apatite + gelatine (Sect. 3) gave the idea to develop a composite material which could be applied in the field of "dental repair".

In fact, an active composite substance (Nanit®active) was prepared by precipitation of nano-hydroxyapatite in the presence of gelatine which together with human saliva acts as a neomineralizing agent on dentine [79]. In this way (in the case of receding gums) the open tubuli running towards

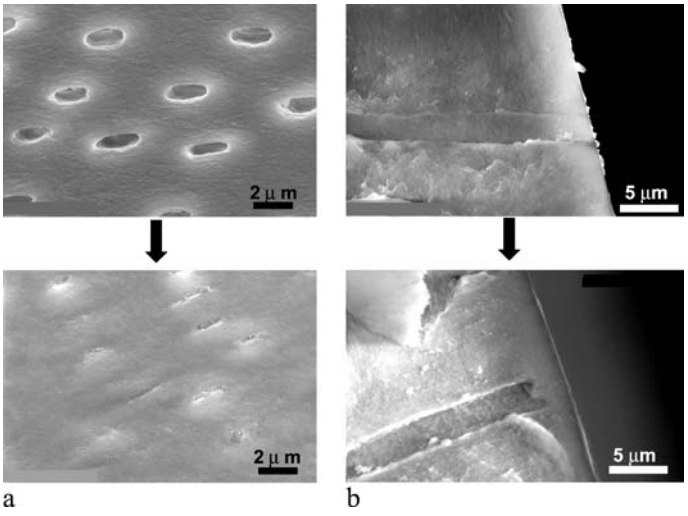

Fig. 47 SEM images of bovine dentin. a-series: top view; b-series: side view. *Top*: open tubuli. *Bottom*: closed tubuli after repeated treatment with a hydroxyapatite-protein-nanocomposite gel (Nanit®active). A biomineralization process leads to the formation of a bioanalogue layer covering the tubuli. (Images disposed by T. Poth, Sustech Darmstadt)

the surface area of the dentine and containing the nerves are covered with a protective layer of dentine-analogous material (Fig. 47). A biomimetic procedure which perfectly stops pain caused by sensitivity to hot/cold- and/or sweet/acid-irritations.

Further medical applications based on apatite-gelatine composites are under investigation.

10 Conclusion and Prospective

The chemical system apatite + gelatine (aqueous solutions) includes essential and attractive components of both basic science and (materials/medical) applications. Although reduced to a relatively low level of complexity (compared with respective processes in related bio-systems), the systems still facilitate observations and investigations of fundamental interest. As was pointed out in Sect. 1.1 all aspects of complexity are included, such as metastability, self-organization (self-assembly), self-similarity, fractals, pattern formation, hierarchy, transfer of information, and others. Even the role of intrinsic dipole fields during morphogenesis proved to be of essential significance.

Although restricted to the fluorapatite variant (Sect. 1.2) the biomimetic system under consideration bears strong resemblance to the bio-system hydroxyapatite-collagen which plays a decisive role in the human body as functional material in the form of bone and teeth (Sect. 8). In both systems, the hierarchical and self-similar organization is of prominent relevance. The apparent similarities between the bio- and the biomimetic systems are of special interest from the conceptional point of view, in that the biomimetic model system is perfectly suited for the study of biomimetic steps closely related to steps in osteo- and dentinogenesis. In this way, fundamental knowledge of the basic principles of nanocomposite formation is acquired which then may penetrate into the fields of application (Sect. 9).

Returning to the aspects of fundamental research, it becomes evident that we are still far away from clearly stating direct causalities for all the highly interesting observations made so far. There is urgent need for continuous and intensive work on the FAP-gelatine-nanocomposites to say nothing of the respective HAP-system which seems to be much more complex. The qualified use of atomistic simulations will become more and more important in order to support and supplement experimental observations and to give an idea of the chemical processes running on the microscopic length scale in a complex system. Though, it became clear from our own experience in the system calcium phosphate-gelatine-water [63, 64, 80–85] that a lot of preliminary work is needed to establish a qualified and theoretical basis before starting to investigate (smaller) parts of the system under complex aqueous conditions (Sect. 6).

The system under consideration remains a challenge for the future, not only from the point of view of basic research but also from the aspect of composite materials and their applications.

Acknowledgements We would like to thank the Fonds der Chemischen Industrie for generous support. Parts of this work were funded by the Deutsche Forschungsgemeinschaft (SPP 1117 "Prinzipien der Biomineralisation").

References

1. Bronner F, Farach-Carson M (eds) (2003) Bone Formation. Springer, Berlin Heidelberg New York
2. Jahnen-Dechent W (2004) In: Bäuerlein E (ed) Biomineralization, Progress in Biology, Molecular Biology and Application. 2nd Edn. Wiley, Weinheim
3. Teaford MF, Smith MM, Ferguson MWJ (eds) (2000) Development, Function and Evolution of Teeth. Cambridge University Press, Cambridge
4. Reichenmiller K, Klein CH (2004) In: Bäuerlein E (ed) Biomineralization, Progress in Biology, Molecular Biology and Application, 2nd Edn. Wiley, Weinheim
5. Matthew AR, Jasiuk I, Taylor J, Rubin J, Ganey T, Apkarian RP (2003) Bone 33:270
6. Gupta HS, Wagermaier W, Zickler GA, Aroush DRB, Funari SS, Roschger P, Wagner HD, Fratzl P (2005) Nano Lett 5:2108
7. Tang R, Wang L, Orme CA, Bonstein T, Bush PJ, Nancollas GH (2004) Angew Chem Int Ed 43:2697
8. Veis A (2004) Science 307:419
9. Heywood BR, Sparks NHC, Shellis RP, Weiner S, Mann S (1990) Connect Tiss Res 25:103
10. Landis WJ, Hodgens KJ, Arena J, Song MJ, McEwen BF (1996) Micros Res Technol 33:192
11. Kim HW, Kim HE, Salih V (2005) Biomaterials 26:5221
12. Kim HW, Yoon BH, Kim HE (2005) J Mater Sci: Mater in Med 16:1105
13. Chang MC, Ko CC, Douglas WH (2005) J Mater Sci 40:2723
14. Furuichi K, Oaki Y, Imai H (2006) Chem Mater 18:229
15. Kniep R, Busch S (1996) Angew Chem 108:2787
16. Kniep R, Busch S (1996) Angew Chem Int Ed Engl 35:2624
17. Busch S, Dolhaine H, DuChesne A, Heinz S, Hochrein O, Laeri F, Podebrad O, Vietze U, Weiland T, Kniep R (1999) Eur J Inorg Chem 10:1643
18. Busch S, Schwarz U, Kniep R (2001) Chem Mater 13:3260
19. Busch S, Schwarz U, Kniep R (2003) Adv Func Mater 13:189
20. Simon P, Carrillo-Cabrera W, Formanek P, Gobel C, Geiger D, Ramlau R, Tlatlik H, Buder J, Kniep R (2004) J Mater Chem 14:2218
21. Göbel C, Simon P, Buder J, Tlatlik H, Kniep R (2004) J Mater Chem 14:2225
22. Kniep R (2004) In: Müller A, Quadbeck-Seeger HJ, Diemann E (eds) Facetten einer Wissenschaft. Wiley, Weinheim
23. Simon P, Schwarz U, Kniep R (2005) J Mater Chem 15:4992
24. Tlatlik H, Simon P, Kawska A, Zahn D, Kniep R (2006) Angew Chem Int Ed 45:1905
25. Simon P, Zahn D, Lichte H, Kniep R (2006) Angew Chem Int Ed 45:1911
26. Arends J, Davidson CL (1975) Calcif Tissue Res 18:65
27. Verbeek RMH, De Maeyer CAP, Droessens FCM (1995) Inorg Chem 34:2084
28. Nancollas GH, Wu WJ (2000) J Cryst Growth 211:137

29. Zhang HG, Zhu Q, Wang Y (2005) Chem Mater 17:5824
30. Wilke K-Th, Bohm J (1988) Kristallzüchtung. Verlag Harri Deutsch, Thun, Frankfurt/Main, Germany
31. Henisch HK (1996) Crystal Growth in Gels. Dover Publications, Inc., New York
32. Busch S (1998) PhD Thesis, University of Technology, Darmstadt, Germany
33. Ostwald's Klassiker der exakten Naturwissenschaften: Selbstorganisation chemischer Strukturen (1987) Akademische Verlagsgesellschaft Geest & Portig KG, Leipzig
34. Grigor'ev DP (1965) Ontongeny of Minerals. Israel Program for Scientific Translations, Jerusalem
35. Prymak O, Sokolova V, Peitsch T, Epple M (2006) Cryst Growth & Design 6:499
36. Haeckel E (1925) Kristallseelen. Verlag Alfred Kröner, Leipzig (Reprint) (2005) Hesse & Becker, Leipzig
37. Mandelbrot BB (1991) Die fraktale Geometrie der Natur. Birkhäuser Verlag, Basel
38. Maleev MN (1972) Tschermaks Min Petr Mitt 18:1216
39. POVRAY 3.1e@, 1991–1999, The Persistence of Vision Team, http://www.povray.org
40. Schröder HE (1992) Orale Strukturbiologie. Thieme, Stuttgart
41. Sheldrick GM (1997) SHELXL 97-2. Program for refinement of crystal structures. University of Göttingen, Göttingen
42. Akselrud L, Grin J, Pecharsky V, Zavalij P. Computer program package WINCSD. Lviv National University, Ukraine; Max-Plank Institute, Germany; Ames Lab, USA; Binghamton University, USA
43. Sudarsanan K, Mackie PE, Young RRA (1972) Mat Res Bull 7:1331
44. Mackie PE, Young RA (1973) J Appl Chryst 6:26
45. Posner AS, Diorio AF (1967) Acta Cryst 1:1948
46. Sudarsanan K, Young RA (1969) Acta Crystallogr B 25:1534
47. Newesely H, Helmke JG (1971) Biomineralization 3:39
48. LeGeros RZ, Bonel G, Legeros R (1978) Calcif Tiss Res 26:111
49. Berman A, Addadi L, Weiner S (1988) Nature 331:546
50. Young RA, van der Lugt W, Elliott JC (1969) Nature 223:729
51. Newesely H, Müller H (1988) Z Kristallogr 182:197
52. Young RA, Holcomb DW (1984) Calcif Tissue Int 36:60
53. Freud F, Knobel MJCS (1976) Dalton 6/2151:1136
54. Berman A, Addadi L, Weiner S (1988) Nature 331:546
55. Mann S (2001) In: Compton RG, Davies SG, Evans J (eds) Biomineralization. Oxford University Press, Oxford
56. Schwenzer N (1985) Zahn- Mund- Kiefer- Heilkunde, Vol 1–4. Thieme, Stuttgart
57. Cölfen H, Antonietti M (2005) Angew Chem 117:5714
58. Cölfen H, Antonietti M (2005) Angew Chem Int Ed 44:5576
59. Thompson JB, Kindt JH, Drake B, Hansma HG, Morse DE, Hansma PK (2001) Nature 414:773
60. Currey J (2001) Nature 414:699
61. Fantner GE, Hassenkam T, Kindt JH, Weaver JC, Birkedal H, Pechenik L, Cutroni JA, Cidade GA G, Stucky GD, Morse DE, Hansma PK (2005) Nature Mater 4:612
62. Zahn D, Hochrein O (2003) Phys Chem Chem Phys 5:4004
63. MacKerell AD, Bashford D, Bellott RL, Dunbrack RL, Evanseck JD, Field MJ, Fischer S, Gao J, Guo H, Ha S, Joseph-McCarthy D, Kuchnir L, Kuczera K, Lau FT K, Mattos C, Michnick S, Ngo T, Nguyen DT, Prodhom B, Reiher WE, Roux B, Schlenkrich M, Smith J, Stote CR, Straub J, Watanabe M, Wiorkiewicz-Kuczera J, Yin D, Karplus DM (1998) J Phys Chem B 102:3586
64. Kawska A, Brickmann J, Hochrein O, Zahn D (2005) Z Anorg Allg Chem 631:1172

65. Kawska A, Brickmann J, Kniep R, Hochrein O, Zahn D (2006) J Chem Phys 124:24513
66. Yamashita K, Oikawa N, Umegaki T (1996) Chem Mater 8:2697
67. Calvert P, Mann S (1997) Nature 386:127
68. Lang SB (1966) Nature 212:704
69. Kitagawa K, Morita T, Kimura S (2005) Angew Chem Int Ed 117:6488
70. Lichte H, Lehmann M (2002) In: Advances in Imaging and Electron Physics, Electron Holography: A Powerful Tool for Analysis of Nanostructures. Elsevier, New York 123:225
71. Lichte H, Reibold M, Brand K, Lehmann M (2002) Ultramicroscopy 93:199
72. Höhling HJ (1966) Die Bauelemente von Zahnschmelz und Dentin aus Morphologischer, Chemischer und Struktureller Hinsicht. Hanser, Munich
73. Goldberg M, Carreau JP, Arends J (1987) J Arch Oral Biol 32:765
74. Edgar WM, Mullane DM (1990) Saliva and Dental Health. British Dental Journal, London
75. Okazaki M, Tokahashi J, Kimura H (1989) J Osaka Univ Dent Sch 29:47
76. Daculsi G, Menanteau J, Kerebel LM (1984) Calcif Tissue Int 36:550
77. Schatz A, Martin JJ (1965) Zahnheilkunde 26:191
78. Schwenzer N (1988) Zahn- Mund- Kiefer- Heilkunde, Vol 4: Konservierende Zahnheilkunde. Thieme, Stuttgart
79. Braunbarth C, Franke K, Poth T, Schechner G, Kniep R, Kropf C, Wülknitz P (2003) VDI-Reports No. 1803
80. Zahn D, Hochrein O (2003) Phys Chem Chem Phys 5:4004
81. Zahn D (2004) Z Anorg Allg Chem 630:1507
82. Hochrein O, Zahn D, Kniep R, Brickmann J (2004) Z Anorg Allg Chem 630:1740
83. Zahn D, Hochrein O (2005) Z Anorg Allg Chem 631:1134
84. Hochrein O, Kniep R, Zahn D (2005) Chem Mater 17:1978
85. Zahn D, Hochrein O (2006) Z Anorg Allg Chem 632:79

Top Curr Chem (2007) 270: 127–153
DOI 10.1007/128_075

Published online: 27 October 2006

Inorganic-Organic Interfacial Interactions in Hydroxyapatite Mineralization Processes

Kimiyasu Sato

National Institute of Advanced Industrial Science and Technology (AIST), Anagahora 2266-98, Shimoshidami, Moriyama-ku, 463-8560 Nagoya, Japan
sato.kimiyasu@aist.go.jp

Abstract Details of our recent attempts to clarify the self-organization mechanism of hydroxyapatite (HAp) mineralization in natural bodies are presented in this work. In biomineralization processes, inorganic crystals precipitate onto organic matrix surfaces. Organic molecules assembled to monolayer films were employed to reproduce the organic matrices in natural bodies, and the HAp mineralization process onto the organic monolayers were subjected to spectroscopic and structural analytical approaches. Knowledge of interfacial atomic structures is also essential for interpretation of the inorganic-organic interface. We determined the most stable atomic arrangement of the HAp {100} facet using high-resolution transmission electron microscopy. A mechanism of HAp mineralization proposed in view of the experimental results is the highlight of this work.

Keywords Electron microscopy · Hydroxyapatite · Interfacial interactions · IR spectroscopy · Organic matrices

Abbreviations

DF	defocus
FT-IR	Fourier transform IR
HAp	hydroxyapatite
HRTEM	high-resolution transmission electron microscopy
LB	Langmuir–Blodgett
OCP	octacalcium phosphate
SAED	selected area electron diffraction
SAM	self-assembled monolayer

SBF simulated body fluid
SEM scanning electron microscopy
TEM transmission electron microscopy
TF-XRD thin-film X-ray diffraction
XRD X-ray diffraction

1 Introduction

Specific structural aspects of inorganic solids often dominate the exploitable properties of the solids. Therefore, many new technological applications require fabrication processes that provide control over the phase, size, morphology and crystallographic orientation of inorganic crystals. The ability of constructing materials organized at nanoscale level from molecular processes is of immediate requirement. Biomineralization processes, or the biological synthesis of inorganic crystals, yield materials with highly regulated structures under moderate conditions of temperature and pressure [1–3]. Furthermore, the crystallochemical specificity of inorganic solids in the biological systems induces so-called self-organized peculiar crystal morphologies. The resultant structural architectures are customized for each property that biological tissues provide. Recently, there has been growing interest in the principles governing the architectures and methods to form a variety of biominerals, such as those found in bones, teeth and shells. Much of this interest stems from the desire to create new highly functionalized synthetic materials, consuming little energy in their production. Owing to serious global environmental problems, all the manufacturing industries are forced to pay more attention to energy consumption. As the understanding of the processes involved in biomineralization developed, researchers have realized a new area of study that takes some inspiration from nature in an effort to construct interesting new structures. Such nature-inspired studies were termed "biomimetics" [4–8]. Indeed, a good deal of the current focus in intelligent materials is centered around mimicking of biological tissues. The formation processes of the biominerals are the results of 40 to 50 million years of fine-tuning by evolution. They must be replete with material scientific key components and the elucidation of biomineralization processes offers valuable insights into material science and engineering.

Biomineralization is characterized by the close association of inorganic and organic substances throughout the entire process. In general biological systems, an organism creates the proper organic matrix on which inorganic crystals can precipitate and the interfacial interactions between them provides the control over the resultant composite structures [3, 4, 9–11]. The molecular interactions at the inorganic-organic interfaces are an important

aspect of biomineralization since the nucleation, growth and organization of biominerals are mediated by the organic supramolecular system.

Calcium phosphate is the main constituent of bone and teeth and is one of the most important biominerals. Hydroxyapatite (HAp), $Ca_5(PO_4)_3OH$, is the most stable calcium phosphate phase in fluids and humid atmospheres under neutral to alkaline conditions [12] and is easily formed in the bodies of vertebrates. There is considerable academic and commercial interest in the development of HAp bioceramics and HAp-loaded polymers for bone replacement. Bone is a nanocomposite material in which collagen fibers are effectively reinforced by an assembly of nano-sized HAp crystallites [13–15]. This structure suggests that bioactive artificial bones such as bone-repairing materials can be essentially obtained through the formation of the nanocomposite structure. Furthermore, the *c*-axes of biological HAp crystallites and the helical axes of the collagen molecules show a strongly preferred orientation along the longitudinal direction of the bone. It is generally accepted that such unique alignment of biological HAp crystallites accompanied with the orientation of collagen fibrils is closely related to macroscopic mechanical properties. The alignment effects of both collagen and HAp on the strength of bone have been investigated experimentally and theoretically, and strong anisotropy in Young's modulus, hardness, fracture strength, bending strength, and fracture toughness has been documented [16–19]. Recently, attempts to fabricate artificial bone materials having bone-like nanostructure and chemical composition have been made [20, 21]. The artificial bone prepared with mimesis of the bone nanostructure can be incorporated into the metabolic system as bone tissue at the recipient sites. The orientated mineralization of HAp crystallites occurs automatically without any physical support by cells. In order to develop new kinds of bioactive materials, it is important to understand the detailed mineralization process of the well-organized bone nanostructure. But it still remains to be clarified from the viewpoint of materials science.

The study of biomineralization, especially on the inorganic-organic interfaces, offers valuable insights into the scope of materials chemistry. However, the interfaces between inorganic-organic materials in living bodies possess such a small and tangled structure that the interfacial interaction cannot be studied directly. Therefore, a model system that can reproduce the inorganic-organic interfaces with simplified structure is required. In this work, as described below, recent attempts to clarify the self-organization mechanism of HAp mineralization through some model systems are reviewed.

2
Organic Matrix-Mediated Crystallization of HAp

2.1
Organic Molecule Assemblages

The tendency for insoluble amphiphilic molecules to accumulate at the gas/solution interface and form highly organized monomolecular films is a physical process that has been widely exploited since the first identification of this phenomenon by Fraulein Pöckels a hundred years ago [22]. For biologists and biophysicists, monolayer films present a versatile and controllable model system that approximates to half the bilayer structure of a biomembrane. In the materials science, interest in the system is linked to the facility for monolayer transfer to solid supports for the formation of multilayers, which have electronics applications [23]. The organic monolayers at the gas/solution interface are called Langmuir films and the organic thin films transferred onto solid substrates are Langmuir–Blodgett (LB) films.

Self-assembled monolayers (SAMs) are surfaces consisting of a single layer of molecules on a substrate [24, 25]. SAMs can be prepared simply by adding a solution of the desired molecule onto the substrate surface and washing off the excess. Common examples are alkane thiol molecules and organosilane molecules chemisorbed onto gold and hydrated oxide surfaces, respectively. Such SAMs are frequently utilized to change physical and chemical properties of surfaces.

An important aspect common to biomineralization processes is the role played by functional groups at the surface of organic crystallization sites. Therefore, for biomineralization researchers, interest has centered on the use of such films as templates for inorganic crystal precipitation. One approach to investigate the inorganic-organic interactions in vitro has been to use the molecular assemblages as organized organic surfaces for inorganic crystallization. When the organic assemblages are placed in simulated body fluids, inorganic crystals precipitate onto the surfaces of the assemblages. Molecules assembled in the above-mentioned forms have been often employed as model organic matrices, such as Langmuir monolayer films [26–43], LB films [44–46], and SAMs [47–52]. Especially, crystallization of calcium carbonate on the organic templates is studied extensively. In the process of calcium carbonate formation in living bodies, the polymorph switching and growth directions are suggested to be controlled by organic membranes. The unexplained mechanism for polymorph switching and directional control has attracted many researchers' interest. As to calcium phosphate crystals represented by HAp, several groups reported that organic functional groups as surface residues of macromolecules are able to induce HAp nucleation [42, 43, 45, 46, 52] and that knowledge is now accepted widely.

2.2 HAp Crystallization on the LB Films

Surfaces of Langmuir films and LB films can be adopted as model systems to study inorganic-organic interfaces, owing to the opportunities to engineer the surface properties (functional group identity, polarity, molecular alignment periodicity, etc.) in a manner that is controllable. In our works, organic monolayer films prepared by the LB method were used to investigate the nucleation mechanism of HAp crystals in a simulated body environment [45, 46]. The LB films with the same functional groups as collagen (i.e., carboxyl groups and amino groups) were placed in a simulated body environment. LB monolayers of arachidic acid ($C_{19}H_{39}COOH$) and stearyl amine ($C_{18}H_{37}NH_2$) were accumulated on fused silica or calcium fluoride (CaF_2) substrates as follows: Arachidic acid or stearyl amine was spread on the water subphase. The obtained organic film on the water surface was slowly compressed up to a surface pressure needed for the ordering of the organic molecules. In the condensed monolayer states, the molecules are closely packed and oriented with their hydrocarbon chains pointing away from the water surface. Subsequently, the monolayer of arachidic acid or stearyl amine was transferred onto a substrate by dipping the substrate into the water subphase; then, the substrate was dropped into the subphase (Fig. 1). The amphiphilic arachidic acid or stearyl amine molecules are standing almost perpendicularly on the substrate and the outermost layer of the LB film is, therefore, occupied by carboxyl groups or amino groups, respectively.

The biomineralization is solidification processes of inorganic ions contained in body fluid. The model system should be constituted from an organic matrix and an adequate aqueous solution. The main constituents of bone are HAp in the form of nanometer-sized crystals and collagen acting as structural protein. When the biomineralization mechanism in natural bone is consid-

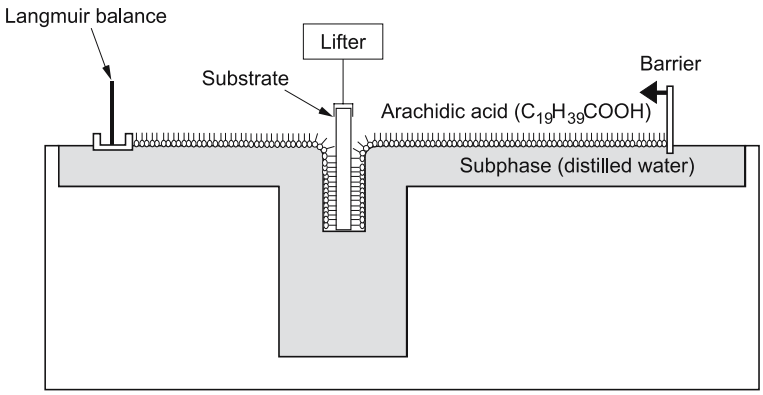

Fig. 1 The trough system for LB film depositions

ered, the surrounding aqueous solution must be the precipitation medium for calcium phosphate crystals. We employed an acellular simulated body fluid (SBF) proposed by Kokubo et al. [53, 54] as the model system for inorganic ions in natural bodies. SBF possesses inorganic ion concentrations and a pH value almost equal to those of human blood plasma. SBF was prepared by dissolving NaCl, $NaHCO_3$, KCl, $K_2HPO_4 \cdot 3H_2O$, $MgCl_2$, $CaCl_2$ and Na_2SO_4 in distilled water and buffered at pH 7.4 with 50 mM of $(CH_2OH)_3CNH_2$ and 45 mM of HCl. The ion concentrations of prepared SBF are given in Table 1. The substrates with the LB films were immersed in SBF for various periods at 36.5 °C and taken out of the fluid. After being gently washed with ion-exchanged distilled water and dried at room temperature, the specimens were evaluated.

The surfaces of fused silica substrates soaked in SBF were subjected to thin-film X-ray diffraction (TF-XRD) measurements. Figure 2 shows the TF-XRD patterns of the LB films. Before soaking a fused silica substrate in SBF, only a broad peak was observed, ascribed to an amorphous structure of glass. In the case of the hydrophobic and hydrophilic glass substrates without LB film, even after being soaked in SBF for 10 days, no appreciable change was detected in the XRD patterns. Similarly, no change in XRD pattern was observed also for the stearyl amine monolayer. However, in the case of the fused-silica substrate with arachidic acid monolayers, new peaks appeared in the XRD pattern after being soaked in SBF; the peaks could be attributed to the apatite or octacalcium phosphate (OCP) structure [55]. Similarity between the diffraction pattern of HAp with low crystallinity and that of OCP at the high angle region prevents the discrimination between HAp and OCP. The most diagnostic 100 diffraction peak of OCP, which is located at almost 4.7°, cannot be identified due to high background. From the results of the XRD measurements, it was indicated that the calcium phosphate crystals could form only on the arachidic acid monolayer but not on the stearyl amine monolayer. In other words, only carboxyl groups could act as a nucleation center for the calcium phosphate formation in SBF.

The surface topography of the crystals grown on the LB films was investigated using a scanning electron microscope (SEM). Figure 3 shows SEM micrographs of the surface with the arachidic acid LB film soaked in SBF for 10 days. The surface of the substrate is partly covered with hemispherical ag-

Table 1 Ion concentrations of simulated body fluid and human blood plasma

	Ion concentration (mM)							
	Na^+	K^+	Ca^{2+}	Mg^{2+}	Cl^-	HCO_3^-	HPO_4^{2-}	SO_4^{2-}
Human blood plasma	142.0	5.0	2.5	1.5	103.0	4.2	1.0	0.5
SBF	142.0	5.0	2.5	1.5	148.3	4.2	1.0	0.5

gregates. SEM micrographs with a higher magnification (Fig. 4) revealed that the hemispherical aggregates are composed of plate-like, curled fragments. At the interface, the crystals are directly attached to the substrate materials as seen in Fig. 4.

The calcium phosphate crystallites were examined by transmission electron microscopy (TEM). Two specimens on fused silica substrates were attached together with epoxy resin; then they were sliced and thinned using argon ion milling as is used for conventional cross-sectional TEM observations [56, 57]. Figure 5a shows the TEM image of the calcium phosphate crystals grown on the LB film surface, which was soaked in SBF for 10 days. The amorphous material at the bottom is the fused silica substrate, on which an aggregate of calcium phosphate nanocrystallites is observed. The nanocrystallites exhibit an elongated plate-like form of 50–100 nm in length and about 10 nm thick. The lattice-fringe image of the nanocrystallites observed is shown in Fig. 5b together with its Fourier transform. The spots indicated by arrows correspond to the periodicity of 0.82 nm, which can be assigned

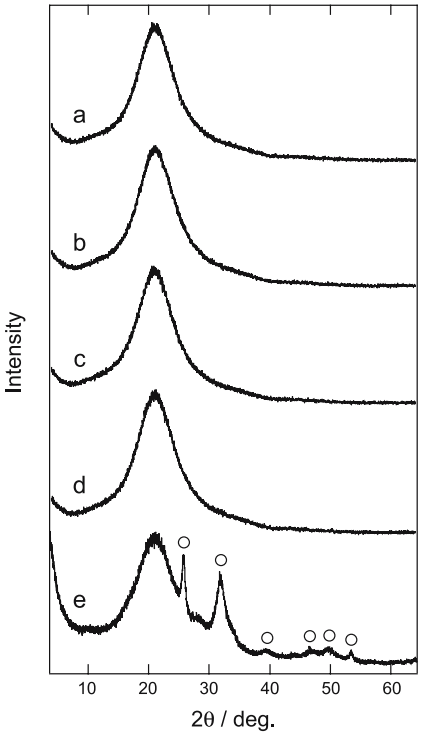

Fig. 2 The TF-XRD patterns of substrates and LB films soaked in SBF for 10 days: **a** hydrophobic glass substrate before soaking; **b** hydrophobic glass substrate; **c** hydrophilic glass substrate; **d** stearyl amine LB film; **e** arachidic acid LB film. (○) Apatite peaks

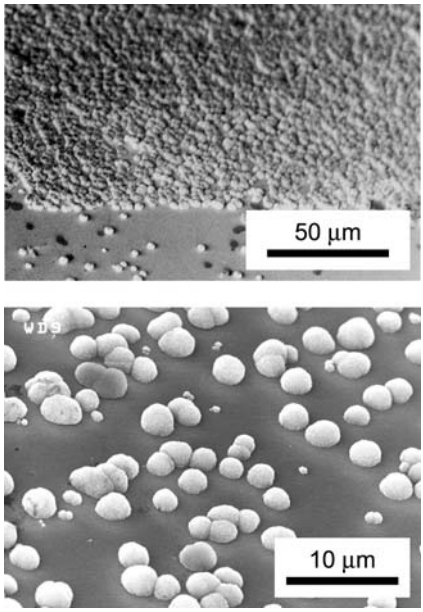

Fig. 3 SEM images of the arachidic acid LB film surface soaked in SBF for 10 days. (Reproduced with permission from [43]. © 2005 The Ceramic Society of Japan)

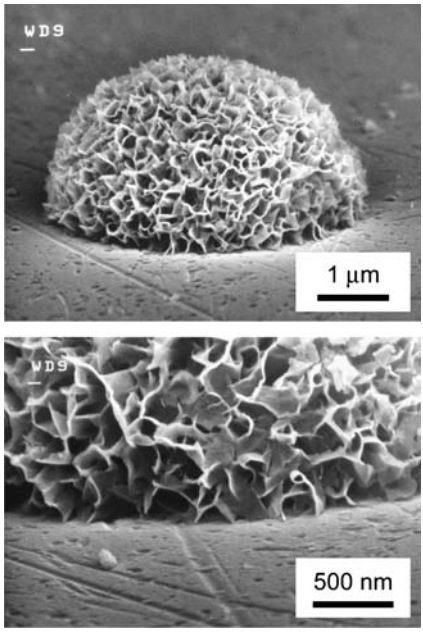

Fig. 4 SEM images of the arachidic acid LB film surface soaked in SBF for 10 days. (Reproduced with permission from [46]. © 2001 Elsevier)

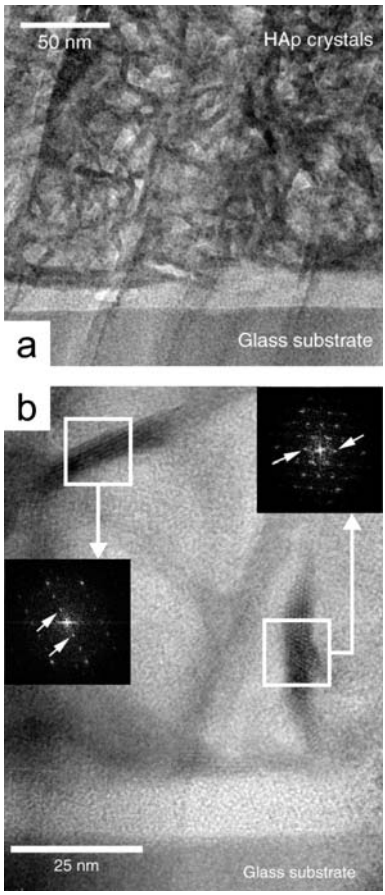

Fig. 5 **a** TEM image of the interface between the LB film and the HAp aggregates. Note that the apparent elongated crystals are in a plate-like form viewed edge-on. **b** Fourier transforms of the lattice-fringes and the corresponding areas are shown. *Arrows* in the Fourier transforms indicate the spots corresponding to the 0.82 nm which is ascribed to the interplanar spacing of {100} in HAp. (Reproduced with permission from [46]. © 2001 Elsevier)

to the interplanar spacing of {100} in the HAp structure [1]. In the right-hand inlet, hexagonal alignment of the spots indicates that the HAp nanocrystallite is oriented with its [001] in parallel to the electron beam. Neither OCP

[1] The crystal structure of HAp was ascribed to hexagonal symmetry with the space group $P6_3/m$ by analogy with fluorapatite [58, 59]. Elliot et al. [60], however, have revealed that stoichiometric HAp has the space group $P2_1/b$ (monoclinic) at room temperature. Now it is generally believed that pure and stoichiometric HAp is monoclinic [61]. The ordered arrangement of OH ions along the OH columns lowers the symmetry of the HAp crystal structure. The difference between hexagonal and monoclinic symmetry is, however, negligible in the present study and we express the crystal structure according to the hexagonal symmetry

d(100) at 1.86 nm nor its collapsed spacing in vacuum at 1.65 nm [62] was observed during TEM inspection. These results indicate that the crystalline phase on the LB film surface is only HAp. The elongated form of HAp in the TEM images is interpreted to be the cross-section of plate-like shape of the HAp nanocrystallites as revealed in the SEM observation (Fig. 4). Figure 6 shows TEM images of HAp single crystals with lattice fringes and their Fourier transforms. The spots corresponding to the interplanar spacing of

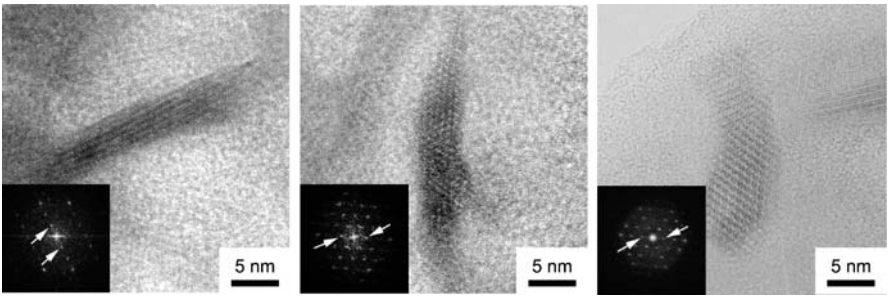

Fig. 6 TEM images of HAp single crystals with lattice fringes and their Fourier transforms. *Arrows* in the Fourier transforms indicate the spots which are ascribed to the interplanar spacing of {100}. Note those spots are found in the direction vertical to the elongated form

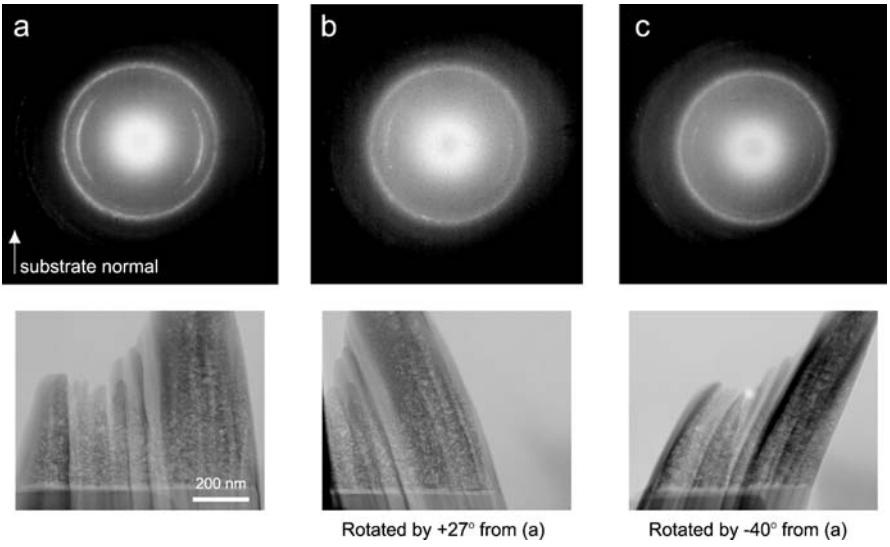

Fig. 7 Change of the selected-area electron diffraction patterns from the HAp crystals near the interface with rotation along the normal of the substrate. The corresponding TEM images are shown below the diffraction patterns. (Reproduced with permission from [46]. © 2001 Elsevier)

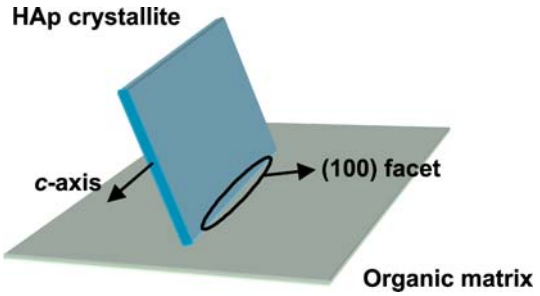

Fig. 8 Schema showing the relationship between the crystallographic property of the HAp crystals and the LB film

0.82 nm are found in the direction vertical to the elongated form, indicating that the plate-like HAp single crystals are parallel to {100} planes.

As shown above, carboxyl groups of LB films induced HAp nucleation and HAp crystallite aggregates were formed on the surface of arachidic acid LB monolayer in the simulated body environment. Figure 7a shows the selected area electron diffraction (SAED) patterns taken from an area of ~ 200 nm in diameter inside the HAp aggregate adjacent to the inorganic-organic interface. The Debye ring of the 002 reflection takes a crescent-like form; the direction linking the centers of two crescents is parallel to the interface. As shown in Fig. 7b,c, the diffraction patterns changed with the rotation along the axis normal to the interface; that is, the crescent-like Debye ring gradually disappeared with increasing the rotation angle. This indicates that the *c*-axes of the HAp crystals are preferentially oriented in a specific direction parallel to the interface. If the topography observed by SEM and crystallographic properties elucidated by TEM are taken into consideration, HAp crystal growth on the surface of the LB film, with one of {100} faces parallel to the interface, is suggested (Fig. 8). The single crystal could be adjacent to the LB film with the small (100) facet.

2.3 Initial Stage of HAp Nucleation Induced by Carboxyl Groups

As is well known, the body fluid is supersaturated with respect to HAp under the normal condition. Under such an environment, once HAp nuclei are formed, they can grow spontaneously by consuming calcium and phosphate ions from the surrounding body fluid. However, the supersaturation of the body fluid is not so high to induce homogeneous nucleation of HAp [63]. In the above study, nucleation was induced by carboxyl groups on the LB film surface and followed by growth of HAp nanocrystallites. In this section the chemical interactions of inorganic-organic interfaces are analyzed using IR spectroscopy. IR spectroscopy probes the vibrational features of organic

molecules. Developments in Fourier transform IR (FT-IR) techniques have increased the sensitivity sufficiently so as to observe reliable IR spectra at the monomolecular layer level. Therefore, IR spectroscopy provides a convenient and useful way for the analysis of constituent groups in a LB film. A CaF_2 crystal is transparent in the wavelength region from 0.13 to 12.0 μm. The LB film formed on the CaF_2 substrates were subjected to IR transmission spectral measurement.

Figure 9 shows IR transmission spectra of the arachidic acid LB film at several soaking stages. A strong absorption peak found at 1702 cm^{-1} for the specimen before soaking in SBF (Fig. 9a) is assigned to the stretching mode of C = O in a carboxyl group. The observation of this peak indicates that the arachidic acid molecules without covering of inorganic ions kept a nonionized state COOH. After soaking in SBF for 1 h, as shown in Fig. 9b, the C = O stretching peak entirely disappeared while antisymmetric $-CO_2^-$ stretching peaks appeared at 1576 and 1543 cm^{-1}, indicating that the carboxyl group was ionized by adsorbing ions in SBF. After soaking in SBF for 24 h (Fig. 9c), some

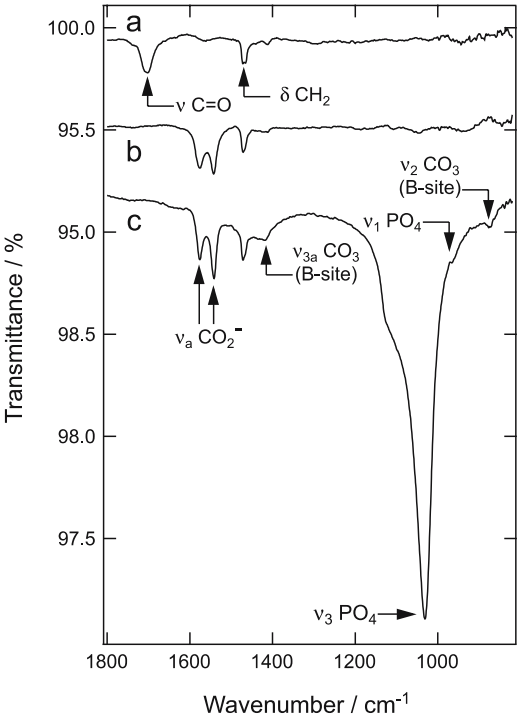

Fig. 9 IR transmission spectra of an arachidic acid LB film and samples soaked in SBF. **a** Before soaking; **b** after being soaked in SBF for 1 hour; **c** after being soaked in SBF for 24 hours. The spectra are offset for clarity. (Reproduced with permission from [46]. © 2001 Elsevier)

IR peaks ascribed to HAp containing carbonate ions appeared: i.e., 965 cm^{-1} and 1031 cm^{-1} for PO_4, 875 cm^{-1} and 1413 cm^{-1} for CO_3^{2-} [64, 65]. Although CO_3 ions can replace both the OH site (A site) and the PO_4 site (B site) in the HAp structure, the CO_3 peaks shown in Fig. 9c are assigned only to the B site. It is known that the CO_3 substitution at the A site in HAp crystals is limited to the preparation in aqueous systems, as has been proved in the present study [55]. The nanocrystallites grown on the LB film surface exhibit a plate-like morphology reminiscent of OCP, which may form as a transient phase because of the relatively high supersaturation of SBF. TEM observation showed that the deposited crystals have HAp structure. As shown in the results of the IR spectra measurement, the crystals precipitated on the LB films are B-type carbonate HAp. It is reported that carbonate ions incorporated in HAp can cause reduction in crystallinity (decrease in crystal size) and change morphology to flatten crystals with hexagonal symmetry maintained [66].

Figure 10 shows the IR transmission spectra of arachidic acid monolayers soaked in various solutions. After soaking in SBF for 1 h, as shown in Fig. 9b, a C = O stretching peak vanished while an antisymmetric $-CO_2^-$ stretching peak correspondingly appeared. It is worthwhile to note that the $-CO_2^-$ stretching vibration formed a doublet at 1576 and 1543 cm^{-1}. Figure 10 gives the IR spectra of the arachidic acid monolayers soaked in an aqueous solution containing Ca^{2+} and/or Na^+ (Fig. 10b–d). Compositions of LB film aqueous soaking solutions are presented in Table 2. When the LB films were soaked in $CaCl_2$ and/or NaCl solutions, a C = O stretching absorption peak could be found at 1702 cm^{-1}, indicating the existence of nonionized COOH, and an antisymmetric $-CO_2^-$ stretching peak was simultaneously found as a broad singlet at 1558 cm^{-1}. Figure 10e shows the IR spectrum of the arachidic acid LB film soaked in $CaCl_2$ aqueous solution for 1 h and subsequently in K_2HPO_4 aqueous solution for 1 h. The antisymmetric $-CO_2^-$ stretching peak showed a doublet at the same wavenumber region as that of the SBF-soaked monolayer.

The arachidic acid LB film surface is negatively charged under the simulated body environment, as determined from zeta-potential measurements[2]. The cations should first adsorb on the carboxyl groups; therefore, when the monolayer was soaked in $CaCl_2$ or NaCl solutions, the divalent Ca^{2+} ion or monovalent Na^+ ion could be adsorbed on it. In the $CaCl_2$/NaCl mixed solution the divalent and monovalent cations could both adsorb on the arachidic acid monolayer. The IR spectra for the monolayers soaked in $CaCl_2$ and/or

[2] We evaluated the zeta-potentials of the LB films in the simulated body environment. The values of arachidic acid and stearyl amine monolayers were – 61 and + 41 mV, respectively, while that of the fused silica substrate without LB monolayer was – 41 mV. The negative zeta-potential for the arachidic acid monolayer corresponded to a charged group $-CO_2^-$ and the positive potential for the stearyl amine monolayer corresponded to a charged group $-NH_3^+$. The electrostatic properties of the LB monolayer surfaces depend on the functional groups

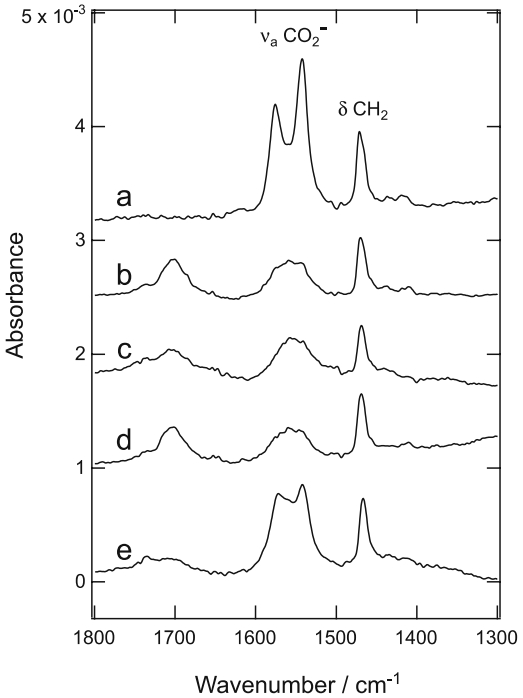

Fig. 10 IR transmission spectra of arachidic acid LB films soaked in various solutions: **a** SBF for 1 hour; **b** $CaCl_2$ solution for 1 hour; **c** NaCl solution for 1 hour; **d** $CaCl_2$ and NaCl solution for 1 hour; **e** $CaCl_2$ solution for 1 hour and subsequently in K_2HPO_4 solution for 1 hour. The spectra are offset for clarity. (Reproduced with permission from [45]. © 2000 Wiley)

Table 2 Compositions of LB film aqueous soaking solutions

	Compound	Concentration (mM)
Solution 1	$CaCl_2$	2.5
Solution 2	NaCl	5.0
Solution 3	$CaCl_2$	2.5
	NaCl	5.0
Solution 4	K_2HPO_4	1.0

NaCl solutions were almost identical but very different from the IR spectra for the monolayers soaked in calcium and phosphoric ion containing solutions. When the arachidic acid LB film covered with Ca^{2+} was soaked in K_2HPO_4 solution, phosphoric ions could adsorb on the Ca^{2+} layer. Therefore, the doublet with the splitting of 33 cm^{-1} in the $-CO_2^-$ stretching peak was ascribed

to the effect of *low site symmetry* because of the adsorption of calcium ions followed by the adsorption of phosphoric ions, which reduced the symmetry of $-CO_2^-$. In SBF the calcium and phosphoric ions could adsorb on the carboxylate layer, resulting in the HAp nucleation process.

It was shown that crystallization of HAp was induced by the chemical interaction between carboxyl groups and inorganic ions in the body fluid. The carboxyl group could adsorb calcium ion and subsequently phosphoric ion upon itself. This is thought to be the initial process of HAp nucleation.

2.4 In-Situ IR Spectral Measurement in HAp Crystallization

As the controlling mechanism of biominerals' crystallographic orientations, two potential models, a geometric model and a stereochemical model have been investigated [3, 4]. The geometric model is based on the idea that the close matching between lattice spacing in certain crystal faces and distances that separate functional groups periodically arranged on the organic surface determines the crystallographic features. The stereochemical model can be described as follows: when inorganic ions bind to the organic matrices, the resultant atomic arrangement around each organic functional group binding inorganic ions resembles the specific crystal structure to such an extent that the interfacial energy associated with nucleation of the crystal is specifically lowered. However, macromolecules often display considerable molecular dynamics in their surface residues as well as along the polypeptide or polysaccharide backbone. The static models should be inadequate to examine the biomineralization processes in a comprehensive manner. Accordingly, to reveal the principles governing biomineralization processes, behaviors of the organic matrix during the biominerals formation should be studied. In the present work, we attempted to study the HAp nucleation process in-situ. We employed IR external reflection spectroscopy for the in-situ analysis of the nucleation process. The external reflection spectroscopy is a powerful tool to probe the structures of organic thin films at air-water interfaces [28, 67, 68]. Structural changes of Langmuir monolayer films with carboxyl groups, which are capable of inducing HAp nucleation, were studied during HAp crystallization.

Arachidic acid was spread on a subphase of distilled water or SBF. The residual organic film upon the subphase (Langmuir monolayer film) was subjected to the in-situ IR spectra measurement. A Langmuir trough was built into a grazing angle accessory in the sample chamber of an IR spectrometer, and the external reflection spectra for the organic thin films at the air-solution interfaces were recorded (Fig. 11). The incident beam was nonpolarized and irradiated at the air-solution interfaces at a near-normal incidence (10°). The spectrum obtained with the film was ratioed with the background spectrum collected without the film.

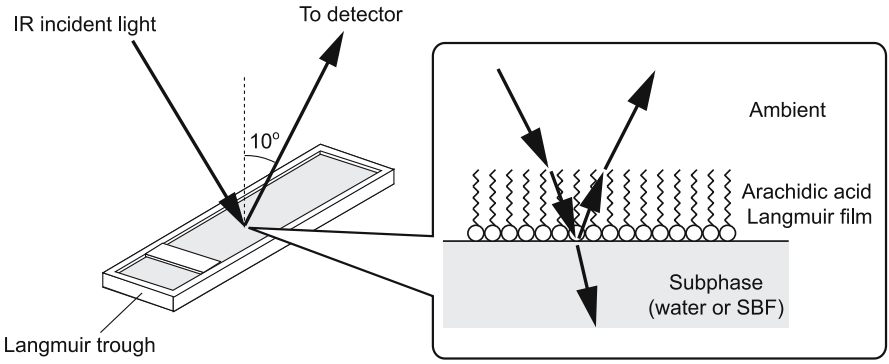

Fig. 11 Schema of the IR external reflection spectroscopy accessory

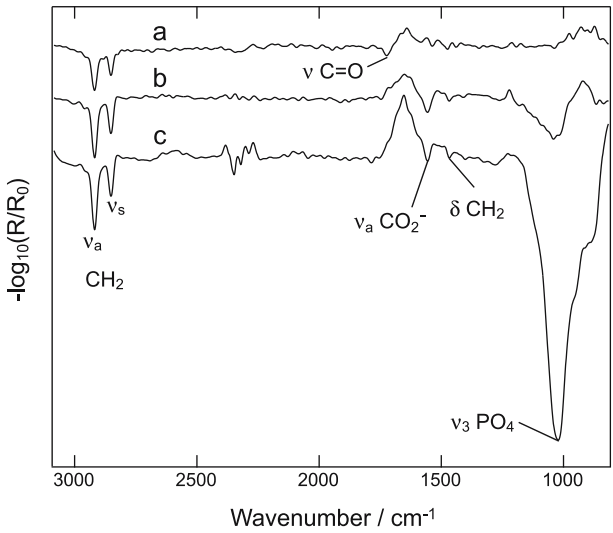

Fig. 12 IR external reflection spectra of arachidic acid Langmuir monolayer film: **a** on pure water subphase; **b** on SBF; **c** 12 hours later of **b**. (Reproduced with permission from [43]. © 2005 The Ceramic Society of Japan)

Figure 12 gives IR spectra of arachidic acid monolayer films spread on pure water and SBF. In the absorption band found in the 2800–3000 cm^{-1} region, the peaks at 2920 and 2850 cm^{-1} were assigned to the antisymmetric and symmetric vibrations of the methylene groups (– CH_2 –), respectively. Theoretical calculations using classical electromagnetic theory have been studied for organic thin films at the air-solution interfaces [69, 70]. At 10° incidence, the condition used in the present study, the *E* field of the light is parallel to the solution surface. Hence, vibrations that have dipole moments parallel to the surface are preferentially observed. The dipole moments of the methylene

groups' vibrations are perpendicular to the alkyl chain axis of the arachidic acid molecule. Therefore, the alkyl chains should be rather vertical on the surfaces of the subphase. The appearance of these absorption bands means that the Langmuir monolayer film of arachidic acid was successfully formed on the subphase.

As to the Langmuir film on the pure water, an absorption band was found around 1700 cm^{-1}, which was assigned to the stretching mode of C = O in a carboxyl group. This band indicates that the arachidic acid molecules on the pure water subphase were not ionized entirely but some molecules were kept in a nonionized state – COOH. In Fig. 12b, a C = O stretching band vanished while an antisymmetric – CO_2^- stretching band correspondingly appeared, indicating that the carboxyl groups were ionized by adsorbing ions in SBF. In the spectrum, an IR band ascribed to PO_4 was also found at 1030 cm^{-1}. The spectrum from the Langmuir film laid upon the SBF subphase for 12 hours is shown as Fig. 12c. The absorption band ascribed to PO_4 grew much stronger, indicating that HAp crystal nucleation had proceeded below the Langmuir film. These results agree with our knowledge that the carboxyl groups in the Langmuir monolayer film act as nucleation centers for HAp crystals formation.

Spectra of the C – H stretching region taken during the HAp nucleation process are shown in Fig. 13. Concurrently with the HAp nucleation, the intensities of the antisymmetric and symmetric methylene stretching vibrations varied with time, while their peak positions remain the same. The serial

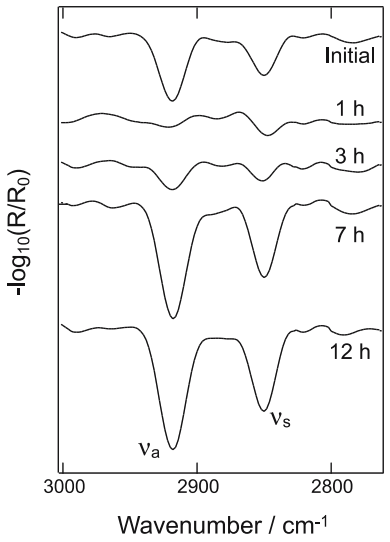

Fig. 13 Spectral changes in C – H stretching region during HAp crystallization under arachidic acid Langmuir monolayer film at the air-solution (SBF) interface. The elapse times are initial (0 hour), 1 hour, 3 hours, 7 hours and 12 hours from *top* to *bottom*. (Reproduced with permission from [43]. © 2005 The Ceramic Society of Japan)

change in the absorption intensities did not occur when the Langmuir film is placed upon a pure water subphase, and should be a characteristic phenomenon of the Langmuir films below which HAp nucleation proceeds. The C – H stretching band intensities shrank to almost nothing at 1 hour after crystallization started, and then increased again to become larger than the initial state. The intensities of the antisymmetric and symmetric vibrations of the methylene groups decreased, indicating that the alkyl chains reoriented away from the subphase surface normal. The changes in the C – H stretches indicate the occurrence of conformation changes in the Langmuir film. For long-chain hydrocarbon molecules, the wavenumbers of the antisymmetric and symmetric vibrations are conformation sensitive due to perturbation by Fermi resonance, and that they can be correlated with the ordering of the hydrocarbon chains. Lower wavenumbers are characteristic of highly ordered all-*trans* conformations, while the number of gauche conformation (the disorder of the chains) increases with increasing wavenumbers [71, 72]. The peak positions of the methylene groups' vibrations in this experiment, 2920 and 2850 cm^{-1}, correspond to ordered all-*trans* conformations. Throughout the structural change of Langmuir monolayer film associated with HAp nucleation, no distortion in the molecular structure of arachidic acid was detected. Hence, the conformation changes in the Langmuir film was not triggered by intermolecular interactions among alkyl chains. Arachidic acid molecules incorporated in the Langmuir film are facing the SBF surface directly with their carboxyl groups, and the carboxyl groups act as nucleation centers for HAp. The adsorption of calcium ions to carboxyl groups followed by the adsorption of phosphoric ions results in the formation of embryonic clusters of ions. When the expenditure of the free energy required for creating a new interface is overcome by the energy released in the formation

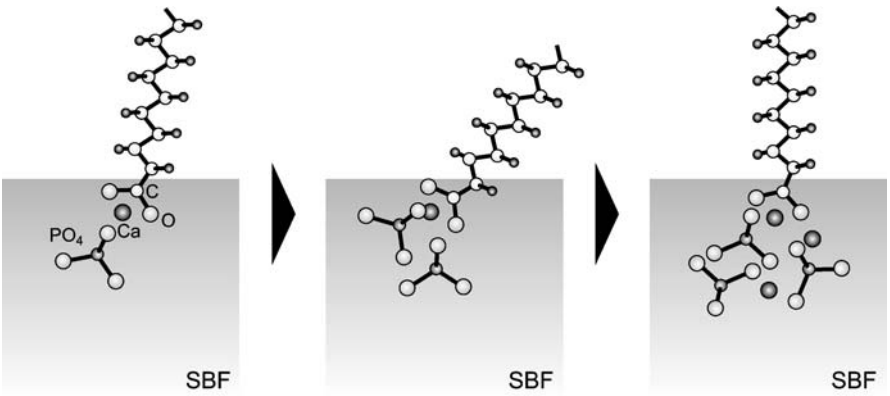

Fig. 14 Schema showing the probable HAp nucleation process mediated by the arachidic acid monolayer and associated structural change of the organic monolayer. (Reproduced with permission from [43]. © 2005 The Ceramic Society of Japan)

of chemical bonds in the solid phase, the embryonic clusters can act as the HAp crystal nuclei and spontaneous crystal growth occurs. With the formation of embryonic clusters composed of carboxyl groups and inorganic ions, the hydrocarbon chains connected to the carboxyl groups should change their conformation, i.e., their positions or inclinations to the SBF surface (Fig. 14). The present result implies that the organic matrices change their structures to induce HAp nucleation, and adapt themselves to optimize geochemical or stereochemical fit to the grown HAp crystals.

The present study revealed that organic matrices that can induce HAp nucleation change their structures during HAp crystallization. The organic matrices should not be treated as a rigid template, but their structural changes associated with the formation of crystal embryos should be taken into account, when the biomineralization mechanism is discussed. At least, the matching between lattice spacing in crystal faces and periodicity in functional group arrangement on the organic surfaces should not be the principal cause of the crystallographic features determination.

3 Atomic Scale {100} Interfacial Structure in HAp

To enable discussion on the interfacial interactions between HAp and organic substances, a thorough understanding of the surface structure and composition of HAp is fundamental. Apart from the importance of HAp as a constituent of biomimetic materials, surface structure determination of HAp is still very significant for the basic understanding of this material. For instance, morphology of crystals is generally dominated by the surface energy states of crystal faces. The surface energy states cannot be discussed without the knowledge of the atomic structure. Although the bulk structure of HAp has been extensively studied, the surface structure of HAp is poorly studied. Recent developments in surface science are clarifying surface structures of various materials at atomic scale. However, the complexity of the crystal structure, lack of electric conductivity and weakness against various probes prevent the study of the surface structure of HAp.

Both natural and synthetic HAp crystals are often facetted with the possible six equivalent faces, expressed as {100} planes in hexagonal symmetry. As described in Sect. 2.2, carboxyl groups can react to the {100} surfaces of HAp during its crystallization process. Hence, the surface structure of {100} planes is especially important. We have investigated the structural termination of sintered HAp crystals at the interfaces parallel to the {100} plane using high-resolution transmission electron microscopy (HRTEM) [73]. We examined crystalline-amorphous interfaces formed by the electron beam damage, and grain boundaries parallel to {100}. These structures must be related to a stable atomic arrangement of the {100} surfaces of HAp.

Synthetic HAp powder was sintered to be a dense specimen. XRD study indicated that the specimen consisted of only apatite as a crystalline phase. The FT-IR spectrum showed absorption bands at 3570 and 630 cm^{-1} which are ascribed to the hydroxyl stretching and librational modes in HAp, respectively [64]. No absorption band related to carbonate ions was observed [74]. As a result, it was confirmed that the specimen was pure HAp, carbonate-free and not dehydrated by sintering. Sintered HAp was polished mechanically, and thinned to electron transparency by argon ion-milling. HRTEM observations were performed at 200 kV of accelerating voltage. Details in the obtained images were interpreted to provide atomic information by comparison with multi-slice simulated images [75]. The simulated images were calculated using MacTempas software (Total Resolution Co).

Figure 15 shows a view of the HAp structure observed down to [001] and Fig. 16 indicates corresponding simulated HRTEM images as functions of defocus values and specimen thickness. The simulated images were calculated at two defocus values. Hexagonally arranged bright spots which correspond to Ca1 sites are distinctive at the defocus value around – 42 nm (Scherzer defocus) with the specimen thickness larger than 7.5 nm. These bright contrasts are due to dense packing of Ca ions along the [001] direction (hereafter referred as Ca1 columns). On the other hand, a characteristic hexagonal pinwheel-like contrast appears around OH columns in the structure when the defocus value is around – 5 nm and the specimen thicker than 10 nm [76]. These two characteristic features are useful to make correspondence between the image contrasts and the atomic structure of HAp. In the following section, the former focusing condition is referred as DF1 and the latter as DF2.

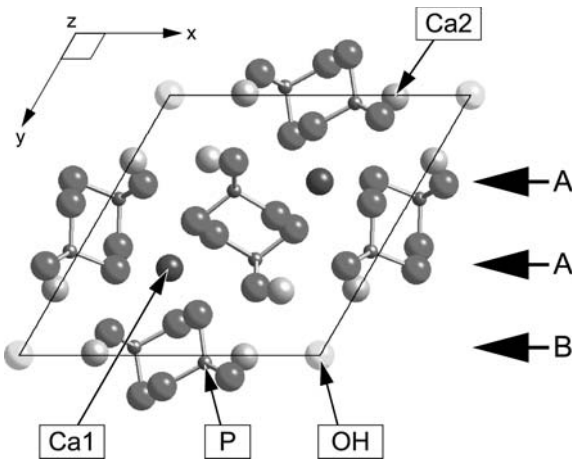

Fig. 15 HAp crystal structure observed along ⟨001⟩. The planes "A" and "B" are the possible positions where a HAp structure can be terminated

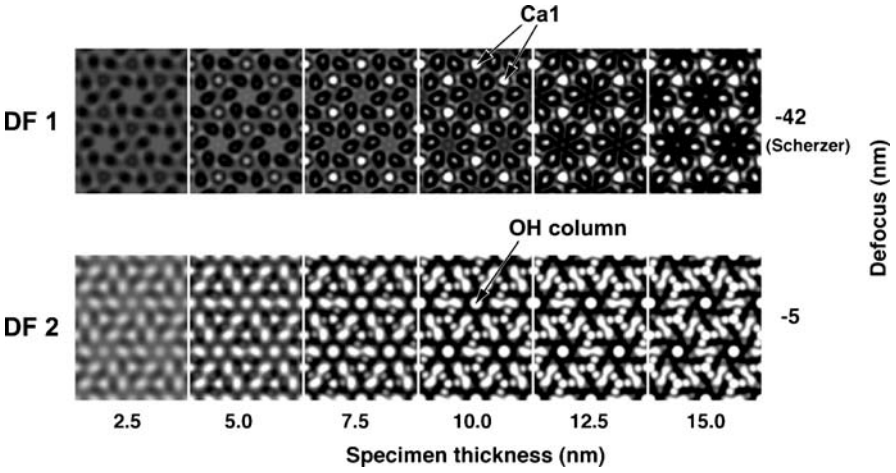

Fig. 16 HRTEM images simulated for a HAp structure along ⟨001⟩: multislice simulations were performed at two defocus values (DF). The *hexagonally arranged bright spots* at $DF = -42$ nm (Scherzer defocus) correspond to Ca1 sites. A characteristic pinwheel contrast corresponding to the OH column appears at $DF = -5$ nm. (Reproduced with permission from [73]. © 2002 The American Ceramic Society)

When a HAp crystal was oriented as its ⟨001⟩ direction was parallel to the incident beam and observed at high magnification, characteristic radiation damage was formed in the crystal by the electron beam. Figure 17 shows a HRTEM image (DF1 condition) of the damaged crystal formed by radiation lasting a few minutes with a beam current density of 1–2 A/cm^2 on the specimen. Hexagonally shaped areas, whose boundaries are parallel to {100}, are observed in which the material is amorphized. Examination of the contrast in the remaining crystal adjacent to the boundaries indicates that the crystal thickness is at least 5–10 nm. As a result the amorphized regions are regarded as three-dimensional hexagonal prisms surrounded by {100} planes of the HAp crystal. Such hexagonally shaped damaged regions in HAp have already been reported [77]. However, it is not possible to discuss the atomic structure at the interfaces as described below until sharp HRTEM images such as those shown in this work are available. Figure 18 represents a HRTEM image (DF2 condition) of a considerably damaged area. The contrasts at several interfaces between crystalline and amorphous regions (indicated by the arrowheads in the figure) are almost identical. It is also observed in several places that the contrast in the crystalline region is sharply changed with the {100} plane as the boundary, suggesting that the crystal thickness is step-likely changed.

Figure 19a shows a magnified image at one of the {100} crystalline-amorphous interfaces indicated by the arrowheads in Fig. 18. To determine the terminated structure of HAp in this image, we performed the multi-slice image simulations using artificial large unit cells where almost the upper half

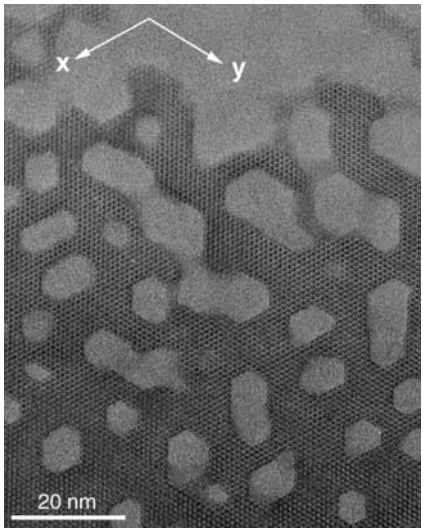

Fig. 17 HRTEM image observed for a HAp crystal in which the electron radiation damage occurred: the beam direction is ⟨001⟩. The defocus is close to the Scherzer conditions. (Reproduced with permission from [73]. © 2002 The American Ceramic Society)

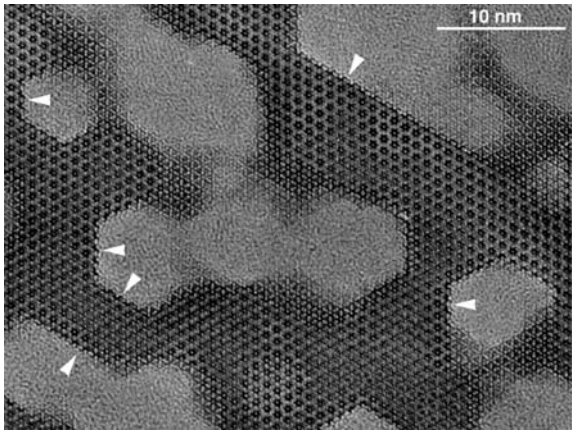

Fig. 18 HRTEM image of electron radiation damage in HAp at $DF = -5$ nm. Notice that the contrasts at the boundaries of the crystal, indicated by the *arrowheads*, are almost identical. (Reproduced with permission from [73]. © 2002 The American Ceramic Society)

is vacant and the lower is the atomic arrangement of HAp with various terminations. Figure 19b,c indicates the simulated image of the {100} interface that agrees best with the experimental one (Fig. 19a) and the termination model used in the simulation, respectively. At the interface, the HAp crystal struc-

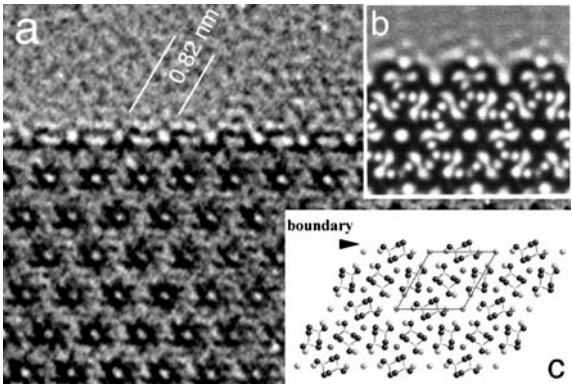

Fig. 19 Observed (**a**) and simulated (**b**) images of the {100} boundary of HAp. The **b** image was calculated using the boundary structure model at the *bottom right* of the figure (**c**). (Reproduced with permission from [73]. © 2002 The American Ceramic Society)

ture is terminated with the plane on which the OH columns, Ca2 site and PO_4 tetrahedra exist. Simulation images for structure models without outermost OH ions or oxygen atoms coordinating Ca2 and P were identical to Fig. 19b because of their weak charge potential. Therefore, for instance, whether OH ions reside in the outermost OH columns or not cannot be discussed.

In addition to the crystalline-amorphous interfaces formed by radiation damage, we tried to determine the atomic structure of the {100} planes at the grain boundaries in the specimen. Figure 20 shows a result of HRTEM recording at the grain boundary where the lower grain is aligned along ⟨001⟩ and attached to the upper grain with stepped {100} planes. The original image, which was recorded at the DF1 condition, was compressed to one third in the horizontal direction to make the boundary clear. The lattice fringe in the upper grain reaches to the grain boundary, indicating the boundary was not damaged during the observation and recording. The {100} terraces in the HAp structure are terminated with the specific contrast as indicated by the arrowheads in Fig. 20. The tracing from the inside of the crystal revealed that a pair of horizontal white dot rows (denoted "A" at the left of the figure) corresponds to Ca1 columns and OH columns locate at the dark lines ("B") between them (see also Fig. 15). The contrasts of the {100} terraces at the boundaries are all at these dark lines, suggesting the HAp structure is terminated at the plane connecting the OH columns. This result is the same as that obtained at the crystalline-amorphous interfaces as described above.

The atomic arrangement observed at the crystalline-amorphous interface and grain boundary is probably one of the stable structures for the {100} surface of HAp. This terminated structure is the same as the edge of the cluster model in amorphous calcium phosphate proposed from X-ray diffraction study [78]. When the HAp structure is amorphized by electron beam radia-

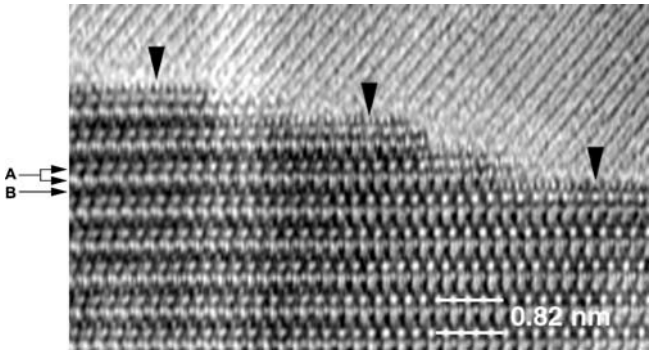

Fig. 20 HRTEM image of a grain boundary in HAp. The original image was compressed to one-third in the horizontal direction to make the boundary structure clear. The planes denoted "A" and "B" correspond to those given in Fig. 15. (Reproduced with permission from [73]. © 2002 The American Ceramic Society)

tion, or when the crystal growth proceeds on {100} facets by sintering, the crystal may be broken and grow with this cluster like a block. It has also been proposed that clusters of similar size exist in solutions supersaturated with HAp and the HAp crystal in the solutions grows by adsorption of the clusters [79].

We observed the crystalline-amorphous interfaces and the grain boundaries of sintered HAp by HRTEM. When the interfaces or boundaries are parallel to {100}, both of them showed the same atomic arrangement for the termination of the HAp crystal. The crystal structure of HAp is terminated at a plane crossing the OH columns on which Ca2 sites and PO_4 tetrahedra are located. This atomic arrangement for the {100} surfaces of HAp probably has a low surface energy and may be common in HAp crystals formed by various conditions.

4 Concluding Remarks

When the results of above mentioned HAp crystallization experiments on the organic molecule assemblages and the knowledge withdrawn from the HRTEM observations are combined, a model for HAp crystals nucleation and growth can be developed (Fig. 21). Carboxyl groups on the organic matrices act as nucleation centers for HAp. The carboxyl groups could adsorb inorganic ions upon themselves; especially calcium ions and phosphoric ions were adsorbed in the body environment. The resultant embryonic clusters of ions composed of the carboxyl group, calcium and phosphoric ions are the origination of HAp formation. The embryo could correspond to the Ca2 site and PO_4 tetrahedron on the most stable HAp {100} surface, and the HAp crystals

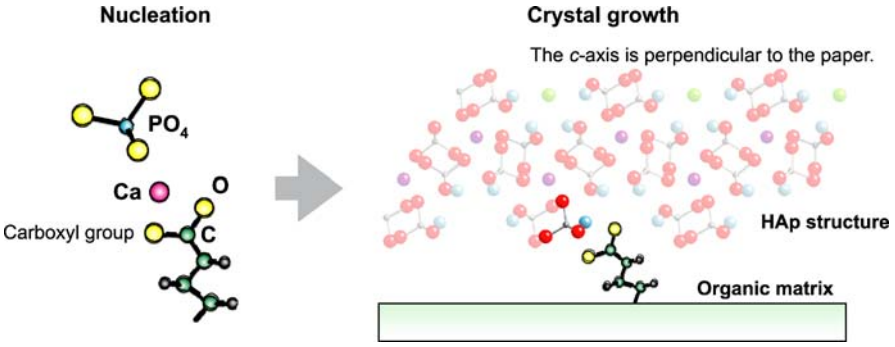

Fig. 21 The mechanism of HAp mineralization proposed in view of the experimental results

grow with their {100} surfaces parallel to the interface. Actually, changes in bond energies caused by water molecules mediation, lattice relaxations of the crystal surface structure, and molecular movements in the surface residues of the organic matrices might result in more complex phenomena at the interface. Continued investigations on this issue are expected to offer further valuable insights into biomimetic materials chemistry.

Acknowledgements I am pleased to acknowledge the collaborators who have supported and nurtured this work, in particular, Prof. Junzo Tanaka (Tokyo Institute of Technology), Prof. Toshihiro Kogure (University of Tokyo) and Ms. Yuri Kumagai (Japan Science and Technology Agency, CREST). More recently, the support of Dr. Koji Watari (AIST) has been significant.

References

1. Addadi L, Weiner S (1992) Angew Chem Int Ed Engl 31:153
2. Weiner S, Addadi L, Wagner HD (2000) Mat Sci Eng C 11:1
3. Mann S (2001) Biomineralization: principles and concepts in bioinorganic materials chemistry. Oxford University Press, New York
4. Mann S (1996) Biomineralization and biomimetic materials chemistry. In: Mann S (ed) Biomimetic materials chemistry. VCH Publishers, New York, p 1
5. Dujardin E, Mann S (2002) Adv Mater 14:775
6. Estroff LA, Hamilton AD (2001) Chem Mater 13:3227
7. Li C, Kaplan DL (2003) Curr Opin Solid State Mat Sci 7:265
8. Sarikaya M, Tamerler C, Jen AKY, Schulten K, Baneyx F (2003) Nature Mater 2:577
9. Mann S, Archibald DD, Didymus JM, Douglas T, Heywood BR, Meldrum FC, Reeves NJ (1993) Science 261:1286
10. Mann S (1993) Nature 365:499
11. Mann S (1988) Nature 332:119
12. Aoki H (1992) Science and medical applications of hydroxyapatite. Ishiyaku-Euro America, Tokyo
13. Jackson SA, Cartwright AG, Lewis D (1978) Calcif Tiss Res 25:217

14. Posner AS (1985) Clin Orthop Rel Res 200:87
15. Bloom W, Fawcett DW (1994) Bone. In: A textbook of histology. Chapman & Hall, New York, p194
16. Bonfield W, Grynpas MD (1977) Nature 270:453
17. Katz JL (1980) Nature 283:106
18. Sasaki N, Matsushima N, Ikawa T, Yamamura H, Fukuda A (1989) J Biomech 22:157
19. Wagner HD, Weiner S (1992) J Biomech 25:1311
20. Kikuchi M, Itoh S, Ichinose S, Shinomiya K, Tanaka J (2001) Biomaterials 22:1705
21. Kikuchi M, Matsumoto HN, Yamada T, Koyama Y, Takakuda K, Tanaka J (2004) Biomaterials 25:63
22. Petty MC (1996) Langmuir-Blodgett films: an introduction. Cambridge University Press, New York
23. Roberts G (ed) (1990) Langmuir-Blodgett films. Plenum Press, New York
24. Sagiv J (1980) J Am Chem Soc 102:92
25. Ulman A (1991) An introduction for ultrathin organic films: from Langmuir-Blodgett to self-assembly. Academic Press, San Diego
26. Heywood BR, Mann S (1992) Adv Mater 4:278
27. Heywood BR, Mann S (1994) Adv Mater 6:9
28. Berman A, Ahn DJ, Lio A, Salmeron M, Reichert A, Charych D (1995) Science 269:515
29. Zhao XK, Yang J, McCormick LD, Fendler JH (1992) J Phys Chem 96:9933
30. Lin H, Sakamoto H, Seo WS, Kuwabara K, Koumoto K (1998) J Crystal Growth 192:250
31. Heywood BR, Mann S (1994) Chem Mater 6:311
32. Mann S, Heywood BR, Rajam S, Walker JBA (1991) J Phys D Appl Phys 24:154
33. Rajam S, Heywood BR, Walker JBA, Mann S, Davey RJ, Birchall JD (1991) J Chem Soc Faraday Trans 87:727
34. Heywood BR, Rajam S, Mann S (1991) J Chem Soc Faraday Trans 87:735
35. Heywood BR, Mann S (1992) J Am Chem Soc 114:4681
36. Mann S, Heywood BR, Rajam S, Birchall JD (1988) Nature 334:692
37. Volkmer D, Fricke M, Vollhardt D, Siegel S (2002) J Chem Soc Dalton Trans 4547
38. Ahn DJ, Berman A, Charych D (1996) J Phys Chem 100:12455
39. Berman A, Charych D (1999) J Crystal Growth 198/199:796
40. Berman A, Charych D (1999) Adv Mater 11:296
41. Buijnsters PJJA, Donners JJJM, Hill S, Heywood BR, Nolte RJM, Zwanenburg B, Sommerdijk NAJM (2001) Langmuir 17:3623
42. Lin H, Seo WS, Kuwabara K, Koumoto K (1996) J Ceram Soc Japan 104:291
43. Sato K, Kumagai Y, Ikoma T, Watari K, Tanaka J (2005) J Ceram Soc Japan 113:112
44. Sato K, Kumagai Y, Watari K, Tanaka J (2004) Langmuir 20:2979
45. Sato K, Kumagai Y, Tanaka J (2000) J Biomed Mater Res 50:16
46. Sato K, Kogure T, Kumagai Y, Tanaka J (2001) J Col Int Sci 240:133
47. Küther J, Seshadri R, Knoll W, Tremel W (1998) J Mater Chem 8:641
48. Travaille AM, Donners JJJM, Gerritsen JW, Sommerdijk NAJM, Nolte RJM, Kempen HV (2002) Adv Mater 14:492
49. Küther J, Tremel W (1997) Chem Commun 2029
50. Küther J, Tremel W (1998) Thin Solid Films 327–329:554
51. Han YJ, Aizenberg J (2003) J Am Chem Soc 125:4032
52. Tanahashi M, Matsuda T (1997) J Biomed Mater Res 34:305
53. Kokubo T, Ito S, Huang ZT, Hayashi T, Sakka S, Kitsugi T, Yamamuro T (1990) J Biomed Mater Res 24:331

54. Kokubo T, Kushitani H, Sakka S, Kitsugi T, Yamamuro T (1990) J Biomed Mater Res 24:721
55. Elliott JC (1994) Structure and chemistry of the apatites and other calcium orthophosphates. Elsevier Science, Amsterdam
56. Kogure T (1997) Mineral J 19:155
57. Kogure T, Murakami T (1998) Am Mineral 83:358
58. Posner AS, Perloff A, Diorio AF (1958) Acta Crystallogr 11:308
59. Kay MI, Young RA (1964) Nature 204:1050
60. Elliot JC, Mackie PE, Young RA (1973) Science 180:1055
61. Young RA, Holcomb DW (1982) Calcif Tissue Int 34:S17
62. Nelson DGA, McLean JD (1984) Calcif Tissue Int 36:219
63. Ohtsuki C, Kokubo T, Yamamuro T (1992) J Non-Cryst Solids 143:84
64. Fowler BO (1974) Inorg Chem 13:194
65. Suetsugu Y, Shimoya I, Tanaka J (1998) J Am Ceram Soc 81:746
66. LeGeros RZ (1994) Biological and synthetic apatites. In: Brown PW, Constantz B (eds) Hydroxyapatite and related materials. CRC Press, Boca Raton, p 3
67. Sakai H, Umemura J (1993) Chem Lett 2167
68. Sakai H, Umemura J (2002) Colloid Polym Sci 280:316
69. Dluhy RA (1986) J Phys Chem 90:1373
70. Fina LJ, Tung Y-S (1991) Appl Spectrosc 45:986
71. Gericke A, Hühnerfuss H (1994) Thin Solid Films 245:74
72. Gericke A, Hühnerfuss H (1995) Langmuir 11:225
73. Sato K, Kogure T, Iwai H, Tanaka J (2002) J Am Ceram Soc 85:3054
74. Rey C, Collins B, Goehl T, Dickson IR, Glimcher MJ (1989) Calcif Tissue Int 45:157
75. Cowley JM, Moodie AF (1957) Acta Crystallogr 10:609
76. Henning PA, Landa-Cánovas AR, Larsson A-K, Lidin S (1999) Acta Crystallogr B 55:170
77. Nelson DGA, McLean JD, Sanders JV (1982) Radiat Eff Lett 68:51
78. Posner AS, Betts F (1975) Acc Chem Res 8:273
79. Onuma K, Ito A (1998) Chem Mater 10:3346

Top Curr Chem (2007) 270: 155–185
DOI 10.1007/128_050

Published online: 19 October 2006

Detoxification Biominerals

Clare K. Carney · S. Reese Harry · Sarah L. Sewell · David W. Wright (✉)

Department of Chemistry, Station B. 351822, Nashville, TN 37235, USA
david.wright@vanderbilt.edu

Abstract Biominerals are most often considered in either their more traditional roles as critical structural components of organisms (e.g., teeth, the siliceous shell of diatoms) and important ion reservoirs for cellular function (Ca^{2+} and bone) or in their highly evolved functional roles (e.g., magnetotactic sensing, buoyancy/balance regulation). Increasingly, it is becoming apparent that biominerals also play an important protective role by acting as critical detoxification sinks within certain organisms. Thus, organisms ranging from protozoa to eukaryotes utilize the same principles of biomineralization (cellular processing, supramolecular organization, and interfacial recognition) used to form such materials as Abalone nacre to efficiently remove potentially toxic species from their immediate environment. Thus, as understanding how biological systems exert their nanoscale control over structural biominerals has provided important biomimetic routes to novel materials synthesis, similar advances in both therapeutic development and materials synthesis can be made through the study of detoxification biominerals.

Keywords Biomineralization · Cadmium sulfide · Detoxification · Hemozoin · Noble metals

Abbreviations

ABC	ATP-binding cassette
AtPCS1	PCS from *Arabidopsis*
BNT	Bionucleating template
CD	Circular dichroism
DTT	Dithiolthreitol
EDS	Energy dispersive spectroscopy
EM	Electron micrograph
EPR	Electron paramagnetic resonance
FEISEM	Field emission inlens scanning electron microscopy
Fe(III)PPIX	Ferric protoporphyrin IX
FT-IR	Fourier transform infrared spectroscopy
GSH	Glutathione
HRG	Histidine-rich glycoprotein

HRP	Histidine-rich protein
Ni(II)PcS	Nickel tetrasulfonatophthalocyanine
PCn	Phytochelatin
PcS	Tetrasulfonatophthalocyanine
PCS	Phytochelatin synthase
PPIX	Protoporphyrin IX
SEM	Scanning electron microscope
SDS	Sodium dodecyl sulfate
SDS-PAGE	SDS polyacrylamide gel electrophoresis
SPRB	Surface plasmon resonance band
TEM	Transmission electron microscope
TFE	Tetrafluoroethylene
TWEEN	80 Polyoxyethylene sorbitan monooleate
XRD	X-ray powder diffraction
Zn(II)PPIX	Zinc protoporpyrin IX

1 Hemozoin Biomineralization

Much of Nature's evolutionary success is reflected in its ability to tightly control extremely complex reactions. Biomineralization, a process with roots beginning over 570 million years ago, is a magnificent example of Nature's ability to manipulate limited resources and incorporate them into a larger functional structure, under highly regulated conditions, to produce a stunning array of materials. Often-cited examples include the formation of bones and shells. These provide a fossil record that yields critical insights into history and anthropology [1]. Other common examples include teeth, magnetites [2, 3], gold deposits in unicellular organisms [4], silicates in diatoms [5], and the calcium carbonates and calcium phosphates in nonvertebrate shells [6, 7]. Under metal ion stress, organisms use biomineralization as a method of detoxification. A unique example of such a detoxification biomineral is hemozoin, produced in a variety of blood-feeding organisms including *Plasmodium falciparum, Schistosoma mansoni, Rhodinius prolixus*, and *Heamoproteus columbae* [8–11].

P. falciparum is the most common and deadly species of the human malaria parasite. Once a host has been bitten by the vector mosquito, parasitic sporozoites travel to the host liver where they undergo multiple asexual fission, resulting in merozoites. After 9–16 days in the liver, merozoites are released into the blood stream and invade erythrocytes. After 48 h, the infected erythrocytes are ruptured, releasing the parasite again into the bloodstream to infect more red blood cells. To complete the cycle, a feeding mosquito bites the infected human and ingests gametocytes, which undergo sexual reproduction in the mosquito gut resulting in sporozoites that travel to its salivary gland where they are passed to another human host [12].

Hemozoin formation occurs during the intraerythrocytic stage of the malaria lifecycle (Fig. 1). Inside the red blood cells, the parasites multiply and degrade host hemoglobin in a specialized acidic (pH 4.8–5.2) lysosome called the digestive food vacuole [13–15]. The ordered catabolism of hemoglobin results in the release of toxic free heme. Lacking heme oxygenase, the first enzyme in the mammalian heme degradation pathway, levels of free heme could reach as high as 400 mM [14]. Free heme poses multiple challenges to the parasite including inhibition of digestive vacuole proteases, catalysis of lipid peroxidation, generation of oxidative free radicals and eventual lysis [16, 17]. Since the parasite ingests more than its own weight in host blood every few days, the potential damaging effects of free heme are significant [10]. Consequently, the survival of the parasite depends upon its ability to obtain requisite amino acids for growth and development from hemoglobin catabolism while, at the same time, minimizing the toxicity of the released heme. To circumvent this challenge, a detoxification pathway has evolved whereby the free heme is aggregated into hemozoin, an insoluble, nontoxic biomineral produced exclusively by hemotophagous organisms.

Pagola et al. have shown that the structure of hemozoin is a dimer of five-coordinate ferric protoporphyrin IX (Fe(III)PPIX) linked by reciprocating monodentate carboxylate linkages from one of the protoporphyrin IX's propionate moieties. The biomineral is composed of an extended network of these dimeric units hydrogen bonded via the second propionate group of the protoporophyrin IX (Fig. 2) [18]. Morphologically, the biomineral is composed of long, flat, smooth crystallites. The tightly constrained shape formation of these crystallites suggests controlled cellular processing and possibly templated crystallization [19]. Similar to other biominerals such as calcite or magnetite, the mineral composition of hemozoin is simple and yet its structural characterization is complex, resulting in a lattice structure that reduces the solubility of the biomineral. Other infections that result in the formation of hemozoin include *Schistosoma mansoni, Rhodinius*

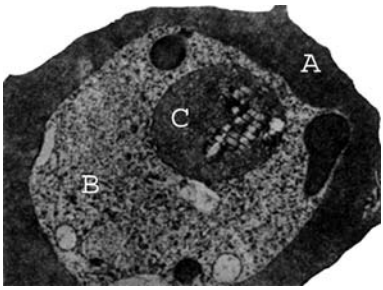

Fig. 1 Electron micrograph of hemozoin formation inside the parasitic digestive food vacuole. *A* Red blood cell, *B* parasite, *C* digestive food vacuole. Image courtesy of Daniel E. Goldberg

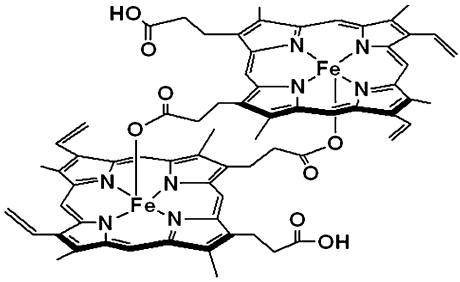

Fig. 2 Structure of hemozoin

prolixus, and *Heamoproteus columbae* and *Echinostoma trivolvis* [20, 21]. At first glance, examination of the hemozoin morphologies produced in these hematophagous species seems to illustrate a heterogeneity of surface morphology (Fig. 3). For example, the hemozoin produced by *Schistosoma mansoni* is much more spherical and heterogeneous in size, ranging from 50 nm to a few micrometers in diameter, as compared to the long, needlelike crystals seen in *P. falciparum* which are much more regular in shape. The differences of the crystal morphologies are due not to different atomic structures but rather to varying crystallization conditions. Closer examination of *S. mansoni* crystals reveals that the spherical aggregates are composed of brick-shaped crystals similar to the *P. falciparum* crystals [11].

While there is little question concerning the function of hemozoin, the mechanism of hemozoin formation remains controversial. Identifying the particular template and understanding how its supramolecular chemistry mediates hemozoin formation is critical in the development of new antimalarials that target hemozoin formation. The precise shape and size uniformity of hemozoin alludes to the tight control with which hemozoin is formed. There have been three proposed causative agents: (1) a heme polymerase, (2) a lipid-mediated process or (3) a nucleating template protein.

Early studies by Slater and Cerami, indicated the potential involvement of an enzyme in hemozoin formation. In this work, whole trophozoite lysates were extracted and reacted with heme at pH 5 to 6. The reaction resulted

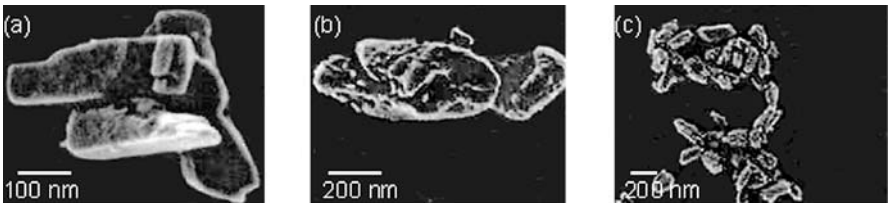

Fig. 3 FEISEM of hemozoin purified from **a** *Plasmodium falciparum*, **b** *Schistosoma mansoni*, **c** *Hemaoproteus columbae*

in the formation of hemozoin in a time-, concentration- and pH-dependent manner that was inhibited by chloroquine, an antimalarial drug. The authors proposed that the formation of the reciprocating Fe–carboxylate linkage was catalyzed by an extractable membrane-associated heme polymerase [22]. The proposed enzyme was found to be heat labile and denatured in the presence of sodium dodecyl sulfate (SDS). Similar results were obtained by Chou and Fitch using extracts from *Plasmodium berghei* (rodent malaria) [23].

This work spurred an avalanche of controversy and subsequent research. Dorn and Ridley countered the heme polymerase hypothesis with results demonstrating the ability of isolated native hemozoin (a material Ridley finds "soul-destroying" [24] to work with) or synthetic hemozoin to propagate hemozoin formation at pH 4.8 [25]. This reactivity was stable for up to 28 days and was resistant to boiling. Furthermore, formation was inhibited by SDS, indicating that the detergent may not be denaturing any enzyme but rather interfering with the assembly of hemozoin. It was concluded that the hemozoin-mediated hemozoin formation was an autocatalytic chemical process mediated by heme-derived material. Additionally, further studies attempting to repeat the work of Slater and Cerami [22] proved arduous. While this work explained hemozoin propagation and certainly challenged the heme polymerase theory, it did not provide insight into the initiation of hemozoin formation and undoubtedly left the possibility open for the involvement of a protein or enzyme in hemozoin formation [25].

Lipids were proposed as a second possible causative agent of hemozoin biomineralization when endogenous lipids were also shown to mediate hemozoin formation at acidic pH [26, 27]. Further complicating the issue was the contention that hemozoin extracts used in previous studies might have been contaminated with such phospholipids. Even the synthetic hemozoin studies potentially had such contaminants since commercial heme is prepared by extraction from intact erythrocytes [27]. A comparison of the different methods to initiate hemozoin formation confirmed the ability of lipids to initiate rapid hemozoin formation [28]. Hemozoin itself also seeded the reaction but the rate is sigmoidal, taking several days before any formation and then increasing after that point. The authors believed that the first few units take a while to form but once there, the extension is rapid [28], suggesting templated crystal growth.

Probing further into the lipid-based mechanism of hemozoin formation, Fitch and coworkers demonstrated that arachidonic, linoleic, oleic, and palmitoleic acids, 1-mono- and di-oleoylglycerol and the detergents SDS, polyoxyethylene sorbitan monooleate (TWEEN 80), and *n*-octylglucopyranoside were able to generate hemozoin from free heme at pH 5.0. It was postulated that some of the biological unsaturated lipids coprecipitate with the free heme inside the digestive vacuole providing an environment that allows for increased solubility of monomeric Fe(III)PPIX and promoting hemozoin formation [29]. Extrapolating from this line of reasoning,

a membrane sacrifice theory was proposed by Bray et al. whereby the host double-membrane transport vesicles are pinched off into the parasitic cytosome. The inner membrane of the transport vesicle is degraded by the toxic free heme released from hemoglobin catabolism, liberating from the membrane the lipids which would increase the solubility of the free heme and aid in the formation of hemozoin. In this way, the sacrifice of the inner membrane prevents further oxidative damage to the outer membrane and the rest of the parasite [30]. More recently, it has been suggested that *Schistosoma mansoni* and *Rhodnius prolixus* form hemozoin in lipid environments [11]. *S. mansoni* crystal formation occurs in close association with an electron-lucent round structure, perhaps resembling a lipid droplet. Extraction of the droplet, followed by reaction with free heme, demonstrated its ability to form hemozoin in vitro. In *R. prolixus*, the crystals are found close to perimicrovillar membrane-derived vesicles, which consist of phospholipid bilayer membranes [11].

If lipids are the bionucleating template, the mechanism of lipid-mediated hemozoin formation must facilitate hemozoin formation. Theoretically, there are several scenarios in which lipid mediation may occur. First, lipids may provide increased solubility of monomeric Fe(III)PPIX providing the requisite concentration for crystallization [29]. Next, the negatively charged hydrophobic headgroups could potentially interact with the iron of the heme, localizing a high concentration of Fe(III)PPIX. After binding, dimer formation could occur via a substitution reaction whereby the water molecule bound to the iron of one porphyrin would be replaced by the propionate side chain of a reciprocating porphyrin (50% of the propionate side chains would be deprotonated and available for binding at pH 4.8). Extension of this network would allow for the formation of the insoluble biomineral, hemozoin. It is also possible, although less likely, that the free heme intercalates into the lipid layer, leaving the negatively charged propionate residues directed out into the hydrophilic environment and primed for binding to the iron of a nearby heme molecule. This mechanism would make it difficult for the iron of the heme wedged in the lipid to interact in binding to form the requisite reciprocating linkages found in hemozoin. While there is much precedence for the involvement of lipids in hemozoin formation, much work remains to elucidate the exact role of lipid involvement in the mechanism of hemozoin formation.

Another possible participant in hemozoin formation is the histidine-rich protein (HRP). Using monoclonal antibodies to probe the proteins of the digestive food vacuole, Sullivan et al. identified two histidine-rich proteins, HRP II and HRP III, and demonstrated that these proteins could mediate the formation of hemozoin [31]. HRP II (M_R 30 kD), is composed of 51 repeats of the tripeptide His-His-Ala with 76% of the overall protein being composed of histidine and alanine residues (Fig. 4) [32]. HRP III (M_R 27 kD) is composed of 28 repeats of the tripeptide with 56% composition alanine

and histidine [33]. At physiological relevant pH (4.8), biophysical characterization of HRP II revealed its ability to bind up to 17 equivalents of heme (Fe(III)PPIX) and promote the formation of hemozoin at levels 20 times that of the background reaction [31, 34]. Additionally, hemozoin aggregation activity of HRP II was inhibited by chloroquine, destroyed by boiling, and had an activity profile with an optimal pH near 4.5, which slowed near pH 6.0 [31]. The Ala-His-His repeat motif of HRP II is reminiscent of a variety of nucleating scaffold proteins found in biomineralization [19, 35]. Here, the 3D structure of the protein yields a preorganized, functionalized surface that serves as a template for nucleation.

Given the lack of a crystallographically determined structure for HRP II, investigators have used a variety of spectroscopic methods to examine the interactions between this template and heme. Using circular dichroism (CD) spectroscopy, binding experiments of Fe(III)PPIX to HRP II demonstrated the importance of pH on the type of interactions that may occur between template and substrate. Chauhan and coworkers found that as the pH increases, heme binding to HRP II also increases but hemozoin formation decreases (Fig. 5) [36]. This inverse relationship between hemozoin formation and heme binding suggests pH-dependent modes of interaction between the protein and the substrate. Further, these studies corroborate the idea that the formation of hemozoin inside the food vacuole (where the pH is 4.8–5.0) results from the productive protein/substrate interactions and must be different from the common heme bis-histidyl binding found in other proteins such as the histidine-rich glycoprotein (HRG) [37, 38]. Based on the pH profile, the group proposed that such productive interactions result from aspartate carboxylate–metal ionic coordination interactions at the physiologically relevant pH. Additionally, the CD spectra of HRP II showed a deep negative peak at 200 nm with a shoulder at 220 nm similar to the left-handed 3_{10} helix of polyproline in tetrafluoroethylene (TFE) [36]. In such a conformation, all of the alanine residues would be aligned on one face and all the histidine and aspartate (charged) residues would be on the opposite face, yielding an amphipathic molecule [36] with a clearly defined nucleating face.

Using resonance Raman and electron paramagnetic resonance (EPR) methods to probe heme binding to HRP II, Marletta and coworkers hinted at

MVSFSKNKVLSAAVFASVLLLDNNNSAFNNNLCSKNAKGLNLNKRLLHETQAHV
DDAHHAHHVADAHHAHHAHHAADAHHAHHAADAHHAHHAADAHHAHHAADAHHA
HHAADAHHAHHAADAHHAHHAADAHHAHHAADAHHAHHAADAHHAHHAAYAHHA
HHASDAHHAADAHHAAYAHHAHHAADAHHAADAHHAAYAHHAHHAADAHHAADA
HHATDAHHAHHAADAHHATDAHHAADAHHAADAHHATDAHHAADAHHATDAHHA
ADAHHAADAHHATDSHHAHHAADAHHAAAHHATDAHHAAAHHATDAHHAAAHHE
AATHCLRH

Fig. 4 Sequence of the histidine-rich protein II (HRP II)

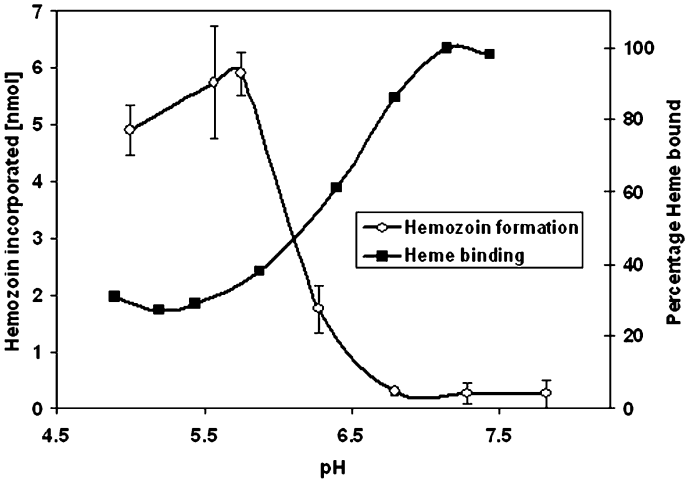

Fig. 5 Effects of pH on HRP II binding of heme and the formation of hemozoin

a bis-histidyl ligation to the heme from the template [39]. Despite the results of Lynn et al. which indicated the importance of acidic pH in heme binding and hemozoin formation, this group opted to work with the easier pH of 7.0 to avoid heme insolubility and other precipitation issues. CD measurements were used to monitor structural changes induced upon Fe(III)PPIX binding to HRP. Prior to heme addition, the CD spectrum was consistent with a random coil structure; however, upon heme binding, HRP changes to a structure more helical in nature that is most consistent with a right-handed 3_{10}-helix structure [34] similar to the left-handed 3_{10}-helix proposed by Lynn et al. [36]. Modeling HRP as a right-handed 3_{10}-helix presents a structure that aligns the histidine and aspartic acid residues on one face with the alanine residues aligned on the opposite face (Fig. 6). Modeling HRP as an α-helix does not result in this type of alignment and is therefore not as appealing a model.

Examining HRP II overexpressed in *E. coli* cells, Schneider et al. observed a species with approximately double the molecular weight of HRP II in nonreducing SDS polyacrylamide gel electrophoresis (SDS-PAGE). Formation of this species was inhibited upon addition of dithiolthreitol (DTT), a reducing reagent, suggesting the formation of an intermolecular disulfide bond. From this data, the group proposed that upon heme binding, two monomers of HRP II align with each providing one of the two histidines necessary for heme binding through axial ligation. The result is a HRP II dimer [34] whose importance cannot be determined since native HRP II has never been isolated and analyzed in this fashion. Additionally, this work was completed at pH 7.0 rather than at the acidic pH of the food vacuole, which begs the question of the relevance to the in vivo system. At the pH of the digestive food

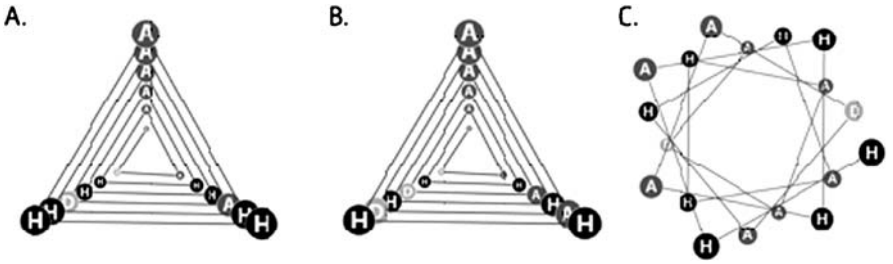

Fig. 6 HRP II repeats modeled as 3_{10}-helix and α-helix. *A* Two repeats of HHAHHAADA modeled as a 3_{10}-helix. *B* Three repeats of HHAADA modeled as a 3_{10}-helix. *C* Two repeats of HHAHHAADA modeled as an α-helices. In models *A* and *B*, the His residues align along two corners of the model and Ala residues align along the third corner. In model *A* the His repeats align next to each other and in model *B* the His residues alternate with either Ala or Asp residues. In model *C*, the His repeats are found all along the perimeter of the helix

vacuole (4.8–5.5), the p*K*a of histidine (5.8) indicates that it would remain mostly protonated (charged) whereas at pH 7.0, it would be deprotonated and therefore uncharged. Typically, a heme–histidine ligation occurs with the deprotonated form only. From a simple pH perspective, one would expect that the mechanism of reaction at pH 4.8–5.5 would likely differ from the mechanism at pH 7.0, which therefore discounts the hypothesis that binding occurs through any axial ligation. In light of the acidic pH of the acidic food vacuole, it is more likely that the aspartic acid residues (deprotonated at pH 4.8) play a vital role in recognition and binding of heme. This is not to imply that the histidine residue is insignificant, but rather that it does not work alone in the mechanism. Clearly, there must be a different mechanism at work in the in vivo system that incorporates the charged aspartic acid residues instead of relying exclusively on the histidine residues.

Working with the tandem repeat motif of HRP II [40], Wright and coworkers developed two peptide dendrimer templates (Fig. 7). The peptide dendrimers, called bionucleating templates (BNTs), were designed specifically as templates to study the epitaxial growth of hemozoin. The branched nature of dendrimers allows for the presentation of multiple nucleating sites to solution. BNT I incorporates four individual binding domains attached to the tetralysine dendrimer core for eight tri-Ala-His-His repeats, while BNT II contains two nucleating domains coupled to each of the branches of the tetralysine core, to generate a total of 16 tri-Ala-His-His repeats. Both templates tested positive against monoclonal antibodies for HRP II using a commercial test ("*Para*sight F") for *P. falciparum* malaria. The templates were also examined for their ability to form hemozoin using the in vitro heme polymerization assay developed by Sullivan and coworkers (Fig. 8) [31]. Significantly, both templates were able to mediate the formation of hemozoin in a pH-, time-, and template concentration-dependent manner. BNT II was able

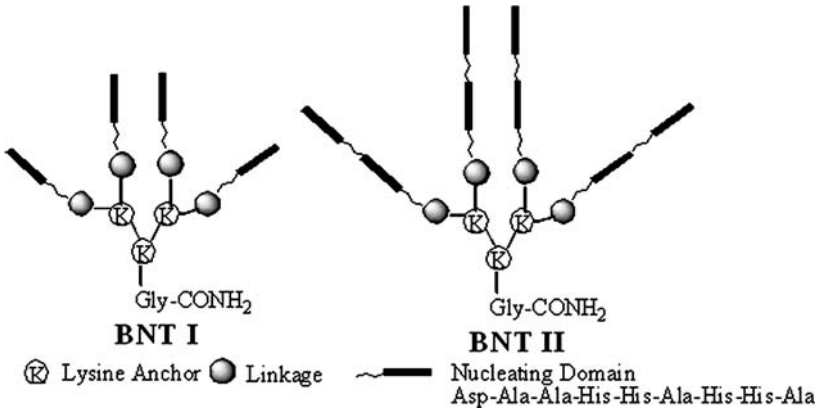

Fig. 7 Generalized diagram of dendrimeric templates

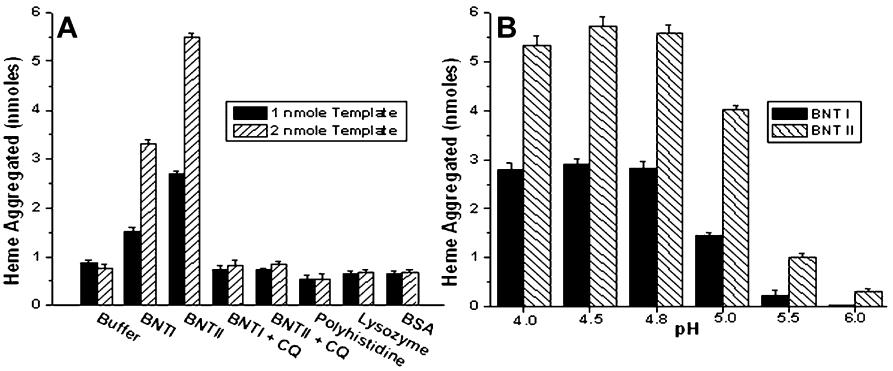

Fig. 8 **A** Hemozoin aggregation mediated by BNT I and II. **B** Effect of pH on hemozoin aggregation

to nucleate twice as much hemozoin as BNT I, and this activity was greatly decreased as the pH rose above 4.8 and approached the p*K*a of the histidine side chain (5.8). Additionally, the antimalarial chloroquine was able to completely inhibit the formation of hemozoin, consistent with previous reports of HRP II inhibition by this drug [31].

Characterization of the heme-containing product was performed using FT-IR, SEM, and XRD and compared to native hemozoin. Fourier transform infrared (FT-IR) spectroscopy reveals characteristic vibrational frequencies at 1660 cm^{-1} and 1210 cm^{-1} [41]. The scanning electron microscopy (SEM) revealed long, needle-like projections indicating a morphological similarity with native hemozoin [20]. Finally, the powder X-ray diffraction (XRD) pattern matched the published fingerprint of native hemozoin and verified the absence of crystalline heme [42]. Taken together, the characterization

confirmed that the material produced in the BNT assay is chemically and morphologically identical to native hemozoin [40].

The substrate specificity of the BNT templates was also examined. They were capable of binding not only (Fe(III)PPIX) but also protoporphyrin IX (PPIX), zinc protoporphyrin IX (Zn(II)PPIX), tetrasulfonatophthalocyanine (PcS), and nickel tetrasulfonatophthalocyanine (Ni(II)PcS) in 100 mM acetate buffer at pH 4.8 (Table 1). Working with the BNT templates, Ziegler et al. found that both were able to bind to PPIX as well as Zn(II)PPIX with binding stoichiometries similar to Fe(III)PPIX. The ability of the templates to bind the heme free of the metal negates the hypothesis that the nucleating domain binds to the metal of the heme via an axial ligation of the histidine to the iron. Furthermore, replacement of the Fe with Zn did not significantly decrease the binding, suggesting recognition of the porphyrin moiety rather than the specific metal at the core. Recognition of the skeletally similar phthalocyanines is also indicative of ligand recognition rather than specific metal binding [40]. The substrate binding results obtained from the template studies indicated that the recognition of the substrate by HRP is not dependent upon the axial ligation between the imidazole of histidine and the porphyrin Fe but perhaps through π–π stacking and/or electrostatic interactions [40]. The BNT templates offer a biologically functional model of HRP, containing the same nucleating domain, producing the same material (hemozoin), in a process that is inhibited by chloroquine but clearly offers the flexibility of a model system which allows for easier experimentation.

Circular dichroism (CD) was utilized to examine the secondary structure of the BNT II templates. As a control, the CD of the linear peptide models (AHHAHHAAD and $(AHHAHHAAD)_2$) which were unable to nucleate the formation of hemozoin, were examined and found to possess only a random coiled structure. BNT I was similar to the $(AHHAHHAAD)_2$ spectra but contained a slightly ordered structure. In contrast, the CD spectra of BNT II revealed a much higher ordered structure overall, reminiscent of the CD spectra of native HRP II (Fig. 9). Addition of hemin chloride to BNT II, resulted in a conformation change in the structure (Fig. 9, inset) that is visible as a shift in the CD from 197 nm to 202 nm, a spectrum consistent with a 3_{10}-helix. The

Table 1 Substrate binding stoichiometries of BNT I and BNT II

Substrate	BNT I (8)	BNT II (16)
Fe(III)PPIX	7.1 ± 0.7	12.2 ± 1.0
PPIX	7.7 ± 0.2	10.4 ± 1.0
Zn(II)PPIX	6.8 ± 0.5	14.0 ± 0.6
PcS	5.7 ± 0.2	13.2 ± 1.0
Ni(II)PcS	6.5 ± 0.1	11.0 ± 1.0

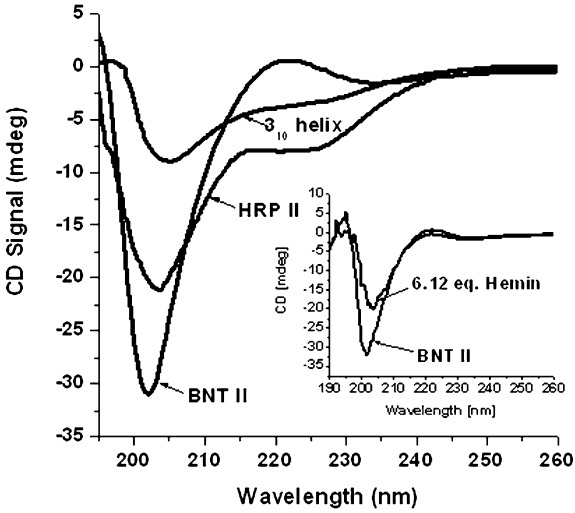

Fig. 9 Circular dichroism (CD) spectra of a 3–10 helix, HRP II, and BNT II. *Inset*: BNT II spectral change upon the addition of hemin

fact that heme binding results in conformational changes in each of the four branches of the template to be more of a 3_{10}-helix, suggests that in order for hemozoin biomineralization to take place, there is a requirement for a highly ordered structure, a preorganization of a nucleating face [43].

Examining HRP II as a potential bionucleating template, the idea of a 3_{10}-helical structure results in an interesting model system. There would be three residues per turn, leaving a hydrophobic face of alanine residues based on the amino acid sequence of the minimal binding domain. Since polyhistidine was unable to nucleate the formation of hemozoin [44], it is likely that the alanine residues may be acting as important spacers in the sequence, setting up the appropriate metrics within the secondary structure for binding porphyrin. Recent site-directed mutagenesis studies of the 9-mer repeat Ala-His-His-Ala-His-His-Ala-Ala-Asp in BNT I and II, indicate that the His-His repeat is essential for activity whereby any mutation to it results in decreased binding and substantially less hemozoin formation. Additionally, the aspartic acid residue appears to play an important role in polarity. The electrostatics of this residue are essential for hemozoin formation, but not necessarily for porphyrin binding. These data reflect the importance of the preorganization of a nucleating face [43].

Piecing together the data currently available on hemozoin formation yields an intriguing picture. In aqueous solution, there would be a hydrophobic face of alanine residues and a nucleating face of histidine and aspartic acid residues. In the BNT templates, interactions between the alanine faces would result in the collapse of the four arms of the dendrimeric template to a 4-helix

bundle leaving the histidine and aspartic acid residues facing out and in position for binding the Fe(III)PPIX. A similar interaction may be occurring in HRP in which coiled-coil interactions allow for the presentation of the nucleating face. In this scenario, the histidine and aspartic acid residues are aligned along the 3_{10} secondary structure forming a putative nucleating face to bind heme via electrostatics and π–π stacking interactions. Minimal hemozoin dimer formation could occur along the interface, creating a locally high concentration of dimers. Extension of this network through hydrogen bonding would allow for the formation of the insoluble biomineral, hemozoin. A final possibility is that the formation involves the use of both the lipids and HRP II. The lipids would provide a favorable environment for hydrogen bond formation while the HRP II would act as the bionucleating template to bind the heme and link heme molecules together [45].

While these interfacial molecular recognition hypotheses are theoretical, they point towards the importance of understanding how the template recognizes its substrate. This is an event that occurs in all biomineralization events and represents the final guiding principle behind molecular tectonics. As the understanding of hemozoin formation increases, the ability to propose inhibitory mechanisms will also increase, allowing the development of interventions that would reduce the devastation caused by this and other deadly parasites. At the very least, the detoxification of heme by the formation of hemozoin is a unique pathway that offers an elegant example of the complexity and diversity of biomineralization and reflects the importance of continued efforts in this vast field.

2 Biomineralization of Cadmium Sulfide

Since the industrial revolution, there has been a significant and continued increase in the demand for heavy metals for use in fuels, solvents, lubricants, stabilizers, fire retardants, pigments, and preservatives, to name a few. The release of heavy metals into the biosphere results in elevated levels in the soil and water in addition to increased levels in the atmosphere, usually in the form of dust particulates or vapors [46]. While certain levels of heavy metals are necessary for cellular metabolism, the presence of heavy metals such as cadmium at high levels can be detrimental to a variety of organisms.

Elevated levels of Cd^{2+} induce toxicity due to their ability to mimic essential metal ions such as Zn^{2+} and Ca^{2+}, acting as their substitute in enzyme active sites resulting in enzymatic dysfunction. The presence of these ions at high levels can result in extensive denaturing of proteins and DNA, ultimately leading to cell death [47]. In order to defend against these detrimental biological effects, natural systems have evolved unique detoxification mechanisms to eradicate the problematic metal [48]. An intriguing example of Cd^{2+} de-

toxification involves the sequestration of the metal by small selective peptides followed by coprecipitation with inorganic sulfide to form nontoxic metal sulfide clusters. This type of protective biomineralization has been well documented in plants [49], yeasts [50], several fungi [51], and sulfate-reducing bacteria [48, 52] and represents a precisely controlled nanoparticle synthesis that adheres to the molecular tectonics of biomineralization as established by Mann et al. [53].

In plants and yeast, cadmium detoxification is accomplished intracellularly and consists of a metal-triggered biosynthetic pathway, sequestration of the metal ions by small thiol-rich peptides, and assembly with inorganic sulfide ions to generate nontoxic CdS nanoparticles [50, 54]. The cornerstone of this mechanism is the use of small thiol-rich peptides composed of Glu, Cys, and Gly [55], capitalizing on the high reactivity of heavy metals such as Cd^{2+} to thiols [50]. These chelating peptides, called phytochelatins (PC_n) are structurally related to the tripeptide glutathione (GSH), γ-Glu-Cys-Gly, and display the general structure $(\gamma\text{-Glu-Cys})_n$-Gly [56], where n represents the number of dipeptide repeats (Fig. 10). The peptide sequences vary in length ($n = 2$–11) depending on the metal concentration and duration of exposure [57]. Furthermore, PCs display an extensive binding capacity for Cd^{2+} ions with a K_{3Cd} of $\sim 10^9$ [58]. Although the primary function of PCs is to protect against heavy metal toxicity, these peptides are also associated with maintaining homeostasis within the cell by balancing its essential micronutrients [49]. The presence of these heavy metal chelating peptides has been identified in several species of yeasts such as *Candida glabrata* [59], *Schizosaccharomyces pombe* [60], and in all studied plants to date [49].

The biosynthesis of PCs during episodes of heavy metal stress consists of a specific biosynthetic pathway triggered by the presence of the metal. The basic building block, GSH, and the PCs exhibit the presence of a γ-peptide bond demonstrating that they are synthesized enzymatically and not on the ribosome [61]. The enzyme responsible for PC synthesis, phytochelatin syn-

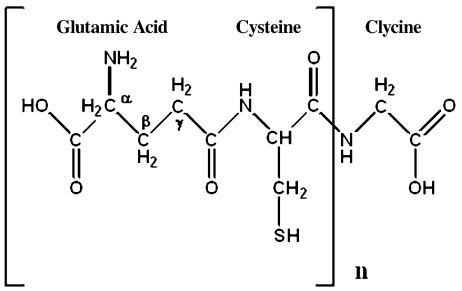

$(\gamma$-Glu-Cys$)_n$-Gly Phytochelatins

Fig. 10 Generalized structure of phytochelatins

thase ($Mr = 95\,000$), is a γ-glutamylcysteine dipeptidyl transpeptidase that catalyzes the biopolymerization of GSH to PC_n ($n = 2$–11) [62]. Since the enzyme is constitutively expressed and PC formation only occurs in the presence of heavy metals, enzyme activation has long been thought to be heavy metal dependent [63]. Although it has been shown that Zn^{2+}, Pb^{2+}, Ag^{2+}, Cu^{2+}, Ni^{2+}, and Sb^{2+} moderately activate PC synthesis, Cd^{2+} proves to be the most efficient heavy metal for activating the enzyme that produces PCs, phytochelatin synthase [64, 65]. While the crystal structure of the phytochelatin synthase (PCS) has not yet been determined, there are two primary domains, the *N*- and the *C*-terminus, which both contain multiple cysteine residues thought to bind the metal. Early studies indicated that the *N*-terminus is highly conserved among species whereas the *C*-terminus is not [66].

The activation of PCS has long been thought to be dependent upon metal binding directly to the enzyme in the *C*-terminus. Indeed, metal binding at the sensor site was thought to be an obligate step prior to the assembly of the active site, through which conformational changes would allow the assembly of the active site and subsequent substrate (GSH) binding [67]. Recent work on the enzyme obtained from recombinant PCS from *Arabidopsis* (AtPCS1) has identified the location of the functional active site to be in the *N*-terminus and determined that deletion of the *C*-terminus has no deleterious effect on enzyme activity [63]. If direct metal binding to the metal sensor domain in the *C*-terminus is not essential for enzyme activity, what other mechanism could result in the metal-dependent activation of PCS?

Reexamining the activation of PCS using AtPCS1, Vatamaniute et al. demonstrated that heavy metal ions reacted with GSH to form heavy metal peptide thiolates (CdGSH) that, along with free GSH, serve as cosubstrates for the enzyme [68]. In the first step in enzyme activation, GSH acts as a γ-Glu-Cys donor and acylates the PCS, releasing Gly. The active γ-Glu-Cys-AtPCS1 acyl intermediate then transfers the γ-Glu-Cys unit to the second substrate to generate a product extended by the condensation of one new γ-Glu-Cys repeat with the *N*-terminus of the receptor. For this reaction mechanism to work, a thiol group of one of the substrates must be blocked, likely through heavy metal thiolate coordination. This reaction is augmented by, but not dependent upon, the direct binding of free heavy metal ions to the enzyme, probably not at the active site [68]. While the *C*-terminus is nonessential for activity, it does impart a degree of stability to the *N*-terminus. Additionally, the last 113 residues of the *C*-terminus are vital to sensing Hg^{2+} and Zn^{2+}, indicating that the *C*-terminus may also function to generalize the ability of the enzyme to respond to a wider variety of heavy metals [63]. In the end, once activated, the enzyme catalyzes a condensation reaction in which two molecules of GSH react to produce the simplest form of the chelating peptide, PC_2 with the release of water and a glycine residue [50]. PCS appears to be a self-regulated enzyme and becomes down-regulated by the exhaustion of Cd^{2+}, whereby free thiols (GSH and apo-PCs) compete with thiolates

for the high affinity active site of the synthase. Removal of the enzyme substrate thiolates via sequestration into vacuoles and biomineralization ensures that only the needed concentration of PCs are generated [68]. By sequestering the Cd^{2+}/PC_2 complexes inside vacuoles, the organism ensures that the toxic metal is removed from important metabolic chambers and simultaneously confines the biomineralization process to a tight space, effectively restricting the size of the resulting nanoparticles.

Studies by Vogeli-Lange and Wagner with tobacco leaves conclusively showed that essentially all of the Cd^{2+}/PC_2 complexes formed in the cytosol were sequestered into vacuoles [69]. Examination of a cadmium-sensitive *Schizosaccharomyces pombe* mutant deficient in the accumulation of a sulfide-containing cadmium complex revealed that transport of the Cd^{2+}/PC_2 complex into the vacuole appears to be regulated by the gene product of *hmt1*, a protein with homology to ABC (ATP-binding cassette)-type transport proteins. This family of proteins has been found to mobilize proteins and other compounds across membrane barriers. Further studies localized the HMT1 polypeptide to the vacuolar membrane. Additionally, overexpression of the *htm1* allele, led to increased accumulation of Cd^{2+}/PC_2 in the vacuole, confirming the role of HTM1 polypeptide as one of intracellular sequestration rather than efflux [70].

In order to gain a better understanding of the biological function of PC complexes, Johanning and Strasdeit performed a potentiometric titration using the Cd^{2+}/PC_2 complex as a model for elucidating the thermodynamic stabilities of the heterogeneous native complex [71]. Since PC_2 exists as a pentabasic acid, stable Cd^{2+}/PC_2 complexes are only formed by ligands having at least one deprotonated thiol. The authors were able to distinguish two well-defined categories of Cd^{2+}/PC_2 complexes: complexes that are composed of equal numbers of ligand to Cd^{2+} ($\log K^{Cd} = 9.9–13.3$) and complexes that are composed of more ligands than Cd^{2+} ($\log K^{Cd} = 16.3–19.3$) [71]. Based on conclusions from the generated complex distribution, $[Cd_2(H_2L)(HL)_2]^{7-}$ is the dominant complex at pH 7.3 (pH in the plant cytoplasm) and is in agreement with formation of an S_4 coordination environment. At pH 5.4 (pH in the plant vacuole), 62% of the complexed cadmium is released and at nontoxic concentrations essentially 100% of the complexed Cd^{2+} would be liberated [71]. These findings are indicative of an acid/base storage transfer mechanism that allows for Cd^{2+}/PC_n formation in basic conditions (cytoplasm) and Cd^{2+} release in slightly acidic conditions [71].

Chelation of the Cd^{2+} with subsequent release into vacuolar storage does not eradicate the toxic Cd^{2+} from the cell and indeed would be equivalent to storing live dynamite. It makes more biological sense to deactivate the dynamite (transforming the toxic Cd^{2+} into a nontoxic nanocrystal) rather than leaving it in a more toxic form. This is efficiently accomplished by providing a flux of acid-labile sulfide ions (S^{2-}) into the vacuole, resulting in the self-assembly of PC-capped CdS nanocrystals [72]. Although the source of

inorganic sulfide is unknown, the generation of S^{2-} ions is thought to originate either from the adenine biosynthetic pathway [70] or from the sulfate reduction pathway [72]. Alternatively, recent elucidation of the Fe – S cluster biosynthesis pathway suggests that the sulfide may originate from ISCS, a homodimer containing pyridoxal phosphate. ISCS catalyzes the formation of L-alanine and elemental sulfide from a L-cysteine substrate [73]. Regardless of the precise source of S^{2-}, the formation of nanocrystals is a more efficient means of binding Cd^{2+} ions at lower cellular metabolic cost. For example, Mehra and Winge showed that Cd^{2+} binding capacity by PC_2 peptides isolated from the yeast *Candida glabrata* increased from 0.5 mol equivalents to 5 mol equivalents when the sulfide level was increased [74].

The self-assembled PC-capped CdS nanocrystals have a very narrow size distribution with PCs capping the nanocrystal to radii of ~ 1.2 nm [72]. Tight control over size is a typical property of all biomineralization processes [53] and demonstrates the importance of the capping template (PCs) in controlling particle formation. Optimizing the PC coat prohibits the formation of extremely large nanocrystals, which would rupture the vacuole preventing the separation of the nanocrystal or unincorporated free Cd^{2+} ions from the cytosol. A variety of organisms employ this detoxification mechanism resulting in the self-assembly CdS nanocrystals with similar structural characteristics but with slightly different compositions and connectivity patterns (Scheme 1) [75].

When the CdS crystallites generated by *C. glabrata* and *S. pombe* were first isolated (Fig. 11), they displayed greater monodispersity and much greater stability than previously chemically synthesized examples [76, 77]. Intercellular CdS crystallites synthesized by *C. glabrata* and *S. pombe* had approximate diameters of 2.0 and 1.8 nm with sulfide/cadmium ratios of 0.7 and 0.6, respectively [77]. The CdS crystallites isolated in this study exhibited a band gap transition between 310 and 315 nm [77]. Additionally, CdS crystallites produced by *C. glabrata* and *S. pombe* were not prone to Ostwald ripening, a process of natural aggregation that often occurs among chemically synthesized CdS particles [76]. Each CdS crystallite core is composed of approximately 85 CdS units with approximately 30 PC_n ($n = 2$–3) peptides coating the Cd^{2+}-rich surface of the crystallite [77]. Larger, extracellular CdS nanoparticles 2.9 ± 0.5 nm in diameter that exhibit a zinc-blend structure with a band gap transition at 365 nm were also found [77]. The extracellular particulates potentially represent the endpoint of detoxification resulting from exocytosis of CdS, forming vesicles via the yeast secretory pathway [78].

The detoxification of Cd^{2+} in plants and yeast is also accomplished through the self-assembly of CdS nanoparticles [61]. Ahmad and Sastry [51] reported the formation of extracellular CdS nanoparticles by the fungus *Fusarium oxysporum* upon exposure to Cd^{2+} and SO^{4-} [51]. The extracellular synthesis employs the use of sulfate reductases secreted by the organism that yield acid-labile sulfide [51]. A significant biomass of *F. oxysporum* was incubated

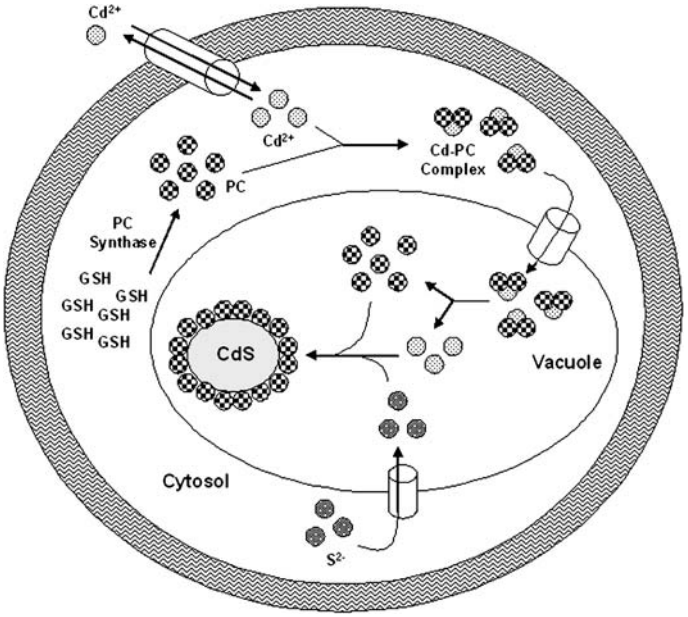

Scheme 1 Biomineralization mechanism of CdS beginning with Cd^{2+} uptake, phytochelatin synthesis, metal–phytochelatin complex formation, acid-labile sulfide incorporation, and precipitation of PC-capped CdS nanoclusters

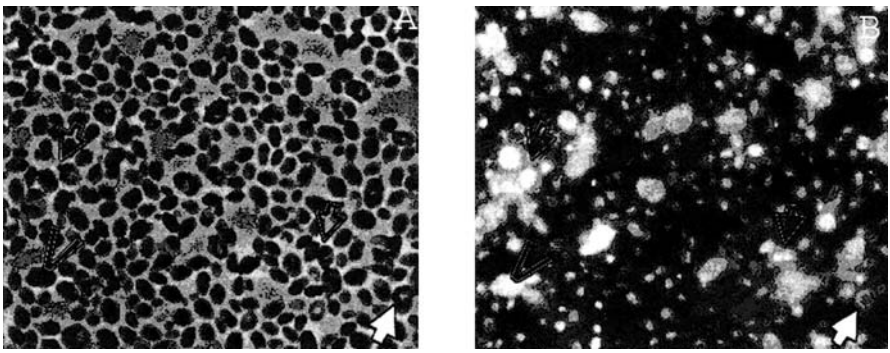

Fig. 11 **a** Phase contrast and **b** fluorescence analysis of Cd(II) exposed *Candida glabrata* yeast cells

at room temperature with millimolar $CdSO_4$ for 12 days [51]. Concurrent with reduction of sulfate to S^{2-}, well-dispersed and stable CdS nanoparticles 5–20 nm in diameter were formed [51]. UV-vis spectroscopy (absorption at 280 nm) and polyacrylamide gel electrophoresis (PAGE) revealed the presence of protein in the reaction supernatant, which the authors suggested may be sulfate-reducing enzymes responsible for CdS nanoparticle formation and

stability [51]. *F. oxysporum* was the first reported fungus to employ the use of an aerobic sulfate reduction pathway capable of secreting sulfate-reducing enzymes to synthesize extracellular CdS nanoparticles as a means of cadmium ion detoxification [51].

Similarly, sulfate-reducing bacteria such as *Clostridium thermoaceticum* [48] and *Klebsiella pneumoniae* [52] utilize an anaerobic sulfate reduction pathway to generate acid-labile sulfide as a mechanism for heavy metal ion detoxification [47]. According to Cunningham and Lundie [48], Cd^{2+} detoxification by *C. thermoaceticum* begins with a fine white precipitate ($CdCO_3$) that is gradually converted to a bright yellow precipitate (CdS) via the production of H_2S [48]. Atomic absorption analysis of the culture media was used to monitor the detoxification process with complete removal of Cd^{2+} after 72 h [48]. Based on a series of starvation studies, the biosynthesis of CdS by *C. thermoaceticum* proved to be an energy-dependent process that required cysteine, indicating that CdS formation proceeds via a cysteine desulfhydrase enzyme that converts cysteine to H_2S and alanine [47, 48]. The electron-dense CdS particles are strictly produced extracellularly and localized to the cell surface and surrounding media [48]. Unlike *C. thermoaceticum*, *K. pneumoniae* Cd^{2+} detoxification occurs under a range of conditions dependent on the buffer composition of the growth media [47, 52]. Cadmium tolerance proved to be optimal in phosphate buffered growth media (2 mM Cd^{2+}) while growth media buffered with Tris, Bistris propane, Bes, Tes, and Hepes resulted in a much lower tolerance (10–150 μM) [52]. Upon Cd^{2+} exposure, electron micrographs show extracellular CdS crystallite formation is localized to the cell surface with particles ranging from 20 to 200 nm in size and a Cd : S ratio of 1 : 1 based on quantitative energy dispersive X-ray analysis [52]. The total cellular content of labile sulfide and cadmium has a molar ratio of 0.5–2.0 of Cd : S [52]. Based on electron absorption spectroscopy measurements, all electron-dense particles synthesized by *K. pneumoniae* consist of CdS but the exact mechanism of sulfide generation is unclear [47]. These nanoparticles formed without a protein cap undergo Ostwald ripening and eventually grow to the bulk. This results in the production of larger particles that appear to be aggregations of smaller particles, with a greater variety of particles formed.

The formation of CdS nanoparticles represents a beautiful example of a detoxification biomineral. These organisms have evolved a tightly controlled detoxification scheme that involves the preorganized availability of the PCS enzyme to generate a sequestering, capping template. Activation of PCS yields the formation of phytochelatins, which act to recognize and bind the free metal ion through the peptide thiol moieties and sequester it in vacuoles. Inside the vacuoles, Cd^{2+} is released from the Cd^{2+}/PC_2 complex and coprecipitated with sulfide to produce nontoxic CdS nanoparticles that are exported outside the cell, rendering them harmless to the organism. Similar to the biomineralization of free heme into hemozoin, the formation of

CdS nanoparticles occurs inside a defined vacuolar space where the resulting particles are no longer able to harm the organism.

3 Noble Metal Biomineralization

Compared to the previously presented cases of hemozoin and CdS, the detoxification of noble metals represents an emerging story in the biochemistry of a detoxification biomineral. Noble metals such as silver and gold are naturally found in sea water, soil, and rocks in nanogram to microgram levels. While silver and gold are not the most reactive metals on the periodic table, they are able to act as electron sinks disrupting vital respiratory enzymes and electron transport within organisms. Silver can also block the permeability of the outer membrane, inhibiting growth [54, 79]. As a result, trace amounts of these metals can have detrimental effects on an organisms. Consequently, biological systems have been using biomineralization (Table 2) as a type of detoxification mechanism for noble metals for over 2.8 billion years [80], as witnessed by placer gold deposits around the world. Biomineralization detoxification of silver and gold metal ions can be accomplished by way of three different modes: intracellular, extracellular, and intercellular.

Table 2 Summary of noble metal detoxification nanoparticles

Organism	Species	Product	Size (nm)	Shape	SPRB (nm)	Location
Actinomycete	*Rhodoccous* sp.	Au	5–16	Spherical	550	Intracellular
Bacteria	*Pseudomonas stutzeri* AG259	Ag	2–200	Hexagonal, triangular	n/a	Intracellular
Fungus	*Verticillium* sp.	Au	12–28	Spherical	540	Intracellular
Fungus	*Verticillium* sp.	Ag	13–27	Spherical	450	Intracellular
Fungus	*Fusarium oxysporum*	Au	20–40	Spherical, triangular	545	Extracellular
Fungus	*Fusarium oxysporum*	Ag	5–50	Spherical, triangular	413	Extracellular
Actinomycete	*Thermomonospora* sp.	Au	7–12	Spherical	520	Extracellular
Plant	*Pelargonium graveolens*	Au	20–40	Rods, triangular, spherical	551	Extracellular
Plant	*Pelargonium graveolens*	Ag	16–40	spherical, ellipsoidal	370	Extracellular
Plant	Alfalfa	Au	2–20	Spherical	n/a	Intercellular
Plant	Alfalfa	Ag	2–20	Spherical	n/a	Intercellular

Many features of intracellular detoxification of silver and gold are reminiscent of other biomineralization detoxification schemes. The reduction of the metal ion results in the formation of metal nanoparticles that deposit primarily in the cell wall or the cytoplasmic membrane, well-removed from the mitochondrial respiratory chain, in a process that does not inhibit cellular growth. Genetically encoded resistance is a common mechanism of silver detoxification and is exemplified by *Pseudomonas stutzeri* AG259, a bacteria that was first isolated from the soil near a silver mine in Utah. This bacterium was found to contain three plasmids (small circular DNA molecules that possess genes). The largest of the plasmids was pkk1 ($M_R = 49.4 \times 10^6$), which contained genes encoding resistance to silver [81]. For *Pseudomonas stutzeri* AG259 Ag^+ is reduced to nontoxic Ag^0 in the form of triangular, hexagonal, and spherical Ag^0 and Ag_2S nanoparticles found in vacuole-like granules (ranging from a few to 200 nm in diameter) between the outer and the plasma membranes [82]. Haefeli et al. proposed the possibility of a bioreduction pathway involving a metallothionein-like molecule [81], while Slawson et al. proposed an energy-dependent pathway [83]. The flat triangular and hexagonal morphologies were thought to be caused by the confined space resulting in the observed plate-like morphology, allowing growth along the crystallographic plane bearing the highest atomic density [84]. This is perhaps an orchestrated process of regulation resulting from the simple allocation of bioreductants. On the other hand, it is possible in a test tube to form silver and gold nanoparticles with GSH in which GSH acts as both a sacrificial reductant (GSH-GSH is the product) and as capping ligand. If there is more stress than the intracellular reductant pool of GSH can handle, S_2^- production may be upregulated. This proposed mechanism harkens back to the detoxification of Cd^{2+} discussed earlier whereby the phytochelatins (formed from GSH) act to scavenge the free metal and eventually act to cap the growing CdS nanoparticles.

Verticillium fungal cells can detoxify Ag^+ and both *Verticillium* and the noval alkaloterant actinomycete, *Rhodococcus* sp. have been found to form intracellular gold nanoparticles after incubation with millimolar concentrations of Au^{3+}. These organisms alleviate toxicity by reducing the metal cation to nontoxic zero-valent nanoparticles [85, 86]. Exposure of *Verticillium* fungal cells to high micromolar concentrations of Ag^+ for 72 h resulted in the formation of spherical silver nanoparticles uniformly distributed on the cell surface with average sizes of 25 ± 12 nm. Similarly, exposure to Au^{3+} leads to the reduction to Au^0, forming nanoparticles of 20 ± 8 nm in size as observed by TEM. Gold nanoparticles of 100 nm were also observed inside the cytoplasm, displaying triangular and hexagonal particles as well [85]. *Rhodococcus* sp. was also found to form intracellular gold nanoparticles after incubation with millimolar concentrations of Au^{3+} for 24 h. Not only was formation more rapid than *Verticillium* (24 v. 72 h), the nanoparticles demonstrated much more monodispersity, averaging 9 ± 2 nm in diameter [87]. In all of these

cases, the aqueous medium of the reaction remained clear, indicating that no extracellular reduction of the metal ions was occurring. This was further substantiated by the lack of plasmon absorbance in the UV-vis of the medium after reaction completion. If the reduction were occurring extracellularly, there would have been characteristic surface plasmon resonance bands (SPRB) at 450 nm for silver and 540 nm for gold [85, 86] in the UV-vis of the medium. In the case of *Verticillium*, Mukherjee et al. proposed that the metal cations are first trapped at the cell surface via electrostatic interactions. The positively charged metal ions were proposed to interact with the negatively charged carboxylate groups of enzymes in the cell wall [85, 86].

Previously, it was shown that sugar-persubstituted poly(amidoamine)dendrimers can spontaneous reduce Au^{3+} to form gold nanoparticles; therefore, it is possible that sugars may be potential cell wall ligands in this case [88]. Mukherjee et al. investigated this possibility by treating fungi of different genera with Au^{3+} under exactly the same conditions as for *Verticillium*. Since this did not result in intracellular formation of nanoparticles, it was concluded that sugars cannot possibly be the reducing reagents. The authors also argued that as most of the gold nanoparticles form on the cytoplasmic membrane, sugars can be ruled out as the reductants [85]. While their evidence is interesting, the involvement of sugars in trapping the metals cannot be completely ruled out without further study. Once trapped, the cationic metal is reduced by cell wall enzymes leading to the formation of metallic nuclei, which grow by further reduction of metal ions and accumulation on these nuclei. Similar chemistry has been observed in the cowpea chlorotic mottle viruses of unmodified SubE (yeast). Here, surface tyrosine residues of the virus provide electrons sufficient to reduce the gold [89]. Similarly, the tyrosine residues of the cell wall enzymes may be reducing the trapping metal ions. Since there was no evidence of AgS or AuS nanoparticles, Mukherjee et al. proposed that the reduction cannot be mediated by glutathione [85, 86]. However, the autooxidation of GSH releases electrons that would be able to reduce the metal without the direct involvement of the GSH thiol. GSH is the major intracellular reductant and as such is the cell's electron reservoir, making it possible for GSH to be involved in the reduction of silver and gold without introducing S^{2-} into the nanoparticle structure.

EM studies revealed a higher concentration of the gold particles in the cytoplasm of the cell with smaller concentrations on the cell wall in *Rhodococcus* sp., perhaps indicating a different mechanism of reduction and nanoparticle formation to that in *Verticillium*. Powder X-ray diffraction (XRD) analysis of actinomycete films clearly showed the (111), (200), (220), and (311) Bragg reflections indicative of highly crystalline Au^0. Sastry et al. noted that the intensity of the (311) reflection in relation to the normally most intense (111) reflection indicated a degree of oriented growth. While the mechanism of detoxification is entirely unexplored, Sastry et al. propose that it is either similar to *Verticillium*, whereby it is controlled by enzymes present

in the cell wall, or perhaps it is mediated by insoluble proteins in the organism similar to calcium carbonate crystal formation [87]. Neither of these mechanisms makes a cohesive argument. Clearly, the mechanism is different from *Verticillium* as there are more particles found in the cytoplasm with greater monodispersity. The results are indicative of a more oriented, more controlled growth but suggesting a mechanism similar to calcium carbonate formation is not a well formed alternative. The exquisite control over shape and form displayed in the shells indicates a much more complex formation than for the simple spheres of *Rhodococcus*. Without a doubt, significantly more careful research is required to determine the mechanism of nanoparticle formation in this organism.

While very little information is currently available about the discrete biochemical mechanisms of intracellular detoxification of silver and gold, there is a great deal more known about extracellular detoxification. Here, there is definitive evidence for the role of proteins in the reduction of the metal ions. Exposure of the fungus *Fusarium oxysporum* to millimolar Ag^+ for 72 h led to the extracellular formation (monitored in the UV-vis at 413 nm) of extremely stable spherical and triangular silver nanoparticles ranging in size from 5 to 15 nm in diameter [90]. In addition to the plasmon band at 413 nm, a second absorption at 270 nm suggested the presence of proteins released into the aqueous medium [90]. Similarly, geranium (*Pelargonium graveoleus*) leaf broth forms stable extracellular silver nanoparticles of 16–40 nm in diameter upon exposure to Ag^+ with 90% reaction completion at 9 h [91]. Exposing *F. oxysporum* and geranium leaves to Au^{3+} led to similar results. Here, the extracellular formation of gold nanoparticles between 20–40 nm in diameter is observed after 48 h and 60 min, respectively. The extremeophilic actinomycete *Thermomonospora* sp. also reduced Au^{3+} to form stable spherical Au^0 nanoparticles of ~ 8 nm in diameter extracellularly after 120 h of incubation [92]. The mechanism behind formation of the gold nanoparticles was proposed to be identical to the silver nanoparticle formation [93, 94]. In all cases, examination of the media using FT-IR demonstrated bands consistent with protein presence in the medium. Bands at 1650 and 1540 cm^{-1} indicated amide I and II bands due to the carbonyl stretch and – N – H stretching vibrations in the amide linkages of the proteins, respectively. A band at 1450 cm^{-1} was interpreted as the methylene scissoring vibrations.

Geranium leaves contain high levels of terpenoids, which may also play a role in nanoparticle formation and stabilization. Terpenoids are primarily composed of citronellol and geraniol with a minor contribution of linalool. The C = C of these alcohols may account for the stretch at 1607 cm^{-1}. If terpenoids are involved in nanoparticle formation, extraction of the terpenoids from the geranium leaves, followed by incubation with either Ag^+ or Au^{3+}, should result in the formation of nanoparticles [91, 94].

Further analysis using gel electrophoresis demonstrated the presence of at least four high molecular weight (10–66 kDa) proteins in the extracellu-

lar medium of *F. oxysporum* geranium leaves, and *Thermomonospora* sp. Gel electrophoresis was the only method utilized to identify the nature of the molecules in the medium. It would be extremely beneficial to have identification of these proteins using *N*-terminal sequencing and/or mass spectrometry. Once identified, the mechanism of reduction could be deduced, either from the known function of the proteins or by further biophysical characterization. Additionally, the presence of specifically four protein bands in the gel electrophoresis for a variety of organisms begs the question of how well the bands are resolved. The gel electrophoresis data is not shown in the literature but if the bands are not well resolved, it may be worthwhile to examine the gel matrix to determine how to achieve better resolution. In the case of *F. oxysporum*, the authors proposed that one of the proteins was a NADP-dependent reductase enzyme, based on their finding that nanoparticle formation could be induced by adding NADP to a solution of Ag^+ and the protein-containing medium. Without NADP, no nanoparticle formation was found to occur, indicating that the enzyme in the medium responsible for reducing the Ag^+ to Ag^0 must be NADP-dependent. However, there was no control reported to see if NADP alone (an electron reservoir itself) could reduce the metal.

These proteins were organism-specific and Sastry et al. proposed that they play an important role not only in the reduction of the silver ions but also in the formation of the silver nanoparticles. The TEM and optical microscopy studies of the nanoparticles formed by *F. oxysporum* showed no flocculation and very little aggregation of the particles. This would result in the observed increased stability as well as control the particle growth. The authors proposed binding of protein to the surface of nanoparticles, which has been seen in other systems where it does not affect the tertiary structure of the protein [90]. In geranium leaves, Sastry et al. noticed the formation of a strong plasmon resonance band at 440 nm and a shoulder at 370 nm in the UV-vis, which they assign to the longitudinal plasmon and tranverse vibrations, respectively. The authors attributed the presence of these two distinct peaks to an open quasilinear superstructure formed by the nanoparticles. The morphology of the particles was predominantly spherical with a small percentage being ellipsoidal (Fig. 12). The particles did appear to have assembled into "stringlike" structures, the open, quasilinear superstructure indicated in the UV-vis. However, it is possible that the quasilinear structures observed in the TEM may be an artifact due to the drying process on the TEM grid and not actual morphologies. This structure should be further examined in order to verify the assembly of such quasilinear structures. Further, TEM imaging revealed a 5 nm coating around the nanoparticles that was proposed to be a bioorganic component in the broth [91]. While Sastry et al. proposed this coating to be protein capping of the nanoparticle, the TEM only really shows carbonatious material on the surface. If protein capping is truly occurring in either of these organisms, than a simple kill reaction in which the nanoparticles are analyzed by degradation would result in verification of sur-

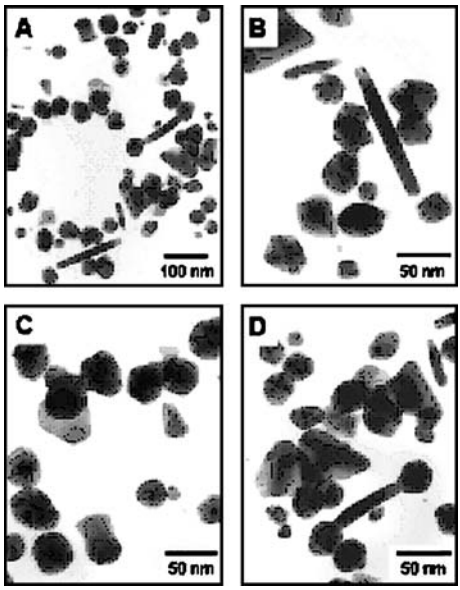

Fig. 12 TEM images of extracellularly produced gold nanoparticles formed in geranium leaves

face proteins. Without this type of analysis, the idea of protein capping in this case is merely speculation.

Some organisms utilize both an intra- and an extracellular mechanism of detoxification. One example is found in bacterial strains of *Lactobacillus* isolated from buttermilk. Here, the silver and gold cations would be reduced extracellularly by L-lactic acid (a component of whey protein) or by charged carbohydrates, forming small clusters. These small clusters may then perhaps be coated with sugars that allow them to be transported into the bacterium. Once inside, the smaller particles are sacrificed to the formation of larger particles. Exposure to Ag^{+} and whey protein results in the formation of Ag^{0} clusters within 12 h with a bimodal distribution in sizes centered around 15 and 500 nm. The coalescence of the larger particles inside the bacterium resulted in the protrusion of the particles into the cell wall lining, and eventual cell wall rupture with preservation of the bacterial contour (Fig. 13) [95]. Exposure to Au^{3+} resulted in a bimodal distribution of Au^{0} nanoparticles ranging in size from 20–50 and > 100 nm in size. The smaller clusters are found both outside and inside the bacterium but the larger crystals, mainly hexagonal morphologically, are found exclusively inside. Very little is known about the supramolecular preorganization or the interfacial recognition of the silver and gold cations in this system except that it may involve proteins and sugars [95]. Alfalfa plants utilize a similar scheme whereby exposure to Ag^{+} or Au^{3+} results first in the reduction of the metal ion in the solid me-

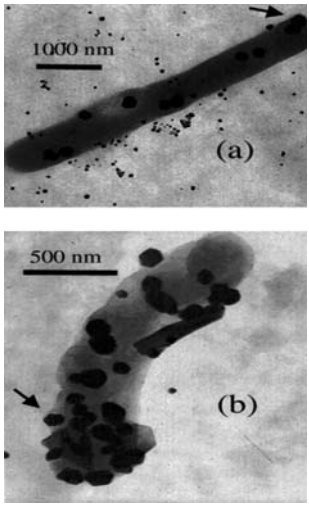

Fig. 13 Electron micrograph of intercellularly formed gold nanoparticles formed in *Lactobacillus* strains. *Arrows* indicate where the nanoparticles are being pushed out of the bacterium

dia, followed by active transport into the roots, and eventually to the shoots as spherical Ag^0 or Au^0 nanoparticles 2–20 nm in diameter [96, 97]. Currently, there is little known about intercellular detoxification. Potentially, the organisms are releasing reducing agents into the agar medium. Extraction and gel electrophoresis techniques would determine if these reducing agents are proteins and if so, *N*-terminal sequencing and/or mass spectrometry could aid in their identification. Further investigations are needed to explain how the nanoparticles are brought inside the organism. Are these nanoparticles trapped inside by ion flux mechanisms or actively transported inside the organism? Biologically, we know little about the detoxification of silver and gold via biomineralization pathways, especially when compared to the other systems described, but research efforts based on the principles of biomineralization will provide rational hypotheses to pursue.

4 Summary

Biominerals are most often considered in either their more traditional roles as critical structural components of organisms (e.g., teeth, the siliceous shell of diatoms) and important ion reservoirs for cellular function (Ca^{2+} and bone) or in their highly evolved functional roles (e.g., magnetotactic sensing, bouyancey/balance regulation) [53]. Increasingly, it is becoming apparent that biominerals also play an important protective role by acting as critical

detoxification sinks within certain organisms. Thus, organisms ranging from protozoa to eukaryotes utilize the same principles of biomineralization (cellular processing, supramolecular organization, and interfacial recognition) to form such materials as Abalone nacre to efficiently remove potentially toxic species from their immediate environment. Thus, as understanding how biological systems exert their nanoscale control over structural biominerals has provided important biomimetic routes to novel materials synthesis, similar advances in both therapeutic development and materials synthesis and can be made through the study of detoxification biominerals.

If the hypothesis is that HRP does in fact mediate the formation of hemozoin within the digestive food vacuole, there are several limiting cases in which the inhibitors may disrupt its aggregation (Scheme 2). An inhibitor may bind the heme substrate in such a manner that the heme–inhibitor complex cannot be recognized by the template. Alternately, a drug could interact with the template, blocking the heme binding site. Finally, a hemozoin aggregation inhibitor might trap the heme bound to the template, preventing formation of the dimeric unit or nucleation of the extended crystallite. An important realization is that each of these possible modes of inhibition are predicated upon classical biomineralization concepts of electrostatic, geometric, and stereochemical complementarities that explain the forces dictating how the heme substrate may interact with the crystallization template [98]. The power of these concepts has recently been demonstrated by Marletta and coworkers, who employed HRP II-mediated formation of hemozoin as a screen against which to test new libraries of compounds for antimalarial activity [99]. Similarly, Wright and coworkers have used their bionucleating templates as a proxy for HRP II to examine the mode of efficacy of a number of different classes of inhibitors, including other metalloporphyrins [100] and

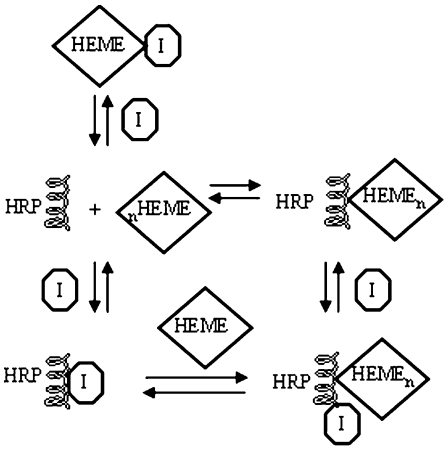

Scheme 2 Potential inhibition pathways to hemozoin aggregation

unique Schiff-base metallodrugs [101]. In each of these cases, inhibitors that act in all of the imagined functions have been discovered that may one day result in new treatments for malaria.

Similarly, the unique biominerals formed as a result of the detoxification of heavy metals such as cadmium provide new approaches to thinking about nanoparticle synthesis. When challenged by high levels of Cd^{2+} ions, a variety of species will precipitate a small peptide-encapsulated CdS nanoparticle. From the perspective of nanotechnology, this is a fascinating process. Not only does the organism control the size of the nanoparticle by using an iso-peptide encapsulating ligand, it adds considerable chemical functionality to that surface; a functionality that stands in sharp contrast to typical hydrophobic TOPO ligands or to the complex ligand exchange methodologies required to create water-soluble nanoparticles in the laboratory. Indeed, phytochelatins represent an intriguing starting point for the identification of functional ligands capable of stabilizing CdS nanoparticles.

The relationship of ligand structure to the chemical and physical properties of nanoparticles is a central theme in nanomaterials chemistry. While there have been significant advances in the strategies for the synthesis of the materials, they have been largely empirical. In contrast, by leveraging the evolutionary success of the cadmium ion detoxification pathways in certain plants, fungi, and bacteria, Wright and coworkers have been able to employ combinatorial peptide synthesis using a library based on the $n = 3$ phytochelatin to predict the molecular weight, dispersity, and photophysical properties of the CdS nanocluster simply on the basis of the stabilizing ligand [102]. This type of approach emphasizes the power of understanding unique biological detoxification systems to impart new properties and functionality into materials. Indeed, the elucidation of the detailed mechanisms of noble metal detoxification may provide a similar advance in the synthesis and control of that class of nanoparticles.

Acknowledgements This work was supported by a National Science Foundation CAREER award (CHE-0196540) and by the National Institutes of Health (1RO3 AI 060827-01).

References

1. Mann S (2001) Biomineralization: principles and concepts in bioinorganic materials chemistry. Oxford University Press, Oxford
2. Otto A (1984) Light scattering in solids IV. Springer, Berlin Heidelberg New York
3. Raman CV, Krishman KS (1928) Indian J Physiol 2:399
4. Nie S, Emory SR (1997) Science 275:1102
5. Benabid F (2002) Science 298:399
6. Bloembergen N (1967) Am J Phys 35:989
7. Agrawal GP (1989) Nonlinear fiber optics. Academic, San Diego
8. Sullivan DJ Jr (2002) Biopolymers. Wiley, Weinheim

9. Chen MM, Shi L, Sullivan DJ Jr (2001) Mol Biochem Parasitol 113:1
10. Oliveira MR, Silva JR, Dansa-Petretski M, De Souza W, Braga CMS, Masuda H, Oliveira PL (2000) FEBS Lett 477:95
11. Oliveira MR, Kycia SW, Gomez E, Kosar AD, Bohle DS, Hemplemann E, Menezes D, Vannier-Santos MA, Oliveira PL, Ferreira ST (2005) FEBS Lett 579:6010
12. Sherman IW (1998) Malaria: parasite biology, pathogenesis, and protection. ASM, Washington DC
13. Brinksworth RI, Prociv P, Loukas A, Brindley PJ (2001) J Biol Chem 276:38844
14. Goldberg DE, Slater AFG, Cerami A, Henderson GB (1990) Proc Natl Acad Sci USA 87:2931
15. Francis SE, Sullivan DJ Jr, Goldberg DE (1997) Annu Rev Microbiol 51:97
16. Green MD, Ziao L, Lal AA (1996) Mol Biochem Parasitol 83:183
17. Tappel AL (1953) Arch Biochem Biophys 44:378
18. Pagola S, Stephens PW, Bohle DS, Kosar AD, Madsen SK (2000) Nature 404:307
19. Mann S (1993) Nature 365:499
20. Chen MM, Shi L, Sullivan DJ Jr (2001) Mol Biochem Parasitol 113:1
21. Pisciotta JM, Ponder EL, Fried B, Sullivan D (2005) Int J Parasitol 35:1037
22. Slater AFG, Cerami A (1992) Nature 355:167
23. Chou AC, Fitch CD (1992) Life Sci 51:2073
24. Ridley RG (1996) Trends Microbiol 4:253
25. Dorn A, Stoffel R, Matile H, Bubendorf A, Ridley RG (1995) Nature 374:269
26. Ridley RG, Dorn A, Matile H, Kansy M (1995) Nature 378:138
27. Bendrat K, Berger BJ, Cerami A (1995) Nature 378:139
28. Dorn A, Vippagunta SR, Matile H, Bubendorf A, Vennerstrom JL, Ridley RG (1998) Biochem Pharm 55:737
29. Fitch CD, Cai GZ, Chen YF, Shoemaker JD (1999) Biochim Biophys Acta 1454:31
30. Hemplemann E, Motta C, Hughes R, Ward SA, Bray PG (2003) Trends Parasitol 19:23
31. Sullivan DJ Jr, Gluzman IY, Goldberg DE (1996) Science, p 271
32. Wellems TE, Howard RJ (1986) Proc Natl Acad Sci USA 83:6065
33. Stahl HD, Kemp DJ, Crewther PE, Scalon DB, Woodrow G, Brown GV, Bianco AE, Anders RF, Coppel RL (1985) Nucleic Acids Res 13:7837
34. Schneider EL, Marletta MA (2005) Biochemistry 44:979
35. Mann S (1993) J Chem Soc, Dalton Trans Inorg Chem (1972–1999):1
36. Lynn A, Chandra S, Malhotra P, Chauhan VS (1999) FEBS Lett 459:267
37. Morgan WT (1985) Biochemistry 24:1496
38. Burch MK, Morgan WT (1985) Biochemistry 24:5919
39. Choi CY (1999) Biochemistry 38:16916
40. Ziegler J, Chang RT, Wright DW (1999) J Am Chem Soc 121:2395
41. Slater AFG, Swiggard WJ, Orton BR, Flitter WD, Goldberg DE, Cerami A, Henderson GB (1991) Proc Natl Acad Sci USA 88:325
42. Bohle DS, Dinnebier RE, Madsen SK, Stephens PW (1997) J Biol Chem 272:713
43. Pasierb L (2005) The role of histidine-rich proteins in the biomineralization of hemozoin. Duquesne University Press
44. Pandey AV, Joshi R, Tekwani BL, Singh RL, Chauhan VS (1997) Mol Biochem Parasitol 90:281
45. Pandey AV, Babbarwal VK, Okoyey JN, Joshi R, Puri SK, Singh RL, Chauhan VS (2003) Biochem Biophys Res Commun 308:736
46. Ayres RU (1992) Proc Natl Acad Sci USA 89:815
47. Holmes JD, Richardson DJ, Saed S, Evans-Gowing R, Russel DA, Sodeau JR (1997) Microbiology 143:2521

48. Cunningham DP, Leon L, Lundie J (1993) Appl Environ Microbiol 59:7
49. Kneer R, Zenk MH (1992) Phytochemistry 31:2663
50. Perego P, Howell SB (1997) Toxicol Appl Pharmacol 147:312
51. Ahmad A, Mukherjee P, Mandal D, Senapati S, Khan MI, Kumar R, Sastry M (2002) J Am Chem Soc 124:12108
52. Holmes JD, Smith PR, Gowing RE, Richardson DJ, Russell DA, Sodeau JR (1995) Arch Microbiol 163:143
53. Mann S (1993) Nature 365:499
54. Slocik JM, Knecht MR, Wright DW (2004) In: Nalwa HS (ed) Encyclopedia of nanoscience and nanotechnology, vol 1. American Scientific, p 293
55. Rauser WE (1990) Ann Rev Biochem 59:61
56. Grill E, Winnacker EL, Zenk MH (1985) Science 230:674
57. Ruegsegger A, Schmutz D, Brunold C (1990) Plant Physiol 93:1579
58. Reese RN, Wagner GJ (1987) Biochem J 241:641
59. Rauser WE (1995) Plant Physiol 109:1141
60. Williams P, Keshavarz-Moore E, Dunnill P (1996) J Biotechnol 48:259
61. Al-Lahham A, Zimmermann M (1999) Yeast 15:385
62. Grill E, Loffler S, Winnacker EL, Zenk MH (1989) Proc Natl Acad Sci USA 86:6838
63. Ruotolo R, Peracchi A, Bolchi A, Infusini G, Amoresano A, Ottonello S (2004) J Biol Chem 279:14686
64. Grill E, Winnacker E-L, Zenk MH (1987) Proc Natl Acad Sci USA 84:439
65. Grill E, Winnacker EL, Zenk MH (1986) FEBS Lett 197:115
66. Cobbett CS (1999) Trends Plant Sci 4:335
67. Klapheck S, Schlunz S, Bergmann L (1995) Plant Physiol 107:515
68. Vatamaniuk OK, Mari S, Lu Y, Rea PA (2000) J Biol Chem 275:31451
69. Vogeli-Lange R, Wagner GJ (1990) Plant Physiol 92:1086
70. Ortiz DF, Kreppel L, Speiser DM, Scheel G, McDonald G, Ow DW (1992) EMBO J 11:3491
71. Johanning J, Strasdeit H (1998) Angew Chem Int Ed 37:2464
72. Bae W, Mehra RK (1998) J Inorg Biochem 69:33
73. Zheng L, White RH, Cash VL, Jack RF, Dean DR (1993) Proc Natl Acad Sci USA 90:2754
74. Mehra RK, Tarbet EB, Gray WR, Winge DR (1988) Proc Natl Acad Sci USA 85:8815
75. Dameron CT, Dance IG (1996) In: Mann S (ed) Biomimetic materials chemistry. Wiley, New York, p 69
76. Williams P, Keshavarz-Moore E, Dunnill P (1996) Enzyme Microb Technol 19:208
77. Dameron CT, Reese RN, Mehra RK, Kortan AR, Carroll PJ, Steigerwald ML, Brus LE, Winge DR (1989) Nature 338:596
78. Roberts CJ, Nothwehr SF, Stevens TH (1992) J Biol Chem 119:69
79. Li X-Z, Nikaido H, Williams KE (1997) J Bacteriol 179:6127
80. Mann S (1992) Nature 357:358
81. Haefeli C, Frankline C, Hardy K (1984) J Bacteriol 158:389
82. Klaus T, Joerger R, Olsson E, Granqvist C-G (1999) Proc Natl Acad Sci USA 96:13611
83. Slawson RM, Trevors JT, Lee H (1992) Arch Microbiol 158:398
84. Sarikaya M (1999) Proc Natl Acad Sci USA 96:14183
85. Mukherjee P, Ahmad A, Mandal D, Senapati S, Sainkar S, Khan MI, Ramani R, Parischa R, Ajayakumar PV, Alam M, Sastry M, Kumar R (2001) Angew Chem Int Ed 40:3585
86. Mukherjee P, Ahmad A, Mandal D, Senapati S, Sainkar S, Khan MI, Parischa R, Ajayakumar PV, Alam M, Kumar R, Sastry M (2001) Nano Lett 1:515

87. Ahmad A, Senapati S, Khan MI, Kumar R, Ramani R, Srinivas V, Sastry M (2003) Nanotechnology 14:824
88. Esumi K, Hosoya T, Suzuki A, Torigoe K (2000) Langmuir 16:2978
89. Slocik JM (2005) J Mater Chem 15:749
90. Ahmad A, Mukherjee P, Senapati S, Mandal D, Khan MI, Kumar R, Sastry M (2003) Colloids Surf B: Biointerfaces 28:313
91. Shankar SS, Ahmad A, Sastry M (2003) Biotech Prog 19:1627
92. Ahmad A, Senapati S, Khan MI, Kumar R, Sastry M (2003) Langmuir 19:3550
93. Mukherjee P, Senapati S, Mandal D, Ahmad A, Khan MI, Kumar R, Sastry M (2002) Chem Bio Chem 5:461
94. Shankar SS, Ahmad A, Pasricha R, Sastry M (2003) J Mater Chem 13:1822
95. Nair B, Pradeep (2002) Cryst Growth Des 2:293
96. Gardea-Torrsedey JL, Gomez E, Peralta-Videa JR, Parsons JG, Troiani H, Jose-Yacaman M (2003) Langmuir 19:1357
97. Gardea-Torrsedey JL, Parsons JG, Gomez E, Peralta-Videa J, Troiani HE, Santiago P, Yacaman JM (2002) Nano Lett 2:397
98. Carney CK, Pasierb L, Wright D (2005) ACS Symposium Series 903:263
99. Choi CYH, Schneider EL, Kim JM, Gluzman IY, Goldberg DE, Ellman JA, Marletta MA (2002) Chem Biol 9:881
100. Ziegler J, Pasierb L, Cole KA, Wright DW (2003) J Inorg Biochem 96:478
101. Ziegler J, Schuerle T, Pasierb L, Kelly C, Elamin A, Cole KA, Wright DW (2000) Inorg Chem 39:3731
102. Whitling JM, Spreitzer G, Wright DW (2000) Adv Mater (Weinheim, Germany) 12:1377

Author Index Volumes 251–271

The volume numbers are printed in italics

Subject Index